

**STUDY ON PHOTOLUMINESCENCE PROPERTIES
OF UNSENSITIZED AND Bi^{3+} SENSITIZED $\text{M}_2\text{O}_3\text{:Ln}^{3+}$
($\text{M} = \text{Gd}, \text{Y}$ & $\text{Ln}^{3+} = \text{Eu}^{3+}, \text{Sm}^{3+}$) PHOSPHORS**

by

OINAM SHANTAJIT SINGH



Submitted to

NAGALAND UNIVERSITY

In Partial Fulfillment of the Requirements for Award of Degree

of

DOCTOR OF PHILOSOPHY IN PHYSICS

**DEPARTMENT OF PHYSICS
SCHOOL OF SCIENCES
NAGALAND UNIVERSITY
LUMAMI – 798627
NAGALAND INDIA**

2022



नागालैण्ड विश्वविद्यालय NAGALAND UNIVERSITY

DEPARTMENT OF PHYSICS

(संसद द्वारा पारित अधिनियम 1989, क्रमांक 35 के अंतर्गत स्थापित केंद्रीय विश्वविद्यालय)
(A Central University established by an Act of Parliament No.35 of 1989)

मुख्यालय : लुमामी, जिला : जुन्हेबोटो (नागालैण्ड), पिनकोड - 798627

Hqrs: Lumami, Dist. Zunheboto (Nagaland), Pin Code - 798627

वेबसाइट / Website : www.nagalanduniversity.ac.in

DECLARATION

I, Mr. **OINAM SHANTAJIT SINGH**, bearing registration No. **854/2020** dated **22/09/2016** hereby declare that the subject matter of the thesis entitled “*Study on Photoluminescence Properties of unsensitized and Bi^{3+} sensitized $M_2O_3:Ln^{3+}$ ($M = Gd, Y \& Ln^{3+} = Eu^{3+}, Sm^{3+}$) Phosphors*” is the record of work done by me, that the contents of this thesis did not form basis of the award of any previous degree to me or to the best of my knowledge to anybody else, and the thesis has not been submitted by me for any research degree in any other university/institute. This is being submitted to the Nagaland University for the degree of Doctor of Philosophy in Physics.

(Oinam Shantajit Singh)

(Dr. Naorem Shanta Singh)

Supervisor

(Prof. M. S. Rawat)

Dean, School of Sciences &

Head of the Department (i/c)



नागालैण्ड विश्वविद्यालय NAGALAND UNIVERSITY

DEPARTMENT OF PHYSICS

(संसद द्वारा पारित अधिनियम 1989, क्रमांक 35 के अंतर्गत स्थापित केंद्रीय विश्वविद्यालय)
(A Central University established by an Act of Parliament No.35 of 1989)

मुख्यालय : लुमामी, जिला : जुन्हेबोटो (नागालैण्ड), पिनकोड - 798627

Hqrs: Lumami, Dist. Zunheboto (Nagaland), Pin Code - 798627

वेबसाइट / Website : www.nagalanduniversity.ac.in

CERTIFICATE

This is to certify that the thesis entitled “*Study on Photoluminescence Properties of unsensitized and Bi^{3+} sensitized $M_2O_3:Ln^{3+}$ ($M = Gd, Y$ & $Ln^{3+} = Eu^{3+}, Sm^{3+}$) phosphors*” is a record of original research work carried out by **Mr. Oinam Shantajit Singh** under my supervision. He is a registered research scholar, bearing the registration no. **854/2020** dated **22/09/2016** of the Department of Physics.

The candidate has fulfilled all the requirements of Ph.D. regulations of Nagaland University for the submission of thesis. The work is original and neither the thesis nor any part of it has been submitted elsewhere for the award of any degree or distinctions. The thesis, therefore, forwarded for adjudication and consideration for the award of degree of Doctorate of Philosophy in Physics under Nagaland University.

(Dr. Naorem Shanta Singh)

Supervisor

ACKNOWLEDGMENT

I would like to express my sincere thanks to Dr. Naorem Shanta Singh, Assistant Professor, Department of Physics, Nagaland University, Lumami, Nagaland for his supervision, inspiration, guidance, constant encouragement and support throughout the course of the research work. Without him I would not have been able to complete my thesis.

I would like to express my sincere thanks to Professors M. Indira Devi and Sangyu Yaden, then Deans, School of Sciences and HoD in-charge of the Department of Physics for their support during my research work.

I am also thankful to other faculty members of the Department of Physics Dr. Y. Sundarayya, Dr. Ng. Bedamani Singh and Dr. Sanatombi Sorokhaibam for sharing their valuable knowledge and encouragement towards my research work.

A very big thanks to my brother as well as my Research Mate Mr. Ranjoy Wangkhem for all the help he had extended during my research work which will ever remain unforgettable throughout my journey of life. Also, I am very thankful to my beloved Lab. Mate Dr. N. Premananda Singh for his valuable help during my research work. I am also thankful to my other Lab. Mates Takhe Yaba and Kedukhro Khupfu for their help. I am also thankful to my fellow research scholars Kulendra Borah and Sahab Uddin Mazumdar for their support.

I sincerely appreciate Dr. W. Shambhunath Singh, Principal, Manipur College, Imphal and the faculty members of the Department of Physics, Manipur College, Imphal for their physical and moral support.

My Sincere thanks to SAIF, NEHU, Shillong for providing TEM images. I also thank NIT, Manipur and NIT Nagaland, Nagaland for the XRD measurements.

Last but not the least, I am extremely grateful to my family members for their support and encouragement throughout my research work.

(OINAM SHANTAJIT SINGH)

Department of Physics
Nagaland University, Lumami

NAGALAND UNIVERSITY



Sl. No. : 16- 35960

STATEMENT OF MARKS

Ph. D COURSE WORK EXAMINATION 2017

DEPARTMENT OF PHYSICS

The following are the marks secured by Mr. Oinam Shantajit Singh
Roll No. PHPH1602 of Ph.D Course Work Examination held in 2017

Subject(s)/Paper(s)	Max. Marks	Minimum Qualifying Marks	Marks Secured
Course No. PHY-801 Research Methodology	100	50	64
Course No. PHY-802 (B) Experimental Techniques (Theory)	100	50	65
Course No. PHY-803 Literature review, Report Writing and Seminar	100	50	70
Total Aggregate Marks			199
Average Pass Mark – 50 %			

Result	Division	Percentage
Passed	I Division	66 %



COE/Dy. Reg./AR (Exams)

NAGALAND UNIVERSITY



HEAD QUARTERS : LUMAMI

Ph. D COURSE WORK EXAMINATION

This is to certify that Mr/Ms. Oinam Shantajit Singh
of Nagaland University bearing Roll No. PHPH1602 is qualified in the Ph.D Course Work Examination
in the Department of Physics Nagaland University held in the Year 20. 17

Head of the Department
Head of Department of Physics
Nagaland University, Lumami

Dean
Dean
School of Science
Nagaland University
Hq. Lumami Nagaland

Preface

Lately, enormous interests have grown among the researchers towards the various applications of lanthanide activated nanophosphors. This is because of the fact that the lanthanide activated phosphors possess numerous such as display devices, phosphor lamps, cathode ray tubes, bioimaging, drug delivery, metal ions sensing, anti-counterfeiting ink, as well as active laser materials. Generally, in lanthanide activated phosphors, the light emission is generated from the $4f-4f$ transitions. These are sharp, true in colour emission and signature of the particular lanthanide use. The various instances may be mentioned. Various lanthanide activated luminescent materials, such as $\text{Y}_2\text{O}_3:\text{Eu}^{3+}$, $\text{YVO}_4:\text{Eu}^{3+}$, $\text{GdVO}_4:\text{Eu}^{3+}$, $\text{CaWO}_4:\text{Eu}^{3+}$, $\text{CaMoO}_4:\text{Eu}^{3+}$, $\text{SrWO}_4:\text{Eu}^{3+}$, SrF_2 , CaF_2 , etc. good red emitting phosphors. Recently, these red phosphors have shown promising for solid state lighting applications. Also, these materials have shown capable of detecting the heavy metal ions present in water. The up-converted lanthanide based luminescent materials such as NaGdF_4 , LaF_3 , GdF_3 , NaYF_4 , etc. have found applications in various optical imaging and magnetic resonance imaging applications. These materials are useful for real time imaging during drug delivery.

The present thesis entitled “*Study on Photoluminescence Properties of unsensitized and Bi^{3+} sensitized $\text{M}_2\text{O}_3:\text{Ln}^{3+}$ ($M = \text{Gd}, \text{Y}$ & $\text{Ln}^{3+} = \text{Eu}^{3+}, \text{Sm}^{3+}$)*” discusses the luminescence and energy transfer in the lanthanide activated Gd_2O_3 and Y_2O_3 phosphors. The theis comprises of six chapters. The thesis elaborates the synthesis, characterizations and luminescence properties using techniques such as X-ray diffraction, transmission electron microscopy, infrared spectroscopy and spectrofluorometer, etc.

Chapter 1 addresses the general introduction and literature review. Basic fundamentals of luminescence are briefly presented. Here, the properties of some of lanthanide ions and their role in lanthanide are mentioned in short. The various synthesis methods suitable for synthesizing phosphor materials and some of the applications are summarized.

Chapter 2 discusses the basic principle and working of the instruments used during the entire research work is presented in brief.

Chapter 3 focuses on the luminescence studies of Eu^{3+} or Sm^{3+} activated Y_2O_3 phosphors. Hydrothermal synthesis technique is successful for synthesizing rod shape Y_2O_3 based phosphors. Investigation of the luminescence properties of the $\text{Y}_2\text{O}_3:\text{Eu}^{3+}$ shows the optimum range of Eu^{3+} concentration $\sim 13 - 17$ at.% Eu^{3+} . Around this range, the emission of the Eu^{3+} is efficient. Luminescence study shows the more Eu^{3+} occupation in the C_2 site symmetry of the Y_2O_3 . This is further supported from the asymmetric ratio parameter as well as the second order crystal parameter. This scenario is independent of various ranges of Eu^{3+} use as well as the different excitation wavelengths use for emission of Eu^{3+} . In the case of Sm^{3+} activated phosphors, the emission of Sm^{3+} mostly lies in the orange-red region of the electromagnetic spectrum. The concentration quenching the emission is much faster in the case of Sm^{3+} doping compared to Eu^{3+} . Both the luminescence and decay lifetime results corroborate the concentration quenching and enhancement in the luminescence with increasing annealing temperature.

Chapter 4 devotes the energy transfer occurred due to the sensitization with Bi^{3+} in Eu^{3+} or Sm^{3+} activated Y_2O_3 . The energy transfer from the host Bi^{3+} to the activator Eu^{3+} or Sm^{3+} is well investigated from the photoluminescence spectroscopy. And it is found to be occurred mainly through dipole-dipole interaction. Luminescence and decay lifetime studies clearly confirm the existence of energy transfer from the Bi^{3+} to the excited states of Eu^{3+} and Sm^{3+} . Not only sensitizing effect, it also can shift the excitation wavelength necessary for efficient emission towards near ultraviolet region compared to ultraviolet region which common in unsensitized Y_2O_3 based phosphors. In sensitized $\text{Y}_2\text{O}_3:\text{Eu}^{3+}$, the emission colour is very much tunable with the variation of Eu^{3+} concentration and wavelength of excitation. Interestingly, red emission of $\text{Y}_2\text{O}_3:\text{Eu}^{3+}$ can be obtained by various wavelength excitations. Though, in sensitized $\text{Y}_2\text{O}_3:\text{Sm}^{3+}$, such flexibility is not observed.

Chapter 5 presents on the luminescence studies of Eu^{3+} or Sm^{3+} activated Gd_2O_3 phosphors. Hydrothermal synthesis technique adopted gives hexagonal phase $\text{Gd}(\text{OH})_3$ and post annealing changes the phase to cubic Gd_2O_3 having rod shape. Optimum range of Eu^{3+} concentration ~ 17 at.% is obtained for good emission intensity. Around this range, the emission of the Eu^{3+} is efficient. The more Eu^{3+} occupation in the C_2 site symmetry of the Gd_2O_3 is confirmed from the luminescence studies. The asymmetric

ratio greater than one as well as high value of second order crystal parameter also suggest the occupation of Eu^{3+} in an asymmetric environment. This environment does not change with the variation of doping concentration of Eu^{3+} as well as the different excitation wavelengths used for emission of Eu^{3+} . In the case of Sm^{3+} activated Gd_2O_3 , the emission of Sm^{3+} is mostly better in the range of 2 – 4 at.% Sm^{3+} . Beyond this, heavy concentration quenching exists. Both the luminescence and decay lifetime results corroborate the concentration quenching.

Chapter 6 will be concerned on the sensitization effect due to presence of Bi^{3+} sensitizer in Eu^{3+} or Sm^{3+} activated Gd_2O_3 phosphors. Hydrothermal synthesis technique adopted gives hexagonal phase $\text{Gd}(\text{OH})_3$ and post annealing changes the phase to cubic Gd_2O_3 having rod shape. From the luminescence studies, it is clear that energy transfer from the Bi^{3+} to the excited states of Eu^{3+} and Sm^{3+} exists. The energy transfer so exist occurs through multipolar interactions between the sensitizer and activator ions present in Gd_2O_3 . In both the cases, the occurrence of energy transfer from Bi^{3+} to the Eu^{3+} is corroborated from both the steady state and decay lifetime studies. Strong red emission from Bi^{3+} sensitized $\text{Gd}_2\text{O}_3:\text{Eu}^{3+}$ phosphors under wide range of excitation at 330 – 380 nm. This gives advantage is multiple uses including solid state lighting applications. However, such flexibility is not observed in $\text{Gd}_2\text{O}_3:\text{Sm}^{3+}$ phosphors.

List of Figures

	Page No.
Fig. 1.1. Schematic diagram showing different types of photoluminescence.	4
Fig. 1.2. Energy levels associated with lanthanide ions	10
Fig. 1.3. Schematic representation of (a) Top-down and (b) Bottom-up synthesis technique	12
Fig. 1.4. Schematic representation of energy transfer from Bi ³⁺ ions to Eu ³⁺ ions.	14
Fig. 2.1. Schematic representation of Bragg's law for X-ray diffraction	26
Fig. 2.2. Schematic picture of a Transmission electron microscope.	28
Fig. 2.3. A schematic diagram of an FTIR spectrometer.	29
Fig. 2.4. A schematic diagram of a Spectrofluorometer	31
Fig. 2.5. Electronic schematic for TCSPC.	31
Fig. 3.1. The X-ray diffraction (XRD) patterns of (a) 500 and (b) 900 °C annealed Y ₂ O ₃ :Eu ³⁺ (Eu ³⁺ = 1, 3, 7, 11, 15, 19, 21 and 25 at.%).	37
Fig. 3.2. The X-ray diffraction (XRD) patterns of (a) 500 and (b) 900 °C annealed Y ₂ O ₃ :Sm ³⁺ (Sm ³⁺ = 0, 1, 2, 4, 6, 8, 10 and 12 at.%).	38
Fig. 3.3. FTIR spectra of 500 and 900 °C annealed Y ₂ O ₃ :Eu ³⁺ (3 at.%) samples.	38
Fig. 3.4. TEM images (a) along with HR-TEM (b) and SAED images (c) of a selected region of 500 °C annealed Y ₂ O ₃ :Eu ³⁺ (3 at.%).	39
Fig. 3.5. TEM images along with HR-TEM of 900 °C annealed Y ₂ O ₃ :Eu ³⁺ (3 at.%).	40
Fig. 3.6. PL excitation spectra of (a) 500 and (b) 900 °C annealed Y ₂ O ₃ :Eu ³⁺ samples monitored at $\lambda_{em} = 611$ nm. Concentrations of Eu ³⁺ are given in the figure.	40
Fig. 3.7. Expanded region (~220 – 300 nm) region of PL excitation spectra of (a) 500 and (b) 900 annealed Y ₂ O ₃ :Eu ³⁺ samples monitored at $\lambda_{em} = 611$ nm. Concentrations of Eu ³⁺ are given in the figure.	41
Fig. 3.8. PL emission spectra of Y ₂ O ₃ :Eu ³⁺ (7 at.%) samples annealed at (a) 500 and (b) 900 °C. Excitation wavelengths are 255 nm (Eu–O CTB), 393 (Eu ³⁺ , ⁷ F ₀ → ⁵ L ₆) and 464 (Eu ³⁺ , ⁷ F ₀ → ⁵ D ₂) nm.	41
Fig. 3.9. PL emission spectra of 500 (a, c, e) and 900 °C (b, d, f) of Y ₂ O ₃ :Eu ³⁺ (Eu ³⁺ = 1, 3, 5, 7, 9, 13, 17, 21 and 25 at.%) samples. Excitation wavelengths are given in the figures.	43
Fig. 3.10. Asymmetric ratio at different concentrations in (a) 500 and (b) 900 °C annealed Y ₂ O ₃ :Eu ³⁺ (Eu ³⁺ = 1, 3, 5, 7, 9, 13, 17, 21 and 25 at.%) samples. $\lambda_{ex} = 255, 393$ and 464 nm.	44
Fig. 3.11. Variation of B_{20} versus Eu ³⁺ concentration of (a) 500 and (b) 900 °C annealed Y ₂ O ₃ :Eu ³⁺ (Eu ³⁺ 1, 3, 5, 7, 9, 13, 17, 21 and 25 at.%) samples under the excitation of 255 nm. Solid lines are guide to the eye.	45

- Fig. 3.12.** Integrated emission intensities of $\text{Y}_2\text{O}_3:\text{Eu}^{3+}$ ($\text{Eu}^{3+} = 1, 3, 5, 7, 9, 13, 17, 21$ and 25 at.%) samples. $\lambda_{\text{ex}} = 255, 393$ and 464 nm. 45
- Fig. 3.13.** PL decay curves of $^5\text{D}_0$ level of Eu^{3+} emission in 500 (a & c) and 900 °C (b & d) $\text{Y}_2\text{O}_3:\text{Eu}^{3+}$ ($1, 3, 5, 7, 9, 13, 17, 21$ and 25 at.%) samples. Excitation wavelengths are 255 and 464 nm. 47
- Fig. 3.14.** Typical fitting of decay curve for Eu^{3+} emission ($\lambda_{\text{ex}} = 255$ and 464 nm and $\lambda_{\text{em}} = 611$ nm) in $\text{Y}_2\text{O}_3:\text{Eu}^{3+}$ (7 at.%) sample. 47
- Fig. 3.15.** CIE chromaticity coordinate positions of (a) 500 and (b) 900 °C annealed $\text{Y}_2\text{O}_3:\text{Eu}^{3+}$ ($1, 3, 5, 7, 9, 13, 17, 21$ and 25 at.%) samples. Excitation wavelength is 255 nm. 48
- Fig. 3.16.** PL excitation spectra of (a) 500 and (b) 900 °C Annealed $\text{Y}_2\text{O}_3:\text{Sm}^{3+}$ ($0.5, 1, 2, 4, 6, 8, 10$, and 12 at.%) samples monitored at $\lambda_{\text{em}} = 606$ nm. 49
- Fig. 3.17.** PL emission spectra of $\text{Y}_2\text{O}_3:\text{Sm}^{3+}$ ($0.5, 1, 2, 4, 6, 8, 10$ and 12 at.%) samples monitored at $\lambda_{\text{ex}} = 406$ nm. 50
- Fig. 3.18.** Integrated PL emission of 500 and 900 °C annealed $\text{Y}_2\text{O}_3:\text{Sm}^{3+}$ ($0.5, 1, 2, 4, 6, 8, 10$ and 12 at.%) samples. Excitation wavelength is 406 nm. 50
- Fig. 3.19.** PL decay curves of $^5\text{G}_{5/2}$ level of Sm^{3+} emission in $\text{Y}_2\text{O}_3:\text{Sm}^{3+}$ ($1, 2, 4, 6$, and 8 at.%). $\lambda_{\text{em}} = 606$ nm and $\lambda_{\text{ex}} = 406$ nm. 51
- Fig. 3.20.** CIE chromaticity coordinate positions of $\text{Y}_2\text{O}_3:\text{Sm}^{3+}$ ($0.5, 1, 2, 4, 6, 8, 10$ and 12 at.%) samples excited at 406 nm. 52
- Fig. 4.1.** The X-ray diffraction (XRD) patterns of (a) 500 and (b) 900 °C annealed $\text{Y}_2\text{O}_3:\text{Eu}^{3+}$ ($\text{Eu}^{3+} = 1, 3, 5, 7, 11, 13$ and 17 at.%)/ Bi^{3+} (1 at.%). 61
- Fig. 4.2.** The X-ray diffraction (XRD) patterns of (a) 500 and (b) 900 °C annealed $\text{Y}_2\text{O}_3:\text{Sm}^{3+}$ ($\text{Sm}^{3+} = 0, 1, 2, 4, 6, 8, 10$ and 12 at.%)/ Bi^{3+} (1 at.%). 62
- Fig. 4.3.** FT-IR spectra of 500 and 900 °C annealed $\text{Y}_2\text{O}_3:\text{Bi}^{3+}$ (1 at.%)/ Eu^{3+} (3 at.%) samples. 63
- Fig. 4.4.** (a) TEM (b) HRTEM image and (c) SAED pattern of 500 °C annealed 1 at.% Bi^{3+} sensitized $\text{Y}_2\text{O}_3:\text{Eu}^{3+}$ (3 at.%). 64
- Fig. 4.5.** (a) TEM (b) HRTEM image and (c) SAED pattern of 900 °C annealed 1 at.% Bi^{3+} sensitized $\text{Y}_2\text{O}_3:\text{Eu}^{3+}$ (3 at.%). 64
- Fig. 4.6.** PL (a) emission spectra at $\lambda_{\text{ex}} = 315\text{--}375$ nm (with the increment of 5 nm), and (b) excitation spectra monitored at $\lambda_{\text{em}} = 400\text{--}550$ nm (with the increment of 10 nm) of 500 °C annealed $\text{Y}_2\text{O}_3:\text{Bi}^{3+}$ (1 at.%). 65
- Fig. 4.7.** PL (a) emission spectra at $\lambda_{\text{ex}} = 315\text{--}375$ nm (with the increment of 5 nm), and (b) excitation spectra monitored at $\lambda_{\text{em}} = 400\text{--}550$ nm (with the increment of 10 nm) of 900 °C annealed $\text{Y}_2\text{O}_3:\text{Bi}^{3+}$ (1 at.%). 66
- Fig. 4.8.** PL excitation spectra of 500 °C (Right) and 900 °C (Left) annealed 68

$\text{Y}_2\text{O}_3:\text{Bi}^{3+}$ ($\text{Bi}^{3+} = 0, 0.25, 0.5, 0.75, 1, 3, 5$ and 7 at.%) / Eu^{3+} (5 at.%). Emission wavelength, $\lambda_{\text{em}} = 611$ nm. (insets show the comparison of Bi^{3+} absorption with Eu-O CT band in 1 at.% Bi^{3+} sensitized $\text{Y}_2\text{O}_3:\text{Eu}^{3+}$ (5 at.%))

Fig. 4.9. PL emission spectra of (a) 500 and (b) 900 °C annealed $\text{Y}_2\text{O}_3:\text{Eu}^{3+}$ (7 at.%) / Bi^{3+} (1 at.%). Excitation wavelengths, $\lambda_{\text{ex}} = 255, 330$ and 371 nm. 68

Fig. 4.10 PL emission spectra of 500 °C annealed samples of $\text{Y}_2\text{O}_3:\text{Eu}^{3+}$ (5 at.%) / Bi^{3+} (x at.% = $0.25, 0.5, 0.75, 1, 3, 5, 7$) under the excitation wavelengths of (a) 330 and (b) 371 nm. 69

Fig. 4.11. Variation of B_{20} versus Eu^{3+} concentration of (a & c) 500 and (b & d) 900 °C annealed $\text{Y}_2\text{O}_3:\text{Eu}^{3+}$ (x at.% = $1, 2, 3, 5, 7, 9, 11, 13, 15, 17, 19$) / Bi^{3+} (1 at.%) samples. Excitation wavelengths (λ_{ex}) are indicated in the graph. Dash (red) line is the guide to the eye. 71

Fig. 4.12. Spectral overlap between the excitation spectrum of Eu^{3+} ions and emission spectrum of Bi^{3+} ions in Y_2O_3 . 72

Fig. 4.13. Normalized PL (normalized at 611 nm) emission spectra of (a) 500 and (b) 900 °C annealed samples of $\text{Y}_2\text{O}_3:\text{Eu}^{3+}$ (x at.% = $0, 1, 2, 3, 5, 7, 9, 11, 13, 15, 17, 19$) / Bi^{3+} (1 at.%) under the excitation wavelengths of 330 nm. 73

Fig. 4.14. Normalized PL (normalized at 611 nm) emission spectra of (a) 500 and (b) 900 °C annealed samples of $\text{Y}_2\text{O}_3:\text{Eu}^{3+}$ (x at.% = $0, 1, 2, 3, 5, 7, 9, 11, 13, 15, 17, 19$) / Bi^{3+} (1 at.%) under the excitation wavelengths of 371 nm. 73

Fig. 4.15. Energy transfer efficiency (η_T) of different concentration of Eu^{3+} (x at.% = $0, 1, 2, 3, 5, 7, 9, 11, 13, 15, 17, 19$) in Bi^{3+} (1 at.%) sensitized Y_2O_3 annealed samples. Descriptions are given in the legend. 74

Fig. 4.16. Dependence of I_{S_0}/I_S of Bi^{3+} on (a) $C_{\text{Bi}^{3+}+\text{Eu}^{3+}}^{6/3}$, (b) $C_{\text{Bi}^{3+}+\text{Eu}^{3+}}^{8/3}$, (c) $C_{\text{Bi}^{3+}+\text{Eu}^{3+}}^{10/3}$ (annealed at 500 °C) and (d) $C_{\text{Bi}^{3+}+\text{Eu}^{3+}}^{6/3}$, (e) $C_{\text{Bi}^{3+}+\text{Eu}^{3+}}^{8/3}$, (f) $C_{\text{Bi}^{3+}+\text{Eu}^{3+}}^{10/3}$ (annealed at 900 °C). Excitation wavelength for both cases is 330 nm. 76

Fig. 4.17. Dependence of I_{S_0}/I_S of Bi^{3+} on (a) $C_{\text{Bi}^{3+}+\text{Eu}^{3+}}^{6/3}$, (b) $C_{\text{Bi}^{3+}+\text{Eu}^{3+}}^{8/3}$, (c) $C_{\text{Bi}^{3+}+\text{Eu}^{3+}}^{10/3}$ (annealed at 500 °C) and (d) $C_{\text{Bi}^{3+}+\text{Eu}^{3+}}^{6/3}$, (e) $C_{\text{Bi}^{3+}+\text{Eu}^{3+}}^{8/3}$, (f) $C_{\text{Bi}^{3+}+\text{Eu}^{3+}}^{10/3}$ (annealed at 900 °C). Excitation wavelength for both cases is 371 nm. 76

Fig. 4.18. PL Decay lifetime curves of Bi^{3+} ($\lambda_{\text{em}} = 495$ nm and $\lambda_{\text{ex}} = 330$ nm) of (a) 500 and (b) 900 °C annealed $\text{Y}_2\text{O}_3:\text{Eu}^{3+}$ (x at.%) / Bi^{3+} (1 at.%) samples. Inset shows the PL decay time, τ_{av} (ns) against the Eu^{3+} concentration. 78

Fig. 4.19. PL Decay lifetime curves of $^5\text{D}_0$ level of Eu^{3+} of (a & b) 500 and (c & d) 900 °C annealed $\text{Y}_2\text{O}_3:\text{Eu}^{3+}$ (x at.%) / Bi^{3+} (1 at.%) samples. 79

Excitation wavelengths: (a & c) 330 and (b & d) 371 nm.

- Fig.4.20.** CIE chromaticity coordinate positions of $\text{Y}_2\text{O}_3:\text{Eu}^{3+}$ (x at.%)/ Bi^{3+} (1 at.%) for (a) 500 and (b) 900 °C annealed samples excited at 330, 355 and 371 nm respectively (CIE Coordinates, See Table 4.6). 81
- Fig. 4.21.** Physical photographs of $\text{Y}_2\text{O}_3:\text{Eu}^{3+}$ (x at.%)/ Bi^{3+} (1 at.%) (Eu^{3+} concentration in at.% is indicated on the top row) 500 °C annealed samples excited at (a) 330 nm, (c) 355 nm and (e) 371 nm, along with 900 °C annealed samples excited at (b) 330 nm, (d) 355 nm and (f) 371 nm, respectively. 83
- Fig. 4.22.** CIE chromaticity coordinate positions of $\text{Y}_2\text{O}_3:\text{Eu}^{3+}$ (3 at.%)/ Bi^{3+} (1 at.%) for (a) 500 and (b) 900 °C annealed samples under different wavelengths (positioned in the colour space). (Also see Table 4.7). 83
- Fig. 4.23.** Physical photographs of $\text{Y}_2\text{O}_3:\text{Eu}^{3+}$ (3 at.%)/ Bi^{3+} (1 at.%) for (a) 500 °C and (b) 900 °C annealed samples excited at different wavelength (Top row indicates the excitation wavelengths). 84
- Fig. 4.24.** PL excitation spectra of 900 °C annealed Bi^{3+} (1 at.%) sensitized $\text{Y}_2\text{O}_3:\text{Sm}^{3+}$ (1, 2, 4, 6, 8, 10 and 12 at.%) samples monitored at $\lambda_{\text{em}} = 606$ nm 85
- Fig. 4.25.** PL emission spectra of 900 °C annealed $\text{Y}_2\text{O}_3:\text{Bi}^{3+}$ (1 at.%)/ Sm^{3+} (1 at.%) samples under different excitations at 335 nm (Bi^{3+} , related to C_2 site) and 375 nm (Bi^{3+} , related to S_6 site) and 406 nm ($f-f$ absorption). 86
- Fig. 4.26.** Normalized PL emission of (a) 500 and (b) 900 °C annealed $\text{Y}_2\text{O}_3:\text{Bi}^{3+}$ (1 at.%)/ Sm^{3+} (0, 0.5, 1, 2, 4, 6, 8, 10 and 12 at.%) samples under the excitation at 330 nm. 87
- Fig. 4.27.** Normalized PL emission of (a) 500 and (b) 900 °C annealed $\text{Y}_2\text{O}_3:\text{Bi}^{3+}$ (1 at.%)/ Sm^{3+} (0, 0.5, 1, 2, 4, 6, 8, 10 and 12 at.%) samples under the excitation at 370 nm. 87
- Fig. 4.28.** Energy transfer efficiency (η_T) of different concentration of Sm^{3+} ($\text{Sm}^{3+} = 0, 0.5, 1, 4, 6, 8, 10$ and 12 at.%) in Bi^{3+} (1 at.%) sensitized Y_2O_3 samples annealed at (a) 500 and (b) 900 °C. 87
- Fig. 4.29.** Energy transfer efficiency (η_T) of different concentration of Sm^{3+} ($\text{Sm}^{3+} = 0, 0.5, 1, 4, 6, 8, 10$ and 12 at.%) in Bi^{3+} (1 at.%) sensitized Y_2O_3 samples annealed at (a) 500 and (b) 900 °C. 88
- Fig. 4.30.** Dependence of I_{S_0}/I_S of Bi^{3+} on (a) $C_{\text{Bi}^{3+}+\text{Sm}^{3+}}^{6/3}$, (b) $C_{\text{Bi}^{3+}+\text{Sm}^{3+}}^{8/3}$, (c) $C_{\text{Bi}^{3+}+\text{Sm}^{3+}}^{10/3}$ ($\lambda_{\text{ex}} = 330$ nm) and (d) $C_{\text{Bi}^{3+}+\text{Sm}^{3+}}^{6/3}$, (e) $C_{\text{Bi}^{3+}+\text{Sm}^{3+}}^{8/3}$, (f) $C_{\text{Bi}^{3+}+\text{Sm}^{3+}}^{10/3}$ ($\lambda_{\text{ex}} = 370$ nm) for samples annealed at 500 °C. 89
- Fig. 4.31.** Dependence of I_{S_0}/I_S of Bi^{3+} on (a) $C_{\text{Bi}^{3+}+\text{Sm}^{3+}}^{6/3}$, (b) $C_{\text{Bi}^{3+}+\text{Sm}^{3+}}^{8/3}$, (c) $C_{\text{Bi}^{3+}+\text{Sm}^{3+}}^{10/3}$ ($\lambda_{\text{ex}} = 330$ nm) and (d) $C_{\text{Bi}^{3+}+\text{Sm}^{3+}}^{6/3}$, (e) $C_{\text{Bi}^{3+}+\text{Sm}^{3+}}^{8/3}$, (f) $C_{\text{Bi}^{3+}+\text{Sm}^{3+}}^{10/3}$ ($\lambda_{\text{ex}} = 370$ nm) for samples annealed at 900 °C. 89
- Fig. 4.32.** TCSPC decay profiles of Bi^{3+} (1 at.%) in $\text{Gd}_2\text{O}_3:\text{Sm}^{3+}$ (0, 1, 2, 4, 6, 8, and 10 at.%) samples annealed at (a) 500 and (b) 900 °C. 90

Excitation and emission wavelengths were monitored at 330 and 504 nm respectively. Inset shows the calculated average lifetime values at different concentration of Sm^{3+} .

- Fig. 4.33.** PL Decay lifetime curves of $^5\text{G}_{5/2}$ level of Sm^{3+} of (a & b) 500 and (c & d) 900 °C annealed $\text{Y}_2\text{O}_3:\text{Sm}^{3+}$ (x at.%)/ Bi^{3+} (1 at.%) samples. Excitation wavelengths: (a & c) 330 and (b & d) 370 nm. 91
- Fig. 4.34.** CIE chromaticity coordinate positions of $\text{Y}_2\text{O}_3:\text{Bi}^{3+}$ (1 at.%)/ Sm^{3+} (0.5, 1, 2, 4, 6, 8, 10 and 12 at.%) samples excited at (a and b) 330 nm, (c and d) 370 nm. 92
- Fig. 5.1** XRD patterns of as-prepared (a) $\text{Gd}(\text{OH})_3:\text{Eu}^{3+}$ ($\text{Eu}^{3+} = 1, 11$ and 19 at.%) and (b) $\text{Gd}(\text{OH})_3:\text{Sm}^{3+}$ ($\text{Sm}^{3+} = 1, 4$ and 10 at.%). 100
- Fig. 5.2** XRD patterns of 900 °C annealed samples of (a) $\text{Gd}_2\text{O}_3:\text{Eu}^{3+}$ ($\text{Eu}^{3+} = 1, 3, 7, 11, 15$ and 19 at.%) and (b) $\text{Gd}_2\text{O}_3:\text{Sm}^{3+}$ ($\text{Sm}^{3+} = 1, 2, 4, 6, 8$ and 10 at.%). 100
- Fig. 5.3.** FT-IR spectra of as-prepared (a) $\text{Gd}(\text{OH})_3:\text{Eu}^{3+}$ (5 at.%) and (b) 900 °C annealed $\text{Gd}_2\text{O}_3:\text{Eu}^{3+}$ (5 at.%) samples. 101
- Fig. 5.4.** TEM images (a) along with HR-TEM (b) and SAED images (c) of a selected region of as-prepared $\text{Gd}(\text{OH})_3:\text{Eu}^{3+}$ (9 at.%). 102
- Fig. 5.5.** TEM images along with HR-TEM image of 900 °C annealed $\text{GdO}_3:\text{Eu}^{3+}$ (9 at.%). 103
- Fig. 5.6.** PL excitation spectra of $\text{Gd}_2\text{O}_3:\text{Eu}^{3+}$ ($\text{Eu}^{3+} = 1, 3, 7, 11, 15, 19, 21$ and 25 at.%) samples monitored at $\lambda_{\text{em}} = 611$ nm 1.4
- Fig. 5.7.** Expanded region ($\sim 250 - 280$ nm) region of PL excitation spectra of $\text{Gd}_2\text{O}_3:\text{Eu}^{3+}$ ($\text{Eu}^{3+} = 1, 3, 7, 11, 15, 19, 21$ and 25 at.%) samples monitored at $\lambda_{\text{em}} = 611$ nm 104
- Fig. 5.8.** PL emission spectra of $\text{Gd}_2\text{O}_3:\text{Eu}^{3+}$ (7 at.%) samples under different excitations at 257 nm (Eu–O CT), 274 nm (Gd^{3+} , S–I), 335 nm, 393 (Eu^{3+} , $^7\text{F}_0 \rightarrow ^5\text{L}_6$) and 464 (Eu^{3+} , $^7\text{F}_0 \rightarrow ^5\text{D}_2$) nm. Inset shows the comparison of emission intensities at these excitation wavelengths. 105
- Fig. 5.9.** PL emission spectra of $\text{Gd}_2\text{O}_3:\text{Eu}^{3+}$ ($\text{Eu}^{3+} = 1, 3, 7, 11, 15, 19, 21$ and 25 at.%) samples. $\lambda_{\text{ex}} =$ (a) 255, (b) 274 (c) 393 and (d) 464 nm. 105
- Fig. 5.10.** Asymmetric ratio at different concentration of Eu^{3+} in $\text{Gd}_2\text{O}_3:\text{Eu}^{3+}$ ($\text{Eu}^{3+} = 1, 3, 7, 11, 15, 19, 21$ and 25 at.%) samples. $\lambda_{\text{ex}} = 255, 274, 393$ and 464 nm. 107
- Fig. 5.11.** Variation of B_{20} versus Eu^{3+} concentration of $\text{Gd}_2\text{O}_3:\text{Eu}^{3+}$ ($\text{Eu}^{3+} = 1, 3, 7, 11, 17, 21$ and 25 at.%) samples. Excitation wavelengths (λ_{ex}) are indicated in the graph. Dash (red) line is guide to the eye. 108
- Fig. 5.12.** Integrated emission intensities of $\text{Gd}_2\text{O}_3:\text{Eu}^{3+}$ ($\text{Eu}^{3+} = 1, 3, 7, 11, 15, 19, 21$ and 25 at.%) samples. $\lambda_{\text{ex}} = 255, 274, 393$ and 464 nm. 108
- Fig. 5.13.** PL decay curves of $^5\text{D}_0$ level of Eu^{3+} emission in $\text{Gd}_2\text{O}_3:\text{Eu}^{3+}$ (1, 3, 7, 11, 15, 19, 21 and 25 at.%) samples under (a) 255 and (b) 464 nm excitation and the emission is monitored at 611 nm. 109
- Fig. 5.14.** Typical fitting of decay curve for Eu^{3+} emission ($\lambda_{\text{ex}} = 464$ nm and 110

$\lambda_{em} = 611 \text{ nm}$) in $\text{Gd}_2\text{O}_3:\text{Eu}^{3+}$ (7 at.%) sample.	
Fig. 5.15. CIE chromaticity coordinate positions of $\text{Gd}_2\text{O}_3:\text{Eu}^{3+}$ (0, 1, 3, 5, 7, 9, 11, 13, 15, 17, 19, 21 and 23 at.%) samples excited at (a) 255 nm and (b) 274 nm.	111
Fig. 5.16. PL excitation spectra of $\text{Gd}_2\text{O}_3:\text{Sm}^{3+}$ (0.5, 1, 2, 4, 6, 8, 10 and 12 at.%) samples monitored at $\lambda_{em} = 606 \text{ nm}$.	112
Fig. 5.17. PL excitation spectra of $\text{Gd}_2\text{O}_3:\text{Sm}^{3+}$ (0.5, 1, 2, 4, 6, 8, 10 and 12 at.%) samples in the region of 395 – 420 nm.	112
Fig. 5.18. PL emission spectra of $\text{Gd}_2\text{O}_3:\text{Sm}^{3+}$ (0.5, 1, 2, 4, 6, 8, 10 and 12 at.%) samples monitored at $\lambda_{ex} = 406 \text{ nm}$.	113
Fig. 5.19. PL emission spectra of $\text{Gd}_2\text{O}_3:\text{Sm}^{3+}$ (0.5, 1, 2, 4, 6, 8, 10 and 12 at.%) samples in the region of 580 – 630 nm.	114
Fig. 5.20. PL decay curves of $^5\text{G}_{5/2}$ level of Sm^{3+} emission in $\text{Gd}_2\text{O}_3:\text{Sm}^{3+}$ (1, 2, 4, 6, 8, 10 and 12 at.%). $\lambda_{em} = 606 \text{ nm}$ and $\lambda_{ex} = 406 \text{ nm}$.	115
Fig. 5.21. CIE chromaticity coordinate positions of $\text{Gd}_2\text{O}_3:\text{Sm}^{3+}$ (0.5, 1, 2, 4, 6, 8, 10 and 12 at.%) samples excited at 406 nm.	116
Fig. 6.1. XRD patterns of as-prepared 1 at.% Bi^{3+} sensitized (a) $\text{Gd}(\text{OH})_3:\text{Eu}^{3+}$ ($\text{Eu}^{3+} = 1, 9$ and $17 \text{ at.}\%$) and (b) $\text{Gd}(\text{OH})_3:\text{Sm}^{3+}$ ($\text{Sm}^{3+} = 1, 4$ and $10 \text{ at.}\%$).	124
Fig. 6.2 XRD patterns of 900 °C annealed samples of 1 at.% Bi^{3+} sensitized (a) $\text{Gd}_2\text{O}_3:\text{Eu}^{3+}$ ($\text{Eu}^{3+} = 1, 5, 9, 11, 17$ and $21 \text{ at.}\%$) and (b) $\text{Gd}_2\text{O}_3:\text{Sm}^{3+}$ ($\text{Sm}^{3+} = 1, 2, 4, 6, 8$ and $10 \text{ at.}\%$).	124
Fig. 6.3. FT-IR spectra of as-prepared $\text{Gd}(\text{OH})_3:\text{Bi}^{3+}$ (1 at.%) / Eu^{3+} (3 at.%) (below) and 900 °C annealed $\text{Gd}_2\text{O}_3:\text{Bi}^{3+}$ (1 at.%) / Eu^{3+} (3 at.%) (above) samples.	125
Fig. 6.4. TEM images (a) along with HR-TEM (b) and SAED images (c) of a selected region of as-prepared $\text{Gd}(\text{OH})_3:\text{Bi}^{3+}$ (1 at.%) / Eu^{3+} (9 at.%).	126
Fig. 6.5. TEM images (a) along with HR-TEM (b) and SAED images (c) of a selected region of 900 °C annealed $\text{Gd}_2\text{O}_3:\text{Bi}^{3+}$ (1 at.%) / Eu^{3+} (9 at.%).	127
Fig. 6.6. PL excitation spectra of Bi^{3+} (0.25, 0.5, 1, 2, 4, 6 and 8 at.%) sensitized $\text{Gd}_2\text{O}_3:\text{Eu}^{3+}$ (1 at.%) samples monitored at $\lambda_{em} = 611 \text{ nm}$	128
Fig. 6.7. PL emission spectra of $\text{Gd}_2\text{O}_3:\text{Bi}^{3+}$ (1 at.%) / Eu^{3+} (7 at.%) samples under different excitations at 257 nm ($\text{Eu}-\text{O}$ CT), 274 nm (Gd^{3+} , S-I), 335 nm (Bi^{3+} , related to C_2 site) and 380 nm (Bi^{3+} , related to S_6 site). Inset shows the comparison of emission intensities at these excitation wavelengths.	129
Fig. 6.8. PL emission spectra of Bi^{3+} (0.25, 0.5, 1, 2, 4, 6 and 8 at.%) sensitized $\text{Gd}_2\text{O}_3:\text{Eu}^{3+}$ (1 at.%) samples under the 335 nm excitation. Inset shows the comparison of emission intensities at different concentration of Bi^{3+} .	129
Fig. 6.9. Asymmetric ratio at different concentration of Eu^{3+} in $\text{Gd}_2\text{O}_3:\text{Bi}^{3+}$ (1 at.%) / Eu^{3+} (1, 3, 5, 7, 9, 11, 13, 15, 17, 19, 21 and 23 at.%) samples	131

at 335 and 380 nm excitation.

Fig. 6.10. Normalized PL emission (normalized at 611 nm) $\text{Gd}_2\text{O}_3:\text{Bi}^{3+}$ (1 at.%) / Eu^{3+} (0, 1, 3, 5, 7, 9, 11, 13, 15, 17, 19, 21 and 23 at.%) samples under the excitation of (a) 335 and (b) 380 nm. 132

Fig. 6.11. Energy transfer efficiency (η) from the sensitizer (Bi^{3+}) to the excited states of activator (Eu^{3+}) in $\text{Gd}_2\text{O}_3:\text{Bi}^{3+}$ (1 at.%) / Eu^{3+} (0, 1, 3, 5, 7, 9, 11, 13, 15, 17, 19, 21 and 23 at.%) samples under the excitation of (a) 335 and (b) 380 nm. 133

Fig. 6.12. Dependence of I_{S_0}/I_S of Bi^{3+} on $C_{\text{Bi}^{3+}+\text{Eu}^{3+}}^{n/3}$ where $n = 6$ (dipole-dipole), $n = 8$ (dipole-quadrupole) and $n = 10$ (quadrupole-quadrupole) interactions respectively, at 335 nm excitation, C_2 symmetry site (a-c) and at 380 nm excitation, S_6 symmetry site (d-f) in $\text{Gd}_2\text{O}_3:\text{Bi}^{3+}$ (1 at.%) / Eu^{3+} (0, 1, 3, 5, 7, 9, 11, 13, 15, 17, 19, 21 and 23 at.%) samples. 134

Fig. 6.13. TCSPC decay profiles of Bi^{3+} (1 at.%) in $\text{Gd}_2\text{O}_3:\text{Eu}^{3+}$ (0, 1, 3, 5, 7, 9, 11, 13, 15, 17, 19, 21 and 23 at.%). Excitation and emission wavelengths were monitored at 335 and 504 nm respectively. Inset shows the calculated average lifetime values at different concentration of Eu^{3+} . 135

Fig. 6.14. Typical fitting of decay curve for Bi^{3+} emission ($\lambda_{ex} = 335$ nm and $\lambda_{em} = 504$ nm) in 900 °C annealed $\text{Gd}_2\text{O}_3:\text{Bi}^{3+}$ (1 at.%) / Eu^{3+} (1 at.%) sample. 136

Fig. 6.15. PL decay curves of $^5\text{D}_0$ level of Eu^{3+} emission in $\text{Gd}_2\text{O}_3:\text{Bi}^{3+}$ (1 at.%) / Eu^{3+} (1, 3, 5, 7, 9, 11, 13, 15, and 17 at.%) samples under 335 nm excitation and the emission is monitored at 611 nm. 137

Fig. 6.16. PL decay curves of $^5\text{D}_0$ level of Eu^{3+} emission in $\text{Gd}_2\text{O}_3:\text{Bi}^{3+}$ (1 at.%) / Eu^{3+} (1, 3, 5, 7, 9, 11, 13, 15, and 17 at.%) samples under 464 nm excitation and the emission is monitored at 611 nm. 138

Fig. 6.17. Typical fitting of decay curve for Eu^{3+} emission ($\lambda_{ex} = 335$ nm and $\lambda_{em} = 611$ nm) in 900 °C annealed $\text{Gd}_2\text{O}_3:\text{Bi}^{3+}$ (1 at.%) / Eu^{3+} (1 at.%) sample. 138

Fig. 6.18. CIE chromaticity coordinate positions of $\text{Gd}_2\text{O}_3:\text{Bi}^{3+}$ (1 at.%) / Eu^{3+} (0, 1, 3, 5, 7, 9, 11, 13, 15, 17, 19, 21 and 23 at.%) samples excited at (a) 335 nm, (b) 380 nm (Details of CIE coordinate and position on the colour space are tabulated in Table 6.4) and (c) physical photograph of $\text{Gd}_2\text{O}_3:\text{Bi}^{3+}$ (1 at.%) / Eu^{3+} (17 at.%) excited at different wavelengths where the colour saturation is mentioned inside the parenthesis. 140

Fig. 6.19. (a) CIE color coordinates of $\text{Gd}_2\text{O}_3:\text{Bi}^{3+}$ (1 at.%) / Eu^{3+} (17 at.%) at different excitation wavelength ($\lambda_{ex} = 330, 340, 350, 360, 370$, and 380 nm) and (b) Color saturation calculated from CIE chromaticity coordinates for Bi^{3+} (1 at.%) sensitized $\text{Gd}_2\text{O}_3:\text{Eu}^{3+}$ (17 at.%) sample at 350 nm excitation. **a** = distance between source coordinate 142

and equal energy locus (1/3, 1/3: white); **b** = distance between equal energy locus (1/3, 1/3: white) and dominant wavelength.

- Fig. 6.20.** PL excitation spectra of Bi³⁺ (1 at.%) sensitized Gd₂O₃:Sm³⁺ (1, 2, 4, 6, 8, 10 and 12 at.%) samples monitored at $\lambda_{em} = 606$ nm 143
- Fig. 6.21.** PL emission spectra of Gd₂O₃:Bi³⁺(1 at.+)/Sm³⁺ (2 at.%) samples under different excitations at 274 nm (Gd³⁺, S-I), 335 nm (Bi³⁺, related to C₂ site) and 375 nm (Bi³⁺, related to S₆ site) and 406 nm (*f-f* absorption). 144
- Fig. 6.22.** Normalized PL emission Gd₂O₃:Bi³⁺ (1 at.+)/Sm³⁺ (0, 1, 2, 4, 6, 8, 10 and 12 at.%) samples under the excitation of (top) 335 and (bottom) 375 nm. 145
- Fig. 6.23.** Energy transfer efficiency (η) from the sensitizer (Bi³⁺) to the excited states of activator (Sm³⁺) in Gd₂O₃:Bi³⁺ (1 at.+)/Sm³⁺ (0, 1, 2, 4, 6, 8, 10 and 12 at.%) samples under the excitation of (a) 335 and (b) 375 nm. 145
- Fig. 6.24.** Dependence of I_{S_0}/I_S of Bi³⁺ on $C_{Bi^{3+}+Sm^{3+}}^{n/3}$ where n = 6 (dipole-dipole), n = 8 (dipole-quadrupole) and n = 10 (quadrupole-quadrupole) interactions respectively, at 335 nm excitation, C₂ symmetry site (a-c) and at 375 nm excitation, S₆ symmetry site (d-f) in Gd₂O₃:Bi³⁺ (1 at.+)/Sm³⁺ (0, 1, 2, 4, 6, 8, 10, and 12 at.%) samples. 146
- Fig. 6.25.** TCSPC decay profiles of Bi³⁺ (1 at.%) in Gd₂O₃:Sm³⁺ (0, 1, 2, 4, 6, 8, 10 and 12 at.%). Excitation and emission wavelengths were monitored at 335 and 500 nm respectively. Inset shows the calculated average lifetime values at different concentration of Sm³⁺. 147
- Fig. 6.26.** PL decay curves of ⁵G_{5/2} level of Sm³⁺ emission in Gd₂O₃:Bi³⁺ (1 at.+)/Sm³⁺ (1, 2, 4, 6, 8, 10 and 12 at.%) monitored at 606 nm. Excitation wavelengths (a) 335 nm (left) and 406 nm (right) 148
- Fig. 6.27.** CIE chromaticity coordinate positions of Gd₂O₃:Bi³⁺ (1 at.+)/Sm³⁺ (0.5, 1, 2, 4, 6, 8, 10 and 12 at.%) samples excited at (a) 335 nm, (b) 375 nm. 149

List of Tables

	Page No.
Table 1.1. Different types of luminescence based on the mode of excitation	3
Table 1.2. Electronic configurations of lanthanide series	9
Table 3.1. Calculated crystallite size for Eu^{3+} or Sm^{3+} doped Y_2O_3 500 and 900 °C annealed samples, using Scherrer relation.	37
Table 3.2. The average lifetime calculated for the decay curves of $^5\text{D}_0$ level of Eu^{3+} in 500 and 900 °C annealed $\text{Y}_2\text{O}_3:\text{Eu}^{3+}$ (1, 3, 5, 7, 13, 17, 21 and 25 at.%) samples.	48
Table 3.3. The average lifetime calculated for the decay curves of $^5\text{G}_{5/2}$ level of Sm^{3+} by monitoring at 606 nm emission in $\text{Y}_2\text{O}_3:\text{Sm}^{3+}$ (1, 2, 4, 6, and 8 at.%) samples.	51
Table 4.1. Calculated crystallite size for 1 at.% Bi^{3+} sensitized and Eu^{3+} or Sm^{3+} doped Y_2O_3 500 and 900 °C annealed samples, using Scherrer relation.	62
Table 4.2. Decay lifetime (τ_{av}) values of Bi^{3+} in $\text{Y}_2\text{O}_3:\text{Eu}^{3+}$ (x at.%) / Bi^{3+} (1 at.%) samples annealed at 500 °C and 900 °C. Excitation wavelength, $\lambda_{ex} = 330$ nm and emission wavelength, $\lambda_{em} = 495$ nm.	78
Table 4.3. Decay lifetime (τ_{av}) values of $^5\text{D}_0$ level of Eu^{3+} in $\text{Y}_2\text{O}_3:\text{Eu}^{3+}$ (x at.%) / Bi^{3+} (1 at.%) samples annealed at 500 °C and 900 °C. Excitation wavelength, $\lambda_{ex} = 330$ nm and emission wavelength, $\lambda_{em} = 611$ nm.	80
Table 4.4. Decay lifetime (τ_{av}) values of $^5\text{D}_0$ level of Eu^{3+} in $\text{Y}_2\text{O}_3:\text{Eu}^{3+}$ (x at.%) / Bi^{3+} (1 at.%) samples annealed at 500 °C and 900 °C. Excitation wavelength, $\lambda_{ex} = 371$ nm and emission wavelength, $\lambda_{em} = 611$ nm.	80
Table 4.5. Quantum yields of $\text{Y}_2\text{O}_3:\text{Eu}^{3+}$ (x at.%) / Bi^{3+} (1 at.%) samples annealed at 500 °C and 900 °C. Excitation wavelength, $\lambda_{ex} = 330$ nm.	81
Table 4.6. CIE coordinates of 500 °C and 900 °C annealed $\text{Y}_2\text{O}_3:\text{Eu}^{3+}$ (x at.%) / Bi^{3+} (1 at.%) under the different excitation wavelengths (λ_{ex}) i.e. 330 nm (C_2), 355 nm and 371 nm (S_6) respectively. Positions in the CIE diagram under 330, 355 and 371 (See Fig. 4.20).	82
Table 4.7. CIE coordinates for $\text{Y}_2\text{O}_3:\text{Eu}^{3+}$ (3 at.%) / Bi^{3+} (1 at.%) sample heated at 500 and 900 °C under different excitation wavelengths. CIE Positions (See Fig. 4.22).	84
Table 4.8: Decay lifetime (τ_{av}) values of Bi^{3+} in $\text{Y}_2\text{O}_3:\text{Sm}^{3+}$ (x at.%) / Bi^{3+} (1 at.%) samples annealed at 500 °C and 900 °C. Excitation wavelength, $\lambda_{ex} = 330$ nm and emission wavelength, $\lambda_{em} = 504$ nm.	90

Table 4.9. Decay lifetime (τ_{av}) values of $^5G_{5/2}$ level of Sm^{3+} in $Y_2O_3:Sm^{3+}$ (x at.%)/ Bi^{3+} (1 at.%) samples annealed at 500 °C and 900 °C. Excitation wavelength, $\lambda_{ex} = 330$ and 370 nm and emission wavelength, $\lambda_{em} = 606$ nm.	91
Table 5.1: Calculated crystallite size for Eu^{3+} or Sm^{3+} doped $Gd(OH)_3$ and 900 °C annealed Gd_2O_3 samples, using Scherrer relation.	101
Table 5.2. The average lifetime calculated for the decay curves of 5D_0 level of Eu^{3+} and Quantum yield in $Gd_2O_3:Eu^{3+}$ (1, 3, 7, 11, 15, 19, 21 and 25 at.%) samples.	110
Table 5.3. The average lifetime calculated for the decay curves of $^5G_{5/2}$ level of Sm^{3+} by monitoring at 606 nm emission and Quantum yield in $Gd_2O_3:Sm^{3+}$ (0.5 1, 2, 4, 6, 8, 10 and 12 at.%) samples.	115
Table 6.1. Calculated crystallite size for 1 at.% Bi^{3+} sensitized and Eu^{3+} or Sm^{3+} doped $Gd(OH)_3$ and 900 °C annealed Gd_2O_3 samples, using Scherrer relation.	125
Table 6.2. Calculated fitting parameters of decay lifetime of Bi^{3+} emission in $Gd_2O_3:Bi^{3+}$ (1 at.%)/ Eu^{3+} (0, 1, 3, 5, 7, 9, 11, 13, 15, 17, 19, 21 and 23 at.%) samples at 335 nm excitation and emission monitored at 504 nm.	137
Table 6.3. The average lifetime calculated for the decay curves of 5D_0 level of Eu^{3+} by monitoring at 611 nm emission and Quantum yield in $Gd_2O_3:Bi^{3+}$ (1 at.%)/ Eu^{3+} (1, 3, 5, 7, 9, 11, 13, 15, and 17 at.%) samples.	139
Table 6.4. CIE chromaticity coordinates and position in the color space (Fig. 6.18) of $Gd_2O_3:Bi^{3+}$ (1 at.%)/ xEu^{3+} at 335 nm and 380 nm excitation.	141
Table 6.5. Calculated fitting parameters of decay lifetime of Bi^{3+} emission in $Gd_2O_3:Bi^{3+}$ (1 at.%)/ Sm^{3+} (0, 1, 2, 4, 6, 8, 10 and 12 at.%). Excitation at 335 nm and emission monitored at 500 nm.	147
Table 6.6. The average lifetime calculated for the decay curves of $^5G_{5/2}$ level of Sm^{3+} by monitoring at 606 nm emission and Quantum yield in $Gd_2O_3:Bi^{3+}$ (1 at.%)/ Sm^{3+} (1, 2, 4, 6, 8, 10 and 12 at.%) samples.	148

Contents

Acknowledgement	i
Preface	ii
List of Figures	v
List of Tables	xiii
Chapter 1. General introduction and review	1-24
1.1. Phosphors	1
1.2. Some common Phosphors	1
1.2.1. Yellow Phosphors	1
1.2.2. Blue Phosphor	2
1.2.3. Green Phosphors	2
1.2.4. Red Phosphor	2
1.3. Luminescence	3
1.3.1. Photoluminescence	4
1.3.2. Radiative and Non-radiative transitions	5
1.3.3. Decay lifetime	5
1.3.4. Quantum Yield	6
1.3.5. Quenching	6
1.3.6. CIE Chromaticity	6
1.3.7. Various energy transfer process in photoluminescence	7
1.3.7.1. Resonance energy transfer	7
1.3.7.2. Phonon-assisted energy transfer	7
1.3.7.3. Cross- relaxation	8
1.3.7.4. Migration of excitation energy	8
1.4. Lanthanide doping for Phosphors	8
1.4.1 Lanthanides	8
1.4.2. Doping of lanthanides	9
1.4.3. Dopants used in the present study	10
1.4.3.1. Europium (Eu^{3+})	10
1.4.3.2. Samarium (Sm^{3+})	11
1.4.3.3. Bismuth (Bi^{3+})	11

1.5. Synthesis of nanomaterials	11
1.5.1. Top-down method	11
1.5.1.1. Laser ablation	11
1.5.1.2. Electrospinning	12
1.5.1.3. Mechanical milling	12
1.5.2. Bottom-up method	12
1.5.2.1. Chemical vapor deposition (CVD)	12
1.5.2.2. Solvothermal and hydrothermal methods	13
1.5.2.3 Sol-gel method	13
1.5.2.4. Soft and hard template methods	13
1.5.2.5. Reverse micelle methods	14
1.6. Host material used in the present study	14
1.7. Some applications of Lanthanide doped nanomaterial	17
1.7.1 Optical imaging	17
1.7.2. MRI contrasting agent	18
1.7.3. Display devices	18
1.7.4. Solid state lighting	18
1.7.5. Sensing application	19
1.8 Outlook of the Thesis	19
References	20
Chapter 2. Basic principles of instrumentation	25-33
2.1. Introduction	25
2.2. X-ray Diffraction	25
2.3. Transmission Electron Microscopy	27
2.4. Fourier Transform Infrared Spectroscopy	28
2.5. Luminescence Spectroscopy	30
2.5.1. Steady State Spectrofluorometer	30
2.5.1. Time Resolve Spectrofluorometer	31
References	33
Chapter 3. Photoluminescence properties of $\text{Y}_2\text{O}_3:\text{Ln}^{3+}$ ($\text{Ln}^{3+} = \text{Eu}^{3+}$ & Sm^{3+})	34-56
3.1. Introduction	34

3.2. Experimental methods	35
3.2.1. Materials	35
3.2.2. Synthesis of Eu^{3+} doped Y_2O_3 phosphors	35
3.2.3. Synthesis of Sm^{3+} doped Y_2O_3 phosphors	35
3.2.4. Characterization	36
3.3. Results and discussion	36
3.3.1. X-ray diffraction study	36
3.3.2. Fourier transform infrared spectroscopy study	38
3.3.3. Transmission electron microscopy study	39
3.3.4. Photoluminescence studies of $\text{Y}_2\text{O}_3:\text{Eu}^{3+}$	40
3.3.4.1. Steady state PL study	40
3.3.4.2. PL decay lifetime and quantum yield study	46
3.3.4.3. CIE chromaticity studies	48
3.3.5. Photoluminescence studies of $\text{Y}_2\text{O}_3:\text{Sm}^{3+}$	49
3.3.5.1. Steady state PL study	49
3.3.5.2. PL decay lifetime and quantum yield study	51
3.3.5.3. CIE chromaticity studies	52
3.4. Conclusions	53
References	54
Chapter 4. Photoluminescence properties and energy transfer in Bi^{3+} sensitized $\text{Y}_2\text{O}_3:\text{Ln}^{3+}$ ($\text{Ln}^{3+} = \text{Eu}^{3+}$ & Sm^{3+})	57-96
4.1. Introduction	57
4.2. Experimental methods	59
4.2.1. Materials	59
4.2.2. Synthesis of Bi^{3+} sensitized Y_2O_3 doped with Eu^{3+} phosphors	59
4.2.3. Synthesis of Bi^{3+} sensitized Y_2O_3 doped with Sm^{3+} phosphors	59
4.2.4. Characterization	60
4.3. Results and discussion	60
4.3.1. X-ray diffraction study	60
4.3.2. Fourier transform infrared spectroscopy study	62
4.3.3. Transmission electron microscopy study	63
4.3.4. Photoluminescence (PL) studies of Bi^{3+} sensitized $\text{Y}_2\text{O}_3:\text{Eu}^{3+}$	65

4.3.4.1. PL studies of $\text{Y}_2\text{O}_3:\text{Bi}^{3+}$	65
4.3.4.2. PL studies of $\text{Y}_2\text{O}_3:\text{Bi}^{3+}/\text{Eu}^{3+}$	67
4.3.4.3. Mechanism of energy transfer: Bi^{3+} to Eu^{3+}	71
4.3.4.4. PL decay lifetime and quantum yield study	77
4.3.4.5. CIE chromaticity studies	81
4.3.5. Photoluminescence studies of Bi^{3+} sensitized $\text{Y}_2\text{O}_3:\text{Sm}^{3+}$	84
4.3.5.1. Steady state PL study	84
4.3.5.2. Mechanism of energy transfer: Bi^{3+} to Sm^{3+}	86
4.3.5.3. PL decay lifetime and quantum yield study	90
4.3.5.4. CIE chromaticity studies	92
4.4. Conclusions	93
References	94
Chapter 5. Photoluminescence properties of $\text{Gd}_2\text{O}_3:\text{Ln}^{3+}$ ($\text{Ln}^{3+} = \text{Eu}^{3+}$ & Sm^{3+})	97-119
5.1. Introduction	97
5.2. Experimental methods	98
5.2.1. Materials	98
5.2.2. Synthesis of Eu^{3+} doped Gd_2O_3 phosphors	98
5.2.3. Synthesis of Sm^{3+} doped Gd_2O_3 phosphors	98
5.2.4. Characterization	99
5.3. Results and discussion	99
5.3.1. X-ray diffraction study	99
5.3.2. Fourier transform infrared spectroscopy study	101
5.3.3. Transmission electron microscopy study	102
5.3.4. Photoluminescence studies of $\text{Gd}_2\text{O}_3:\text{Eu}^{3+}$	103
5.3.4.1. Steady state PL study	103
5.3.4.2. PL decay lifetime and quantum yield study	109
5.3.4.3. CIE chromaticity studies	111
5.3.5. Photoluminescence studies of $\text{Gd}_2\text{O}_3:\text{Sm}^{3+}$	111
5.3.5.1. Steady state PL study	111
5.3.5.2. PL decay lifetime and quantum yield study	114
5.3.5.3. CIE chromaticity studies	115

5.4. Conclusions	116
References	117
Chapter 6. Photoluminescence properties and energy transfer in Bi³⁺ sensitized Gd₂O₃:Ln³⁺ (Ln³⁺ = Eu³⁺ & Sm³⁺)	120-153
6.1. Introduction	120
6.2. Experimental methods	122
6.2.1. Materials	122
6.2.2. Synthesis of Bi ³⁺ sensitized Gd ₂ O ₃ doped with Eu ³⁺ phosphors	122
6.2.3. Synthesis of Bi ³⁺ sensitized Gd ₂ O ₃ doped with Sm ³⁺ phosphors	122
6.2.4. Characterization	123
6.3. Results and discussion	123
6.3.1. X-ray diffraction study	123
6.3.2. Fourier transform infrared spectroscopy study	125
6.3.3. Transmission electron microscopy study	126
6.3.4. Photoluminescence (PL) studies of Bi ³⁺ sensitized Gd ₂ O ₃ :Eu ³⁺	127
6.3.4.1. Steady state PL study	127
6.3.4.2. Mechanism of energy transfer: Bi ³⁺ to Eu ³⁺	132
6.3.4.3. PL decay lifetime and quantum yield study	134
6.3.4.4. CIE chromaticity studies	139
6.3.5. Photoluminescence studies of Bi ³⁺ sensitized Gd ₂ O ₃ :Sm ³⁺	143
6.3.5.1. Steady state PL study	143
6.3.5.2. Mechanism of energy transfer: Bi ³⁺ to Sm ³⁺	144
6.3.5.3. PL decay lifetime and quantum yield study	146
6.3.5.4. CIE chromaticity studies	149
6.4. Conclusions	150
References	151

Chapter 1

General introduction and review

1.1. Phosphors

Phosphors or luminescent materials are those can absorb energy from the incident electromagnetic radiation and emit light which is usually in the visible region of the electromagnetic spectrum [1-3]. Sometimes, the emitted light can also be invisible due to the emission in the ultraviolet (UV) or infrared (IR) region of the spectrum [4-8]. In order to meet the various applications, generally phosphor comes in powder form with different morphology. High quality larger crystals having about usually 4 to 5 μm in crystalline state have higher quantum efficiency than amorphous host [9-10].

1.2. Some common Phosphors

1.2.1. Yellow Phosphors

Yellow phosphors can be generated a light in the wavelength region of 565 – 590 nm when it is excited by near ultraviolet (380 – 410 nm) or blue (450 – 480 nm) light source. Since yellow light can be easily made by combining red and green of RGB (Red Green Blue) colour, white light can be produced by combining with blue colour for making white light emitter if high value of colour rendering index (CRI) is not required. Ce^{3+} and Eu^{2+} activator is mainly used for yellow light production. The radiation produced from 5d-4f transition in the above ions is red-shifted to lower energy due to the interaction with host materials. This light has very bright and highly intense due to the allowed dipole transition. Therefore, they are often used in the application of phosphor converted white light emitting diodes (pc-WLEDs) technology. $\text{YAG}:\text{Ce}^{3+}$ which has garnet structure, and it was reported for the first time by Menzer [11-12]. The general formula of garnet structure is defined as $\text{A}_3\text{B}_2(\text{XO}_4)_3$, where A, B, X are cations and O represents oxygen anion. Some examples of oxide garnet are $\text{Ca}_3\text{Sc}_2\text{Si}_3\text{O}_{12}$, $\text{Y}_3\text{Mg}_2\text{AlSi}_2\text{O}_{12}$, $\text{Ca}_2\text{GdZr}_2\text{Al}_3\text{O}_{12}$ etc. YAG has body centered cubic unit having 160 atoms and space group of $1a\bar{3}d$. Here, Y^{3+} is occupying the Wyckoff position and are coordinated to O^{2-} via dodecahedrally, which has D_2 site symmetry. Thus, YAG can be considered as a 3D structure containing AlO_6^{9-} octahedra, AlO_6^{6-} and YO_8^{13-} dodecahedra. In $\text{YAG}:\text{Ce}$, Y^{3+} ion are replaced by Ce^{3+} ion activator. Other examples of yellow phosphors includes $\text{SiAlON}:\text{Eu}^{2+}$, $\text{Li-}\alpha\text{-SiAlON}:\text{Eu}^{2+}$ etc. [13,14].

1.2.2. Blue Phosphor

They are mainly emitted light in the range 420 – 500 nm when it is excited by radiation of wavelength 380 – 410 nm. Due to the constraint of encounter stoke shift, they cannot be excited by the light whose wavelength is greater than 410 nm. So, this limits the possible application of materials which shows excitation emission in these two regions. The main activator used for the production of blue phosphor are Eu^{2+} and Ce^{3+} . Both ions have luminescence band due to the electrons from 5d to 4f energy levels which have radiative decay time of below 1 μs [15-16]. Among the various hosts, oxide-based materials, aluminates, silicates and phosphates are best materials for producing blue phosphor. $\text{Ca}_2\text{PO}_4\text{Cl}$ doped with Eu^{2+} gives intense blue colour when the Eu^{2+} concentration reached 11% [17]. Another material for blue phosphor is silicates. They are quite stable but they should be prepared at elevated temperature than phosphates [18]. Some examples of blue phosphors are $\text{Li}_2\text{Sr}_{1-3x/2}\text{Ce}_x\text{SiO}_4$ ($x = 0.0025\text{--}0.07$), $\text{BaMgAl}_{10}\text{O}_{17}:\text{Eu}^{2+}$ and $\text{BaSi}_7\text{N}_{10}$, etc.

1.2.3. Green Phosphors

Green phosphors emit radiation in the ranges 520 – 565 nm when the materials are excited by either 380 – 410 nm near ultraviolet (NUV) or a 450 – 480 nm blue LED. In most of the cases, both Tb^{3+} and Mn^{2+} supplemented with Eu^{2+} or Ce^{3+} is used for efficient green phosphor. In Tb^{3+} and Mn^{2+} , the luminescence band is due to the emission from 4f-4f and 3d-3d transition. Due to the forbidden nature of these transitions, the emitted light is of very weak intensity. But, in case of Eu^{2+} or Ce^{3+} , there is an allowed transition due to 5d-4f. For this reason, generally, activators like Tb^{3+} and Mn^{2+} are excited by the sensitizer like Eu^{2+} or Ce^{3+} . Some of the common green phosphors are oxides, phosphates, aluminates and silicates etc. Eulytite having formula $\text{Sr}_3\text{Gd}(\text{PO}_4)_3$ prepared through solid state reaction codoped with Ce^{3+} greatly enhanced the green emission from Eu^{2+} ion due to good energy transfer from Ce^{3+} to Eu^{2+} [19]. Double phosphate material like NaCaPO_4 when doped with Tb^{3+} also gives green phosphors. Other examples of this type of phosphors $\text{Ba}_2\text{MgSi}_2\text{O}_7:\text{Eu}^{2+}$, $\text{LiBaBO}_3:\text{Tb}^{3+}$ and $\text{Ca}_2\text{Al}_3\text{O}_6\text{F}:\text{Ce}^{3+}:\text{Tb}^{3+}$ etc. [20-22].

1.2.4. Red Phosphor

Red phosphor has emission in the range 625 – 740 nm when they are excited by the radiation of near ultraviolet (NUV) or blue LED in the range ~380 – 410 nm or 450 – 480 nm. For the production of green phosphor, red emitting component. For achieving

efficient red emission from $5d-4f$ transition, two important factors are necessary. Nephelauxetic effect and strong ligand field should be there. Actually, these factors are highly dependent on only few selected hosts. Another alternative is the use of activators which can give effectively in the red region. Ions like Eu^{3+} and Mn^{4+} are few examples of this type of phosphor. This luminescence is from $4f-4f$ and $3d-3d$ which is parity forbidden electric dipole transition. Therefore, they are very weak and not an ideal phosphor. Some common host materials for red phosphor are oxides, phosphates, silicates, molybdate and tungstate etc. Other common materials for red phosphors are $\text{Cs}_2\text{CaP}_2\text{O}_7$ and $\text{Cs}_2\text{SrP}_2\text{O}_7$ doped with $\% \text{Eu}^{2+}$, $\text{Ca}_3\text{Tb}_{2-x}\text{Eu}_x\text{Si}_3\text{O}_{12}$ ($x = 0-2$) with silico-carnotite structure, Y_2O_3 and YVO_4 doped with Eu^{3+} have been used as red phosphors [23-26]. Fluorite materials like Cs_2GeF_6 , Na_2SnF_6 , Cs_2SnF_6 , KNaSiF_6 and Cs_2SiF_6 etc. doped with Mn^{4+} are also used as common red emitter [27-30].

1.3. Luminescence

Luminescence is a term related to the spontaneous emission of light by a matter from different phenomena but without heating. Therefore, it is quite different from the light generated from heating inside the incandescent light. So, we consider the luminescence as a cold body radiation which can be differentiated from the incandescent light [31]. The term “Luminescence” is derived from Latin word *lumen* which means light. It was coined by the German physicist Eilhard Wiedmann in 1888.

Based on the different phenomena during the excitation process, luminescence is broadly divided into following categories:

Table 1.1. Different types of luminescence based on the mode of excitation

Luminescence type	Mode of excitation
Photoluminescence	Light absorption
Bioluminescence	Biochemical reaction
Electroluminescence	Electric field
Cathodoluminescence	Cathode rays
Triboluminescence	Frictional and electrostatic forces
Sonoluminescence	Ultrasound
Thermoluminescence	Heat absorption
Radioluminescence	Ionization radiation

The main topic of luminescence which will be discussed in this thesis is related to the photoluminescence phenomenon and its importance in the developing of some oxide-based phosphors.

1.3.1. Photoluminescence

Photoluminescence is the phenomenon of spontaneous emission of light from a substance when it is irradiated by an electromagnetic radiation. During this process an electron from the ground state is excited to the higher energy states by absorbing the radiation and subsequent de-excitation back to the ground. During this process, it releases the excess energy in the form of light photon. According the path of the excited electrons, photoluminescence is classified into two types: (i) Fluorescence and (ii) Phosphorescence. Fluorescence is related to the de-excitation process in which the excited electron is directly goes to the ground state with the same spin state. So, the time taken during this process is very small usually lies in the range of $10^{-12} - 10^{-9}$ s [32]. But, in the case of Phosphorescence, the excited photon is not returning to the ground state with same spin. Instead, it goes to another lower spin state (triplet excited state) via intersystem crossing. Finally, it gets de-excited back to the ground state with the release of light photon. This type of photoluminescence has an average life time of about $\sim 10^{-3}$ s to hours. The whole process of photoluminescence can be visualized using Jablonski's diagram (See Fig. 1.1). Here, S_0 represents ground state and S_1 , S_2 and S_n represent higher excited states having same spin state (Singlet). T_1 represents the triplet excited state whose spin is different from singlet state.

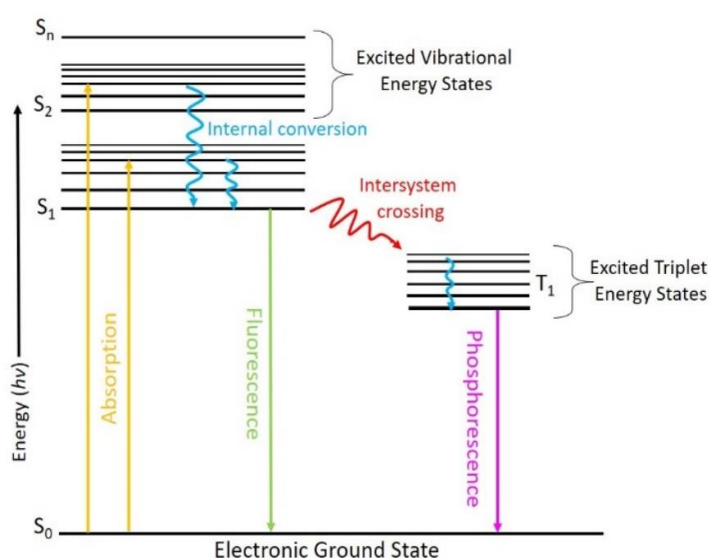


Fig. 1.1. Schematic diagram showing different types of photoluminescence.

1.3.2. Radiative and Non-radiative transitions

After the electrons get excited in the excited states in a luminescent material, the de-excitation or returning of these excited electrons can be broadly two types: (i) Radiative and (ii) Non-radiative transitions. Radiative transitions are the process of returning the excited state electrons with the emission extra energy carried by the electrons in the form light radiation. In certain transitions, the relaxation these excited state electrons to ground state occurs without emitting of radiation mostly in the form of heat is called non-radiative transition. In non-radiative transitions, the excess energy released is converted into the vibrational energy and is dissipated into the medium of the materials. The vibrational bond formed by light element have high vibrational energy. So, in order to minimize the non-radiative loss, it is necessary to avoid the most material having large amount of lattice vibration [33-34]. The amount of these two types of transition will control the various parameters of the photoluminescence.

1.3.3. Decay lifetime

The average life time of a phosphor is very important parameter. It measures the time period of how long the excited electrons are in the excited states before de-excitation through different routes. This is defined as the total time taken when $\sim 36.8\%$ (or $1/e$) of the total excited electrons return back to the ground state. Mathematically, it can be represented by the following equation

$$N(t) = N_0 e^{-t/\tau} \quad (1.1)$$

where, N is the number of excited electrons at any time t , N_0 is the total number of particles before de-excitation and τ is the average life time of the phosphor. Since the number of excited electrons is directly proportional to the Intensity (I) of the phosphor, N can be replaced with I ,

$$I(t) = I_0 e^{-t/\tau} \quad (1.2)$$

The emission intensity as a function of time of a single exponential decay can be represented by

$$I(t) = \alpha e^{-t/\tau} \quad (1.3)$$

where, α and τ are the normalization term and average lifetime. For bi-exponential decay, similar equation can be given

$$I(t) = \alpha_1 e^{-t/\tau_1} + \alpha_2 e^{-t/\tau_2} \quad (1.4)$$

where, α_1 and α_2 are the respective intensities at different time.

1.3.4. Quantum Yield

Quantum yield (η) will define how efficient a phosphor is. It is defined as the ratio of the total emitted photons to the total absorbed photons [35,36]. Following the excitation process, excited electrons return to the ground state by either or both radiative (Γ) decay or non-radiative (k_{nr}) decay. Thus, quantum yield can also be defined as the fraction of radiative emission to the total amount of radiative and non-radiative transition as

$$\phi = \Gamma / (\Gamma + k_{nr}) \quad (1.5)$$

where, ϕ is the quantum yield and this value indicates the efficiency of the phosphor. Higher the value of the quantum yield better is the luminescent material.

1.3.5. Quenching

Quenching is a very important term when the emission intensity, quantum yield and lifetime are discussed. It is defined as the decrease in luminescence intensity of a luminescent material [37]. Different types of process can affect the quenching, like energy transfer, excited state reaction, complex formation and quenching through collision etc. [38-39]. Water, oxygen molecule, transition metal, and halide are most common quencher encountered. Presence of these ions, molecules or metals inside or on the surface or cross proximity of any phosphor material will see quenching. In case of doping, it is necessary to control the amount of dopant concentration in order to minimize the collisional quenching.

1.3.6. CIE Chromaticity

The colour emitted from any luminescent material can be defined by a set of colour coordination which was introduced first by Commission Internationale de l'Eclairage (CIE) back in 1931. The colour of any light emission in the visible region can be identified using coordination involving x and y values [40]. This is first mathematical relation of the wavelength with the physiologically perceived colour. The visible values of this coordinate system are in the shape of horse shoe. The chromaticity coordinate of the three primary colours i.e. red, blue and green is represented by (0.67, 0.33), (0.14, 0.08) and (0.21, 0.71). The standard white light is found in the coordinate $x = y = 1/3$ in the CIE diagram.

1.3.7. Various energy transfer process in photoluminescence

When a substance is irradiated with the photons, it will be excited to the higher-level excited states. It will release its excess energy in the form of heat and light once the process of de-excitation begins. During this whole process, energy can also be transferred to other nearby particle which is termed as energy transfer process [41]. The quality of the luminescence is very good when there is a good energy transfer occur between sensitizer and the activator. Based on the energy transfer between identical – identical pair and identical – non-identical pair, there are several possibilities of energy transfer mechanism:

1.3.7.1. Resonance energy transfer

Resonance energy transfer is a mechanism of energy transfer between two molecules, one of which is acted as a donor while the other is represented as an acceptor. A donor excited molecule can transfer its energy to an acceptor through dipole-dipole coupling. The rate of this transfer is depended on (i) degree of spectral overlap between the pair, (ii) quantum efficiency of the donor, (iii) dipole orientation of donor- acceptor pair, and (iv) the distance between them [42]. According to the Dexter theory of energy transfer, there is a certain distance of separation between the Donor (D) and Acceptor (A) which will lead to the energy transfer between Donor-Acceptor pair. This distance is termed as the critical distance R_c which can be found out using the following equation:

$$R_c = 2 \left(\frac{3V}{4\pi x_c N} \right)^{1/3} \quad (1.6)$$

where, x_c denotes the critical concentration after the intensity is quenched in volume space V having N number of ions present the unit cell [43]. Based on the value of R_c , the resonance energy transfer is classified as (i) Exchange interaction type ($R_c \leq 5\text{\AA}$) and (ii) multipolar type ($R_c > 5\text{\AA}$).

1.3.7.2. Phonon-assisted energy transfer

This mode of energy transfer occurs when there is mismatch of donor and acceptor energy levels. They try to compensate the energy by simultaneous absorption or release of photon energies. Whole energy must be conserved during the transfer process and without any large-scale superposition of phonon. For small energy difference, one or two photons can initiate the energy transfer. For larger energy gap, multi phonon transfer mechanism can initiate. On the basis of Miyakawa-Dexter theory, probability of phonon

assisted energy transfer is given by [44]

$$W_{PAT}(\Delta E) = W_{PAT}(0)e^{-\beta\Delta E} \quad (1.7)$$

where ΔE denotes the energy gap of donor-acceptor pair and β represents the strength of electron-lattice coupling parameter.

1.3.7.3. Cross- relaxation

Cross relaxation is the process of lowering of excitation energy which is localized at one ion by transferring energy to the nearby ion, thus generating lower energy for the both ions. Under this condition, the energy of the donor is lowered by the same amount of energy which is increased by the acceptor and they have the same energy state. Thus cross-relaxation between same rare earth ions can occur when the two pair have the similar energy gap. [45-46]. This type of energy transfer is contributed mainly in the non-radiative transition when the concentration of the ions is very high.

1.3.7.4. Migration of excitation energy

Migration of excited energy is a multi-step process generally occur one ion to another ion of same species. This involves the random transferring of resonance energy which will ultimately act as a quenching centre. This type of energy transfer is more favorable with the low concentration of the acceptor. When the concentration of the two ions are comparable, even the energy transfer between sensitizer i.e. $S \rightarrow S$ is faster than that of the $S \rightarrow A$ transition especially in case of lanthanide ion having small Stoke's shift. Thus, the energy can be transferred within the sensitizer molecule or ion before the energy is transferred from the sensitizer to activator [47].

1.4. Lanthanide doping for Phosphors

1.4.1 Lanthanides

In the bottom part of the modern periodic table, there is separated group which is called *f* block element that consist of two series each consisting of 14 elements. In these series, electrons are subsequently filled in the *f* orbitals. The first series is called Lanthanides while the other series is called Actinides. In lanthanides, the entering electron are placed in the 4*f* orbitals and for actinides, it is occupying the 5*f* orbitals. Lanthanide series starts from Cerium (Ce) and ends with Lutetium (Lu). Electronic configurations of each of the lanthanides are given below in Table 1.2. Lanthanum is not considered as a lanthanide because it has no electron in 4*f* orbitals.

Table 1.2 Electronic configurations of lanthanide series

Atomic number	Name of elements	Electronic configuration
58	Cerium (Ce)	[Xe]4f ¹ 5s ² 5p ⁶
59	Praseodymium (Pr)	[Xe]4f ² 5s ² 5p ⁶
60	Neodymium (Nd)	[Xe]4f ³ 5s ² 5p ⁶
61	Promethium (Pm)	[Xe]4f ⁴ 5s ² 5p ⁶
62	Samarium (Sm)	[Xe]4f ⁵ 5s ² 5p ⁶
63	Europium (Eu)	[Xe]4f ⁶ 5s ² 5p ⁶
64	Gadolinium (Gd)	[Xe]4f ⁷ 5s ² 5p ⁶
65	Terbium (Tb)	[Xe]4f ⁸ 5s ² 5p ⁶
66	Dysprosium (Dy)	[Xe]4f ⁹ 5s ² 5p ⁶
67	Holmium (Ho)	[Xe]4f ¹⁰ 5s ² 5p ⁶
68	Erbium (Er)	[Xe]4f ¹¹ 5s ² 5p ⁶
69	Thulium (Tm)	[Xe]4f ¹² 5s ² 5p ⁶
70	Ytterbium (Yb)	[Xe]4f ¹³ 5s ² 5p ⁶
71	Lutetium (Lu)	[Xe]4f ¹⁴ 5s ² 5p ⁶

Lanthanides are very important since their electrons are not easily affecting by surrounding because the 4f electrons in lanthanides are completely shield by the outer shell 5s²5p⁶ electrons. Thus, the lanthanide transitions show very sharp peaks, but due to forbidden nature of *f-f* transition, the intensity is very weak and also have long life time values. The most stable oxidation state of lanthanide ions is +3 state. Only a few lanthanides can also show other oxidation state like +4 and +2. Cerium can show both +3 and +4 while Europium and Samarium can show +2 and +3 states.

1.4.2. Doping of lanthanides

As stated above, the intensity of the *f-f* transitions in lanthanide is very weak due to the parity forbidden. However, this can be further relaxed when the lanthanide is doped into other hosts. After the doping, the local environment around the lanthanide is changed thus perturbed the crystal field renders splitting of transitions. This also allows the energy transfer from host to the lanthanide activator. This enhances the luminescence properties of the lanthanide ion [48]. Semiconductors like ZnO, SnO₂ have emission at 370 and 490 nm and the incoming radiation is absorbed by the host material and then is transferred to the lanthanide ion so that resulting luminescence is very intense. If the doping

concentration is very high, it can further decrease the luminescence intensity due cross relation among the activator ions. So, it is necessary to check for an optimum concentration of the dopant in order to minimize the quenching effect [49-52].

1.4.3. Dopants used in the present study

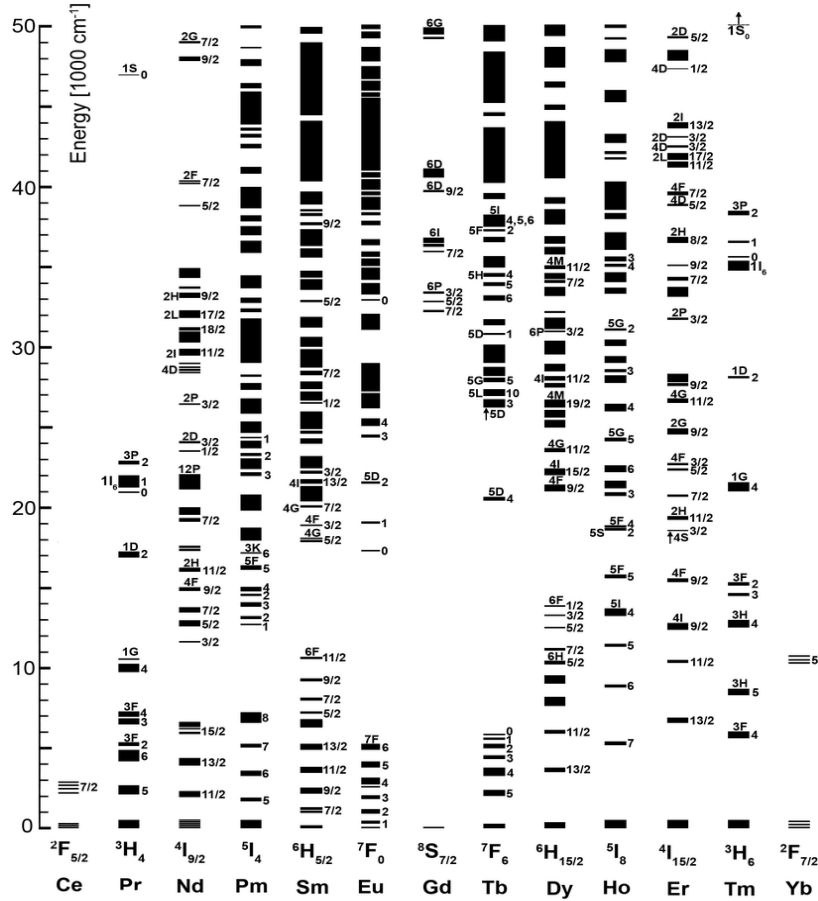


Fig. 1.2 Energy levels associated with lanthanide ions.

1.4.3.1. Europium (Eu^{3+})

Eu^{3+} ion has been used in the display and lighting application as a red emitter [53]. The various transitions originating from $^5\text{D}_0 \rightarrow ^7\text{F}_J$ ($J = 0, 1, 2, 3, 4, 5$ and 6) transitions falls in the red region of the electromagnetic radiation. Various energy levels associated are given Fig. 1.2. The main contributing transition in the Eu^{3+} ion is very sensitive to the local environment around the ion. The magnetic dipole transition ($^5\text{D}_0 \rightarrow ^7\text{F}_1$) observed at around ~ 590 nm is related to Eu^{3+} occupies the site with inversion symmetry. This transition is not much affected by the host environment. But, the other transition ($^5\text{D}_0 \rightarrow ^7\text{F}_2$) which is observed at around 615 nm due to the electric dipole is highly sensitive with respect to the local environment and it is dominating when the Eu^{3+} ion resides the site without inversion symmetry or any asymmetric surrounding. Due to the

spin forbidden transition, the decay life time value of Eu^{3+} has of the order of some milliseconds and cannot be affected by multi-phonon relation [54-55].

1.4.3.2. *Samarium (Sm^{3+})*

Sm^{3+} emits the radiation which have orange-red region of the electromagnetic radiation. The various transitions in Sm^{3+} are originating from $^4\text{G}_{5/2} \rightarrow ^6\text{H}_J$ ($J = 5/2, 7/2, 9/2, 11/2$) transitions [56]. Peak corresponds to electric dipole $^4\text{G}_{5/2} \rightarrow ^6\text{H}_{9/2}$ transition is observed at around 643 nm and dominates when the Sm^{3+} occupies the site without inversion symmetry of the host crystal. The emission peak ~ 601 nm, $^4\text{G}_{5/2} \rightarrow ^6\text{H}_{7/2}$ in many cases become dominant. Another peak which is observed at 561 nm corresponds to the magnetic dipole transition ($^4\text{G}_{5/2} \rightarrow ^6\text{H}_{5/2}$). This peak is somewhat weaker than the electric dipole transition. So, the location site of the Sm^{3+} ion is very crucial in the preparation of phosphor materials [57-58].

1.4.3.3. *Bismuth (Bi^{3+})*

Bi^{3+} has an atomic number 83 and it is placed in the group 15 of the periodic table. Bismuth is a brittle metal with pinkish, silvery metallic lustre and it is the most diamagnetic metal available. It has the electronic configuration of $[\text{Xe}]4f^{14}5d^{10}6s^26p^3$ [59]. The ground of bismuth in trivalent state is singlet state ($^1\text{S}_0$) having $6s^2$ electronic configuration. The excited state, $6s6p$ can form both singlet and triplet state. Among them, $^3\text{P}_0, ^3\text{P}_1, ^3\text{P}_2$ are in triplet state while $^1\text{P}_1$ is in singlet state. The transitions $^1\text{S}_0 \rightarrow ^3\text{P}_0$ and $^1\text{S}_0 \rightarrow ^3\text{P}_2$ are spin forbidden and transitions $^1\text{S}_0 \rightarrow ^3\text{P}_1$ and $^1\text{S}_0 \rightarrow ^1\text{P}_1$ are both parity and spin-allowed transition due to spin-orbit coupling. The life time of Bi^{3+} ion is of the order $10^{-6} - 10^{-8}$ s [60-61].

1.5. Synthesis of nanomaterials

There are two main categories of synthesis: (i) Top-down and (ii) Bottom-up approaches which is given in Fig. 1.3.

1.5.1. *Top-down method*

In this method, large particle so called bulk are finely divided into nanostructured materials. Laser ablation, electrospinning and mechanical milling are the common process included in this method.

1.5.1.1. *Laser ablation*

This method involves the production of nanoparticles using a powerful laser beam to

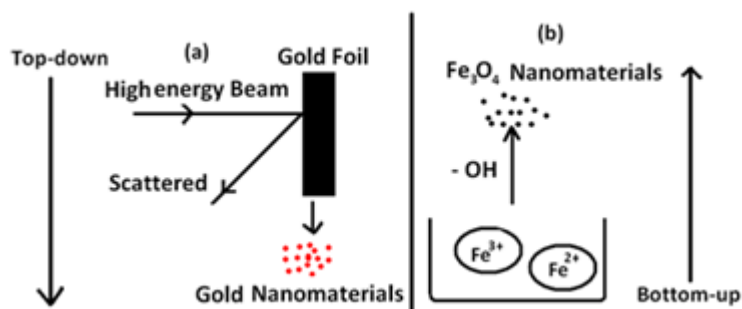


Fig. 1.3 Schematic representation of (a) Top-down and (b) Bottom-up synthesis technique

target the bulk material. Due to the high energy of the laser ablation, the precursor is vaporized and started to form particles of the nano size. This method is considered as green synthesis when the material is noble metals since they don't need any stabilizing agent [62]. Different types of compounds like metal nanoparticles, oxide composite, carbon nanomaterial and ceramics can be produced using this method [63-67].

1.5.1.2. Electrospinning

This is the simplest to-down methods. The breakthrough in electrospinning is the invention of coaxial electrospinning where the spinneret consist of two coaxial capillaries are allowed to mixed in which one of the liquids from a capillary is forming core and the liquid from other capillary is forming shell nanoparticle. Thus, this method is very effective in the production of ultrathin core-shell fibers. This method is also been used in the development of hybrid material, hollow polymer etc. [68].

1.5.1.3. Mechanical milling

This method is cost effective in the production of nanomaterials from the bulk. This method is very useful in the blending of different phases for the synthesis of nanocomposite. During the milling process large bulk materials is finely crushed into a very small nanostructure. Mechanical milling is generally used in the production of strengthening alloy, nanocomposite and wear resistant spray coating etc. [69-70].

1.5.2. Bottom-up method

1.5.2.1. Chemical vapor deposition (CVD)

It is effectively used during the synthesis of carbon-based nanomaterials. In this process a thin film is allowed to form on the surface via a vapor phase chemical reaction of the precursors [71]. In this method, high volatility of the precursor along with the high purity, non-hazardous and good stability is considered for this method. During the synthesis of

carbon nanotube, a substrate is placed inside an oven and after heating at the elevated temperature, carbon containing gas is allowed to pass into the system. Under this heated condition, the gas is slowly degraded and starts forming carbon atom which will deposit on the substrate to form the carbon nanotube. The morphology of the product can be controlled by variation of different catalyst. For example, during the synthesis of graphene, Ni and Co produce multi-layer graphene whereas Cu gives monolayer graphene [72-73].

1.5.2.2. Solvothermal and hydrothermal methods

This is the most common synthesis method used for the synthesis of nanomaterials [74-75]. The heterogeneous reaction is done in an aqueous solution within a sealed vessel and also with the elevated temperature. This is known as hydrothermal method. But, in case of solvothermal the same reaction is carried out in a non-aqueous medium. Recently, microwave assisted hydrothermal or solvothermal has been become a spotlight for engineering highly important nanostructure. The morphology of the material is also highly homogeneous. This method is generally employed in the preparation of nanowire, nanorods, nanosphere etc. [76-78].

1.5.2.3 Sol-gel method

It is a common wet-chemical technique used for the production of nanomaterials. They are employed to produce some high-quality metal oxide nanomaterials. The named sol-gel is given to this synthesis method because during the reaction, the precursors are transformed first in a soft sol and then modified into a hard gel after the completion of reaction [79]. The gel thus formed is converted to nanostructure. This procedure may consist many steps, first the metal oxide is hydrolyzed in water or alcohol to form a sol. In the second step, hydrolysis take place which further increase the viscosity of the solvent to form a porous structure and is left for aging. During the aging process many structural changes are occurred regarding the porosity and distance between the colloidal particles before the formation of gel. Last step is the calcination step to get the required nanomaterials [80]. This method has many advantages because it is an ecofriendly and the nanomaterial thus formed is highly homogeneous.

1.5.2.4. Soft and hard template methods

The soft and hard template can be used to get the required structure. However, the soft template method is a straight forward synthesis process which has a very mild reaction

conditions with different morphology. Here, the nanoporous nanomaterials are formed using the template like block copolymer, organic template and surfactants etc. [81]. Van der Waal forces of attraction or the hydrogen bonding are the main interaction exist between template and the precursor. Even 3D structure can also be prepared using this method by using liquid crystalline micelles. The hard template method is also called nano-casting. Precursor are fitted in the well design solid template in order to get the desire structure. Three main steps are required during the synthesis via this method. First, the template is selected or prepared and in the next step the precursor is filled into the template mesopore to form a solid structure. Finally, the hard template is removed to get the mesoporous replica [82].

1.5.2.5. Reverse micelle methods

This method is very useful when the desired shape and size nanomaterial preparation is necessary. An oil in water emulsion will form a normal micelle where the hydrophobic tails pointed towards the core to hold the oil droplets. But, in a reverse micelles structure, the hydrophilic heads are pointed towards the core and hold the water particle [83]. This small section of the core can act as a nanoreactor for the nanoparticle synthesis. The size of this core can be controlled by controlling the water to surfactant ratio. If the water contain is very low then the size of the core is also very small and the resulting nanomaterial is of very small size. Nanoparticle synthesized using this method are highly homogenous in size and monodispersed in nature [84-85]. Precise size of the desire nanomaterial can be easily prepared following this method

1.6. Host material used in the present study

Y_2O_3 and GdO_3 have ${}^7\text{T}_h$, cubic space group, along with a unit cell which is constructed by two different types of cationic sites, assuming that the two different forms of cationic sites are distributed in two non-symmetrical (non-equivalent) sites. The two non-equivalent sites are 24d of no inversion having C_2 symmetry and the other one is 8b of inversion S_6 (C_{3i}) symmetry [86,87]. When lanthanide is doped into $\text{Y}_2/\text{Gd}_2\text{O}_3$, the emission spectra of lanthanide at C_2 sites benefits from both numbers of C_2 relative to S_6 centers and therefore the resulting spectrum is more intense i.e. characteristic forced electric dipole (ED) emission transitions spectra. On the other hand, the emission spectra from S_6 site are long lifetime and with a weaker intensity, since it contains only the magnetic dipole (MD) transitions i.e., $\Delta J = 0, \pm 1$ which is allowed by the selection rules of centrosymmetric sites [3]. In another words, when the Eu^{3+} ions are present at C_{3i}

(centrosymmetric) site, only one transition i.e., f - f magnetic dipole transitions will be observed. When the Eu^{3+} ions are present at C_2 site, the electric dipole transitions become allowed, it means that most of the intraconfigurational f - f transitions can be seen. The emission spectra from Eu^{3+} ions (C_{3i}) site is not much desirable since it can only generate low intensity emission intensity due to lower transitions probability [88] and this leads to the high nonradiative relaxations probability leading to decrease in overall emission intensity. Therefore, we must prefer the Eu^{3+} ions emission from C_2 site for luminescence study [89].

Yttrium oxide (Y_2O_3) can be considered a good host lattice for lanthanides ions especially for Eu^{3+} ions (red emitting phosphors) due to its unit cell as well as better photo saturation properties. As bulk material, Y_2O_3 can be achieved about 100% quantum yield [90]. Recently, Eu^{3+} ions doped Y_2O_3 nanoparticles are widely studied by various scientist and researcher, due to its highly stable, narrow and excellent red emitter. Eu^{3+} ions doped Y_2O_3 nanoparticles became a promising material in optoelectronics devices, for examples is use as phosphors in LEDs devices or as a red emitter phosphor in displays devices [91]. It also has low toxicity, therefore Y_2O_3 : Eu is use as promising material in nanobiotechnology and medicinal purposed [91].

Photoluminescent properties of $\text{Y}_2\text{O}_3:\text{Sm}^{3+}$ ions nanomaterials are not much investigated [92,93]. The Sm^{3+} ions have $4f^5$ configuration so it can be called as a Kramer ion because of its electronic states that are at least doubly degenerated for any crystal field perturbation [94]. As we know that for any symmetry lower than cubic, Sm^{3+} ion with $^{2S+1}L_J$ state will give the maximum number of the Stark components $J + \frac{1}{2}$ manifold. [95]. Samarium ions are having energy levels with ground level 6H_J and 6F_J and excited level $^4G_{5/2}$ [95]. The emission spectra of Sm^{3+} ions were comprised with intra $4f$ shell transitions. The photoluminescence studies of Sm^{3+} ion doped in different hosts materials has been reported [96,97]. Samarium compounds have long lifetime and narrow line emission like europium compounds, therefore it can be used as materials label in multianalyte assays [98-100].

The emission spectra of Sm^{3+} ions show emissions from 490 to 750 nm in range because of the $^4G_{5/2}$ to $^6H_{J=5/2,7/2,9/2,11/2}$ transitions with large absorption coefficient about 407 nm. The transition $^4G_{5/2}$ to $^6H_{7/2}$ transition is hypersensitive that means it is strongly depends on the host environment [101] On the other hand, Eu^{3+} ions have f - f transitions and show emissions in red to highly intense red region corresponding to 5D_0 to $^7F_{J=0,1,2,3,4}$

transitions [102]. The samarium and europium ions have ionic radius of 0.104 and 0.094 nm which is very closed to ionic radius of yttrium ions i.e. 0.093 nm, therefore samarium and europium ions can easily incorporate in the host Y_2O_3 lattice [103]. There are many reports on studies of Sm^{3+} and Eu^{3+} doped Y_2O_3 nanoparticles [104,105]. When Eu^{3+} ions and Sm^{3+} ions are doped into Y_2O_3 nanoparticles Sm^{3+} ions act as activator and Eu^{3+} behaves like sensitizer [106].

Co-doping is one of the best methods for enhancement of luminescence intensity in lanthanide doped nanoparticles, enhancement of luminescence intensity is important for application in display devices. For LS coupling, electric dipole (ED) within $4f-4f$ transitions of lanthanide ions are forbidden due to selection of parity rule (which is spin forbidden transition in most cases). As a result, the optical absorption spectra are weak and their lifetimes of excited states are long. As we know that the $4f$ electrons of lanthanide ions are shielded from the environment of surroundings by the outer $5s$ and $5p$ electrons; As a result, absorption transitions show sharp lines in the spectra [107], which is undesirable to match excitation sources. In recently years, Bi^{3+} ions have been employed as a codopant in A_2O_3 ($\text{A} = \text{Y}, \text{La}, \text{or Gd}$) to dopant Sm^{3+} , Eu^{3+} and Er^{3+} ions under the UV light excitation (300-390 nm) [108,109,110]. When the Bi^{3+} ions is codoped it highly enhanced by the energy transfer from Bi^{3+} ions to Sm^{3+} , Eu^{3+} and Er^{3+} ions. Bi^{3+} ions are most commonly use as sensitizer in oxides, phosphates, vanadate, phosphate, fluoride and borates nanoparticles [107]. Bi^{3+} ions possess $6s^2$ electronic configuration, the ground state corresponding to $^1\text{S}_0$ state and to $^3\text{P}_0$, $^3\text{P}_1$, $^3\text{P}_2$, and $^1\text{P}_1$ corresponding to first excited states for increasing energies. The Bi^{3+} ions emission show two main peaks corresponding to $^3\text{P}_0-^1\text{S}_0$ and $^3\text{P}_1-^1\text{S}_0$ transition [111]. Mechanism of energy transfer from Bi^{3+} ions to Eu^{3+} ions are shown in Fig. 1.4.

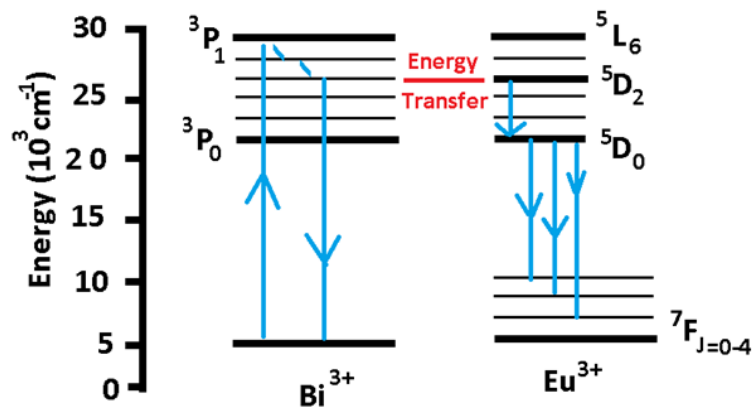


Fig. 1.4. Schematic representation of energy transfer from Bi^{3+} ions to Eu^{3+} ions.

Gadolinium has paramagnetic properties and it is a rare earth (RE) metal, which can improve magnetic resonance imaging (MRI) signal. Gadolinium ions is suitable for MRI since it has seven unpaired electrons in the valence shell and due to this unpaired electron, it has a high magnetic moment. [112]. The gadolinium oxide (Gd_2O_3) nanoparticles is also suitable host for lanthanides. Amongst the lanthanide Eu^{3+} ions doped Gd_2O_3 nanoparticles ($\text{Gd}_2\text{O}_3:\text{Eu}^{3+}$) is attractive in photoluminescence (PL) study. It has many applications in fluorescence lamps, biological labelling [113,114,115], television tubes, MRI contrasting agent [116], hyperthermia [117], and display devices [118]. It is also (Eu^{3+} ions doped Gd_2O_3 nanoparticles) red-emitting phosphors long-term photostability, bright luminescence and thermoluminescent properties [119]. Sm^{3+} ions can also dope in Gd_2O_3 nanoparticles and studies its luminescence properties as well as their applications but there is little known about Sm^{3+} doped Gd_2O_3 nanoparticles [120]. G. Boopathi et al. study optical properties of Sm^{3+} ions doped Gd_2O_3 nanoparticles synthesis by co-precipitation method at 60 °C [121].

For the luminescence enhancement of Eu^{3+} ions by codoping technique, the main key is to choose appropriate codopant ions for cooperating with Eu^{3+} ions. Eu^{3+} ions codoping with Gd^{3+} or Sm^{3+} ions were found to be efficient for improvement the photoluminescence of properties of Eu^{3+} ions, because of the energy transfer as well as cooperative excitation between three ions i.e., Eu^{3+} and $\text{Sm}^{3+}/\text{Gd}^{3+}$ [122]. In particular, it is also show that migration of energy between $\text{Gd}^{3+}-\text{Sm}^{3+}$ might occur and which leads to the change in position of excitation band of Sm^{3+} ions [123], which indicates that the excitation and emission bands of Eu^{3+} ion can be tuned the by Sm^{3+} and Gd^{3+} ions. G. Liu *et al.* investigated enhancement of luminescence properties of Bi^{3+} ion codoped $\text{Gd}_2\text{O}_3:\text{Sm}^{3+}$ nanoparticles synthesis by combustion method [124]. They reported that, after excitation at $^1\text{S}_0-^3\text{P}_1$ transition of Bi^{3+} ions the luminescence intensity of the Sm^{3+} ion was enhanced due to strong energy transfer from Bi^{3+} to Sm^{3+} ions [124]. Wei X.T. et al. reported Eu^{3+} ion codoped $\text{Gd}_2\text{O}_3:\text{Eu}^{3+}$ nanoparticles synthesis by Pechini sol-gel method [125]. They have reported that introduction of Bi^{3+} ions broaden the excitation band of Eu^{3+} ions this indicates that strong energy transfer from Bi^{3+} to Eu^{3+} ions.

1.7. Some applications of Lanthanide doped nanomaterial

1.7.1 Optical imaging

Lanthanide doped nanomaterial can absorb radiation in the NIR (Near infra-red) and emission properties. The codoping of one or more lanthanide activator yield

luminescence in NIR region which helps in the efficient collection of the emitted light. The lanthanide combination of $\text{Yb}^{3+}/\text{Er}^{3+}$, $\text{Yb}^{3+}/\text{Tm}^{3+}$ and $\text{Yb}^{3+}/\text{Ho}^{3+}$ are most commonly employed pair which has emission in the NIR-1 spectroscopic range and the common host material used are NaYF_4 , NaGdF_4 , LiYF_4 and CaF_2 etc [126,127,128,129]. The advantages of this method are that it can be applied for deep tissue imaging that shows much higher resolution. But, due to low quantum yield of this material, they are not efficient to give a high-resolution imaging. To overcome this, generally core shell nanoparticle are used to ensure the protection of the core lanthanide ion from quenching effect.

1.7.2. MRI contrasting agent

MRI is a powerful diagnostic tool in the field of medicine. It has the properties of being non-invasive, high resolution and the absence of ionizing electromagnetic radiation. Design of the contrasting agent must be ensuring to cope with possible toxicity due to paramagnetic ions. Highly stable Gd(III) containing luminescent materials such as $\text{NaGdF}_4:\text{Yb}^{3+}/\text{Er}^{3+}$ or $\text{NaGdF}_4:\text{Yb}^{3+}/\text{Tm}^{3+}$ are generally used as contrasting agent. Gadolinium ion is allowed to combine with protein or macromolecular substrate at the region where the partial charge of the substrate exist. Water soluble complexes of Gd (III) ion have been used to obtain the high relaxivity of the contrasting agent since relaxivity can be altered by the rotational and exchange dynamics. Micellar aggregates, polysaccharides, or even lanthanide ion chelate compounds, zeolite etc. [130].

1.7.3. Display devices

The light produced from cathode ray tube of a television when excited the phosphor present on the screen in the form of tiny dots which enable the screen to form different types of colour. $\text{Y}_2\text{O}_3:\text{Eu}^{3+}$ phosphor, $\text{ZnS}:\text{Ag}$ and $\text{ZnS}:\text{Cu},\text{Al},\text{Au}$ phosphors are used to generate the corresponding light of red, blue and green respectively [131]. In case of Plasma display, the phosphors are excited by vacuum ultraviolet and give two emission at 147 and 172 nm. Different colours of red, green and blue are generated by the discharge xenon lamp in their respective cell. The phosphors $(\text{Y},\text{Gd})\text{BO}_3:\text{Eu}^{3+}$ or $\text{Y}(\text{V},\text{P})\text{O}_4:\text{Eu}^{3+}$, $\text{Zn}_2\text{SiO}_4:\text{Mn}^{2+}$ or $\text{YBO}_3:\text{Tb}^{3+}$ and $\text{BaMgAl}_{10}\text{O}_{17}:\text{Eu}^{2+}$ have been used in plasma display for red, green and blue colors [132].

1.7.4. Solid state lighting

Light emitting diode is one of the most important inventions. With the coming of white

light emitting diode, whole of the solid-state lightening has revolutionized with this excellent efficacy, more energy conservation and ecofriendly and long durability. In the commercial White light emitting diodes (WLEDs), the light is produced by YAG: Ce³⁺ yellow-emitting phosphor coating on the blue InGaN chip [133]. But still, the red component in this WLEDs is not efficient which results in the low rendering index and high color temperature. Recently, BaY₂ZnO₅:Eu³⁺, BaYZn₃AlO₇: Eu³⁺, YVO₄:Eu³⁺ are the newly developed red emitting phosphors which have a superior red component [134,135]. LED lights have been used widely in large outdoor screens, LCD screens, traffic lights, indoor and outdoor lights for cars and buses, in cell phones, and flashlight bulbs etc. [136].

1.7.5. Sensing application

Nowadays, luminescent phosphor is widely used as sensor in different field. The main interaction between phosphor with the biological or chemical active substance, due to the energy transfer between these two makes the luminescence intensity either increase or decrease. Different compounds like glutathione, cyanide, nitro compound in explosive material and other heavy metals can be easily detection with different types of phosphors. For instance, LuNbO₄:Er³⁺, ZnWO₄:Er³⁺/Yb³⁺ and YNbO₄:Er³⁺/Yb³⁺ are used a nanoprobe for temperature sensing [137,138]. La₂O₂CO₃:Eu³⁺/Ho³⁺ is commonly used as probe for the detection of H₂O₂ [139]. YVO₄:Eu³⁺, GdVO₄:Eu³⁺, SrF₂:Ce³⁺/Tb³⁺, Gd₂O₃:Eu³⁺ are used for detection of heavy metal ions [140-143]. Cu Fe₃O₄ and NaYF₄:Yb³⁺/Er³⁺ can form a complex and it is used in the detection of DNA [144].

1.8 Outlook of the Thesis

This thesis covers the results obtained from the investigation of luminescent properties of unsensitized and Bi³⁺ sensitized Y₂O₃ and Gd₂O₃ activated with Eu³⁺ and Sm³⁺. During the course of investigation, it has come to light that the sensitization with Bi³⁺ can enhance the luminescence efficiency of these phosphors. Interestingly, the excitation wavelength can be further pushed towards the near UV region due to the presence Bi³⁺ in the phosphor. Thus, the phosphor produces intense red colour emission in the case of Eu³⁺ activated Y₂O₃ and Gd₂O₃ phosphors. This result is promising for the potential of these phosphors in the fabrication of white light emitting light emitting diodes.

References

1. Z. K. Tang, G. K. L. Wong, P. Yu, Appl. Phys. Lett., 72 (1998) 3270-3272.
2. H. Morkoç, S. Strite, G. B. Gao, M. E. Lin, B. Sverdlov, M. Burns, J. Appl. Phys., 76 (1994) 1363-1398.
3. M. H. Huang, S. Mao, H. Feick, H. Yan, Y. Wu, H. Kind, E. Weber, R. Russo, P. Yang, Science, 292 (2001) 1897-1899.
4. P. W. Barone, S. Baik, D. A. Heller, M. S. Strano, Nat. Mater., 4 (2005) 86-92.
5. R.E. Bailey, S.M. Nie, J. Am. Chem. Soc., 125 (2003) 7100-7106.
6. J.W. Stouwdam, F. V. Veggel Nano Lett., 2 (2002) 733-737.
7. J. Faist, F. Capasso, D. L. Sivco, C. Sirtori, A. L. Hutchinson, A. Y. Cho, Science 264 (1994) 553-556.
8. M.A. Hines, G.D. Scholes, 15 (2003) 1844-1849.
9. J.W.M. Verwey, G. Blasse, Chem. Mater., 2(1990) 458-463.
10. E. Auffray et al., Nucl. Phys. B - Proceedings Supplements, 44 (1995) 57-62.
11. G. Menzer Z. Kristallogr., 69 (1929) 300-396
12. S. Geller Z Kristallogr., 125 (1967) 1-47
13. R-J. Xie, N. Hirosaki, M. Mitomo, K. Takahashi, K. Sakuma, Appl. Phys. Lett., 88 (2006) 101104
14. R-J. Xie, N. Hirosaki, K. Sakuma, Y. Yamamoto, M. Mitomo, Appl. Phys. Lett. 84 (2004) 404-440
15. T. Senden, F.T. Rabouw, A. Meijerink, ACS Nano, 9 (2015) 1801-1808
16. M. Raukas, S.A. Basun, Wv. Schaik, W.M. Yen, U. Happek, Appl. Phys. Lett. 69 (1996) 3300-3302
17. M. Yamaga, Y. Masui, S. Sakuta, N. Kodama, K. Kaminaga, Phys. Rev. B 71(2005) 205102
18. D. J. Robbins, B. Cockayne, B. Lent, J. L. Glasper, Solid State Commun. 20 (1976) 673-676
19. J. Sun, J. Zeng, Y. Sun, H. Du, J Alloys Compd. 540 (2012) 81-84
20. X. Zhang, J. Zhang, R. Wang, M. Gong, J. Am. Ceram. Soc. 93 (2010) 1368-1371
21. P. Li, L. Pang, Z. Wang, Z. Yang, Q. Guo, X. Li, J. Alloys Compd. 478 (2009) 813-815
22. Z. Xia, R-S. Liu J. Phys. Chem. C 116 (2012) 15604-15609
23. A.M. Srivastava, H.A. Comanzo, S. Camardello, S.B. Chaney, M. Aycibin, U. Happek, J. Lumin. 29 (2009) 919-925
24. I. Carrasco, K. Bartosiewicz, M. Nikl, F. Piccinelli, M. Bettinelli, Opt. Mater. 48 (2015) 252-257
25. R.G. Pappalardo, R. B. Hunt J. Electrochem. Soc. 132 (1985) 721-730
26. H. N. Hersh, H. Forest, J. Lumin. 2 (1970) 862-868
27. Y. Arai, S. Adachi, J. Lumin. 131(2011) 2652-2660
28. Y. Arai, S. Adachi, J. Electrochem. Soc. 158 (2011) J179-J183
29. S. Adachi, H. Abe, R. Kasa, T. Arai, J. Electrochem. Soc. 159 (2011) J34-J37
30. Kasa R, Adachi S J. Electrochem. Soc. 159 (2012) J89-J95
31. C. Ronda, Luminescence: From Theory to Applications, Wiley-VCH, Weinheim, Germany, (2008)
32. E. Wiedemann, Abhandlung. Annalen Der Physik Und Chemie, 270 (1888) 446-463
33. M. A. El-Sayed, Acc. Chem. Res. 1 (1968) 8-16
34. K. C. Mishra, J. Collins, ECS J. Solid State Sci. Technol. 9(2020). 066004

35. Adolfas K. Gaigalas, Lili Wang, *J. Res. Natl. Inst. Stand. Technol.*, 113 (2008) 17-28
36. Operating Instructions, Measurement of Fluorescence Quantum Yield using the Integrating Sphere, Edinburg Instruments Ltd., Livingston, U.K., 2 (2012).
37. Q. Pang, J. Shi, M. Gong, *J. Am. Ceram. Soc.*, 90 (2007) 3943-3946
38. X. Zhang, X. Qiao, H. J. Seo, *Curr. Appl. Phys.*, 11 (2010) 442-446
39. L. Ozawa, *ECS J. Solid State Sci. Technol.*, 126, (1979) 106–109
40. Q. Y. Zhang, K. Pita, S. Buddhudu, C. H. Kam, *J. Phys. D* 35 (2002) 3085
41. R. C. Powell, G. Blasse, *Structure and bonding, Luminescence and energy transfer*, Springer-Verlag, Heidelberg, New York, (1980)
42. T. M. Chen, Y. J. Yang, *Phosphors. Up Conversion Nano Particles, Quantum Dots and Their Applications*, Springer-Verlag, Heidelberg, New York, (2017)
43. Q. Pang, J. Sh, M. Gong, *J. Am. Ceram. Soc.*, 90 (2007) 3943-3946
44. [44. R. Reisfeld, *Excited States and Energy Transfer form Donor Cations to Rare Earths in the Condensed Phase*, Springer, Berlin, (2006)
45. Q. Y. Zhang, X. Y. Huang, *Prog. Mater. Sci.*, 55 (2010) 353-427
46. S. Ye, F. Xiao, Y. Y. Ma, Q. Y. Zhang, *Mater. Sci. Eng. R Rep.*, 71(2010) 1-34
47. O.N. Tchaikovskaya, N.G. Dmitrieva, E.N. Bocharnikova, V.S. Chaidonova, P.V. Avramov, *Front. Chem.*, 04 November (2021)
48. S. Cotton, *Lanthanide and Actinide Chemistry*, John Wiley & Sons, Ltd ISBN: 978047 001 0082 (2006)
49. R. S. Ningthoujam, *Enhancement of Luminescence by Rare Earth Ions Doping in Semiconductor host*, in *Synthesis, Characterization and Applications of Multifunctional materials* ed. S. B. Rai and Y. Dwivedi, Nova Science Publishers Inc., Hauppauge, U.S.A. (2012)
50. M. N. Luwang, R. S. Ningthoujam, N. S. Singh, R. Tewari, S. K. Srivastava R. K. Vatsa, *J. Collod Interface Sci.*, 349 (2010), 27-31
51. L. P. Singh, N. V. Jadhav, S. Sharma, B. N. Pandey, S. K. Srivastava, R. S. Ningthoujam, *J. Mater. Chem. C*, 3 (2015) 1965-1969.
52. L. R. Singh, R.S.Ningthoujam, S. D. Singh, *J. Alloy. Comp.*, 487 (**2009**), 466-470.
53. J. Liu, H. Lian and C. Shi, *Opt. Mater.*, 29 (2007) 1591-1594
54. C. Chiu, C. Liu, S. Huang and T. Chen, *J. Electrochem. Soc.*, 154 (2007) J181-J184
55. Y. Chena, H. K. Yanga, S. W. Parka, B. K. Moona, B. C. Choia, J. H. Jeonga and K. H. Kim, *J. Alloys Compd.*, 511 (2012) 123–128
56. S. R. Bowman, S. O'Connor and N. J. Condon, *Opt. Express* 20 (2012) 12906-12911
57. S. Hachani, B. Moine, A. El-akrmi and M. Ferid, *J. Lumin.*130 (2010) 1774–1783
58. H. Ye, M. He, T. Zhou, Q. Guo, J. Zhang, L. Liao, L. Mei, H. Liu and M. Runowski, *J. Alloys Compd.* 757 (2018) 79-86
59. B. J. Deibert, E. Velascom, W. Liu, S. J. Teat, W. P. Lustig and J. Li, *Cryst. Growth Des.*, 16 (2016) 4178 – 4182
60. L. Wang, B. K. Moon, S. H. Park, J. H. Kim, J. Shi, K. H. Kim and J. H. Jeong, *New J. Chem.*, 40 (2016) 3552
61. H. Zhang, F. Kang, Y. Zhao, M. Peng, D. Y. Lei and X. Yang, *J. Mater. Chem. C*, 5 (2017) 314-321
62. V. Amendola, M. Meneghetti, *Phys. Chem. Chem. Phys.* 11 (2009) 3805
63. J. Zhang, M. Chaker, D. Ma, *J. Colloid Interface Sci.* 489 (2017) 138–149
64. R. A. Ismail, M. H. Mohsin, A. K. Ali, K. I. Hassoon, S. Erten-Ela, *Phys. E* 119 (2020) 113997

65. J. Chrzanowska, J. Hoffman, A. Małolepszy, M. Mazurkiewicz, T. A. Kowalewski, Z. Szymanski, L. Stobinski, *Phys. Status Solidi*. 252 (2015) 1860–1867
66. J. Duque, B. Madrigal, H. Riascos, Y. Avila, *Colloids Interfaces* 3 (2019) 25
67. S. S. Su, I. Chang, *Commercialization of Nanotechnologies—A Case Study Approach*, Springer International Publishing, Cham, (2018) pp 15
68. P. S. Kumar, J. Sundaramurthy, S. Sundarajan, V. J. Babu, G. Singh, S. I. Allakhverdiev, S. Ramakrishna, *Energy Environ. Sci.* 7 (2014) 3192–3222
69. T. Prasad Yadav, R. Manohar Yadav, D. Pratap Singh, *Nanosci. Nanotechnol.* 2 (2012) 22–48
70. H. Lyu, B. Gao, F. He, C. Ding, J. Tang, J. C. Crittenden, *ACS Sustainable Chem. Eng.* 5 (2017) 9568–9585
71. A. C. Jones, M. L. Hitchman, in *Chemical Vapour Deposition*, ed. A. C. Jones and M. L.
72. H. Ago, *Frontiers of Graphene and Carbon Nanotubes*, Springer, Japan, Tokyo, 2015, pp. 3–20
73. P. Machac, S. Cichon, L. Lapczak, L. Fekete, *Graphene Technol.* 5 (2020) 9–17
74. X. Wu, G. Q. (Max) Lu, L. Wang, *Energy Environ. Sci.* 4 (2011) 3565
75. S. Cao, C. Zhao, T. Han, L. Peng, *Mater. Lett.* 169 (2016) 17–20
76. Y. Dong, X. Du, P. Liang, X. Man, *Inorg. Chem. Commun.* 115 (2020) 107883
77. Y. Jiang, Z. Peng, S. Zhang, F. Li, Z. Liu, J. Zhang, Y. Liu, K. Wang, *Ceram. Int.* 44 (2018) 6115–6126
78. B. Chai, M. Xu, J. Yan, Z. Ren, *Appl. Surf. Sci.* 430 (2018) 523–530
79. A. E. Danks, S. R. Hall, Z. Schnepf, *Mater. Horiz.* 3 (2016) 91–112
80. M. Parashar, V. K. Shukla, R. Singh, *J. Mater. Sci.: Mater. Electron.* 31 (2020) 3729–3749
81. W. Li, D. Zhao, *Chem. Commun.*, 49 (2013) 943–946
82. Y. Yamauchi, K. Kuroda, *Chem. – Asian J.* 3 (2008) 664–676
83. M. A. Malik, M. Y. Wani, M. A. Hashim, *Arabian J. Chem.* 5 (2012) 397–417
84. M. Soleimani Zohr Shiri, W. Henderson, M. R. Mucalo, *Materials* 12(2019) 1896
85. T.-D. Nguyen, *Nanoscale* 5 (2013) 9455
86. R. W. G. Wyckoff, *Crystal Structures* (Interscience Publishers, 1964 Vol.II).
87. R. P. Leavitt, J. B. Gruber, N. C. Chang, C. A. Morrison, *J Chem Phys.* **76** (1982), 4775–4788.
88. D. Avram, B. Cojocaru, M. Florea, C. Tiseanu, *Opt Mater Express.* 6 (2016) 1635–1643.
89. C. Hang, Z. P. Fen, Z. H. Yang, L. H. Dong, C. Q. Liang, *Chin Phys B* 23 (2014) 057801
90. J. Petry, R. Komban, C. Gimmler, H. Weller, *Nanoscale Adv.* 4 (2022) 858–864.
91. W. Wang, P. Zhu, *Optics Express.* 26 (2018) 34820–34829.
92. J.F. Martel, S. Jandl, B. Viana, D. Vivien, *J. Phys. Chem. Solids* 61 (2000) 1455
93. F. Vetrone, J.-C. Boyer, J.A. Capobianco, A. Speghini, M. Bettinelli, *Nanotechnology* 15 (2004) 75.
94. P.S. May, D.H. Metcalf, F.S. Richardson, R.C. Carter, C.E. Miller, *J. Lumin.* 51 (1992) 249.
95. C.A. Kodaira, R. Stefani, A.S. Maia, M.C.F.C. Felinto, H.F. Brito, *J Lumin.* 127 (2007) 616–622
96. J.B. Gruber, Z. Bahram, M.F. Reid, *Phys. Rev.* 60 (1999) 15643

97. S.B. Stevens, C.A. Morrison, M.D. Seltezer, M.E. Hills, J.B. Gruber, *J. Appl. Phys.* **70** (1991) 948.
98. C.A. Kodaira, R. Stefani, A.S. Maia, M.C.F.C. Felinto, H.F. Brito, *J Lumin.* **127** (2007) 616–622.
99. Tomasz Grzyb, Marcin Runowski, Stefan Lis, *J Lumin.* **154** (2014) 479.
100. G. Lakshminarayana, R. Yang, M. Mao, J. Qiu, I.V. Kityk, *J Non Cryst Solids.* **355** (2009) 2668.
101. B. V. Rao, R. J. Kumar, K. V. Rao, *Inter J Pure Appl Phys.* **13** (2017) 301–316.
102. J. Chen, F. Gu, W. Shao, C. Li, *Physica E*, **41** (2008) 304–308
103. L.S. Chi, R.S. Liu, B.J. Lee, *J Electrochem Soc.* **152**, (2005) J93
104. A. Boukerika, L. Guerbous, *J. Lumin.* **145**, (2014) 148–153
105. A.N. Meza-Rocha, A. Speghini, M. Bettinelli, U. Caldiño, *J Lumin.* **167** (2015) 305–309.
106. Z. Zhu, G. Fu, Y. Yang, Z. Yang, P. Li, *J. Lumin.* **184**, (2017) 96–109.
107. T. Verma, S. Agrawal, *J. Mater. Sci. Mater. Electro.* **145** (2018) 1
108. G. Blasse, B.C. Grabmaier, *Luminescent Materials*, Springer-Verlag, Berlin, 1994.
109. Y. Zhang, M.Y. Wu, W.F. Zhang, *Mod Phys Lett B.* **24** (2010) 475.
110. L. Chi, R. Liu, B. Lee, *J Electrochem Soc.* **152** (2005) J93
111. M. Yang, Y. Sui, S. Wang, X. Wang, Y. Wang, S. Liu, Z. Zhang, Z. Liu, T. Liu, W. Liu, *J Alloys Compd.* **509** (2011) 827.
112. N. A. Setlur, A. M. Srivastava, *Optical Materials* **29** (2006) 410–415.
113. N. M. Maalej, A. Qurashi, A. A. Assadi, R. M. Mohammed, N. Shaikh, M. Ilyas, M. A. Gondal, *Nanoscale Res Lett.* **10** (2015) 215.
114. H. Lu, G. Yi, S. Zhao, D. Chen, L.H. Guo, *J Mater Chem.* **14** (2004) 1336.
115. J.N. Anker, R. Kopelman, *Appl Phys Lett.* **82** (2003) 1102.
116. S.V. Lechevallier, P. Lecante, R. Mauricot, H. Dexpert, D. J. Ghys, H.K. Kong, *Chem Mater.* **22** (2010) 6153.
117. N.S. Singh, H. Kulkarni, L. Pradhan, D. Bahadur, *Nanotechnology* **24** (2013) 065101.
118. J.E. Lee et al., *J Am Chem Soc.* **132** (2010) 552–557.
119. M. Johannsen, U. Gneveckow, L. Eckelt, A. Feussner, N. Waldofner, R. Scholz, *Int J Hyperthermia.* **21** (2005) 637
120. V. Bedekar, D.P. Dulta, M. Mohapatra, S.V. Godbole, R. Ghildiyal, A.K. Tyagi, *Nanotechnology.* **20** (2009) 5707.
121. W. Rossner, B.C. Grabmaier, *J. Lumin.* **48** (1991) 29.
122. M. Goldys, K. Drozdowicz-Tomsia, S. Jinjun, D. Dosev, I. M. Kennedy, S. Yatsunenko, M. Godlewski *J. Am. Chem. Soc.* **128** (2006) 14498–14505.
123. G. Boopathi, S. G. Raj, G. R. Kuma3, R. Mohan, *AIP Conference Proceedings* **1591**, (2014) 1677.
124. S. Yan, J. Zhang, X. Zhang, S. Lu, X. Ren, Z. Nie, X. Wang, *J Phys Chem. C* **111** (2007) 13256.
125. Y. Zhou, J. Lin, S.J. Wang, *Solid State Chem.* **171** (2003) 391.
126. G. Liu, Y. Zhang, J. Yin, W.F. Zhang, *J Lumin.* **128** (2008) 2008–2012
127. A. Gnach, K. Prorok, M. Misiak, B. Cichy, A. Bednarkiewicz, *J. Rare Earths*, **32** (2014) 207
128. J. Ryu, H. Y. Park, K. Kim, H. Kim, J. H. Yoo, M. Kang, K. Im, R. Grailhe, R. Song, *J. Phys. Chem. C* **114** (2010) 21077.
129. G. Gao, C. L. Zhang, Z. J. Zhou, X. Zhang, J. B. Ma, C. Li, W. L. Jin, D. X. Cui, *Nanoscale* **5** (2013) 351

130. M. Pedroni, F. Piccinelli, T. Passuello, S. Polizzi, J. Ueda, P. Haro-Gonzalez, L. M. Maestro, D. Jaque, J. Garcia-Sole, M. Bettinelli, A. Speghini, *Cryst. Growth Des.*, 2013, 13, 4906.
131. M. Botta, L. Tei, *Eur. J. Inorg. Chem.*, 135 (2012) 1945.
132. C. R. Ronda, T. Justel and H. Nikol, *J. Alloys Compd.* 275 (1998) 669–676
133. S. Zhang, *IEEE Transactions on Plasma Science* 34 (2006) 294
134. T. Gessmann, E. F. Schubert, *J. Appl. Phys.* 95 (2004) 2203
135. G. Rajkumar, V. Ponnusamy, G. V. Kanmani, M. T. Jose, *Ceram. Int.*, 48 (2022) 10-21
136. J. Cho, J. H. Park, J. K. Kim E. F. Schubert, *Laser Photonics Rev.* 11(2017) 1600147
137. X. Chai, J. Li, X. Wang, Y. Li, X. Yao, *Optics Express* 24 (2016) 22438
138. X. Dou, Y. Li, T. Vaneckova, R. Kang, Y. Hu, Wen, H., X. Gaoe, S. Zhanga, M. Vaculovicovac, G. Han, *J. Lumin.* 215 (2019) 116635
139. X. Wang, X. Li, S. Xu, L. Cheng, J. Sun, J. Zhang, L. Li, B. Chen, *Mater. Res. Bull.* 11,(2019) 77-182.
140. S. Sarkar, M. Chatti, V.N.K.B. Adusumalli, V. Mahalingam, *ACS Appl. Mater. Interfaces* 7 (2015) 25702.
141. C. Chen, J. Li, C. Li, H. Huang, C. Liang, Y. Lou, D. Liu, Z. Wang, Z. Shi, S. Feng, *ChemistrySelect* 1 (2016) 1417.
142. H. Kim, H. Jeong, S.-H. Byeon, *ACS Appl. Mater. Interfaces* 8 (2016) 15497.
143. D. Ghosh, M.N. Luwang, *J. Lumin.* 171 (2016) 1
144. G. F. Wang, Q. Peng, Y. D. Li, *Acc. Chem. Res.* 44 (2011).322-332

Chapter 2

Basic principles of instrumentation

2.1. Introduction

Understanding the basic principles and fundamentals of the instruments use during the characterization of the materials is important. This allows the selection of suitable characterizing techniques required to investigate the physical characteristics and properties of the materials of interest. This will guarantee the proper understanding of the properties. During the course of this work, some minimum required characterizing techniques have been utilized in understanding the characters and properties of materials investigated. Some of them include X-ray diffraction (XRD), Transmission electron microscopy (TEM), Fourier transform infrared (FT-IR) spectroscopy and Luminescence spectroscopy. The following explains briefly the basic principles of working of these mentioned techniques.

2.2. X-ray Diffraction

X-ray diffraction is one of basic characterizing technique to understand the crystalline nature of the solids. The solids materials of many kinds of metal, inorganic compounds, inorganic compounds, insulators, semiconductors, metals, ceramics, polymers, etc. The techniques can give the information such as structure, symmetry of the atomic arrangement, atomic positions pertaining to the crystalline materials under investigation. The diffraction pattern also allows estimating the crystalline size.

X-ray corresponds belongs to the electromagnetic radiation whose wavelength in range of $1 - 2 \text{ \AA}$. The X-rays are produced when a charge particle possessing very high energy in the range of several thousand of electron volt suddenly decelerated by a heavy metal. These heavy metals are commonly called as target metals. Most commonly, copper or molybdenum is used.

The X-ray diffraction occurs when the X-ray undergo scattering from the atoms arranged in a crystalline material following the Bragg's law. The Bragg's law can be briefly understood with the schematic figure presented in Fig. 2.1.

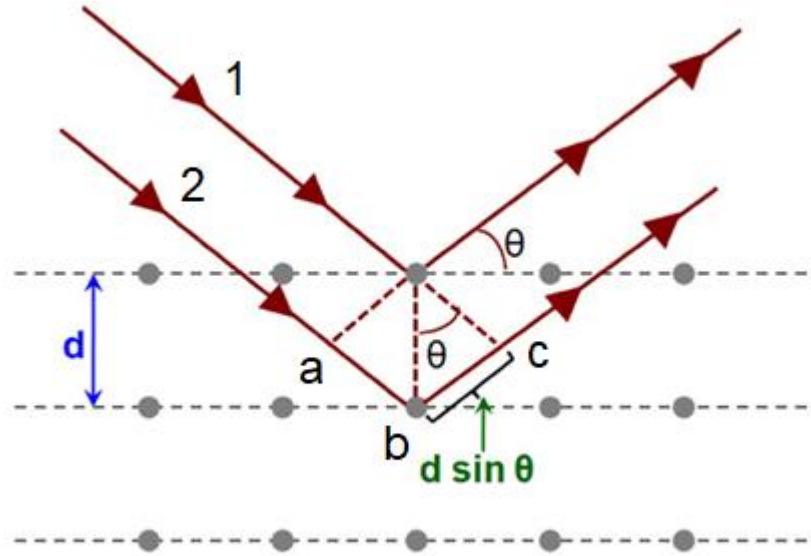


Fig. 2.1. Schematic representation of Bragg's law for X-ray diffraction

When two beams of monochromatic X-ray (designated as 1 and 2 here) are scattered from the atoms located in a plane, one of the beam (beam 2) travels an extra distance compared to ray-1. This difference is called as path difference. With the help trigonometric formula, the extra path travelled by the ray-2 is

$$ab + bc = d\sin\theta + d\sin\theta \quad (2.1)$$

When this path difference is equal to whole number ' n ' of the wavelength (λ) of the monochromatic X-ray used, the scattered rays 1 and 2 will be completely in phase.

$$2d\sin\theta = n\lambda \quad (2.2)$$

This is known as Bragg's law. When the Bragg's law is satisfied, the rays interfere constructively. Thus, the diffraction peaks from the planes where atoms are arranged. This is true for any other crystalline planes present in the solid. Two geometrical laws are worth to mention: (i) The incident beam which is normal to the reflecting plane and the diffracted beam are always coplanar and (ii) The angle between the transmitted and diffracted beam is always 2θ . This is known as diffraction angle which is experimentally measured against the diffraction peaks. From the diffraction position corresponding to ' 2θ ', the phase of the material can be determined with the help of available Powder Diffraction File (Joint Committee on Powder Diffraction Standards, Swarthmore, USA). Using Eqn. 2.2, d -spacing and corresponding hkl planes can be computed and so thus lattice parameters of the materials using the following:

$$(i) \text{ For cubic system, } \frac{1}{d^2} = \frac{h^2 + k^2 + l^2}{a^2} \quad (2.3)$$

$$(ii) \text{ For tetragonal system, } \frac{1}{d^2} = \frac{h^2 + k^2}{a^2} + \frac{l^2}{c^2} \quad (2.4)$$

$$(iii) \text{ For hexagonal system, } \frac{1}{d^2} = \frac{4}{3} \left(\frac{h^2 + hk + k^2}{a^2} \right) + \frac{l^2}{c^2} \quad (2.5)$$

$$(iv) \text{ For monoclinic system, } \frac{1}{d^2} = \frac{1}{\sin^2 \beta} \left(\frac{h^2}{a^2} + \frac{k^2 \sin^2 \beta}{b^2} + \frac{l^2}{c^2} - \frac{2hl \cos \beta}{ac} \right) \quad (2.6)$$

Where a , b , c are lattice parameters of the crystal and β is angle.

The size of the individual crystal is less than 100 nm, the term ‘particle size’ or more commonly termed as ‘crystallite size’ presently can be calculated from the broadening of the diffraction peaks using the following equation,

$$t = \frac{0.9\lambda}{\beta \cos \theta} \quad (2.7)$$

where, β = broadening of the diffraction line measured at half its maximum intensity (in radians), t = diameter of the crystalline particle. The ‘ θ ’ is the corresponding angle of the diffraction. This is known as Scherrer formula.

2.3. Transmission Electron Microscopy

One of the key characterizing techniques ever since the emergence nanosize particles, imaging the morphology and precise measurement of the particle size has become very important. Although, XRD can estimate the crystalline size, it is limited in understanding the morphology and size of the amorphous particles. The transmission electron microscopy (TEM) though imaging and its high resolution mode can help in deeper understanding of the particles.

The TEM usually operates a very high voltage typically with ~200 kV or more. Unlike the optical microscope where conventional light is used to produce the image, TEM uses high energetic electrons are used to focus the specimen for the production of the image. TEM usually has 3 (three) main compartments. First one is the illumination compartment. In this compartment, highly energetic electrons are generated from so called electron gun. These electron guns are made of tungsten filament, lanthanum hexaboride LaB₆ etc. The accelerated electrons from this are now condensed in the compartment through condenser before hitting the specimen. The first condenser lens

will set the demagnification also often labeled as spot size. The second condenser lens will provide the control over convergence angle of the beam before leaving the compartment. The parallel beam exited will illuminate the specimen. Now, the electron beams passing through specimen (some of them scattered) will be focused by the objective lens. This lens plays the role of first image formation and diffraction pattern. Subsequently, the image is enlarged by the projector lenses. Later, this enlarged image is displayed on the viewing screen.

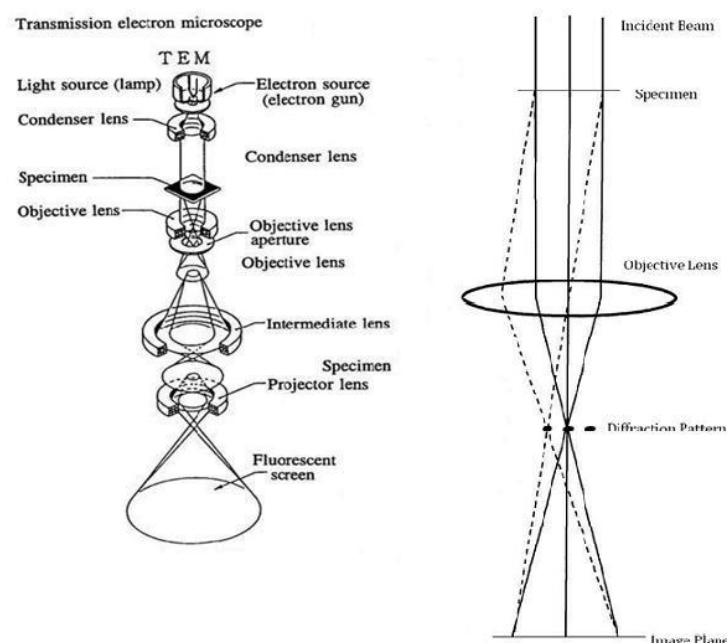


Fig. 2.2. Schematic picture of a Transmission electron microscope.

2.4. Fourier Transform Infrared Spectroscopy

Infrared absorption spectra correspond to a range from about 100 to about 5000 cm^{-1} ; that is, far away from the optical range. Thus, infrared absorption spectra are generally measured by so-called Fourier Transform Infrared (FT-IR) spectrometer. It provides useful information on the phonon structure of solids. The presence of different functional groups can be found out from the different vibrational absorption bands observed from the spectrum.

The basic configuration of an FTIR spectrometer is schematically shown in Fig. 2.3. The essential instrument of this spectrometer is a Michelson interferometer that consists of a fixed mirror, a moving mirror, and a beam splitter. When the IR beam, coming from a source, reaches the beam splitter, it is divided into two halves. Half of

the beam is reflected in the beam splitter to the fixed mirror, while the remaining half passes through the beam splitter toward the moving mirror. These two beams are reflected in the fixed and moving mirrors, respectively, and come back to the beam splitter, where they recombine into a new beam that passes through the sample and is finally focused on to the detector.

Instruments for measuring IR absorption required a source of continuous IR radiation and an IR transducer. The IR sources consist of an inert solid that is heated electrically to a temperature between 1500 and 2200 K. These sources produce continuum radiation approximating that of a blackbody. Some of the sources are Nernst glower, Globars, incandescent wire source, tungsten filament lamp, carbon dioxide laser, semiconductor IR laser.

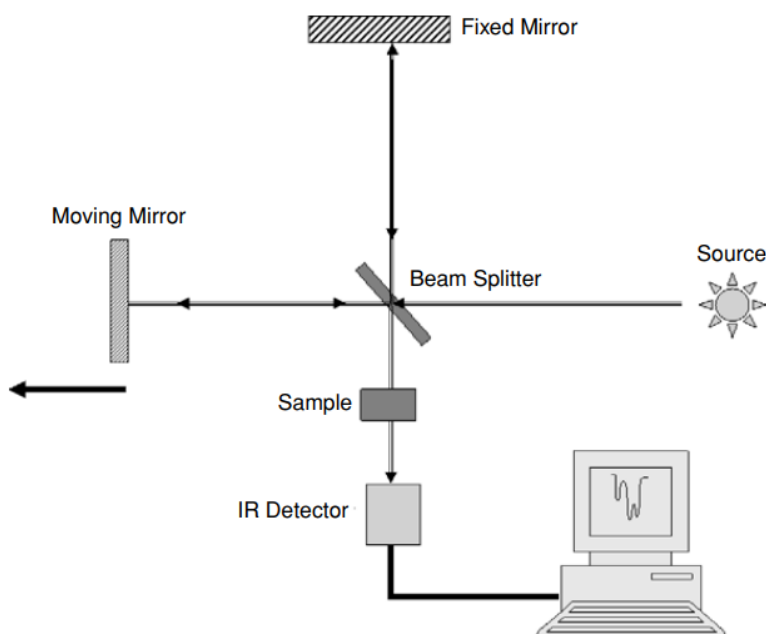


Fig. 2.3. A schematic diagram of an FTIR spectrometer.

IR transducers are of three general types: (1) pyroelectric transducers, (2) photoconducting transducers, and (3) thermal transducers. The first is found in photometers, many FTIR spectrometers, and dispersive spectrophotometers. Photoconducting transducers are also found in FTIR instruments. Thermal detectors are found in older dispersive instruments but are too slow to be used in FTIR spectrometers.

2.5. Luminescence Spectroscopy

The instruments for measuring fluorescence and phosphorescence spectra have similar construction and should be called luminescence spectrometers. But the group of molecules that exhibit fluorescence is by far larger than that exhibiting phosphorescence; hence, the term fluorescence spectrometer is used. The main spectral features of luminescence are spectral distribution, polarization, and radiation lifetime. For analytical purposes, mainly spectral distribution and polarization are used. Measuring of the lifetimes requires rather sophisticated time-resolved spectroscopic techniques.

2.5.1. Steady State Spectrofluorometer

Two basic types of spectra can be produced by a conventional fluorescence spectrometer. In the emission spectrum, the wavelength of the exciting radiation is held constant (at an absorption wavelength of the analyte) and the spectral distribution of the emitted radiation is measured. In the excitation spectrum, the fluorescence signal is measured at a fixed wavelength of the emission selector, as the wavelength of the exciting radiation is varied.

A schematic diagram of a fluorescent spectrometer is shown in Fig. 2.4. The instrument contains the source of UV/vis radiation, an excitation wavelength selector, an emission wavelength selector, a sample chamber, and a detector. Basically, this is a single beam instrument. The fluorescence emitted by the sample is usually measured at 90° in order to avoid disturbances by non-absorbed excitation radiation.

The luminescence intensity is directly proportional to the intensity of the light source, and a high-intensity light source can therefore be used to increase the sensitivity and to lower the detection limits for luminescence analyses. The xenon arc lamp is a commonly used source. The Xe lamp emits continuously over a broad wavelength range and is therefore well suited for spectral scanning. Other sources include mercury arc lamp, halogen lamps, combined xenon-mercury lamps and Lasers.

Photomultiplier tubes (PMTs) are the most commonly used detectors, and various types are available for different applications. Among the more commonly used multichannel detectors are diode arrays, vidicons, silicon intensified target vidicons, CCD and charge-injection devices, and numerous other devices made available by recent technological advances.

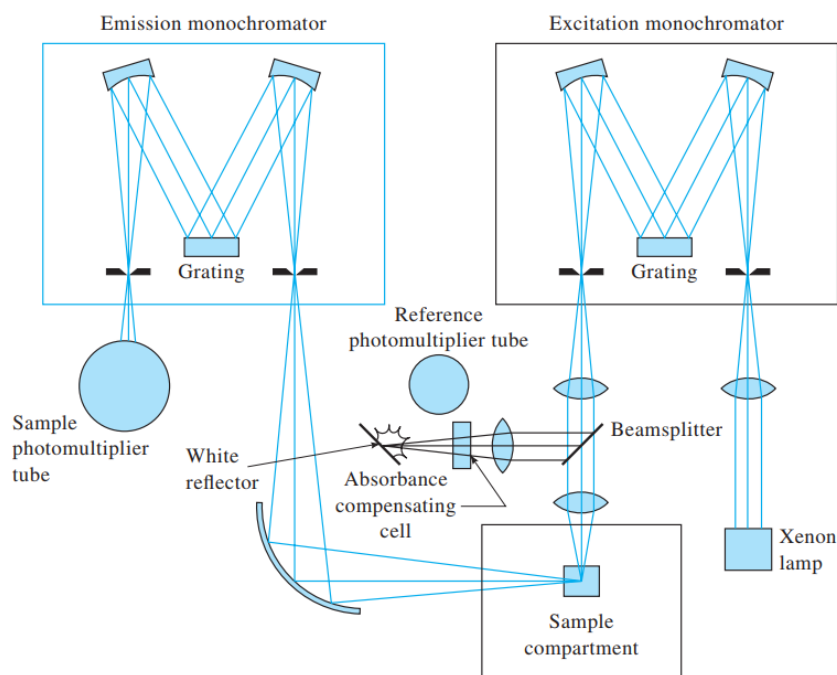


Fig. 2.4. A schematic diagram of a Spectrofluorometer

2.5.1. Time Resolve Spectrofluorometer

Fluorescence lifetime measurements can give information about collisional deactivation processes, about energy transfer rates, and about excited-state reactions. The measurement of luminescence lifetimes was initially restricted to phosphorescent systems, where decay times were long enough to permit the easy measurement of emitted intensity as a function of time. In recent years, however, it has become relatively routine to measure rates of luminescence decay on the fluorescence time scale (10^{-5} to 10^{-9} s).

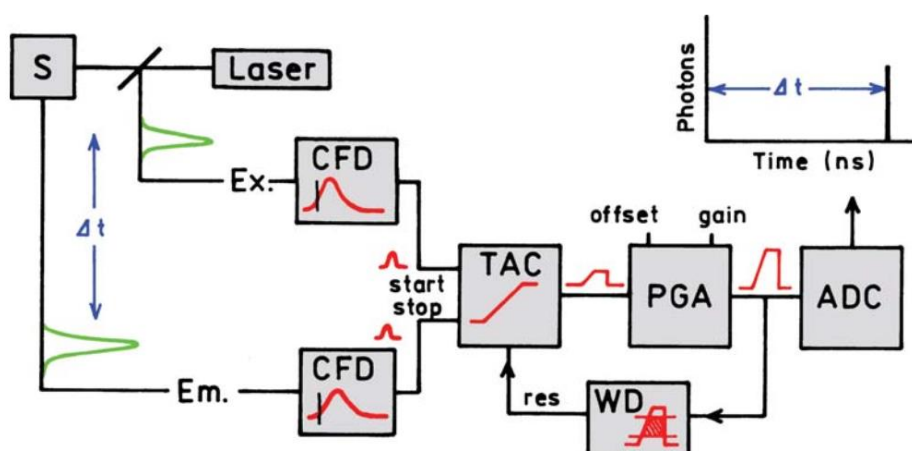


Fig. 2.5. Electronic schematic for TCSPC.

Two widely used approaches are used for lifetime measurements, the time-domain approach and the frequency-domain approach. In time-domain measurements, a pulsed source is used and the time-dependent decay of fluorescence is measured. In the frequency-domain method, a sinusoidally modulated source is used to excite the sample. The phase shift and demodulation of the fluorescence emission relative to the excitation waveform provide the lifetime information. The working of a time correlated single photon counting (TCSPC) is discussed here.

The system requires an excitation pulse that excites the samples and sends a signal to the electronics. This signal is passed through a constant function discriminator (CFD), which accurately measures the arrival time of the pulse. This signal is passed to a time-to-amplitude converter (TAC), which generates a voltage ramp that is a voltage that increases linearly with time on the nanosecond timescale. A second channel detects the pulse from the single detected photon. The arrival time of the signal is accurately determined using a CFD, which sends a signal to stop the voltage ramp. The TAC now contains a voltage proportional to the time delay (Δt) between the excitation and emission signals. As needed, the voltage is amplified by a programmable gain amplifier (PGA) and converted to a numerical value by the analog-to-digital converter (ADC). To minimize false readings, the signal is restricted to a given range of voltages. If the signal is not within this range the event is suppressed by a window discriminator (WD). The voltage is converted to a digital value that is stored as a single event with the measured time delay. A histogram of the decay is measured by repeating this process numerous times with a pulsed-light source.

These instruments use high repetition rate mode-locked picosecond (ps) or femtosecond (fs) laser light sources, and high-speed microchannel plate (MCP) photomultiplier tubes (PMTs). For many applications, these expensive systems are being rapidly replaced by systems using pulsed-laser diodes (LDs), light-emitting diodes (LEDs), and small, fast PMTs.

References

1. B.D. Cullity, *X-ray Diffraction*, Addison-Wesley, Massachusetts, USA, 1958
2. P.J. Goodhew, J. Humphreys, R. Beanland, *Electron Microscopy and Analysis*, Taylor & Francis, London, 2001. J. García Solé, L.E. Bausá, D. Jaque, *An Introduction to the Optical Spectroscopy of Inorganic Solids*, 1st Ed., John Wiley & Sons Ltd, England, 2005.
3. Douglas A. Skoog, F. James Holler, Stanley R. Crouch, *Principles of Instrumental Analysis*, 7th Ed., Cengage Learning, USA, 2018.
4. Gunter Gauglitz, David S. Moore, *Handbook of Spectroscopy*, Volume I, 2nd Ed., Wiley-VCH Verlag & Co. KGaA, Weinheim, Germany, 2014.
5. J. R. Lakowicz, *Principles of Fluorescence Spectroscopy*, 3rd Edition, Springer Science+Business Media, LLC, Singapore, 2006.

Chapter 3

Photoluminescence properties of $\text{Y}_2\text{O}_3:\text{Ln}^{3+}$ ($\text{Ln}^{3+} = \text{Eu}^{3+} \text{ \& \& Sm}^{3+}$)

3.1. Introduction

Lanthanide activated oxides such as Y_2O_3 , La_2O_3 , Lu_2O_3 , Gd_2O_3 , etc. are considered as excellent phosphor materials. They possess low phonon energy. These phosphors are chemically and optically stable than sulfide-based counterparts [1,2]. They are used in various applications including cathode ray tubes [3,4] display [4-6], lamps [5,6], biological and anti-counterfeit applications [7-10]. These phosphors are also potential in solid state lighting (SSL) applications [11-13]. Recently, application of phosphors towards the SSL has become important. This is because of the fact that the commercially available white light emitting diodes (w-LEDs) are made by converting the phosphors emitting yellow down-converted with blue LEDs. It is now anticipated by constructing such w-LEDs by down-converting all three primary colours of red, green, blue with proper appropriate near UV LEDs. Among them, red emitting phosphor is highly demanded. Therefore, various red emitting phosphors such as $\text{Na}_2\text{Y}_2\text{B}_2\text{O}_7:\text{Eu}^{3+}$ [14], $\text{BaZrGe}_3\text{O}_9:\text{Eu}^{3+}$ [15], Eu^{3+} activated $\text{La}_2\text{MoO}_6\text{-La}_2\text{WO}_6$ composite [16], $\text{La}_2\text{Ce}_2\text{O}_7:\text{Eu}^{3+}$ [17], $\text{CaMoO}_4:\text{Eu}^{3+}$ [18-20], $\text{CaWO}_4:\text{Eu}^{3+}$ [21-23], and $\text{YVO}_4:\text{Eu}^{3+}$ [24,25], $\text{Y}_2\text{O}_3:\text{Eu}^{3+}$ [26-29], $\text{Y}_2\text{O}_2\text{S}:\text{Eu}^{3+}$ [30] etc. are recently reported.

Among various rare earth oxide hosts mentioned, Y_2O_3 which having low phonon energy is a good host material for various lanthanides. Generally, Y_2O_3 exists as sesquioxides exhibiting cubic structures [31-34]. Therefore, Y_2O_3 offers two non-equivalent sites viz., C_2 (non-centrosymmetric) and S_6 (centrosymmetric) [33-36]. Y_2O_3 has the advantage of exhibiting the charge transfer band (CTB) arising due to the electron transfer from Oxygen ions to the empty f -shells of lanthanides, e.g. $\text{Eu} - \text{O}$ CTB [35-40]. There are various reports on the luminescence properties Y_2O_3 doped these lanthanides i.e., $\text{Y}_2\text{O}_3:\text{Tb}^{3+}$ [41-43], $\text{Y}_2\text{O}_3:\text{Dy}^{3+}$ [44-46]. $\text{Y}_2\text{O}_3:\text{Eu}^{3+}$ phosphor has been widely reported as potential red phosphor. Lately, these phosphors are reported as potential for solid state lighting applications [26-28]. While, various applications such bio imaging, anti-counterfeit applications, etc. are also reported [8,9]. Similarly, photoluminescence properties of $\text{Y}_2\text{O}_3:\text{Sm}^{3+}$ are also reported [47-49].

In this chapter, simple hydrothermal technique with subsequent post annealing for was adopted for preparing cubic $Y_2O_3:Eu^{3+}$ and $Y_2O_3:Sm^{3+}$. The photoluminescence properties of steady state and decay dynamics of are investigated. We have also studied the emission colour using Commission International de l'Eclairage (CIE) chromaticity diagram.

3.2. Experimental methods

3.2.1. Materials

Yttrium (III) nitrate hexahydrate ($Y(NO_3)_3 \cdot 6H_2O$, 99.9%, Alfa Aesar), europium (III) nitrate hexahydrate ($Eu(NO_3)_3 \cdot 6H_2O$, 99.9%, Alfa Aesar), and samarium (III) nitrate hexahydrate ($Sm(NO_3)_3 \cdot 6H_2O$, 99.9%, Alfa Aesar) were used as received for the sources of Y^{3+} , Eu^{3+} , and Sm^{3+} respectively. Polyvinyl pyrrolidone (PVP, $M_w \sim 40000$, Sigma Aldrich) was used as capping agent.

3.2.2. Synthesis of Eu^{3+} doped Y_2O_3 phosphors

Hydrothermal technique was adopted to synthesize Eu^{3+} doped Y_2O_3 phosphors (denoted as $Y_2O_3:Eu^{3+}$). For the synthesis of $Y_2O_3:Eu^{3+}$ (1 at.%) sample, 1.7 mg of $Eu(NO_3)_3 \cdot 6H_2O$ and 381 mg of $Y(NO_3)_3 \cdot 6H_2O$ were dissolved in 5 mL of deionized water (DIW) in a beaker. To this, 150 mg of polyvinyl pyrrolidone (PVP) was also added. The final volume was made 30 mL with the addition of DIW. The pH of the solution was fixed at 10 using ammonium hydroxide solution (NH_4OH , ~25% NH_3 , Sigma Aldrich). Finally, the solution was transferred to a Teflon lined stainless steel autoclave and heated at 180 °C for 18 h in an oven. The precipitate was centrifuged and washed several times with DIW and acetone. All the remaining samples were synthesized following the same procedure. The as-prepared samples were annealed at 500 and 900 °C for 4 h in the air.

3.2.3. Synthesis of Sm^{3+} doped Y_2O_3 phosphors

Following the similar procedure mentioned in the Sec 3.2.2, $Y_2O_3:Sm^{3+}$ phosphors were also synthesized adopting hydrothermal method. In a typical synthesis of 1 at.% Sm^{3+} doped Y_2O_3 sample, 2.2 mg of $Sm(NO_3)_3 \cdot 6H_2O$ and 381 mg of $Y(NO_3)_3 \cdot 6H_2O$ were dissolved together in 5 mL of DIW. To this, 150 mg of polyvinyl pyrrolidone (PVP) was also added. The whole solution was kept under hydrothermal condition for

18 h at 180 °C. The remaining samples were also prepared with similar process. The as-prepared samples were annealed at 500 and 900 °C for 4 h in the air.

3.2.4. Characterization

X-ray diffractometers Bruker D8 advance and Rigaku Ultima IV with Cu $K\alpha$ radiation were used for crystalline phase identification. Fourier transform infrared (FT-IR) spectrometer (Shimadzu make IR-Affinity-1S) was used to record the FT-IR spectra of the prepared samples. Morphology of the particles was studied using the transmission electron microscopy (TEM) images recorded with JEOL 2000FX. The steady state and dynamics of photoluminescence (PL) as well as quantum yield (QY) were measured using Fluoromax-4CP spectrofluorometer (HORIBA make) equipped 150 W Xenon lamp and 25 W μ s Xenon flash lamp. All the PL measurements were carried out on the glass slides at room temperature with a resolution of ± 1 nm. K-sphere ‘petite’ integrating sphere from Photon Technology International (PTI) was used for QY measurements. For calculation of absolute QY, $\phi(\%) = \frac{I_{emission}}{I_{quartz} - I_{sample}}$ was used.

$I_{emission}$ = luminescence emission intensity of the sample, I_{quartz} = the intensity of light used to excite only the quartz slide and I_{sample} = the intensity of the light used for exciting the sample on the quartz slide. The photon absorbed by the sample is given by the difference between the last two. All the measurements were taken in the emission mode. The QY measurements were carried out on the quartz slides at room temperature.

3.3. Results and discussion

3.3.1. X-ray diffraction study

The X-ray diffraction (XRD) patterns of $Y_2O_3:Eu^{3+}$ ($Eu^{3+} = 1, 3, 7, 11, 15, 19, 21$ and 25 at.%) samples annealed at as prepared, 500 and 900 °C are shown in Fig. 3.1. And, Fig. 3.2 illustrates the XRD patterns of $Y_2O_3:Sm^{3+}$ ($Sm^{3+} = 0, 1, 2, 4, 6, 8$ and 10 at.%) samples annealed at 500 and 900 °C. XRD pattern of as prepared sample ($Y_2O_3:Eu^{3+}$) is found to amorphous in nature. The XRD patterns all the annealed samples are well matched with the cubic phase of Y_2O_3 with ICDD no. 41-1105 [50,51]. No extra phases such as Eu_2O_3 , Sm_2O_3 , etc. are observed. This suggests the formation of solid solution of Eu^{3+} or Sm^{3+} in the host matrix. Such possibility of lattice substitution in Y^{3+} sites of Y_2O_3 by Eu^{3+} or Sm^{3+} is due to near equivalent ionic radii of Eu^{3+} ($r =$

0.947 Å), and Sm^{3+} (0.958 Å) to that of Y^{3+} ($r = 0.9$ Å). The average crystalline sizes of the prepared samples were calculated using Debye-Scherrer, $= \frac{\kappa\lambda}{\beta \cos\theta}$, where, D is the crystalline size, κ is the Scherrer constant ($= 0.9$), λ is the wavelength of the X-ray used, β is the FWHM at Bragg angle and ε is the lattice strain. From the Scherrer equation, the average crystalline sizes of $Y_2O_3:Eu^{3+}$ samples are calculated ~6–25 nm and 26–33 nm were observed respectively for 500 and 900 °C annealed samples. While, the average crystalline sizes of $Y_2O_3:Sm^{3+}$ samples are calculated ~7–9 nm and 23–29 nm were observed respectively for 500 and 900 °C annealed samples. The details are given in Table 3.1.

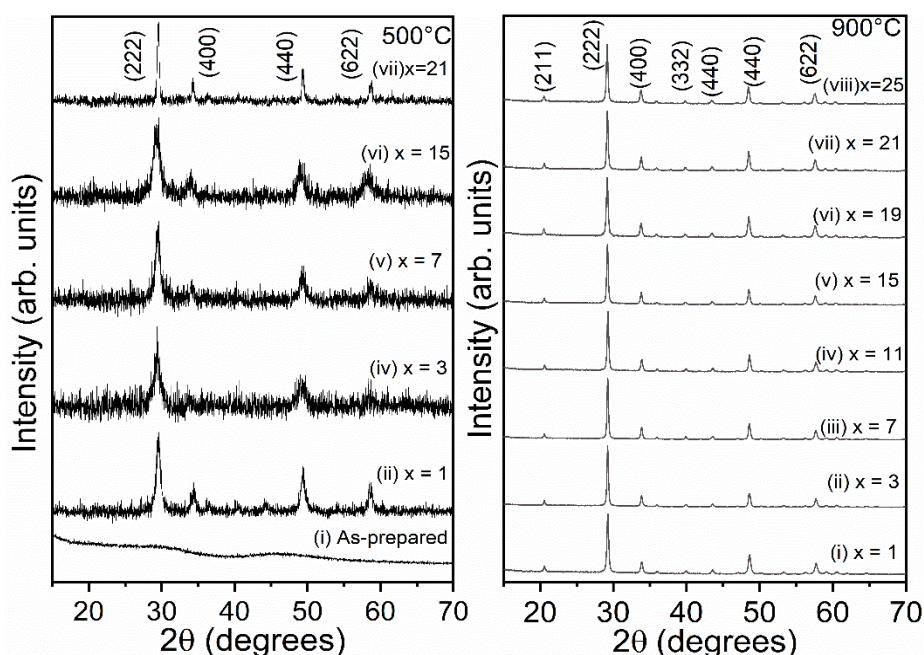


Fig. 3.1. The X-ray diffraction (XRD) patterns of (a) 500 and (b) 900 °C annealed $Y_2O_3:Eu^{3+}$ ($Eu^{3+} = 1, 3, 7, 11, 15, 19, 21$ and 25 at.%).

Table 3.1. Calculated crystallite size for Eu^{3+} or Sm^{3+} doped Y_2O_3 samples annealed at 500 and 900 °C, using Scherrer relation.

Eu^{3+} (%)	Crystallite size (nm)		Sm^{3+} (%)	Crystallite size (nm)	
	500 °C	900 °C		500 °C	900 °C
1	11	27	0	-	27
3	7	32	1	7	28
7	9	33	2	9	29
11	-	30	4	8	26
15	6	31	6	-	28
19	-	26	8	8	23
21	25	30	10	7	27
25	-	28	12	-	27

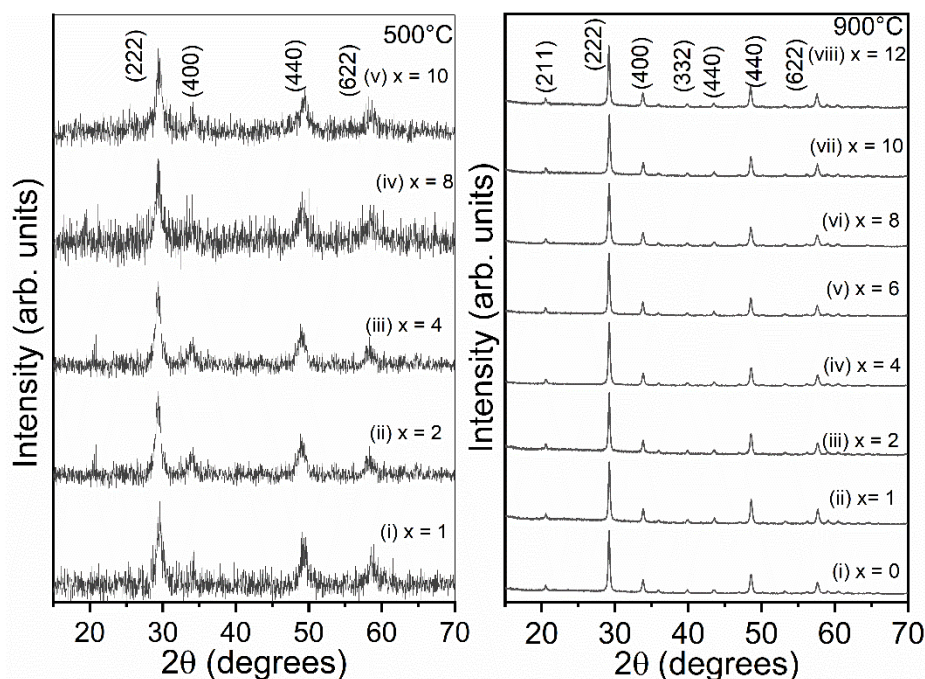


Fig. 3.2. The X-ray diffraction (XRD) patterns of (a) 500 and (b) 900 °C annealed $Y_2O_3:Sm^{3+}$ ($Sm^{3+} = 0, 1, 2, 4, 6, 8, 10$ and 12 at.%).

3.3.2. Fourier transform infrared spectroscopy study

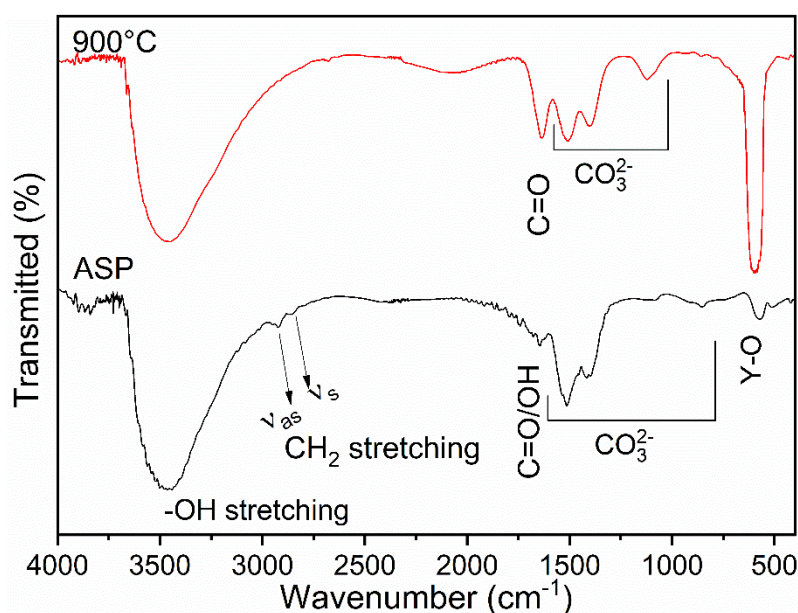


Fig. 3.3. FTIR spectra of 500 and 900 °C annealed $Y_2O_3:Eu^{3+}$ (3 at.%) samples.

FT-IR spectra of 500 and 900 °C annealed samples of $Y_2O_3:Eu^{3+}$ (3 at.%) are shown in Fig. 3.3. Both the spectra show the absorption bands at 3456/3464 cm^{-1} is due to the -OH stretching vibrations [52,53]. The asymmetric and symmetric stretching vibrations of CH₂ are observed at 2924 and 2854 cm^{-1} [54-56]. The absorption peak at 1635/1641 cm^{-1} is due to the asymmetric stretching of C=O bond [54,55]. The -OH

bending vibration which is usually observed at $\sim 1641\text{ cm}^{-1}$ [53] could not be observed. This might be due to the merger with the C=O vibrational peak. The Y-O stretching vibration is observed at $573/592\text{ cm}^{-1}$. Other possible absorption bands of PVP could not be observed from the FTIR spectra as the samples were heated at 500 and 900 °C. The absorption bands at 1516, 1400, 1122 cm^{-1} are coming from the CO_3^{2-} groups.

3.3.3 Transmission electron microscopy study

TEM images of 500 and 900 °C annealed samples are shown in Fig. 3.4 and 3.5 respectively. Particles are in rod shape with an average diameter of $\sim 250 - 450\text{ nm}$ and $\sim 1000 - 1500\text{ nm}$ in length (Fig. 3.4(a)). Whereas, the particles with $\sim 200 - 450\text{ nm}$ in diameter and $\sim 2\text{ }\mu\text{m}$ or more in length are observed in annealed samples (Fig. 3.5(a)). The measured interplanar spacing of 0.33 nm of as-prepared sample corresponds to (222) plane of Y_2O_3 (See Fig. 3.4(b)). On the other hand, interplanar spacing of 0.44 nm corresponds to (211) plane of cubic Y_2O_3 (Fig. 3.5 inset)). Also, the diffraction planes calculated from the SAED images (Fig. 3.4(c)) are well matched with that of Y_2O_3 . This confirms the formation of crystalline Y_2O_3 .

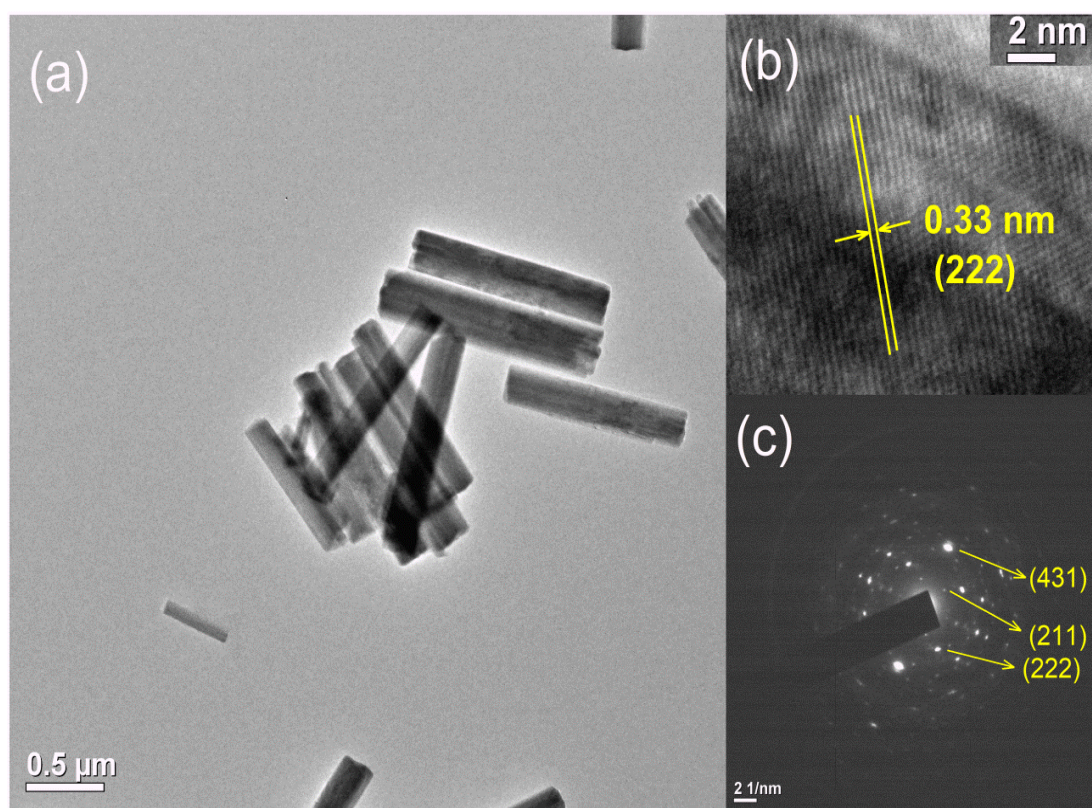


Fig. 3.4. TEM images (a) along with HR-TEM (b) and SAED images (c) of a selected region of 500 °C annealed $Y_2O_3:Eu^{3+}$ (3 at.%).

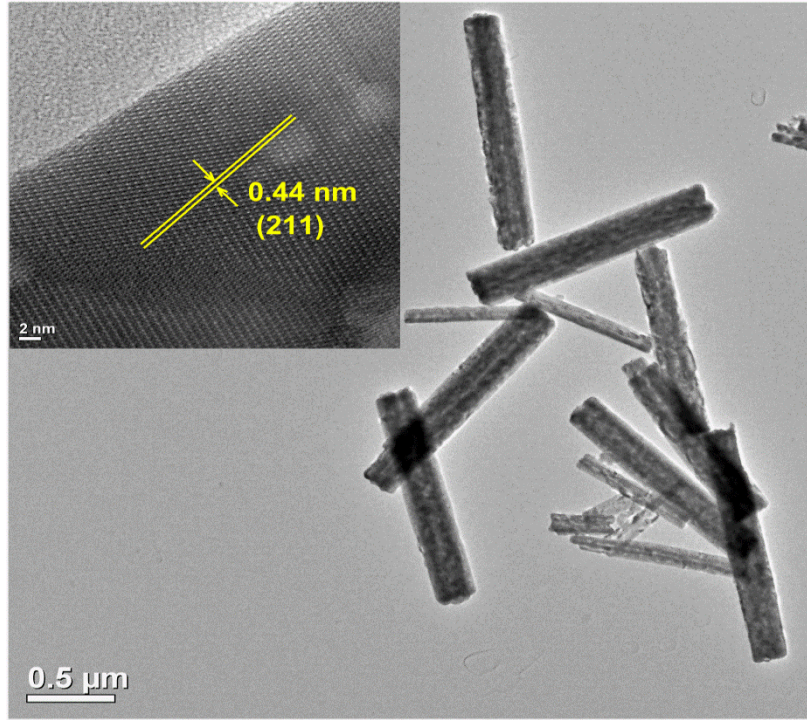


Fig. 3.5. TEM image along with HR-TEM image of 900 °C annealed $Y_2O_3:Eu^{3+}$ (3 at.%).

3.3.4. Photoluminescence studies of $Y_2O_3:Eu^{3+}$

3.3.4.1. Steady state PL study

Excitation spectra of (a) 500 and (b) annealed $Y_2O_3:Eu^{3+}$ samples are illustrated in Fig. 3.6. All the excitation spectra consists a broad peak in the 230 to 290 nm peaking between 254 to 264 nm depending on the concentration of Eu^{3+} . The former peak related to the charge transfer band (CTB) band as a result of electron transfer from the

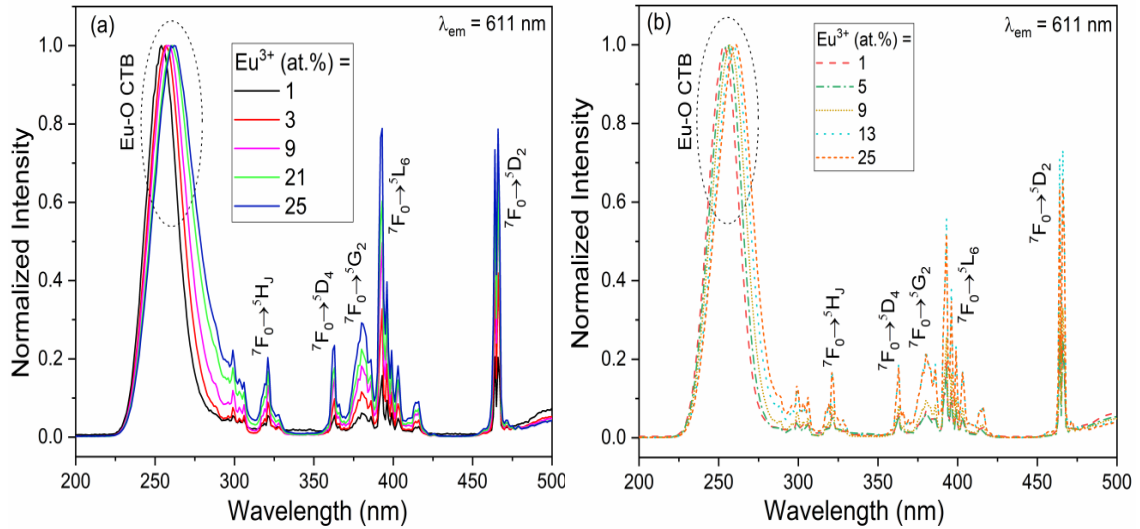


Fig. 3.6. PL excitation spectra of (a) 500 and (b) 900 °C annealed $Y_2O_3:Eu^{3+}$ samples monitored at $\lambda_{em} = 611$ nm. Concentration of Eu^{3+} are given if the figure.

2p orbitals of oxygen to the empty 4f orbitals of the Eu^{3+} (denoted as Eu-O CTB) [26,35,38,50]. And, other sharp peak in the longer wavelength region at 320 (${}^7F_0 \rightarrow {}^5H_J$), 363 (${}^7F_0 \rightarrow {}^5D_4$), 381 (${}^7F_0 \rightarrow {}^5G_2$) 393/396 (${}^7F_0 \rightarrow {}^5L_6$) and 464 (${}^7F_0 \rightarrow {}^5D_2$) nm are due to transitions within *f-f* shell of Eu^{3+} (indicated inside the parenthesis) [30,38,50,57,58]. The careful observation in the Eu-O CTB, the peak is red shifted from ~254 to 264 nm with the increase of Eu^{3+} concentration. The shift is obvious when the Eu-O CTB peak is compared between the Eu^{3+} (1 at.%) and Eu^{3+} (25 at.%). (See Fig. 3.7).

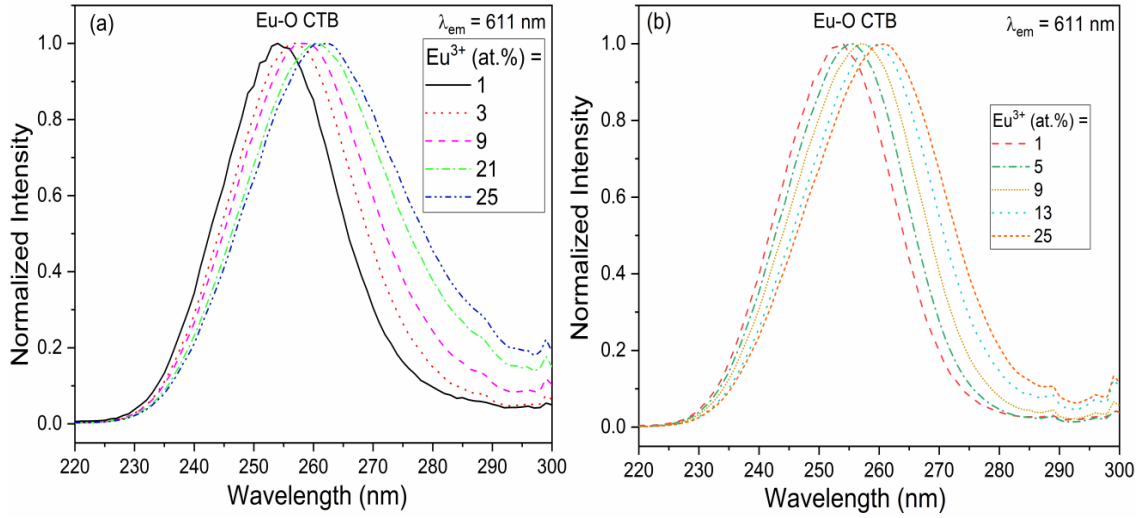


Fig. 3.7. Expanded region (~220 – 300 nm) region of PL excitation spectra of (a) 500 and (b) 900 °C annealed $Y_2O_3:Eu^{3+}$ samples monitored at $\lambda_{em} = 611$ nm. Concentration of Eu^{3+} are given if the figure.

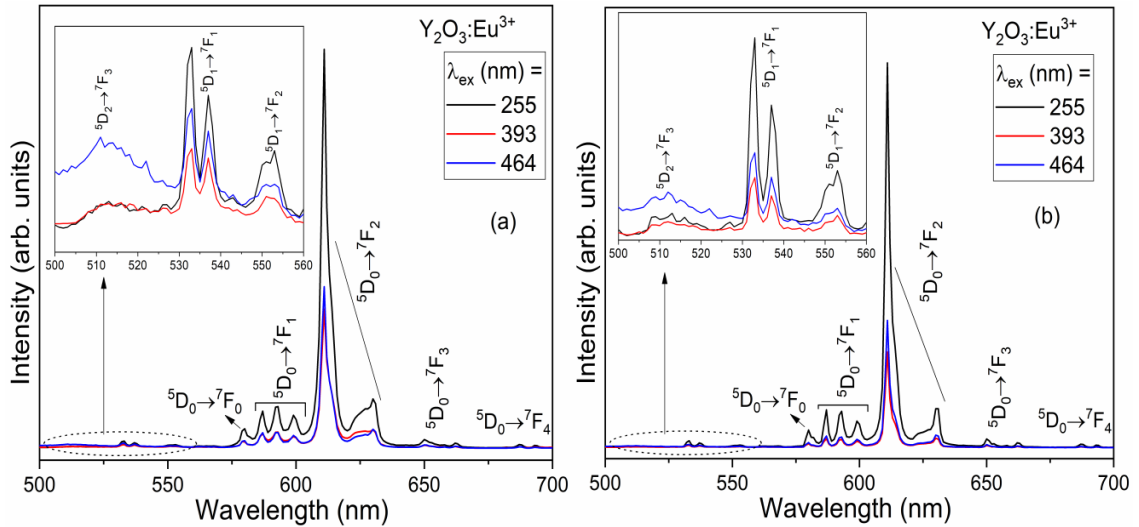


Fig. 3.8. PL emission spectra of $Y_2O_3:Eu^{3+}$ (7 at.%) samples annealed at (a) 500 and (b) 900 °C. Excitation wavelengths are 255 nm (Eu-O CTB), 393 ($Eu^{3+}, {}^7F_0 \rightarrow {}^5L_6$) and 464 ($Eu^{3+}, {}^7F_0 \rightarrow {}^5D_2$) nm.

Fig. 3.8 shows the emission spectra of (a) 500 and (b) 900 °C annealed $Y_2O_3:Eu^{3+}$ (7 at.%) samples under different excitations at 255 nm (Eu–O CT), and direct excitations at 393 ($Eu^{3+}, {}^7F_0 \rightarrow {}^5L_6$) and 464 ($Eu^{3+}, {}^7F_0 \rightarrow {}^5D_2$) nm. Considering the 611 nm emission which is highest among other peaks, it is clearly seen that the emission intensity is highest when excited at 255 nm compared to the remaining excitations. This clearly suggests the efficient transfer of excited photons from the Eu–O CTB to the excited states of Eu^{3+} .

Fig. 3.9 illustrates the emission spectra of $Y_2O_3:Eu^{3+}$ (1, 3, 5, 7, 9, 13, 17, 21 and 25 at.%) samples annealed at 500 (a, c, e) and 900 °C (b, d, f) under 255, 393 and 464 nm excitation. All the emission spectra consist of sharp emission peaks in the region of ~ 500 to 750 nm. These emission peaks are originated from the transitions within the $f-f$ electronic energy levels of Eu^{3+} . These transitions are categorized into 3 groups (i) magnetic dipole transitions: ${}^5D_2 \rightarrow {}^7F_3$ at 512 nm, ${}^5D_1 \rightarrow {}^7F_1$ at 533 and 537 nm, ${}^5D_1 \rightarrow {}^7F_2$ at 553, ${}^5D_0 \rightarrow {}^7F_1$ at 587, 592 and 599 nm, ${}^5D_0 \rightarrow {}^7F_3$ at 651 nm. (ii) Electric dipole transitions: ${}^5D_0 \rightarrow {}^7F_2$ at 611 and 629 nm and (iii) electric quadrupole: ${}^5D_0 \rightarrow {}^7F_4$ at 708 and 711 nm, respectively [18,21,35,38,50]. Apart from these emission peaks, a peak at 581 nm is also observed. This is due to the strictly forbidden ${}^5D_0 \rightarrow {}^7F_0$ transition (discussed later). Among all these Eu^{3+} transitions, emission at 611 nm is strongest.

In all the case, the emission peak due to the electric dipole transitions (${}^5D_0 \rightarrow {}^7F_2$) is dominant over the magnetic dipole transitions (${}^5D_0 \rightarrow {}^7F_1$). As predicted by the Judd-Ofelt theory, the electric dipole transitions are dependent on the nature of the environment of around the Eu^{3+} while the magnetic dipole transitions is independent [59-61]. Such behavior of Eu^{3+} emission in Y_2O_3 can be understood by considering the crystal structure of Y_2O_3 . In cubic Y_2O_3 lattice, non-centrosymmetric, C_2 symmetry sites occupies ~75% while the centrosymmetric, S_6 symmetry has ~25% occupation [29,35,50]. When the Eu^{3+} occupies the C_2 lattice sites which are non-centrosymmetric, the electric dipole transitions occur as forced electric dipole and becomes dominant over other transitions. This is further corroborated by the presence of 3 (three) Stark components in ${}^5D_0 \rightarrow {}^7F_1$ transition in all the spectra. This is against the allowed 2 (two) components whenever Eu^{3+} occupies centrosymmetric sites [63]. The information of

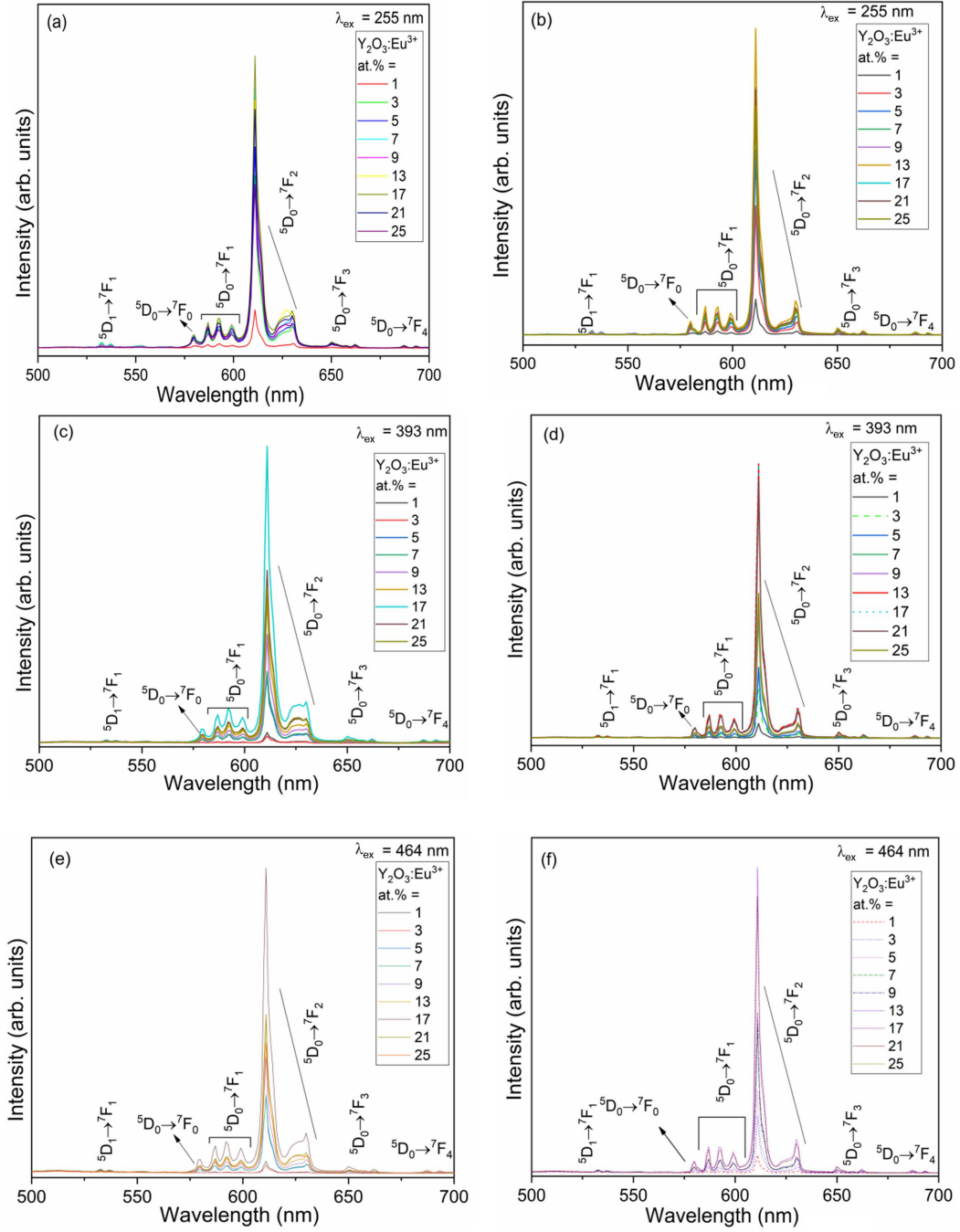


Fig. 3.9. PL emission spectra of 500 (a, c, e) and 900 °C (b, d, f) of $Y_2O_3:Eu^{3+}$ ($Eu^{3+} = 1, 3, 5, 7, 9, 13, 17, 21$ and 25 at.%) samples. Excitation wavelengths are given in the figures.

the asymmetric environment around the Eu^{3+} can be further obtained by calculating the asymmetric ratio (A). The asymmetric ratio (A) is given by the ratio of integrated emission intensity of ${}^5D_0 \rightarrow {}^7F_2$ to ${}^5D_0 \rightarrow {}^7F_1$. The asymmetric ratio (A) is given by

$$A = \frac{\int_{603}^{633} I_{ed} d\lambda}{\int_{585}^{602} I_{md} d\lambda} \quad (3.1)$$

where, I_{ed} and I_m represent the $^5D_0 \rightarrow ^7F_2$ and $^5D_0 \rightarrow ^7F_1$ transitions. The integration limits are wavelengths (nm). Fig. 3.10 shows the asymmetric ratio of the $Y_2O_3:Eu^{3+}$ (1, 3, 5, 7, 9, 13, 17, 21 and 25 at.%) samples annealed at (a) and (b) 900 °C under 255 nm excitation (calculated from the original data of the Fig. 3.9). In all the cases, the ‘A’ value is above 6 for all the Eu^{3+} concentration. This suggests the increase occupancy of the C_2 sites by the Eu^{3+} . Thus, the emission is predominantly from the Eu^{3+} located in the C_2 sites [35,38,50].

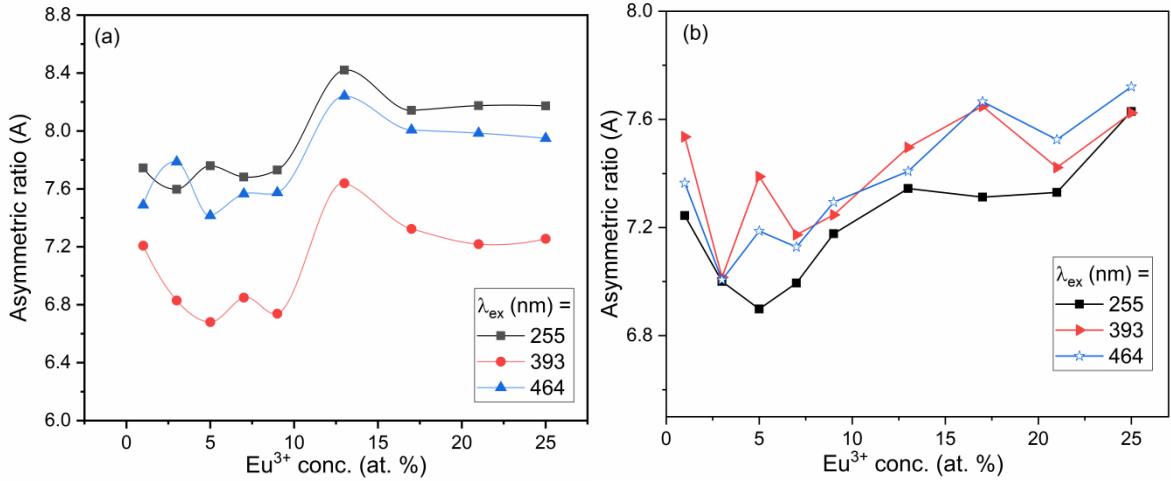


Fig. 3.10. Asymmetric ratio at different concentrations in (a) 500 and (b) 900 °C annealed $Y_2O_3:Eu^{3+}$ ($Eu^{3+} = 1, 3, 5, 7, 9, 13, 17, 21$ and 25 at.%) samples. $\lambda_{ex} = 255, 393$ and 464 nm.

The value of the asymmetric ratio, $A > 1$, indicates the increase in lattice substitution of Eu^{3+} in the C_2 sites of Y^{3+} in $Y_2O_3:Eu^{3+}$ [50,62,63]. The asymmetric ratios in all the cases are in the within ~6-8. This suggests that the Eu^{3+} is located in the asymmetric environment irrespective of variation of Eu^{3+} concentrations. Also, nature of environment around the Eu^{3+} is independent of excitation wavelengths.

Again, the observance of strictly forbidden $^5D_0 \rightarrow ^7F_0$ transition at 581 nm may be reckoned as perturbation in the surrounding of the Eu^{3+} . This perturbation is arisen due to the asymmetric nature around Eu^{3+} at C_2 sites. Such observation cannot be explained by Judd and Ofelt theory which is based on closure approximation of mixing higher lying odd parity state with $4f$ states. The most probable mechanism is reported due to J -mixing. The J -mixing is considered to be dominant contribution arisen from mixing of 7F_0 and 7F_2 compared to the other higher lying f -manifolds in the ground state [64]. This idea is further extended by other authors with the consideration second order crystal field parameter [35,65]. The second order crystal field parameter can be calculated using [35]

$$\frac{I_{0 \rightarrow 0}}{I_{0 \rightarrow 2}} = \frac{4B_{20}^2}{75\Delta_{20}^2} \quad (3.2)$$

where, B_{20} is the second order crystal field parameter, and Δ_{20} is the energy separation between 7F_0 and 7F_2 which value was taken as 900 cm^{-1} . Fig. 3.11 illustrates the variation B_{20} versus the Eu^{3+} concentration in (a) 500 and (b) 900 °C annealed $Y_2O_3:Eu^{3+}$ samples under the excitation of 255 nm. The B_{20} values vary from 795 to 1060 cm^{-1} and 735 to 1040 cm^{-1} respectively for 500 and 900 °C annealed samples. These high values are indication of perturbed environment around the Eu^{3+} .

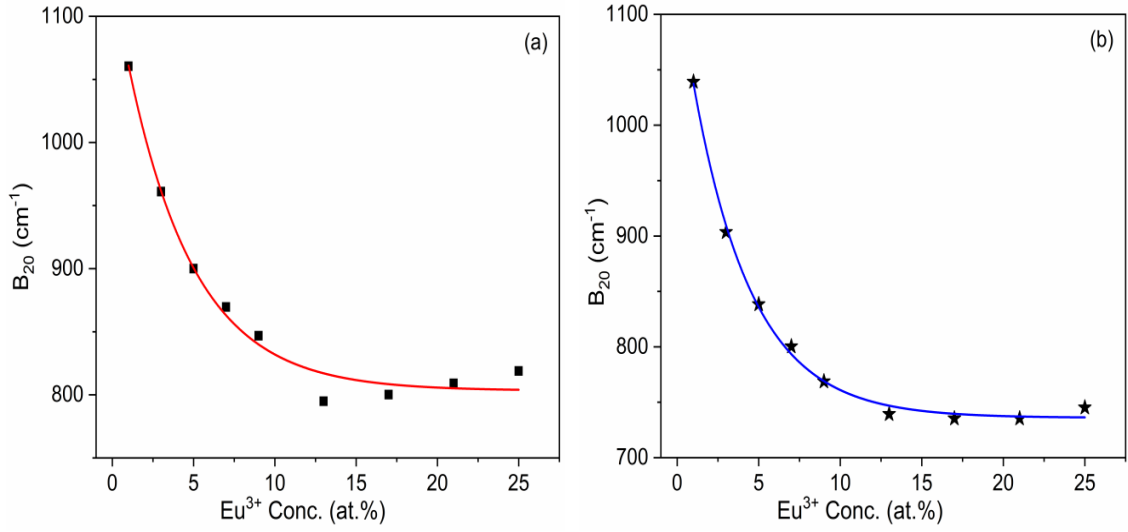


Fig. 3.11. Variation of B_{20} versus Eu^{3+} concentration of (a) 500 and (b) 900 °C annealed $Y_2O_3:Eu^{3+}$ ($Eu^{3+} = 1, 3, 5, 7, 9, 13, 17, 21$ and $25 \text{ at.}\%$) samples under the excitation of 255 nm. Solid lines are guide to the eye.

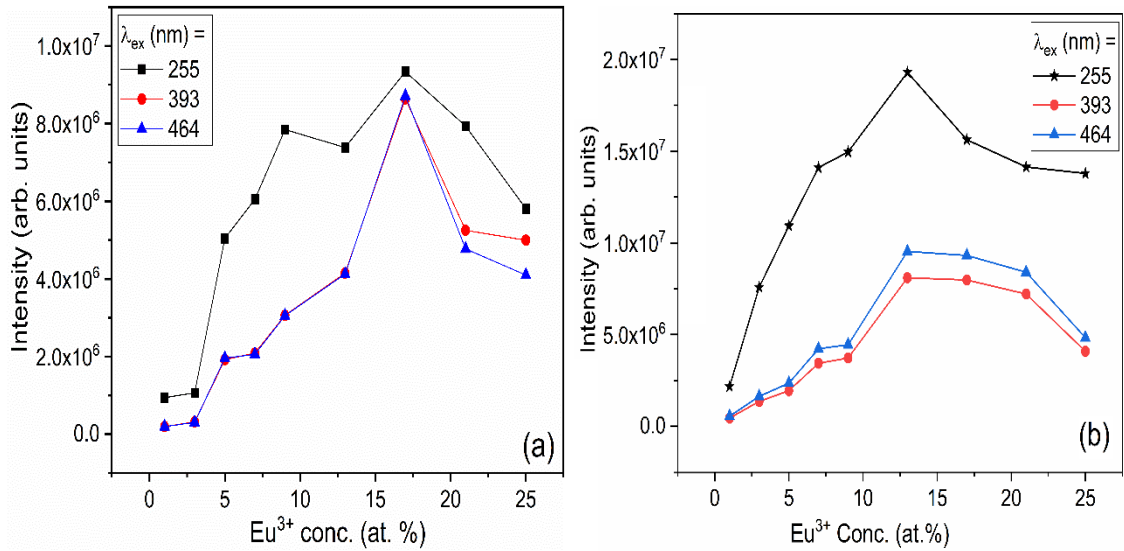


Fig. 3.12. Integrated emission intensities of $Y_2O_3:Eu^{3+}$ ($Eu^{3+} = 1, 3, 5, 7, 9, 13, 17, 21$ and $25 \text{ at.}\%$) (a) 500 and (b) 900 °C samples at $\lambda_{ex} = 255, 393$ and 464 nm .

Fig. 3.12 shows the integrated emission intensities of dominant $^5D_0 \rightarrow ^7F_2$ (611 nm) of 900 °C annealed $Y_2O_3:Eu^{3+}$ (1, 3, 5, 7, 9, 13, 17, 21 and 25 at.%) samples. The excitation wavelengths are 255, 393 and 464 nm. In all the cases, the luminescence intensity increases with the increase of Eu^{3+} concentration. The maximum intensity of the luminescence is observed at ~13 at.% of Eu^{3+} . Thereafter, the intensity decreases with the increase of concentration. This phenomenon is quite common among the lanthanide activated phosphors. When the concentration becomes high, the distance between the Eu^{3+} becomes shorter. This leads to cross-relaxation among them which is non-radiative. This increases the probability of non-radiative transitions.

3.3.4.2. PL decay lifetime and quantum yield study

Fig. 3.13 shows the decay curves of 5D_0 level of Eu^{3+} emission 500 (a & c) and 900 °C (b & d) annealed (1, 3, 7, 11, 15, 19, 21 and 25 at.%) samples by monitoring at 611 nm emission. Excitation wavelengths are 255 and 464 nm. All the decay profiles follow the second order exponential decay,

$$I(t) = I_1 e^{-\frac{t}{\tau_1}} + I_2 e^{-\frac{t}{\tau_2}} \quad (3.3)$$

where I_1 and I_2 stand for intensities at two different times. The τ_1 and τ_2 represent the corresponding lifetimes.

Typical fitting is given in Fig. 3.13. The average decay lifetime can be calculated using,

$$\tau_{av} = \frac{I_1 \tau_1^2 + I_2 \tau_2^2}{I_1 \tau_1 + I_2 \tau_2} \quad (3.4)$$

The average decay lifetime calculated using Eqn. 3.4 is given in Table 3.2. The average decay lifetime under the excitation of 255 nm varies from 0.88 to 1.53 ms and 1.47 to 2.49 ms respectively for 500 and 900 °C annealed samples. And, under direct excitation at 464 nm, the lifetime value changes from 0.81 to 1.6 ms and 1.4 to 1.64 ms respectively for 500 and 900 °C annealed samples. From the Table 3.2, it is observed that the decay lifetime value in the case of 900 °C annealed samples is more than that of 500 °C annealed samples. This behavior is same for both the excitation wavelengths. Such improved lifetime after annealing at higher temperature is may be due to improved luminescence. Such improved luminescence after annealing at higher temperature is due to improved crystallinity. The absolute quantum yield measurements were performed following the report [18,21]. The quantum yields for $Y_2O_3:Eu^{3+}$ (13

at.%) under 255 nm excitation are found to be 7 and 10% respectively for 500 and 900 °C annealed samples.

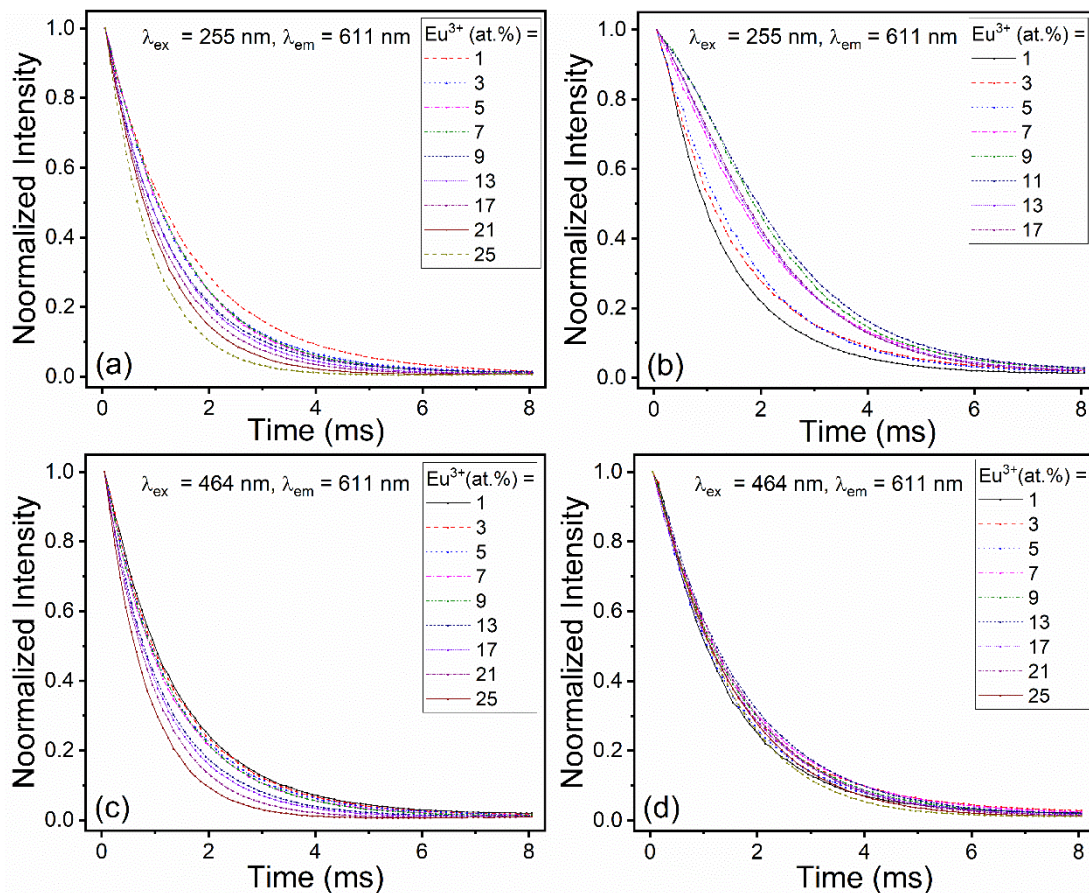


Fig. 3.13. PL decay curves of 5D_0 level of Eu^{3+} emission in 500 (a & c) and 900 °C (b & d) $Y_2O_3:Eu^{3+}$ (1, 3, 5, 7, 9, 13, 17, 21 and 25 at.%) samples. Excitation wavelengths are 255 and 464 nm.

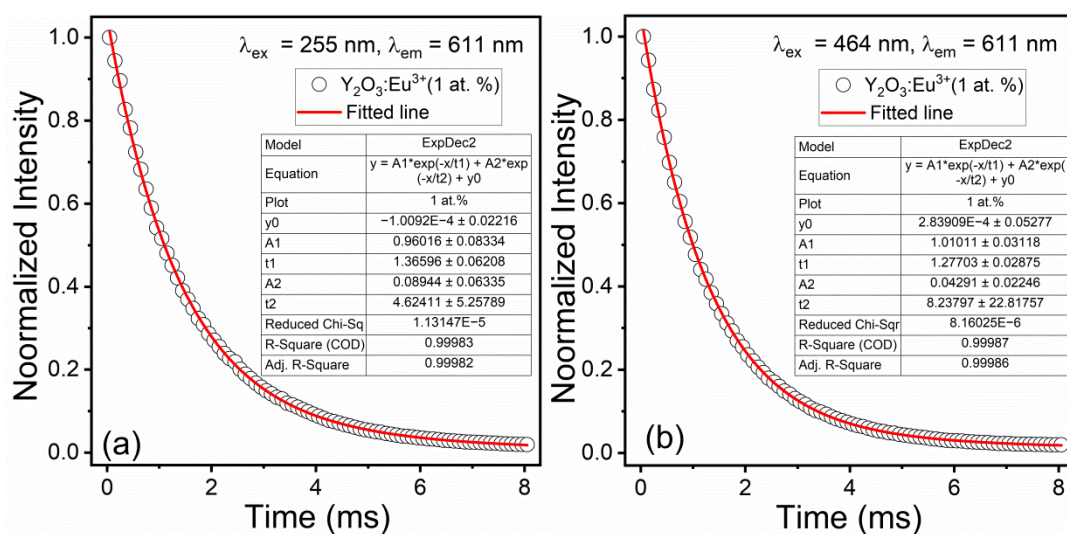


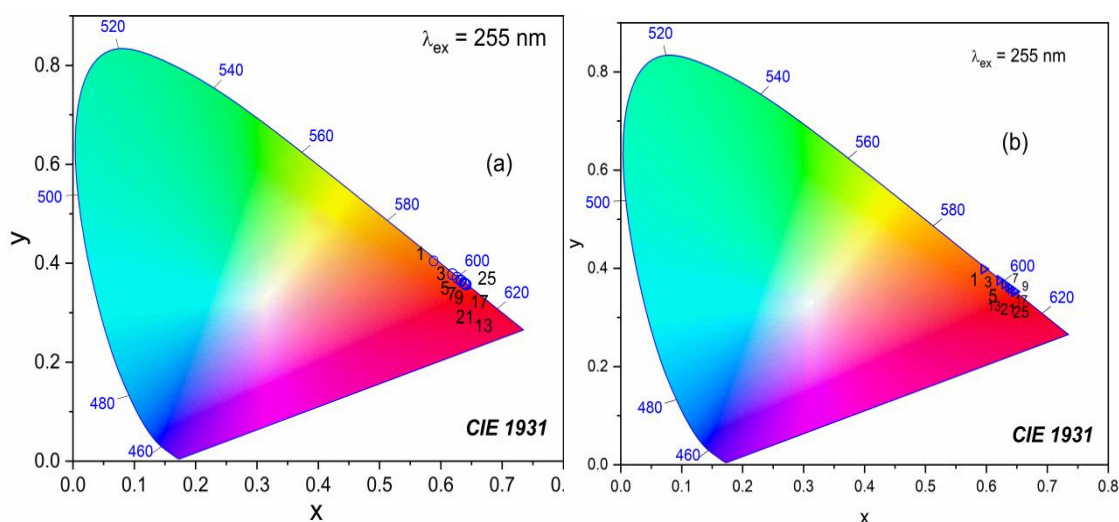
Fig. 3.14. Typical fitting of decay curve for Eu^{3+} emission ($\lambda_{ex} = 255$ and 464 nm and $\lambda_{em} = 611$ nm) in $Y_2O_3:Eu^{3+}$ (7 at.%) sample.

Table 3.2 The average lifetime calculated for the decay curves of 5D_0 level of Eu^{3+} in 500 and 900 °C annealed $Y_2O_3:Eu^{3+}$ (1, 3, 5, 7, 13, 17, 21 and 25 at.%) samples.

Eu^{3+} (at.%)	500 °C				900 °C			
	$\lambda_{ex} = 255$ nm		$\lambda_{ex} = 464$ nm		$\lambda_{ex} = 255$ nm		$\lambda_{ex} = 464$ nm	
	τ_{av} (ms)	R^2	τ_{av} (ms)	R^2	τ_{av} (ms)	R^2	τ_{av} (ms)	R^2
1	1.53	0.99	1.6	0.99	1.47	0.99	1.46	0.99
3	1.35	0.99	1.32	0.99	1.56	0.99	1.4	0.99
5	1.35	0.99	1.29	0.99	2.06	0.99	1.57	0.99
7	1.37	0.99	1.22	0.99	2.34	0.99	1.53	0.99
9	1.21	0.99	1.24	0.99	2.49	0.99	1.64	0.99
13	1.2	0.99	1.08	0.99	2.12	0.99	1.52	0.99
17	1.1	0.99	1.03	0.99	2.17	0.99	1.58	0.99
21	1.01	0.99	0.94	0.99	-	-	1.49	0.99
25	0.85	0.99	0.81	0.99	-	-	1.4	0.99

3.3.4.3. CIE chromaticity studies

To understand the colour of the emission from different samples, the Commission International de l'Eclairage (CIE) chromaticity was analyzed using the spectral data. The CIE positions of the $Y_2O_3:Eu^{3+}$ (1, 3, 7, 11, 15, 19, 21 and 25 at.%) samples under the excitation of 255 are indicated in the diagram (Fig. 3.15). Under both the excitation wavelengths, it is clearly observed that the colour of the emission is mostly concentrated in the red region.

**Fig. 3.15.** CIE chromaticity coordinate positions of (a) 500 and (b) 900 °C annealed $Y_2O_3:Eu^{3+}$ (1, 3, 5, 7, 9, 13, 17, 21 and 25 at.%) samples. Excitation wavelength is 255 nm.

3.3.5. Photoluminescence studies of $Y_2O_3:Sm^{3+}$

3.3.5.1. Steady state PL study

Fig. 3.16 shows the excitation spectra of (a) 500 and (b) 900 °C annealed $Y_2O_3:Sm^{3+}$ (0.5, 1, 2, 4, 6, 8, 10, and 12 at.%) samples monitored at 606 nm. All the excitation spectra consist of sharp peaks originated from the $f-f$ transitions of Sm^{3+} . These are observed at 346 ($^7H_{5/2} \rightarrow ^4K_{17/2}$), 362 ($^7H_{5/2} \rightarrow ^4D_{3/2}$), 378 ($^7H_{5/2} \rightarrow ^6P_{7/2}$), 406 ($^7H_{5/2} \rightarrow ^6P_{3/2}$), 422 ($^7H_{5/2} \rightarrow ^6D_{5/2}$), 467 ($^7I_{11/2} \rightarrow ^6P_{3/2}$), and 492 nm ($^7H_{5/2} \rightarrow ^6G_{7/2}$) [67-70]. These are originated from the $f-f$ shell of Sm^{3+} . Fig. 3.17 illustrates the emission spectra of $Y_2O_3:Sm^{3+}$ (0.5, 1, 2, 4, 6, 8, 10, and 12 at.%) samples under the direct excitations at 406 nm. The sharp emission peaks in the region of ~ 550 to 750 nm are observed.

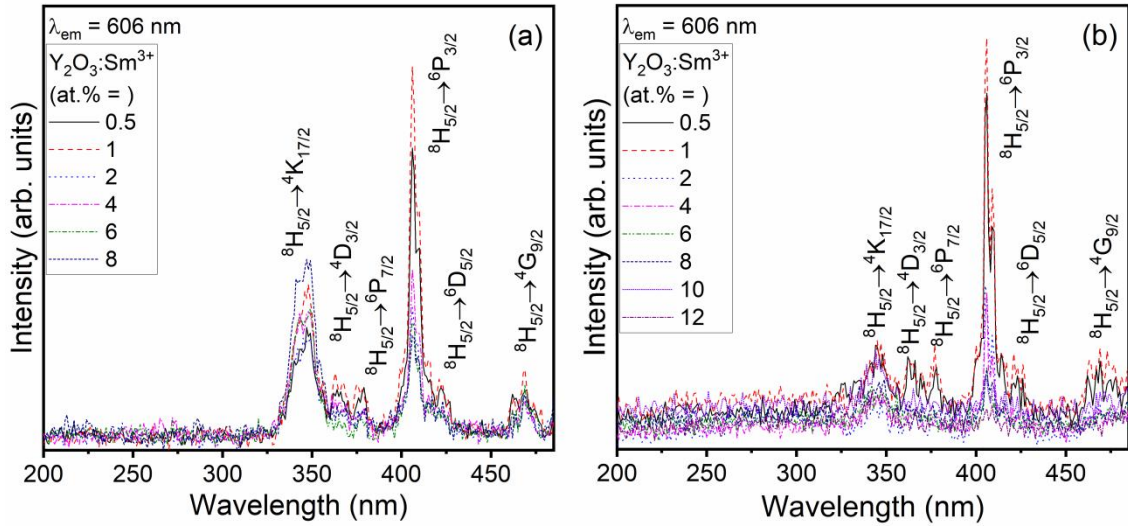


Fig. 3.16. PL excitation spectra of (a) 500 and (b) 900 °C Annealed $Y_2O_3:Sm^{3+}$ (0.5, 1, 2, 4, 6, 8, 10, and 12 at.%) samples monitored at $\lambda_{em} = 606$ nm.

These sharp emission peaks are related to the transitions within the $f-f$ electronic energy levels of Sm^{3+} . These emission peaks are related to the transitions originated from the $^4G_{5/2} \rightarrow ^6H_{5/2}$ (at 564 and 572 nm) and $^4G_{5/2} \rightarrow ^6H_{7/2}$ (at 602, 606 and 611 nm) are related to magnetic dipole transitions. And, the transition at $^4G_{5/2} \rightarrow ^6H_{9/2}$ (at 654 and 665 nm) is due to pure electric dipole transition [67-71]. In all the cases, the transition at $^4G_{5/2} \rightarrow ^6H_{5/2}$ (at 602, 606 and 611 nm) is dominant. Since the $\Delta J = \pm 1$, it is designated as magnetic dipole transition by quantum mechanical selection rule. However, this transition is considered to be dominated by electric dipole transition [70,71].

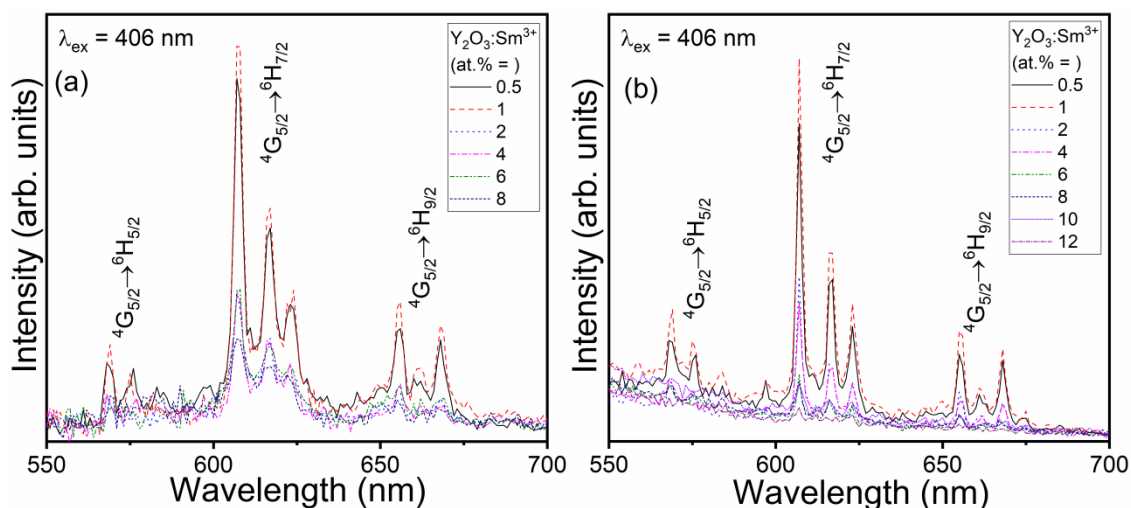


Fig. 3.17. PL emission spectra of $Y_2O_3:Sm^{3+}$ (0.5, 1, 2, 4, 6, 8, 10 and 12 at.%) samples monitored at $\lambda_{ex} = 406$ nm.

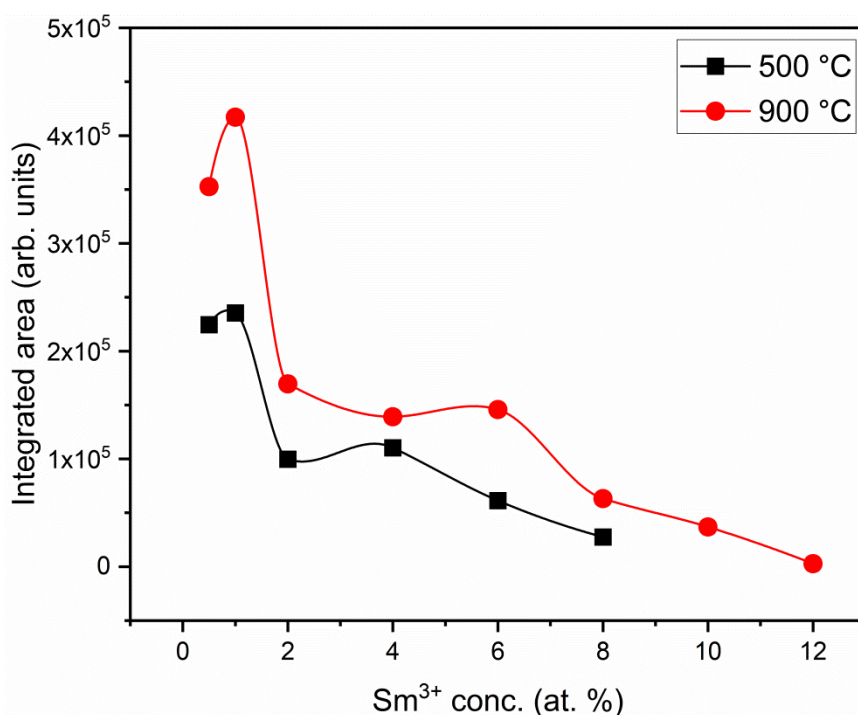


Fig. 3.18. Integrated PL emission of 500 and 900 °C annealed $Y_2O_3:Sm^{3+}$ (0.5, 1, 2, 4, 6, 8, 10 and 12 at.%) samples. Excitation wavelength is 406 nm.

Considering the highest emission peak at 606 nm, the integrated area of this peak is obtained. Fig. 3.18 displays the integrated area against the Sm^{3+} concentration for 500 and 900 °C annealed samples (as indicated in the figure). It can be clearly observed that the emission intensity is gradually increases with the increase of Sm^{3+} concentration and found to saturate at 1 at.%. On further increase of the doping concentration, it is clearly seen that the intensity of the emission is decreased. This is obvious phenomenon in the emission by lanthanide doping. Such decrease in the

emission against the higher concentration of the doping is known as concentration quenching. This quenching occurs when the distance between the doping lanthanide ions is less than certain critical distance, cross relaxation among them dominates. The dominance of cross relaxation induces the increase non-radiative transitions.

3.3.5.2. PL decay lifetime and quantum yield study

Fig. 3.19 shows the decay profiles of $^5G_{5/2}$ level of Sm^{3+} emission in $Y_2O_3:Sm^{3+}$ (1, 2, 4, 6, and 8 at.%) samples by monitoring at 606 nm emission. Excitation wavelength is 406 nm. All the decay profiles follow the second order exponential decay (Eqn. 3.3). The average decay lifetime was calculated using Eqn. 3.4 and given in Table 3.3.

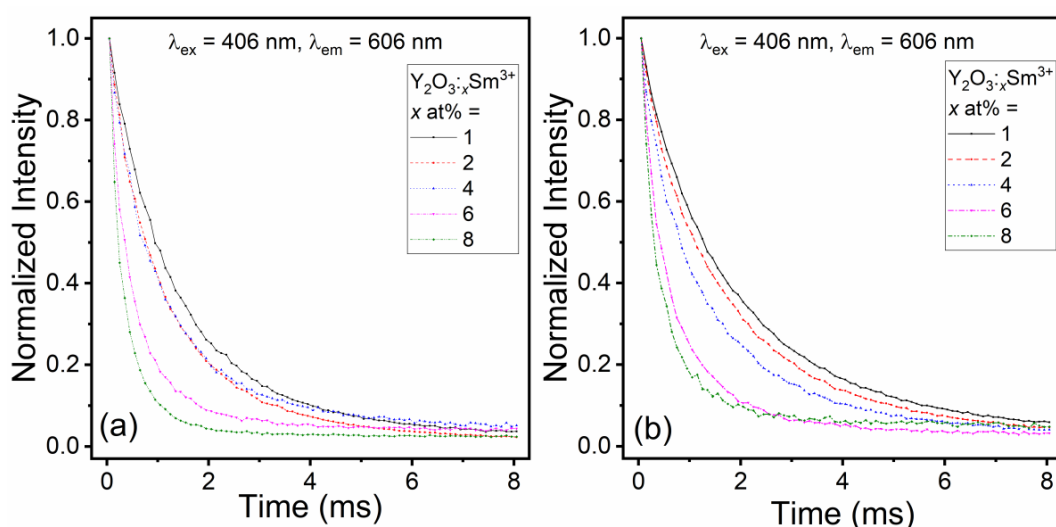


Fig. 3.19. PL decay curves of $^5G_{5/2}$ level of Sm^{3+} emission in $Y_2O_3:Bi^{3+}$ (1 at.%) $/Sm^{3+}$ (1, 2, 4, 6 and 8 at.%). $\lambda_{em} = 606$ nm and $\lambda_{ex} = 406$ nm.

Table 3.3: The average lifetime calculated for the decay curves of $^5G_{5/2}$ level of Sm^{3+} by monitoring at 606 nm emission in $Y_2O_3:Sm^{3+}$ (1, 2, 4, 6, and 8 at.%) samples.

Sm^{3+} (at.%)	500 °C		900 °C	
	τ_{av} (ms)	R^2	τ_{av} (ms)	R^2
1	1.34	0.99	2.07	0.99
2	1.13	0.99	1.85	0.99
4	1.05	0.99	1.6	0.99
6	0.50	0.99	0.91	0.99
8	0.31	0.99	0.66	0.99

The decay lifetime varies from 0.31 to 1.34 ms in the case of 500 °C annealed samples. And, this value changes from 0.66 to 2.07 ms in the case of 900 °C annealed samples. From the Table 3.3, it can be observed that the decay lifetime value in both the cases decreases with the increase of Sm^{3+} concentration. Such decrease in the decay lifetime of emission by lanthanide ions can be ascribed to the increase in the non-radiative transitions. Non-radiative transitions are due to the cross relaxation among lanthanide ions. On the other hand, the corresponding decay lifetime is increased after the annealing temperature is high. Such improvement in the decay lifetime is due to reduction in the extent of non-radiative transitions. This corroborates the behavior of emission intensity variation against the Sm^{3+} concentration in steady state luminescence (see Sec. 3.3.5.1)

3.3.5.3. CIE chromaticity studies

Fig. 5.22 illustrates the CIE chromaticity of (a) 500 and (b) 900 °C annealed Sm^{3+} emission in $Y_2O_3:Sm^{3+}$ (0.5, 1, 2, 4, 6, 8, 10 and 12 at.%) samples under the excitation of 406 nm.

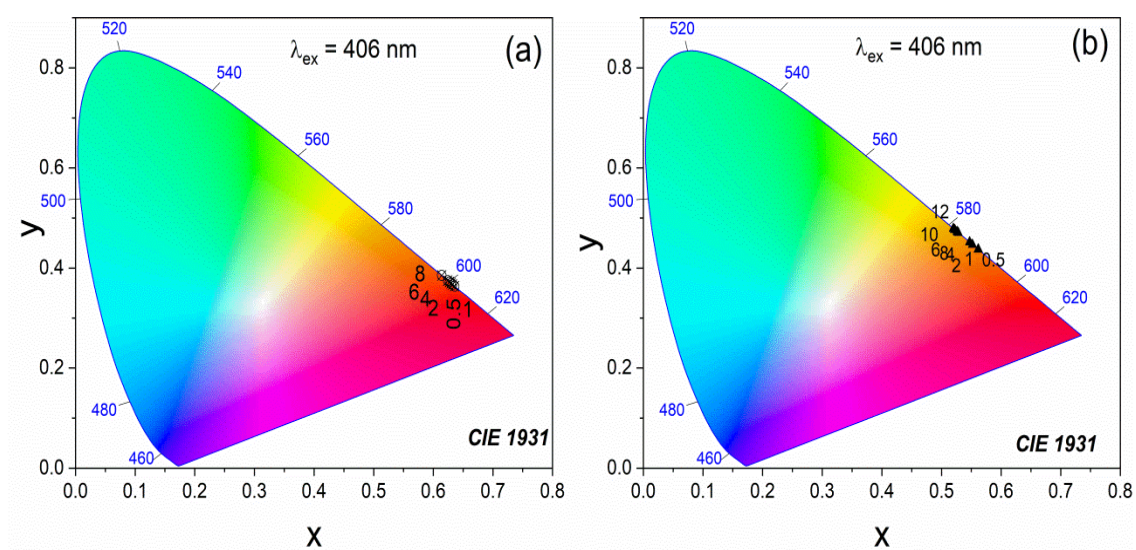


Fig. 3.20. CIE chromaticity coordinate positions of $Y_2O_3:Sm^{3+}$ (0.5, 1, 2, 4, 6, 8, 10 and 12 at.%) samples excited at 406 nm.

From the figure, it can be observed that the emission is spread over the region of orange-red region. These samples under the excitation at 406 nm can promising for red component phosphor for near-UV LED excited phosphor converted white emitting LEDs. However, it requires further improvement in the luminescence.

3.4. Conclusions

Eu^{3+} and Sm^{3+} doped Y_2O_3 were successfully synthesized by hydrothermal method with post annealing at 500 and 900 °C. The as prepared samples have shown to be amorphous. The amorphous phase of the samples crystallizes after heat treatment at 500 °C. All the samples annealed at 500 and 900 °C have shown to crystallize in the cubic structure. In $Y_2O_3:Eu^{3+}$, the maximum emission of Eu^{3+} is observed at ~13 at.% concentration. High asymmetric value of the emission in the entire concentration of Eu^{3+} studied indicates the fair asymmetric environment of Eu^{3+} in Y_2O_3 . This is also supported by the high value of second order crystal field parameter calculated from the spectral data. Thus, the high perturbation due to the asymmetric nature in the surroundings of Eu^{3+} is suggested. Both the steady state and decay dynamics of the PL corroborates the occurrence quenching due to the increase in non-radiative transitions. CIE coordinates suggest red emission by all the samples. In $Y_2O_3:Sm^{3+}$, all the emission are observed in the orange-red region. The highest emission intensity is observed at ~1 at.% of Sm^{3+} . Quenching of emission after 1 – 2 at.% of Sm^{3+} is observed. This is due to the increase in non-radiative transition because of cross-relaxation. This has been corroborated from the decay lifetime of studies of $^5G_{5/2}$ emission of Sm^{3+} . Under the 406 nm excitation, 2 and 4 at.% of Sm^{3+} doped Y_2O_3 samples show the orange-red emission in the CIE study.

References

1. M. Flynn, A.H. Kitai, J. Electrochem. Soc. 148 (2001) H149
2. M. Yu, J. Lin, Y.H. Zhou, S.B. Wang, Mater. Lett. 56 (2002) 1007
3. T. Hirai, T. Hirano, I. Komasaawa, J. Colloid Interface Sci. 253 (2002) 62.
4. K.-M. Lin, Y.-Y Li, Nanotechnology, 17 (2006) 4048 – 4052.
5. C.H. Kim, E.II Kwon, C.H. Cicillini, J. Alloys Compd, 311 (2000) 33.
6. B. Mercier, C. Dujardin, G. Ledoux, C. Louis, O. Tillement, J. Appl. Phys. 96 (2004) 650.
7. J.Y. Choe *et al.*, Appl. Phys. Lett. 78 (2001) 3800.
8. P Kumar, K. Nagpal, B.K. Gupta, ACS Appl. Mater. Interfaces 9 (2017) 14301.
9. D. Chávez-García, P. Sengar, K. Juárez-Moreno, D.L. Flores, I. Calderón, J. Barrera, G.A. Hirata, J. Mater. Res. Technol, 10 (2021) 797.
10. T. Paik, T.R. Gordon, A.M. Prantner, H. Yun, C.B. Murray, ACS Nano, 7 (2013) 2850.
11. X. Huang, Nat. Photonics 8 (2014) 748-749.
12. M. Shang, C. Li, J. Lin, Chem. Soc. Rev. 43 (2014) 1372-1386.
13. N. S. Singh, N. K. Sahu, D. Bahadur, J. Mater. Chem. C 2 (2014) 548.
14. T. Sakthivel, G. Annadurai, R. Vijayakumar, X. Huang, J. Lumin. 205 (2019) 129-135.
15. Q. Zhang, X. Wang, X. Ding, and Y. Wang, Inorg. Chem. 56 (2017) 6990–6998.
16. P. Du, J. S. Yu, Sci. Rep. 7 (2017) 11953.
17. S. Shi, L. Wang, M. Fang, L. Fu, L. D. Carlos, R. A. S. Ferreira, J. Wang, S. Wang, J. Alloys Compd. 814 (2020) 15226-15232.
18. R. Wangkhem, T. Yaba, N. S. Singh, R. S. Ningthoujam, J. Appl. Phys. 123 (2018) 124303.
19. S. Yan, J. Zhang, X. Zhang, S. Lu, X. Ren, Z. Nie, X. Wang, J. Phys. Chem. C, 111 (2007) 13256-13260.
20. A. Xie, X. Yuan, S. Hai, J. Wang, F. Wang and L. Li, J. Phys. D: App. Phys. 42 (2009) 1-7.
21. T. Yaba, R. Wangkhem, N.S. Singh, J. Alloys Compd., 843 (2020) 156022-156031.
22. P. Du, L.K. Bharat, J.S. Yu, J. Alloys Compd. 633 (2015) 37–41.
23. R.B. Pode, S.J. Dhoble, Phys. Stat. Sol. (b) 203 (1997) 571-577.
24. L. Chen, K.J. Chen, C.C. Lin, C.I. Chu, S.F. Hu, M.H. Lee, R.S. Liu, J. Comb. Chem. 12 (2010) 587–594.
25. S. Takeshita, T. Isobe, S. Niikura, J. Lumin. 128 (2008) 1515 – 1522.
26. L. S. Chi, R. S. Liu, B. J. Lee, J. Electrochem. Soc. 152(8) (2005) J93-J98.
27. W. Wang, P. Zhu, Opt. Express 26 (2018) 34820-34829.
28. P. Zhu, W. Wang, H. Zhu, P. Vargas, A. Bont, IEEE Photonics J. 10 (2018) 1-10.
29. G. Ju, Y. Hu, L. Chen, X. Wang, Z. Mu, H. Wu, F. Kang, J. Electrochem. Soc. 158 (2011) J294-J299.
30. T. W. Chou, S. Mylswamy, R. S. Liu, S. Z. Chuang, Solid State Commun. 136 (2005) 205-209.
31. B. Liu, J. Li, G. Duan, Q. Li, Z. Liu, J. Lumin. 206 (2019) 348-358.
32. X. T. Wei, Y. H. Chen, X. R. Cheng, M. Yin, W. Xu, Appl. Phys. B 99 (2010) 763-768.
33. L.G. Jacobsohn, M.W. Blair, S.C. Tornga, L.O. Brown, B.L. Bennett, R.E. Muenchausen, J. Appl. Phys. 104 (2008) 124303.
34. A. Scarangella, F. Fabbri, R. Reitano, F. Rossi, F. Priolo, M. Miritello, Sci. Rep. 7 (2017) 17325.

35. S. Ray, P. Pramanik, A. Singha, A. Roy, $Y_2O_3:Eu^{3+}$, J. Appl. Phys. 97 (2005) 094312.
36. M. Yang, Y. Sui, S. Wang, X. Wang, Y. Wang, S. Lü, T. Lü, W. Liu, J. Alloys Compd. 509 (2011) 266-270.
37. J.F. Martel, S. Jandl, B. Viana, D. Vivien, J. Solid State Chem. 61 (2000) 1455.
38. R. S. Ningthoujam, R. Shukla, R. K. Vatsa, V. Duppel, L. Kienle, A. K. Tyagi, J. Appl. Phys. 105 (2008) 084304.
39. G. Blasse, B.C. Grabmeier, *Luminescent Materials*, Springer-Verlag, (1994) New York.
40. W. Wang, P. Zhu, Opt. Express. 26 (2018) 34820-34829
41. R.S. Yadav, S.B. Rai, J. Alloys Compd. 700 (2017) 228.
42. L. Wang, L. Shi, N. Liao, H. Jia, P. Du, Z. Xi, L. Wang, D. Jin, Mater. Chem. Phys. 119 (2010) 490.
43. G.A. Sotiriou, M. Schneider, S. E. Pratsinis, J. Phys. Chem. C.116 (2012) 4493.
44. K. Mishra, S.K. Singh, A.K. Singh, S.B. Rai, Mater. Res. Bull. 47 (2012) 1339
45. S. Hu, X. Qin, G. Zhou, X. Liu, C. Lu, Z. Xu, S. Wang, J. Alloys Compd. 664 (2016) 304.
46. B. Marappa, M.S. Rudresha, H. Nagabhusana, R.B. Basavaraj, B.K. Prasad, AIP Conf. Proc. 1832 (2017) 050150.
47. R.S. Yadav, S.B. Rai, Opt. Laser Technol. 111 (2019) 169.
48. M.K. Jung, W.J. Park, D.H. Yoon, Sens. Actuators B Chem. 126 (2007) 328.
49. C.A. Kodaira, R. Stefani, A.S. Maia, M.C.F.C. Felinto, H.F. Brito, J. Lumin. 127 (2007) 616.
50. L.R. Singh, R.S. Ningthoujam, V. Sudarsan, I. Srivastava, S.D. Singh, G.K. Dey, S.K. Kulshreshtha, Nanotechnology. 19 (2008) 055201.
51. H.J. Devi, W.R. Singh, R.S. Loitongbam, J. Fluoresc. 26 (2016) 875–889.
52. M. Yang, Y. Sui, S. Wang, X. Wang, Y. Wang, S. Lü, T. Lü, W. Liu, J. Alloys Compd. 509 (2011) 266-270.
53. L. Zhang, P. Li, A. Zhao, X. Li, J. Tang, F. Zhang, G. Jia, C. Zhang, J. Alloys Compd.816 (2020) 152546.
54. G. Liu, Y. Zhang, J. Yin, and W. F. Zhang, J. Lumin. 128 (2008) 2008-2012
55. B. Qian, H. Zou, D. Meng, X. Zhou, Y. Song, K. Zheng, C. Miao and Y. Sheng, CrystEngCom. 20(45) (2018) 7322-73288
56. R.G.A. Kumar, S. Hata, K.G. Gopchandran, J. Ceram. Int. 39(8) (2013) 9125-9136.
57. X. Liu, C. Lin, J. Lin, Appl. Phys. Lett. 90 (2007) 081904
58. L. Francis T., P.K. Rao, M. Thomas, S.K. Mahesh, V.R. Reshmi, T.S. Sreena, Phys. Chem. Chem. Phys. 16 (2014) 17108.
59. M. Buijs, A. Mayerink, and G. Blasse, J. Lumin. 37 (1987) 9-20
60. M. L. Debasu, D. Ananias, A. G. Macedo, J. Rocha, L. D. Carlos, J. Phys. Chem. C 115 (2011) 15297–15303
61. R. Joshi, B.P. Singh, C.L. Prajapat, Y. Kashyap, C. Nayak, D. Bhattacharyya, R.S. Ningthoujam, J. Phys. Chem. C 125 (2021) 17971-17982.
62. E. Zych, J. Phys.: Condens. Matter 14 (2002) 5637–5650
63. G. Pappalardo, R. B. Hunt, Jr., J. Electrochem. Soc. 132 (1985) 721-730
64. G. Nishimura, T. Kushida, Phys. Rev. B. 37 (1988) 9075–9078.
65. A.K. Parchur, R.S. Ningthoujam, RSC Adv. 2 (2012) 10859–10868.
66. R. Wangkhem, N. S. Singh, N. P. Singh, S. D. Singh, L. R. Singh, J. Lumin. 203 (2018) 341-348.

67. N.S. Singh, R.S. Ningthoujam, G. Phaomei, S.D. Singh, A. Vinu, R.K. Vatsa, Dalton Trans. 41 (2012) 4404-4412.
68. O. Tegus, B. Amurinsana, S. Zhiqiang, J. Lumin. 215 (2019) 116624.
69. E. Cavalli, A. Belletti, R. Mahiou, P. Boutinaud, J. Lumin. 130 (2010) 733.
70. G. Lakshminarayana, J. Qiu, J. Lumin. 476 (2009) 470 – 476.
71. P.S. May, D.H. Metcalf, F.S. Richardson, R.C. Carter, C.E. Miller, R.A. Palmer, J. Lumin. 51 (1991) 249.

Chapter 4

Photoluminescence properties and energy transfer in Bi^{3+} sensitized $\text{Y}_2\text{O}_3:\text{Ln}^{3+}$ ($\text{Ln}^{3+} = \text{Eu}^{3+}$ & Sm^{3+})

4.1. Introduction

Lanthanide activated inorganic phosphors have recently gathered enormous interest for their potential applications in solid state lighting [1-4], as fluorescent probe [5-8] and biological imaging, etc. [9-12]. On the front of lighting applications, these inorganic phosphors have become the prefer choice (as potential alternative) ever since the use of yttrium aluminate garnet ($\text{Y}_3\text{Al}_5\text{O}_{12}:\text{Ce}^{3+}$) with GaN light emitting diode (LED) chip has been commercialized for general lighting purposes as replacement for general fluorescent lamp, tube light, incandescent lamps etc. [13-15]. However, this device has certain disadvantages of low colour rendition (< 80 , due to the lack of sufficient red component), temperature and current dependent chromaticity, thermal quenching etc. [13,16-20]. In order to improve the colour rendition, mainly 3 (three) approaches have been reported: (i) To develop entirely white emitting phosphor excitable by UV/near UV (NUV) LED, (ii) Combination of all 3 (three) primary components i.e., red, green and blue phosphor with NUV LED and (iii) Red and green phosphor with blue LED source. The white LEDs (WLEDs) based on the latter two approaches are expected to achieve high colour rendition (> 90) in future with the development of appropriate and efficient red emitting phosphor [18,21-23]. Among these, the three-colour band approach with NUV LED will have the advantage of resulting clearer and brighter view to human eye [16,24,25].

The WLEDs based on the combination of blue, green and red down converted phosphors with UV or NUV LEDs have recently gained as important alternative approach with the expectation of improving colour rendition [24]. In this approach, efficient blue ($\text{BaMgAl}_{10}\text{O}_{17}:\text{Eu}^{2+}$) and green ($\text{SrSi}_2\text{O}_2\text{N}_2:\text{Eu}^{2+}$ or $\text{Ba}_2\text{SiO}_4:\text{Eu}^{2+}$) phosphors are already available [26]. However, highly efficient red phosphors excitable with UV or NUV LEDs are scarce. In this aspect, the broad band Eu^{2+} activated nitride and silicate-based phosphors, such as CaAlSiN_3 , $\text{Sr}_4[\text{LiAl}_{11}\text{N}_{14}]$ etc. [27-29], were reported as efficient red emitters. However, the emission band extends beyond 700 nm thereby reducing efficiency in most cases, since the emission is beyond human eye's

sensitivity (> 700 nm) [14]. Recently, the enhanced energy transfer in La_2MoO_6 - La_2WO_6 composite structure activated with Eu^{3+} , when compared to individual tungstates or molybdates, was reported as potential red component for WLED [25]. Later, we also have reported highly efficient red emission from Bi^{3+} sensitized $\text{CaMoO}_4:\text{Eu}^{3+}$ as possible red component for blue LED converted WLEDs [30]. The recent reports are also available on the Eu^{3+} activated phosphors, such as $\text{Bi}_4\text{Si}_3\text{O}_{12}$ and $\text{Y}_2\text{Mo}_4\text{O}_{15}$, as potential red component for solid state lighting using NUV LED as pumping source [31,32].

Commonly, $\text{Y}_2\text{O}_3:\text{Eu}^{3+}$ and $\text{Y}_2\text{O}_2\text{S}:\text{Eu}^{3+}$ are considered as excellent red phosphors for practical applications, such as displays [33-36]. However, these phosphors usually have absorption in UV (250-260 nm) and low absorption with narrow band NUV ~ 393 nm limiting the practicality in terms of efficiency [25]. While, the $\text{Y}_2\text{O}_3:\text{Sm}^{3+}$ has the absorption at the near UV region ca. ~ 400 nm due to f - f absorption. However, this absorption band weak. There are various reports on the luminescence studies of $\text{Y}_2\text{O}_3:\text{Sm}^{3+}$ [34-41]. In this aspect, sensitization of using Bi^{3+} can be an alternative for efficient near UV excitable red emitter with enhanced emission. This is due to two strong absorption bands of Bi^{3+} from ground state $6s^2$ to the excited state $6s6p$ ($^1\text{S}_0 \rightarrow ^3\text{P}_1$) near UV region (~ 340 and 400 nm) depending on the Bi^{3+} ions substituting the well-known 2 (two) different symmetry sites of Y^{3+} in Y_2O_3 [42-45]. Subsequently, this Bi^{3+} absorption can render the resonance energy transfer. So, many researchers have reported the luminescence properties of Bi^{3+} sensitized $\text{Y}_2\text{O}_3:\text{Eu}^{3+}$ phosphor which is potentially useful for solid state lighting applications [16,46].

In this chapter, the luminescence properties of hydrothermally synthesized Bi^{3+} sensitized Eu^{3+} and Sm^{3+} activated Y_2O_3 is discussed. The energy transfer processes from the sensitizer to the activator through steady state and decay dynamics luminescence is deliberated. The possibility of changing the emission colour through varying excitation wavelength and activator concentration is shown. The details of photoluminescence (PL) decay lifetime, quantum yield and the Commission International de l'Eclairage (CIE) chromaticity diagram are also presented.

4.2. Experimental methods

4.2.1. Materials

Yttrium (III) nitrate hexahydrate ($\text{Y}(\text{NO}_3)_3 \cdot 6\text{H}_2\text{O}$, 99.9%, Alfa Aesar), europium (III) nitrate hexahydrate ($\text{Eu}(\text{NO}_3)_3 \cdot 6\text{H}_2\text{O}$, 99.9%, Alfa Aesar), samarium (III) nitrate hexahydrate ($\text{Sm}(\text{NO}_3)_3 \cdot 6\text{H}_2\text{O}$, 99.9%, Alfa Aesar), bismuth (III) nitrate pentahydrate ($\text{Bi}(\text{NO}_3)_3 \cdot 5\text{H}_2\text{O}$, 99.99%, Alfa Aesar), were used as received for the sources of Y^{3+} , Eu^{3+} , Sm^{3+} and Bi^{3+} respectively. Polyvinyl pyrrolidone (PVP, $M_w \sim 40000$, Sigma Aldrich) was used as capping agent.

4.2.2. Synthesis of Bi^{3+} sensitized Y_2O_3 doped with Eu^{3+} phosphors

Yttrium (III) nitrate hexahydrate ($\text{Y}(\text{NO}_3)_3 \cdot 6\text{H}_2\text{O}$, 99.9%, Alfa Aesar), bismuth (III) nitrate pentahydrate ($\text{Bi}(\text{NO}_3)_3 \cdot 5\text{H}_2\text{O}$, 99.99%, Alfa Aesar), europium (III) nitrate hexahydrate ($\text{Eu}(\text{NO}_3)_3 \cdot 6\text{H}_2\text{O}$, 99.9%, Alfa Aesar) were used as sources of Y^{3+} , Bi^{3+} and Eu^{3+} , respectively. Polyvinyl pyrrolidone (PVP, $M_w \sim 40000$, Sigma Aldrich) was used as a capping agent. All these chemicals were used without further purification. In a typical synthesis of 1 at.% Bi^{3+} sensitized $\text{Y}_2\text{O}_3:\text{Eu}^{3+}$ (1 at.%) sample (termed as $\text{Y}_2\text{O}_3:\text{Eu}^{3+}$ (1 at.%) / Bi^{3+} (1 at.%)), 2.4 mg of $\text{Bi}(\text{NO}_3)_3 \cdot 5\text{H}_2\text{O}$ was dispersed in 2 mL of deionized water (DIW) with continuous stirring. To this, 2.2 mg of $\text{Eu}(\text{NO}_3)_3 \cdot 6\text{H}_2\text{O}$ and 379.2 mg of $\text{Y}(\text{NO}_3)_3 \cdot 6\text{H}_2\text{O}$ were put and mixed together. 150 mg of polyvinyl pyrrolidone (PVP) was also added to the above solution. The volume was made up to 30 mL with the addition of DIW. The pH of the solution was fixed at 10 using ammonium hydroxide solution (NH_4OH , ~25% NH_3 , Sigma Aldrich). Then, the solution was transferred to a Teflon lined stainless steel autoclave and heated at 180 °C for 18 h in an oven. It was cooled down to room temperature naturally. The precipitate was centrifuged and washed several times with DIW and acetone. Then, it was dried at 50 °C overnight. The samples with other $\text{Eu}^{3+}/\text{Bi}^{3+}$ concentrations were synthesized following the same procedure. The as-prepared samples were annealed at 500 for 4 h or 900 °C for 4 h in the air.

4.2.3. Synthesis of Bi^{3+} sensitized Y_2O_3 doped with Sm^{3+} phosphors

Following the similar procedure mentioned in the above section, Bi^{3+} sensitized $\text{Y}_2\text{O}_3:\text{Sm}^{3+}$ phosphors (denoted as $\text{Y}_2\text{O}_3:\text{Bi}^{3+}/\text{Sm}^{3+}$) were also synthesized adopting hydrothermal method. In a typical synthesis of 1 at.% Bi^{3+} sensitized $\text{Y}_2\text{O}_3:\text{Sm}^{3+}$ (1 at.%) sample, 2.4 mg of $\text{Bi}(\text{NO}_3)_3 \cdot 5\text{H}_2\text{O}$ was dissolved in 2 mL of deionized water (DIW)

under continuous stirring. To the above, 2.2 mg of $\text{Sm}(\text{NO}_3)_3 \cdot 6\text{H}_2\text{O}$ and 379 mg of $\text{Y}(\text{NO}_3)_3 \cdot 6\text{H}_2\text{O}$ were added. 150 mg of polyvinyl pyrrolidone (PVP) was also added to the above solution. The whole solution is kept under hydrothermal condition for 18 h at 180 °C. The remaining samples were also prepared with similar process. The as-prepared samples were annealed 500 and 900 °C for 4 h in the air.

4.2.4. Characterization

X-ray diffractometers Bruker D8 advance and Rigaku Ultima IV with $\text{Cu } K\alpha$ radiation were used for crystalline phase identification. Fourier transform infrared (FT-IR) spectrometer (Shimadzu make IR-Affinity-1S) was used to record the FT-IR spectra of the prepared samples. Morphology of the particles was studied using the transmission electron microscopy (TEM) images recorded with JEOL 2000FX. The steady state and dynamics of photoluminescence (PL) as well as quantum yield (QY) were measured using Fluoromax-4CP spectrofluorometer (HORIBA make) equipped with 150 W Xenon lamp and 25 W μs Xenon flash lamp. The fluorescence decay lifetime of Bi^{3+} was recorded by Time correlated single photon counting (TCSPC) technique (HORIBA make DeltaFlex) with pulse LED (340 ± 10 nm) source (pulse width < 1.2 ns). All the PL measurements were carried out by casting samples over the glass slides at room temperature. K-sphere ‘petite’ integrating sphere from Photon Technology International (PTI) was used for quantum yield (QY) measurements. For calculation of absolute QY, $\phi(\%) = \frac{I_{\text{emission}}}{I_{\text{quartz}} - I_{\text{sample}}}$ was used. I_{emission} = luminescence emission intensity of the sample, I_{quartz} = the intensity of light used to excite only the quartz slide and I_{sample} = the intensity of the light used for exciting the sample on the quartz slide. The photons absorbed by the sample is given by the difference between the last two. All the measurements were taken in the emission mode. The QY measurements were carried out on the quartz slides at room temperature.

4.3. Results and discussion

4.3.1. X-ray diffraction study

The X-ray diffraction (XRD) patterns of $\text{Y}_2\text{O}_3:\text{Eu}^{3+}$ ($\text{Eu}^{3+} = 1, 3, 5, 7, 11, 13$ and 17 at.%) / Bi^{3+} (1 at.%) samples annealed at 500 and 900 °C are shown in Fig. 4.1. And, Fig. 4.2 illustrates the XRD patterns of $\text{Y}_2\text{O}_3:\text{Sm}^{3+}$ ($\text{Sm}^{3+} = 0.5, 1, 2, 4, 6, 8$ and 10 at.%) / Bi^{3+} (1 at.%) samples annealed at 500 and 900 °C. All the patterns are well

matched with the cubic phase of Y_2O_3 with ICDD no. 41–1105 [47,48]. The presence of other possible impurity phases such as Eu_2O_3 , Sm_2O_3 , Bi_2O_3 etc. is not observed. This suggests the formation of solid solution of Eu^{3+} and Bi^{3+} ions in the host matrix. Such possibility of lattice substitution in Y^{3+} sites of Y_2O_3 by Eu^{3+} or Sm^{3+} and/or Bi^{3+} is due to near equivalent ionic radii of Eu^{3+} ($r = 0.947 \text{ \AA}$), Sm^{3+} (0.958 \AA), and Bi^{3+} ($r = 1.03 \text{ \AA}$) to that of Y^{3+} ($r = 0.9 \text{ \AA}$). The average crystalline sizes of the prepared samples were calculated using Debye-Scherrer, $= \frac{\kappa\lambda}{\beta \cos\theta}$, where, D is the crystalline size, κ is the Scherrer constant ($= 0.9$), λ is the wavelength of the X-ray used, β is the FWHM at Bragg angle and ε is the lattice strain. From the Scherrer equation, the average crystalline sizes of $\text{Y}_2\text{O}_3:\text{Eu}^{3+}/\text{Bi}^{3+}$ samples are calculated $\sim 10\text{--}12 \text{ nm}$ and $28\text{--}34 \text{ nm}$ were observed respectively for 500 and 900 °C annealed samples. While, the average crystalline sizes of $\text{Y}_2\text{O}_3:\text{Bi}^{3+}/\text{Sm}^{3+}$ samples are calculated $\sim 10\text{--}12 \text{ nm}$ and $25\text{--}28 \text{ nm}$ were observed respectively for 500 and 900 °C annealed samples. The detail of the calculated crystallite sizes of all the samples are given in Table 4.1.

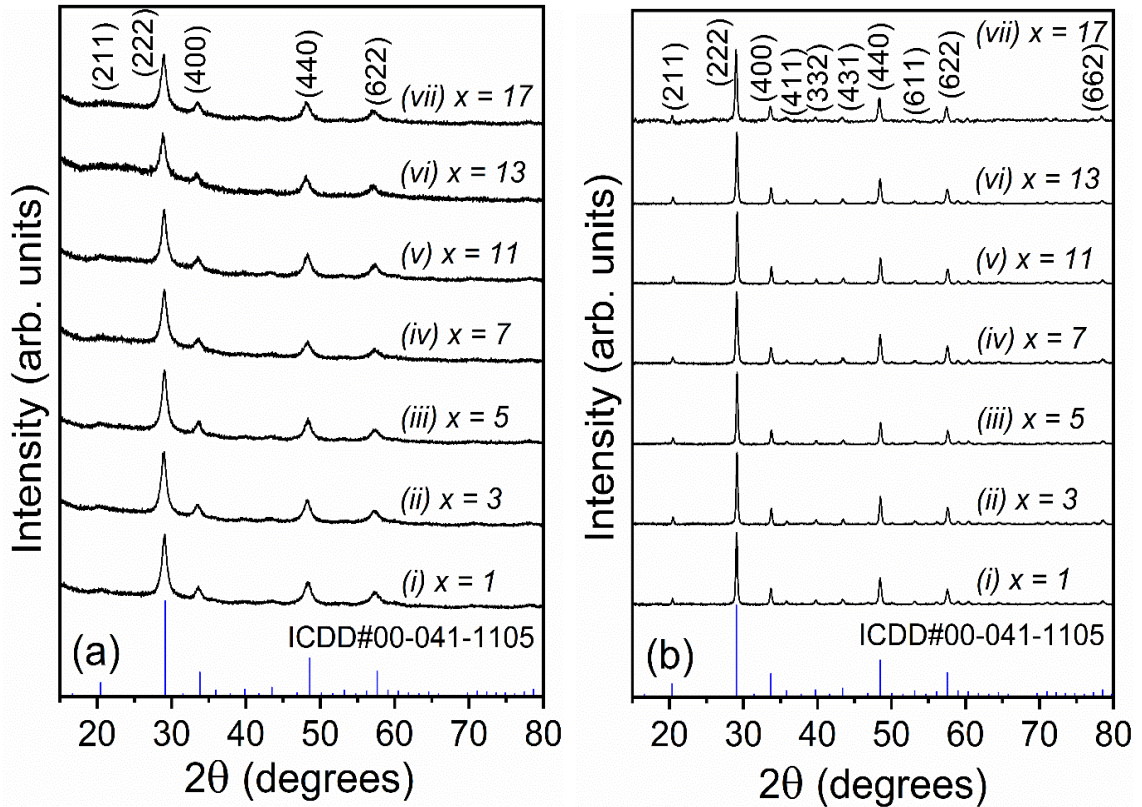


Fig. 4.1. The X-ray diffraction (XRD) patterns of (a) 500 and (b) 900 °C annealed $\text{Y}_2\text{O}_3:\text{Eu}^{3+}$ ($\text{Eu}^{3+} = 1, 3, 5, 7, 11, 13$ and $17 \text{ at.}\%$)/ Bi^{3+} ($1 \text{ at.}\%$).

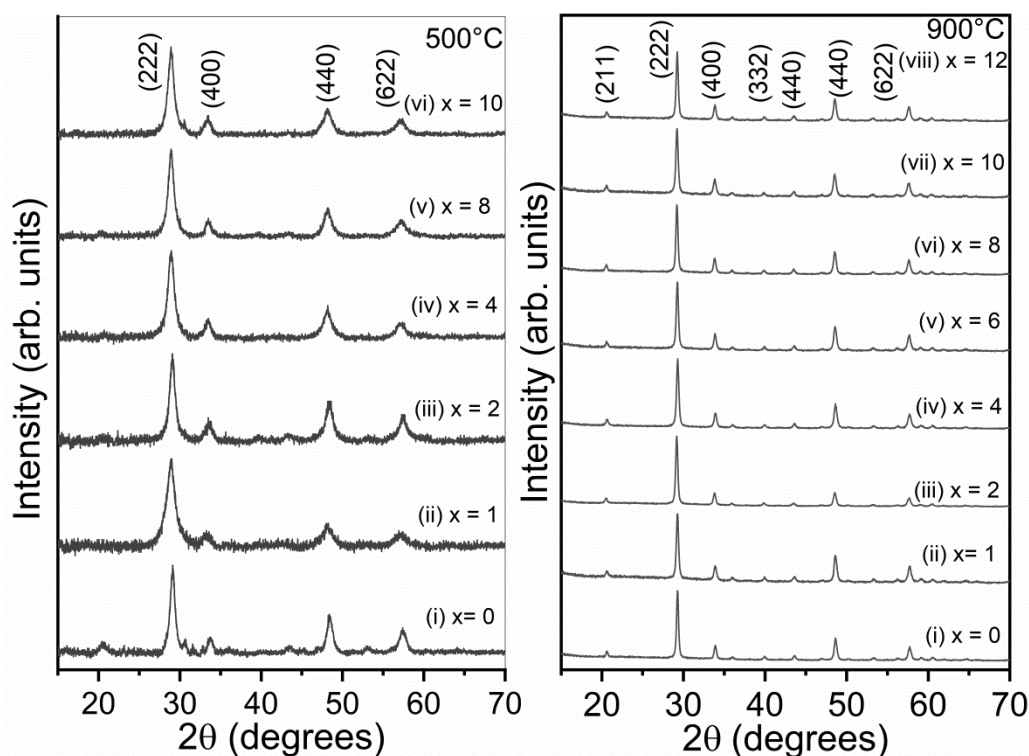


Fig. 4.2. The X-ray diffraction (XRD) patterns of (a) 500 and (b) 900 °C annealed $\text{Y}_2\text{O}_3:\text{Sm}^{3+}$ ($\text{Sm}^{3+} = 0$, 1, 2, 4, 6, 8, 10 and 12 at.%) / Bi^{3+} (1 at.%).

Table 4.1. Calculated crystallite size for 1 at.% Bi^{3+} sensitized and Eu^{3+} or Sm^{3+} doped Y_2O_3 500 and 900 °C annealed samples, using Scherrer relation.

Eu^{3+} (%)	Crystallite size (nm)		Sm^{3+} (%)	Crystallite size (nm)	
	500 °C	900 °C		500 °C	900 °C
1	10	31	0	10	27
3	10	32	1	11	26
5	10	33	2	10	27
7	11	28	4	12	25
11	10	31	6	-	28
13	12	32	8	11	26
17	11	34	10	12	24

4.3.2. Fourier transform infrared spectroscopy study

FT-IR spectra of 500 and 900 °C annealed samples of $\text{Y}_2\text{O}_3:\text{Bi}^{3+}$ (1 at.%) / Eu^{3+} (3 at.%) are shown in Fig. 4.3. In both the figures, The absorption band observed at 3430 cm^{-1} is due to the O-H bending vibration [22,35]. The absorption band at 1653 cm^{-1} is assigned to carbonyl (C=O) vibration.

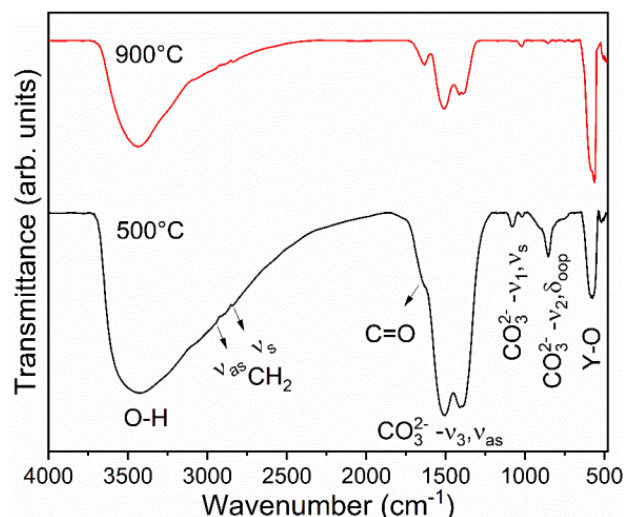


Fig. 4.3. FT-IR spectra of 500 and 900 °C annealed $\text{Y}_2\text{O}_3:\text{Bi}^{3+}$ (1 at.+)/ Eu^{3+} (3 at.%) samples.

The two small bands at 2946 and 2842 cm^{-1} are due to antisymmetric and symmetric stretching vibrations of CH_2 group. The above bands are coming from PVP that was used during the synthesis process [3]. The Y-O stretching vibration is observed at 563/575 cm^{-1} [33,49]. Other possible absorption bands of PVP were not observed from the FTIR spectra and it may be due to PVP decomposition by annealing. The absorption bands at 1508, 1409, 1077 and 855 cm^{-1} are related to CO_3^{2-} groups. According to Tanner and Fu [44], the atmospheric CO_2 reacts with Y_2O_3 to form carbonate during the annealing process. And this carbonate could be completely removed when the samples are heated above 1000 °C. As the prepared samples were heated only up to 900 °C, the presence of CO_3^{2-} may be observed in the FTIR spectra. The bands at 1508 and 1409 cm^{-1} correspond to antisymmetric stretching vibration of CO_3^{2-} . The band at 1077 cm^{-1} is assigned to symmetric stretching vibration of CO_3^{2-} , while 855 cm^{-1} is due to out-of-plane vibration of CO_3^{2-} [35,49].

4.3.3 Transmission electron microscopy study

The TEM images of 1 at.% Bi^{3+} sensitized $\text{Y}_2\text{O}_3:\text{Eu}^{3+}$ (3 at.%) sample annealed at 500 °C are shown in Fig 4.4. The formation of rod-shaped particles is observed from the TEM images. This may be understood from the report by Zhang *et al.* that the observed shape of Y_2O_3 as the aggregates of several nanoparticles fused together in the rod shape due to dipole-dipole interactions [50]. Again, the synthesis was carried out at higher temperature and pressure favouring the anisotropic growth of the particles [51]. The average dimensions of particles are ~120-250 nm in diameter having 550-1075 nm in length. The inter-planar spacing calculated from the high-resolution TEM (HRTEM)

image is found to be 0.31 nm (See Fig. 4.4(b)). This value corresponds to the (222) lattice planes of Y_2O_3 . The diffraction planes from the selected area electron diffraction (SAED) image are also found to belong to the cubic phase of Y_2O_3 (See Fig. 4.4(c)). These confirm the formation of crystalline $\text{Y}_2\text{O}_3:\text{Eu}^{3+}/\text{Bi}^{3+}$.

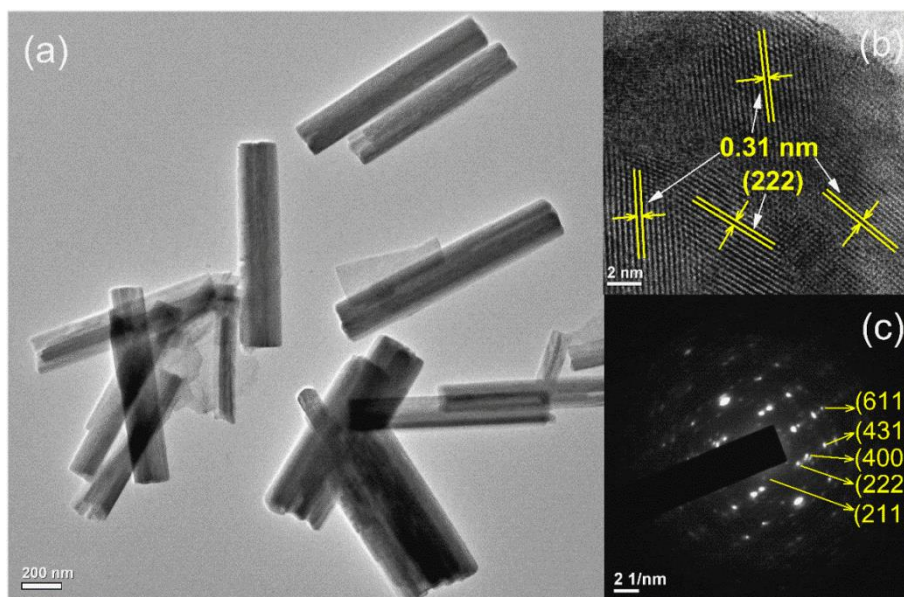


Fig 4.4. (a) TEM (b) HRTEM image and (c) SAED pattern of 500 °C annealed 1 at.% Bi^{3+} sensitized $\text{Y}_2\text{O}_3:\text{Eu}^{3+}$ (3 at.%).

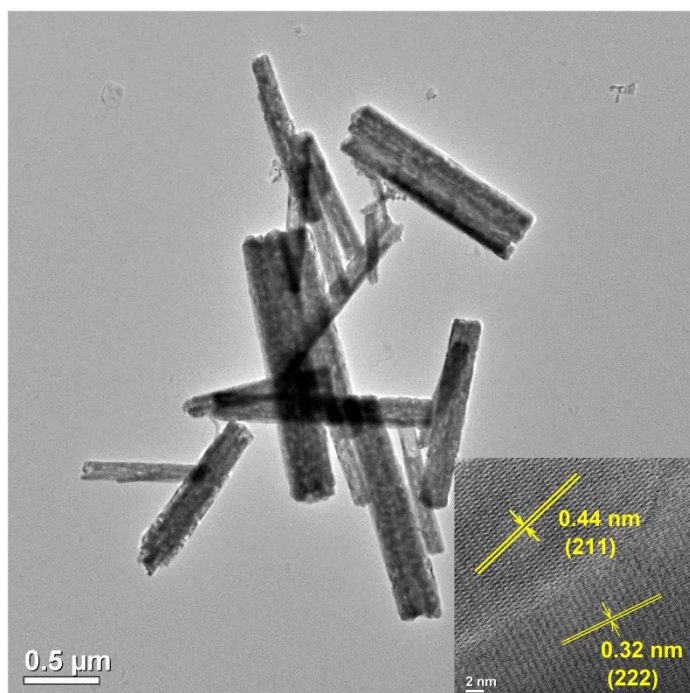


Fig 4.5. (a) TEM (b) HRTEM image and (c) SAED pattern of 900 °C annealed 1 at.% Bi^{3+} sensitized $\text{Y}_2\text{O}_3:\text{Eu}^{3+}$ (3 at.%).

Fig. 4.5 show the TEM images of 1 at.% Bi^{3+} sensitized $\text{Y}_2\text{O}_3:\text{Eu}^{3+}$ (3 at.%) sample annealed at 900 °C sample. The particles are still maintained the rod-shaped morphology. The sizes of the particles are increased to ~200- 450 nm in diameter with ~2 – 3 μm in length. From the high-resolution TEM (HRTEM) image (See Fig. 4.5 inset), the inter-planar spacing is found to be 0.32 and 0.44 nm. These values correspond to the (222) and (211) lattice planes of Y_2O_3 .

4.3.4. Photoluminescence (PL) studies of Bi^{3+} sensitized $\text{Y}_2\text{O}_3:\text{Eu}^{3+}$

4.3.4.1. PL studies of $\text{Y}_2\text{O}_3:\text{Bi}^{3+}$

The PL emission spectra of the 500 °C annealed samples of $\text{Y}_2\text{O}_3:\text{Bi}^{3+}$ (1 at.%) under the excitation of 315–375 nm (with the increment of 5 nm) are shown in the Fig. 4.6(a).

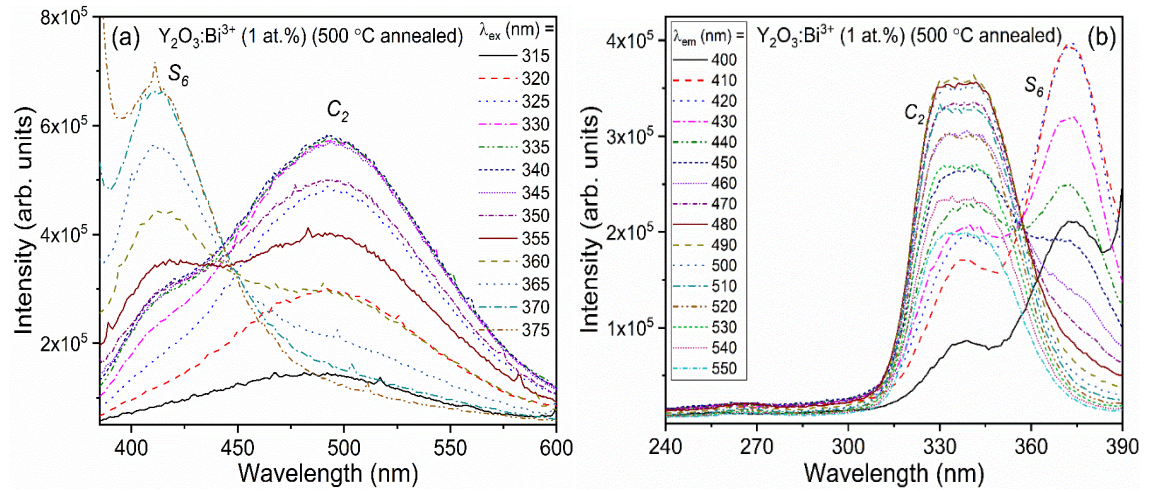


Fig. 4.6. PL (a) emission spectra at $\lambda_{\text{ex}} = 315\text{--}375$ nm (with the increment of 5 nm), and (b) excitation spectra monitored at $\lambda_{\text{em}} = 400\text{--}550$ nm (with the increment of 10 nm) of 500 °C annealed $\text{Y}_2\text{O}_3:\text{Bi}^{3+}$ (1 at.%).

From the curve, it is clearly observed that the emission spectrum consists of a broad band with the maximum at 495 nm (green) in the region of ~400–575 nm under the excitation at 315–325 nm. However, with the further increase in the excitation wavelength from 330 nm to 360 nm, the presence of an additional broad peak at ~410 nm (blue) is observed along with the previous emission peak. When the excitation wavelength is further increased beyond 360 nm, the above convoluted emission spectrum of two peaks transforms to one peak at ~410 (~387–460 nm region). The similar behaviour is observed in the 900 °C annealed samples of $\text{Y}_2\text{O}_3:\text{Bi}^{3+}$ (1 at.%). This is shown in Fig. 4.7. Thus, we can conclude that the emission of Bi^{3+} in Y_2O_3 consists of three characteristic components depending on the excitation wavelengths

employed: (i) characterized by green (495 nm) emission under the excitation of 315–325 nm, (ii) mixed green (495 nm) and blue (410 nm) emission when excitation is 330–360 nm and (iii) blue (410 nm) emission when excitation is 365–375 nm. These emission bands are related to $^3\text{P}_1 \rightarrow ^1\text{S}_0$ transitions of Bi^{3+} .

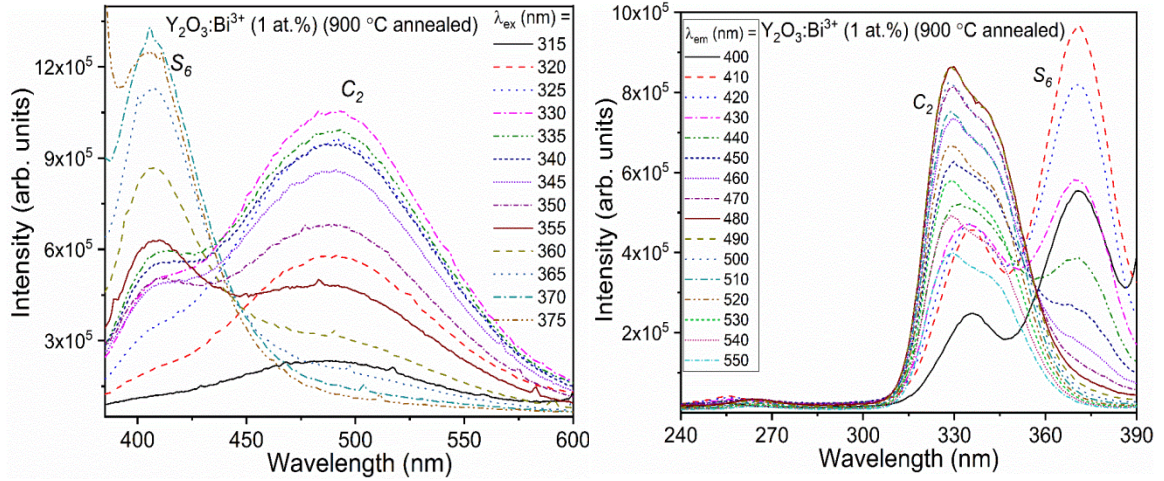


Fig. 4.7. PL (a) emission spectra at $\lambda_{\text{ex}} = 315\text{--}375$ nm (with the increment of 5 nm), and (b) excitation spectra monitored at $\lambda_{\text{em}} = 400\text{--}550$ nm (with the increment of 10 nm) of 900 °C annealed $\text{Y}_2\text{O}_3:\text{Bi}^{3+}$ (1 at.%).

To understand the above behaviour of the emission, the PL excitation spectra of the 500 °C annealed samples of $\text{Y}_2\text{O}_3:\text{Bi}^{3+}$ (1 at.%) monitored at different emission wavelengths (λ_{em}) $\sim 400\text{--}550$ nm (with the increment of 10 nm) were recorded. The spectra are displayed in Fig. 4.6(b). From the spectra, it is clearly observed that the excitation ($\sim 400\text{--}460$ nm emissions) consist of two broad peaks at ~ 338 and 371 nm. While, the further increase in the monitored emission wavelengths to $470\text{--}540$ nm results in the disappearance of 371 nm peak, but, on contrary, the region of 338 nm peak now appears as a convoluted peak of two components at ~ 330 and 343 nm. Similar behaviour is also observed in the 900 °C annealed samples (see Fig. 4.7(b)). These excitation bands are originated due to $^1\text{S}_0 \rightarrow ^3\text{P}_1$ transitions of Bi^{3+} ions. To classify these various transitions of Bi^{3+} during emission and excitation, we revisited the structure of host Y_2O_3 which exists as bcc crystal structure with space group $Ia\bar{3}$ having two non-equivalent 6 coordinated cation sites, namely: (i) highly symmetric S_6 site with inversion symmetry and (ii) non-centrosymmetric C_2 site where oxygen atoms on either side of the face diagonal are 4 (four) and 2 (two) atoms [42,44]. Thus, host Y_2O_3 offers two different cation sites i.e., S_6 and C_2 , appropriate for the activator/sensitizer (i.e., Eu^{3+} and/or Bi^{3+} in the present case). When, $\lambda_{\text{em}} = \sim 400\text{--}460$

nm is monitored, two excitation bands observed at ~338 and 371 nm are due to the splitting of $^3\text{P}_1$ excited state into doublet with respective transitions $^1\text{A}_g \rightarrow ^3\text{A}_u$ and $^1\text{A}_g \rightarrow ^3\text{E}_u$ after Bi^{3+} occupies S_6 site in Y_2O_3 crystal lattice. On the other hand, if the Bi^{3+} occupies at C_2 site in Y_2O_3 crystal lattice, the spin orbit interaction leads the $^3\text{P}_1$ excited state to split into two excitation bands at ~330 ($^1\text{A} \rightarrow ^3\text{A}$) and 343 ($^1\text{A} \rightarrow ^3\text{B}$) nm, when $\lambda_{\text{em}} = 470\text{--}540$ nm [16,43,46,52]. Thus, the emission band characterized by green (495 nm) emission under the excitation of 315–325 nm is solely related to Bi^{3+} located at the C_2 site symmetry. While, the blue (410 nm) emission observed with the excitation ~365–375 nm is related to the $^3\text{E}_u \rightarrow ^1\text{A}_g$ transition of Bi^{3+} . This emission band is originated when Bi^{3+} ions sitting in the S_6 symmetry sites of Y_2O_3 . The presence of both emission bands (mentioned above) during the excitation with 330–360 nm is perhaps due to the simultaneous absorption occurring at both symmetry sites in this wavelength region. This can be observed from the excitation spectra in both figures. This region of excitation may be of interest towards the tuning of light emission colour and generation of white light (discussed later).

4.3.4.2. PL studies of $\text{Y}_2\text{O}_3:\text{Bi}^{3+}/\text{Eu}^{3+}$

The PL excitation spectra monitored at $\lambda_{\text{em}} = 611$ nm of the 500 °C annealed Eu^{3+} (5 at.%) activated Y_2O_3 nanocrystals sensitized with various concentrations of Bi^{3+} (from hereon it will be termed as $\text{Y}_2\text{O}_3:\text{Eu}^{3+}$ (5 at.%) / Bi^{3+} (x at.%)) are shown in Fig. 4.8 (Left). The presence of a peak at 255 nm in the 230–280 nm is observed in all the spectra. This peak is originated due to the charge transfer (CT) from $2p$ orbitals of oxygen to the empty f -shells of Eu^{3+} . While, the 330, 343 (C_2 site) and 371 nm (S_6 site) excitation peaks are related to Bi^{3+} (discussed in the previous para). The observation of the Bi^{3+} related excitation peaks in the spectra associated with the Eu^{3+} emission indicates the occurrence of energy transfer from Bi^{3+} to the excited states of Eu^{3+} ions in the Y_2O_3 crystal. The identical behaviour is also observed in the 900 °C annealed samples as shown in Fig. 4.8 (Right). Interestingly, the absorption peak related to the Bi^{3+} (C_2 site) is more intense than that of Eu-O CT band. For example, nearly ~11 or 10 times enhanced Bi^{3+} absorption compared to Eu-O CT band in 1 at.% Bi^{3+} sensitized $\text{Y}_2\text{O}_3:\text{Eu}^{3+}$ (5 at.%) (insets of Fig. 4.8). This indicates enhanced energy transfer to the excited states of Eu^{3+} upon Bi^{3+} sensitization (discussed later). In addition to these broad peaks, the low intensity sharp peaks in all the spectra are also observed. These

peaks are associated with the absorptions within the f -shell of Eu^{3+} of different transitions viz, ${}^7\text{F}_0 \rightarrow {}^5\text{L}_6$ (~ 393 nm) and ${}^7\text{F}_0 \rightarrow {}^5\text{D}_2$ (~ 464 nm).

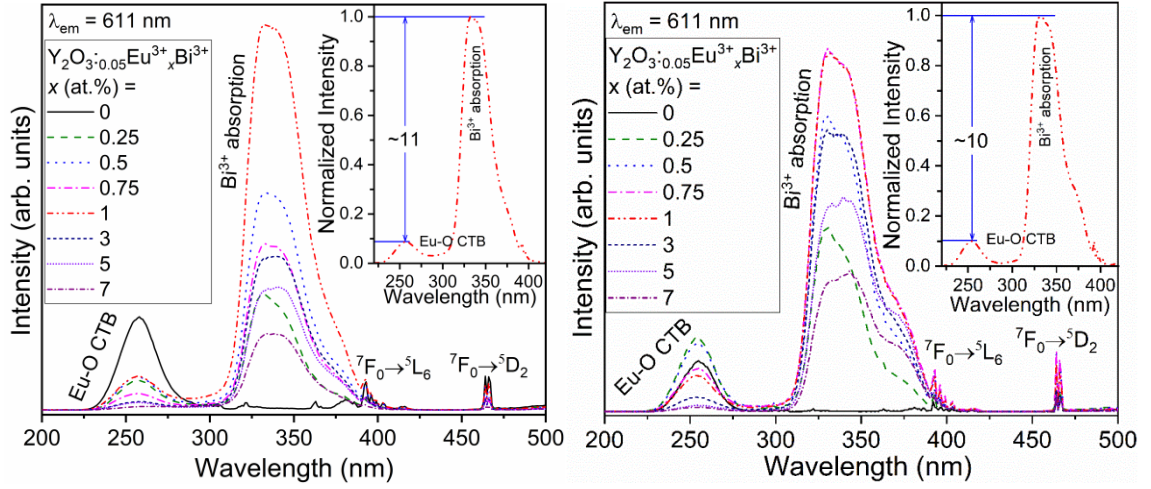


Fig. 4.8. PL excitation spectra of 500 °C (Right) and 900 °C (Left) annealed $\text{Y}_2\text{O}_3:\text{Bi}^{3+}$ ($\text{Bi}^{3+} = 0, 0.25, 0.5, 0.75, 1, 3, 5$ and 7 at.%) / Eu^{3+} (5 at.%). Emission wavelength, $\lambda_{\text{em}} = 611$ nm. (insets show the comparison of Bi^{3+} absorption with Eu-O CT band in 1 at.% Bi^{3+} sensitized $\text{Y}_2\text{O}_3:\text{Eu}^{3+}$ (5 at.%))

The PL emission spectra of the (a) 500 and (b) 900 °C annealed $\text{Y}_2\text{O}_3:\text{Eu}^{3+}$ (7 at.%) / Bi^{3+} (1 at.%) samples under different excitation wavelengths viz., 255 nm (Eu-O CT), 330 nm (Bi^{3+} , C_2 site), and 371 nm (Bi^{3+} , S_6 site) are shown in Fig. 4.9.

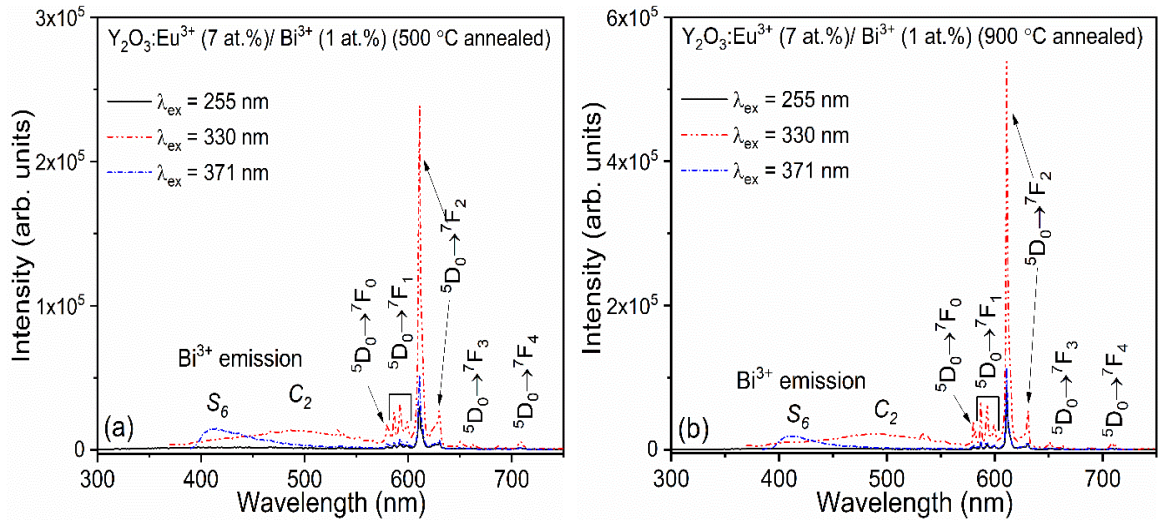


Fig. 4.9. PL emission spectra of (a) 500 and (b) 900 °C annealed $\text{Y}_2\text{O}_3:\text{Eu}^{3+}$ (7 at.%) / Bi^{3+} (1 at.%). Excitation wavelengths, $\lambda_{\text{ex}} = 255, 330$ and 371 nm.

The details of all the emission peaks present in the spectra are discussed in the next paragraph. Considering the highest emission peak at 611 nm, it is clearly observed that the emission intensity is substantially higher when the excitation is through the Bi^{3+}

related absorptions i.e., 330 and 371 nm, particularly at 330 nm. This signifies the enhanced luminescence of Eu^{3+} by sensitization through the energy transfer. From here on, all the remaining studies will be discussed for the 330 and/or 371 nm excitations.

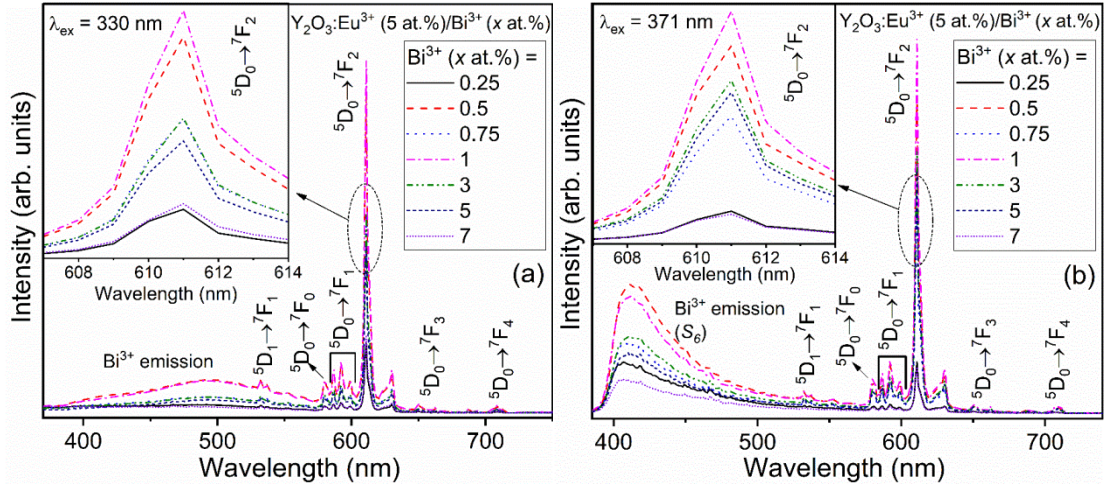


Fig. 4.10 PL emission spectra of 500 °C annealed samples of $\text{Y}_2\text{O}_3:\text{Eu}^{3+}$ (5 at.%)/ Bi^{3+} (x at.% = 0.25, 0.5, 0.75, 1, 3, 5, 7) under the excitation wavelengths of (a) 330 and (b) 371 nm.

The PL emission spectra of the 500 °C annealed samples of $\text{Y}_2\text{O}_3:\text{Eu}^{3+}$ (5 at.%)/ Bi^{3+} (x at.% = 0.25, 0.5, 0.75, 1, 3, 5, 7) are displayed in Fig. 4.10. The excitation wavelengths were 330 and 371 nm. All the spectra shown in the Fig. 4.10(a) consist of two broad emission bands centred at ~410 and ~495 nm. On the other hand, the presence of a broad emission band centred at ~410 nm is observed in Fig. 4.10(b). These peaks are related to the radiative emission from Bi^{3+} following the transition from excited state $^3\text{P}_1$ to the ground state $^1\text{S}_0$. These two peaks are due to Bi^{3+} occupying the two different symmetry sites i.e., S_6 and C_2 , respectively, of Y_2O_3 (as discussed above). While the sharp emission peaks observed in both the figures are originated from the transitions within the f -shell of Eu^{3+} [6, 16, 25, 30, 33-35]. The emission peaks at 532 and 537 nm are related to $^5\text{D}_1 \rightarrow ^7\text{F}_1$; 587, 592 and 599 nm are associated with $^5\text{D}_0 \rightarrow ^7\text{F}_1$ while 650 nm is from $^5\text{D}_0 \rightarrow ^7\text{F}_3$. These transitions are due to magnetic dipole transitions. The emission peak at 581 nm is originated from $^5\text{D}_0 \rightarrow ^7\text{F}_0$ which is considered to be electric dipole character (discussed later). On the other hand, the emission peaks at 611 nm (highest among all the Eu^{3+} related peaks) and 630 nm are from $^5\text{D}_0 \rightarrow ^7\text{F}_2$. These transitions are due to the forced electric dipole transition. While the emission at 709 nm, is because of electric quadrupole transitions ($^5\text{D}_0 \rightarrow ^7\text{F}_4$). Among all the transitions, the highest electric dipole transition, which is forced in nature and sensitive to the local environmental symmetry around the Eu^{3+} , can be

understood from the viewpoint of site symmetry of the Y_2O_3 host (as mentioned above). In cubic Y_2O_3 , the non-centrosymmetric Y^{3+} sites having C_2 symmetry contributes about 75% lattice, and remaining 25% are centrosymmetric, S_6 sites [53]. Thus, the strongest emission intensity among all transitions is expected from ${}^5\text{D}_0 \rightarrow {}^7\text{F}_2$. With this consideration, the intensity of 611 nm (${}^5\text{D}_0 \rightarrow {}^7\text{F}_2$) is compared for various concentration of Bi^{3+} , and the maximum emission intensity is observed when the sample is sensitized with 1 at.% Bi^{3+} . However, the intensity decreased with the increase of Bi^{3+} beyond 1 at.%. This is because of the increase in the non-radiative transitions within Bi^{3+} due to the clustering of Bi^{3+} ions at high concentrations. Similar trend is also observed in the 900 °C annealed samples (not shown here). Such behaviour was earlier reported by us in the Bi^{3+} sensitized $\text{CaMoO}_4:\text{Eu}^{3+}$ phosphors [20]. From here on, remaining investigations are discussed with the fixed amount of 1 at.% Bi^{3+} with varied Eu^{3+} concentrations.

The abovementioned emission peak at 581 nm is associated with ${}^5\text{D}_0 \rightarrow {}^7\text{F}_0$ and it is strictly forbidden for free Eu^{3+} . However, its presence was observed in many hosts such as $\text{Y}_2\text{O}_3:\text{Eu}^{3+}$, $\text{YPO}_4:\text{Li}^+/\text{Eu}^{3+}$, BaFCl , $\text{Y}_2\text{O}_2\text{S}$ crystals and $\text{Ca}(\text{PO}_3)_2$ glass as well [53-57]. It is also widely reported that the observation of this peak could not be explained by Judd and Ofelt theory which is based on closure approximation of mixing higher lying odd parity state with $4f$ states. As proposed by G. Nishimura and T. Kushida, the most probable mechanism is due to J -mixing with the dominant contribution from mixing of ${}^7\text{F}_0$ and ${}^7\text{F}_2$ in comparison with other higher lying f -manifolds in the ground state [57]. They also ruled out the mixing with high lying odd parity states due to large energy gap. Ray *et al.* and Ningthoujam *et al.*, also extended the role of J -mixing effect of ${}^7\text{F}_0$ and ${}^7\text{F}_2$ ground states in $\text{Y}_2\text{O}_3:\text{Eu}^{3+}$ and Li^+ sensitized $\text{YPO}_4:\text{Eu}^{3+}$ nanocrystals respectively with the consideration of second order crystal field parameter in the local crystal field potential [53,54]. Similarly, the second order crystal parameter was calculated using [53]

$$\frac{I_{0 \rightarrow 0}}{I_{0 \rightarrow 2}} = \frac{4B_{20}^2}{75\Delta_{20}^2} \quad (4.1)$$

where, B_{20} is the second order crystal field parameter, and Δ_{20} is the energy separation between ${}^7\text{F}_0$ and ${}^7\text{F}_2$ which value was taken as 900 cm^{-1} . The B_{20} values versus Eu^{3+} concentrations in the 500 and 900 °C annealed samples under the excitation of 330 and 371 nm are represented in Fig. 4.11. Similar trend of the B_{20} values was observed in the

previous report. However, the values obtained in the present study are higher than reported [53]. The B_{20} values vary from 1011 to 1927 cm^{-1} and 1137 to 1990 cm^{-1} under the respective excitations of 330 and 371 nm for the 500 °C annealed samples. While, for the 900 °C annealed samples, the B_{20} values vary from 798 to 1745 cm^{-1} and 826 to 1726 cm^{-1} under the 330 and 371 nm excitations, respectively. Such higher values of B_{20} may be indicative of higher perturbation crystal field around the Eu^{3+} environment due to the Bi^{3+} sensitization [54].

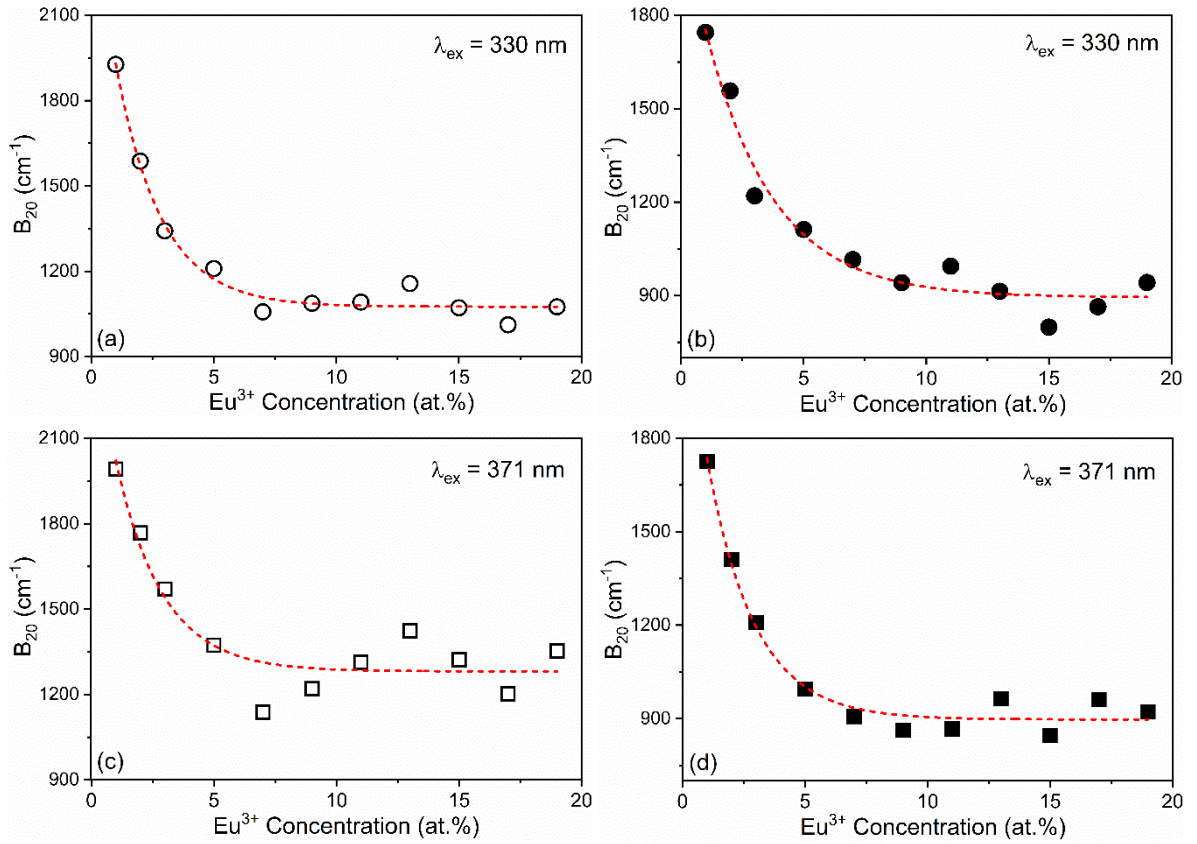


Fig. 4.11. Variation of B_{20} versus Eu^{3+} concentration of (a & c) 500 and (b & d) 900 °C annealed $\text{Y}_2\text{O}_3:\text{Eu}^{3+}$ (x at.% = 1, 2, 3, 5, 7, 9, 11, 13, 15, 17, 19)/ Bi^{3+} (1 at.%) samples. Excitation wavelengths (λ_{ex}) are indicated in the graph. Dash (red) line is the guide to the eye.

4.3.4.3. Mechanism of energy transfer: Bi^{3+} to Eu^{3+}

The energy transfer from the donor/sensitizer to the acceptor (Bi^{3+} and Eu^{3+} respectively, in the present case) occurs understandably as there is a spectral overlap of the Bi^{3+} emissions (S_6 and C_2) with the absorption bands of Eu^{3+} (See Fig. 4.12). The occurrence of such energy transfer is commonly called as resonance type of energy transfer. To investigate the mechanism of the energy transfer from the Bi^{3+} to the

excited states of Eu^{3+} and its efficiency, we considered the emissions at different concentrations of Eu^{3+} ($x \text{ at.}\% = 0, 1, 2, 3, 5, 7, 9, 11, 13, 15, 17, 19$) with the fixed amount of Bi^{3+} (1 at.%) under the excitation of two Bi^{3+} related absorptions i.e. 330 and 371 nm.

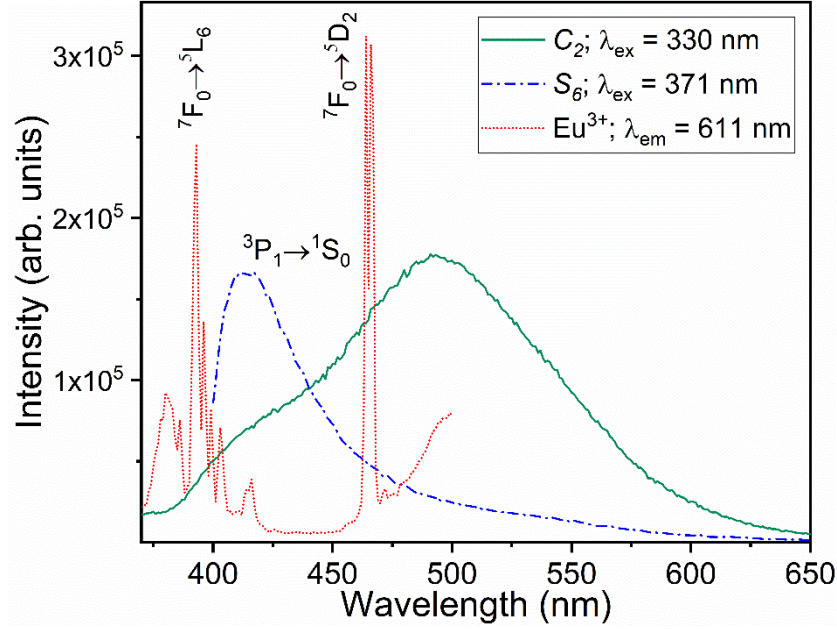


Fig. 4.12. Spectral overlap between the excitation spectrum of Eu^{3+} ions and emission spectrum of Bi^{3+} ions in Y_2O_3 .

In Fig. 4.13, the normalized (normalized at 611 nm) emission spectra are shown for the (a) 500 and (b) 900 °C annealed samples of $\text{Y}_2\text{O}_3:\text{Eu}^{3+}$ ($x \text{ at.}\% = 0, 1, 2, 3, 5, 7, 9, 11, 13, 15, 17, 19$)/ Bi^{3+} (1 at.%) excited at 330 nm. From the spectra, it is clearly observed that the emission related to the Bi^{3+} gradually decreases with the increase of Eu^{3+} concentration in both the cases. The intensity of Bi^{3+} emission almost reduces to baseline when the concentration of Eu^{3+} reaches maximum. Similarly, the normalized (normalized at 611 nm) emission spectra of the (a) 500 and (b) 900 °C annealed nanocrystals of $\text{Y}_2\text{O}_3:\text{Eu}^{3+}$ ($x \text{ at.}\% = 0, 1, 2, 3, 5, 7, 9, 11, 13, 15, 17, 19$)/ Bi^{3+} (1 at.%) excited with 371 nm are displayed in Fig. 4.14. However, the extent of the reduction in the Bi^{3+} emission intensity is slightly less compared to earlier case i.e., 330 nm excitation. This may be an indication of lesser efficient energy transfer, if the excitation is at 371 nm (S_6 site symmetry) when compared to that obtained at the 330 nm (C_2 site symmetry) excitation. Overall, such behaviour of decrease in the Bi^{3+} emission intensity with the increase of Eu^{3+} observed in both the cases mentioned above clearly ascertains the qualitative nature of increase in the energy transfer from the Bi^{3+} to the

randomly distributed Eu^{3+} ions in the host crystal. To corroborate this claim, the luminescence decay dynamics of Bi^{3+} against the increase of Eu^{3+} ions was investigated.

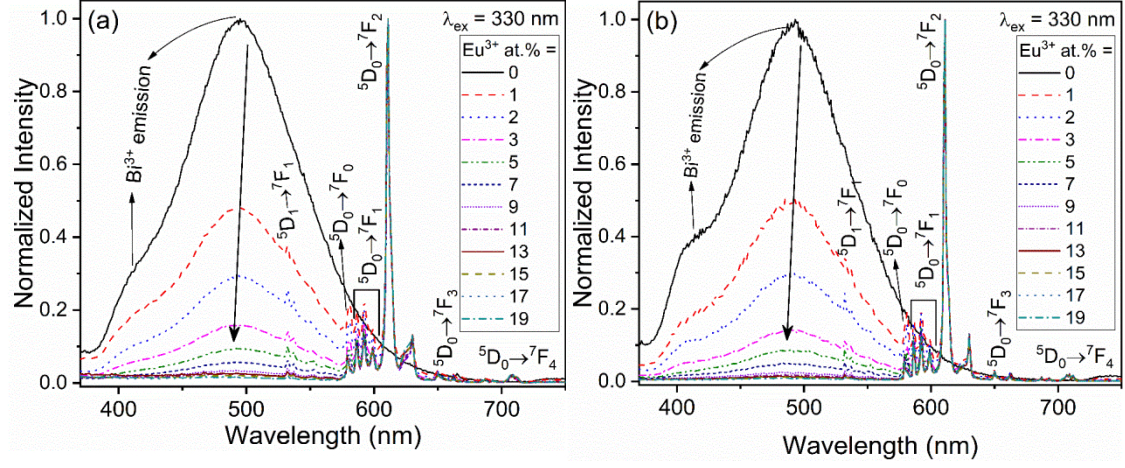


Fig. 4.13. Normalized PL (normalized at 611 nm) emission spectra of (a) 500 and (b) 900 °C annealed samples of $\text{Y}_2\text{O}_3:\text{Eu}^{3+}$ (x at.% = 0, 1, 2, 3, 5, 7, 9, 11, 13, 15, 17, 19)/ Bi^{3+} (1 at.%) under the excitation wavelengths of 330 nm.

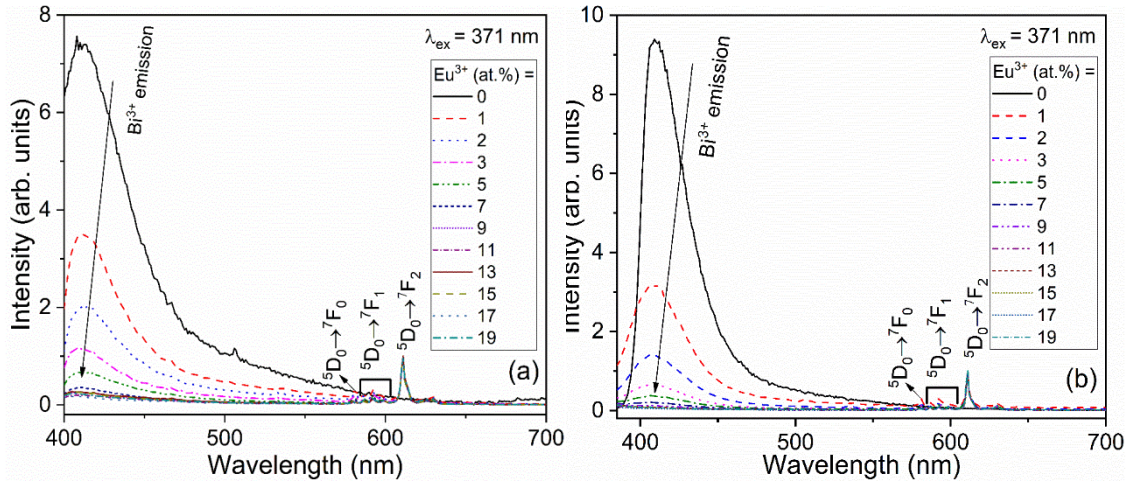


Fig. 4.14. Normalized PL (normalized at 611 nm) emission spectra of (a) 500 and (b) 900 °C annealed samples of $\text{Y}_2\text{O}_3:\text{Eu}^{3+}$ (x at.% = 0, 1, 2, 3, 5, 7, 9, 11, 13, 15, 17, 19)/ Bi^{3+} (1 at.%) under the excitation wavelengths of 371 nm.

To elucidate the efficiency of energy transfer (η) from the sensitizer Bi^{3+} to activator Eu^{3+} , the following relation was used [30,58]:

$$\eta = 1 - \frac{I_s}{I_{s0}} \quad (4.2)$$

where, η is the energy transfer efficiency, I_s and I_{s_0} are the emission intensities of the sensitizer (Bi^{3+}) in the presence and absence of activator (Eu^{3+}), respectively. The energy transfer efficiencies from Bi^{3+} to Eu^{3+} at various concentrations in the 500 and 900 °C annealed samples are shown in Fig 4.15. The excitation wavelengths are 330 and 371 nm. The energy transfer efficiencies of the 500 and 900 °C annealed samples reach up to 97 and 99%, respectively, when the excitation was at 330 nm (Figs. 4.15 (a) and (b)). Under the excitation of 371 nm, the respective energy transfer efficiency reaches up to 85 and 93% (Figs. 4.15 (c) and (d)). The lesser extent of energy transfer when the excitation wavelength was 371 nm may be understood from the lesser resonance of the S_6 related emission with the $f-f$ absorption bands of Eu^{3+} (See Fig. 4.12). Overall, we could see an improvement in the efficiency (η) with increase in heat treatment. This might be due to better crystallization of particles with the increase in heat treatment as well as reduction of quenching centres [45,47,48].

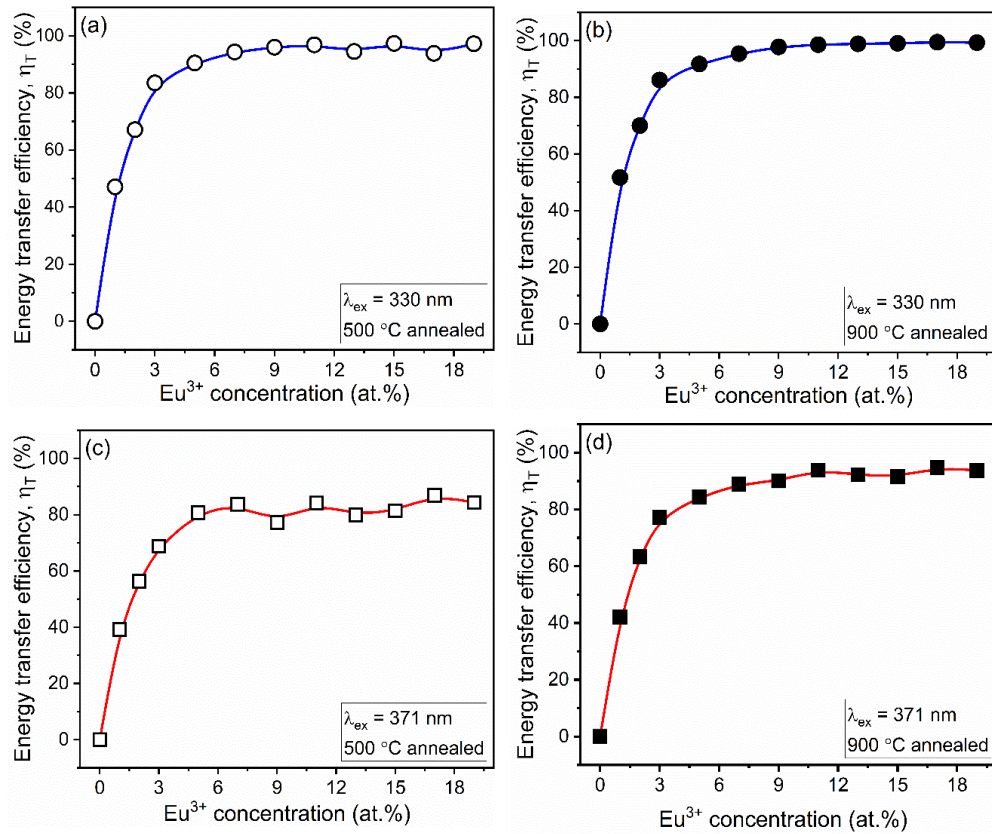


Fig. 4.15. Energy transfer efficiency (η_T) of different concentration of Eu^{3+} (x at.% = 0, 1, 2, 3, 5, 7, 9, 11, 13, 15, 17, 19) in Bi^{3+} (1 at.%) sensitized Y_2O_3 annealed samples. Descriptions are given in the legend.

It is accepted that the mechanisms of resonance type of energy transfer are commonly of two kinds: (i) exchange interactions and (ii) multipolar interactions. Both

the mechanisms are dependent on the distance between the donor and acceptors. So, the critical distance between the donor and acceptor can be calculated using the following relation [46,59],

$$R_c = 2 \left[\frac{3V}{4\pi x_c N} \right]^{1/3} \quad (4.3)$$

where, R_c represents the critical distance, V denotes the volume of the unit cell, x_c is the critical concentration and N is the number of host cation sites (both S_6 and C_2 sites) in the unit cell. Here, the value of $N = 32$. In this case, Y_2O_3 host has the unit cell volume equal to 1229 and 1195 \AA^3 , respectively, for the 500 and 900 $^\circ\text{C}$ annealed samples. The x_c values are 0.08 and 0.18 at.% for the 500 and 900 $^\circ\text{C}$ annealed samples, respectively. The calculated values of R_c are 10 and 7 \AA respectively. These values are greater than the restricted distance (i.e. $\sim 5 \text{\AA}$) of exchange interaction. This suggests that the energy transfer mechanism between Bi^{3+} and Eu^{3+} ions in Y_2O_3 is mainly through multipolar interactions. According to the Dexter's resonance energy transfer through multipolar interactions are of 3 (three) types: dipole-dipole, dipole-quadrupole or quadrupole-quadrupole interactions. Ignoring the much weaker quadrupole-quadrupole interactions, the probability (P_{dd}) per second of energy transfer from sensitizer to the activator through dipole-dipole interaction is given by [60,61]:

$$P_{dd}(R) = \frac{3c^4 \hbar^4 \sigma_A}{4\pi n^4 \tau_D R^6} \int \frac{f_D(E) F_A(E)}{E^4} dE \quad (4.4)$$

where, R is distance between D (sensitizer) and A (activator), n is the refractive index of the host matrix, σ_A is the absorption cross section of A , and τ_D is the radiative lifetime of D . And, energy transfer probability (P_{dq}) through dipole-quadrupole (P_{dq}) is:

$$P_{dq}(R) = \frac{135\pi \alpha c^8 \hbar^9}{4n^6 \tau_D \tau_A R^8} \int \frac{f_D(E) F_A(E)}{E^8} dE \quad (4.5)$$

The integrals in Eqns. (6) and (7) represent the spectral overlap of normalized sensitizer (D) emission (Bi^{3+} in the present case) and activator (A) absorption (Eu^{3+} in the present case), $\alpha = 1.266$, and τ_A is the radiative lifetime of A . Other constants have usual meanings. Such multipolar interactions of Dexter's theory of resonance energy transfer can further be expressed on the basis with Reisfeld's approximation [58,62,63],

$$\frac{I_{s0}}{I_s} \propto C_{\text{Bi}^{3+}+\text{Eu}^{3+}}^{n/3} \quad (4.6)$$

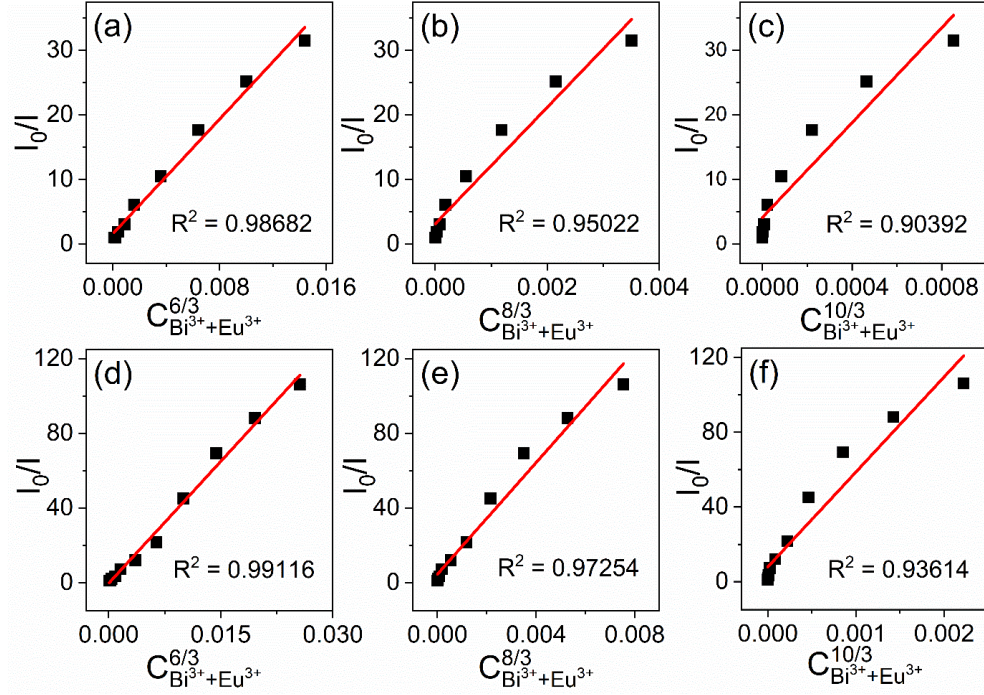


Fig. 4.16. Dependence of I_{S_0}/I_S of Bi^{3+} on (a) $C_{\text{Bi}^{3+}+\text{Eu}^{3+}}^{6/3}$, (b) $C_{\text{Bi}^{3+}+\text{Eu}^{3+}}^{8/3}$, (c) $C_{\text{Bi}^{3+}+\text{Eu}^{3+}}^{10/3}$ (annealed at 500 °C) and (d) $C_{\text{Bi}^{3+}+\text{Eu}^{3+}}^{6/3}$, (e) $C_{\text{Bi}^{3+}+\text{Eu}^{3+}}^{8/3}$, (f) $C_{\text{Bi}^{3+}+\text{Eu}^{3+}}^{10/3}$ (annealed at 900 °C). Excitation wavelength for both cases is 330 nm.

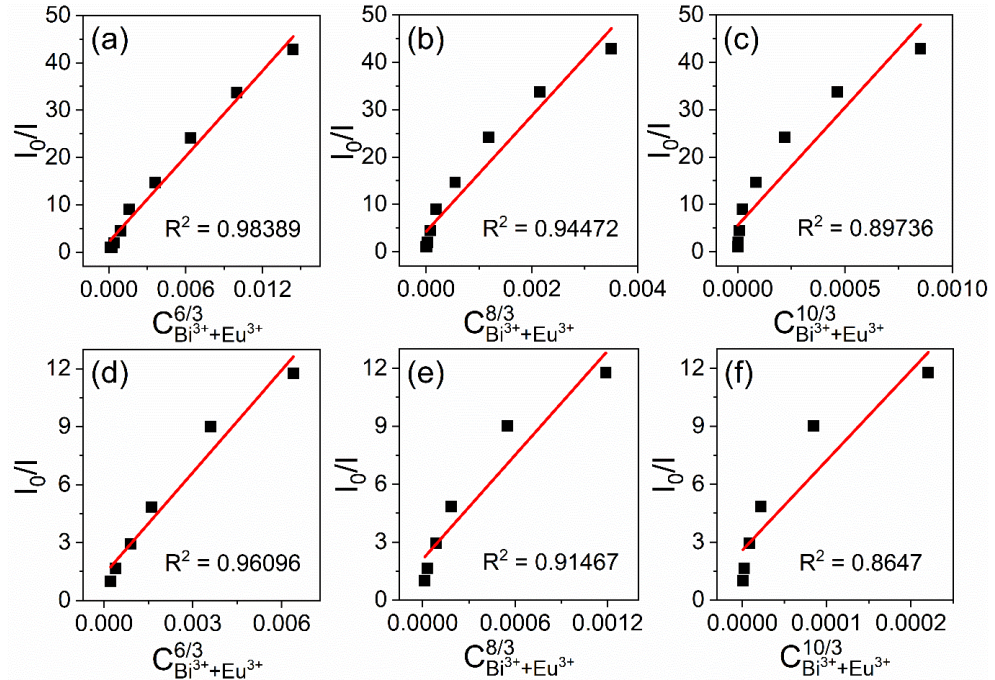


Fig. 4.17. Dependence of I_{S_0}/I_S of Bi^{3+} on (a) $C_{\text{Bi}^{3+}+\text{Eu}^{3+}}^{6/3}$, (b) $C_{\text{Bi}^{3+}+\text{Eu}^{3+}}^{8/3}$, (c) $C_{\text{Bi}^{3+}+\text{Eu}^{3+}}^{10/3}$ (annealed at 500 °C) and (d) $C_{\text{Bi}^{3+}+\text{Eu}^{3+}}^{6/3}$, (e) $C_{\text{Bi}^{3+}+\text{Eu}^{3+}}^{8/3}$, (f) $C_{\text{Bi}^{3+}+\text{Eu}^{3+}}^{10/3}$ (annealed at 900 °C). Excitation wavelength for both cases is 371 nm.

where, C denotes the total concentration of Bi^{3+} and Eu^{3+} ions in the sample. The corresponding interaction is of dipole-dipole, dipole-quadrupole or quadrupole-quadrupole type when the values of ' n ' are 6, 8 or 10, respectively. From the linear fit of the plot using the equation (8), the best fit is observed at $n = 6$. This indicates that the majority of the energy transfer occurs through the dipole-dipole interactions in all the cases. The fitting curves obtained using all the 3 (three) values of ' n ' for the 500 and 900 °C annealed samples under the 330 and 371 nm excitations are shown in Fig. 4.16 and 4.17, respectively.

4.3.4.4. PL decay lifetime and quantum yield study

In order to reveal more information on the energy transfer, we have investigated the luminescence dynamics of Bi^{3+} in $\text{Y}_2\text{O}_3:\text{Eu}^{3+}$ (x at.%) / Bi^{3+} (1 at.%) by measuring the luminescence decay of Bi^{3+} emission related to C_2 sites. The decay curves of Bi^{3+} emission related to S_6 were not measured because the needed exciting source is unavailable. The decay curves of Bi^{3+} emission as a function of Eu^{3+} concentration in the 500 and 900 °C annealed $\text{Y}_2\text{O}_3:\text{Eu}^{3+}$ (x at.%) / Bi^{3+} (1 at.%) with the emission monitored at 495 nm are shown in Fig. 4.18. The samples were excited with pulse LED (340 ± 10 nm) source (pulse width < 1.2 ns). The decay curves are well fitted with the second order decay exponential function [54,64,65]:

$$I(t) = I_1 e^{-\frac{t}{\tau_1}} + I_2 e^{-\frac{t}{\tau_2}} \quad (4.7)$$

where, I_1 and I_2 are the intensities at different times. The τ_1 and τ_2 are the corresponding lifetimes. The average decay lifetime can be calculated using the equation [54,64,65]:

$$\tau_{av} = \frac{I_1 \tau_1^2 + I_2 \tau_2^2}{I_1 \tau_1 + I_2 \tau_2} \quad (4.8)$$

The similar behaviour of decay profiles were also observed for Bi^{3+} decay in $\text{Bi}^{3+}/\text{Mn}^{4+}$ codoped $\text{Ba}_2\text{GdNbO}_6$ as well as Ce^{3+} decay in $\text{Ca}_{1.59}\text{Sr}_{0.35-x}\text{SiO}_4:0.03\text{Ce}^{3+}, 0.03\text{Li}^+, x\text{Eu}^{2+}$ [64,65]. From the curves, it is clearly observed that the decay lifetime of Bi^{3+} decreases continuously with the increase of Eu^{3+} concentration (inset of Fig. 4.18). The decay time decreases from 443 to 75 ns in the 500 °C annealed samples with the increase of Eu^{3+} concentration. Comparatively, in the 900 °C annealed samples, the decrease in decay lifetime is from 554 to 81 ns. This decrease in decay lifetime can be attributed to the increase in the probability of non-radiative energy transfer from Bi^{3+} to the excited

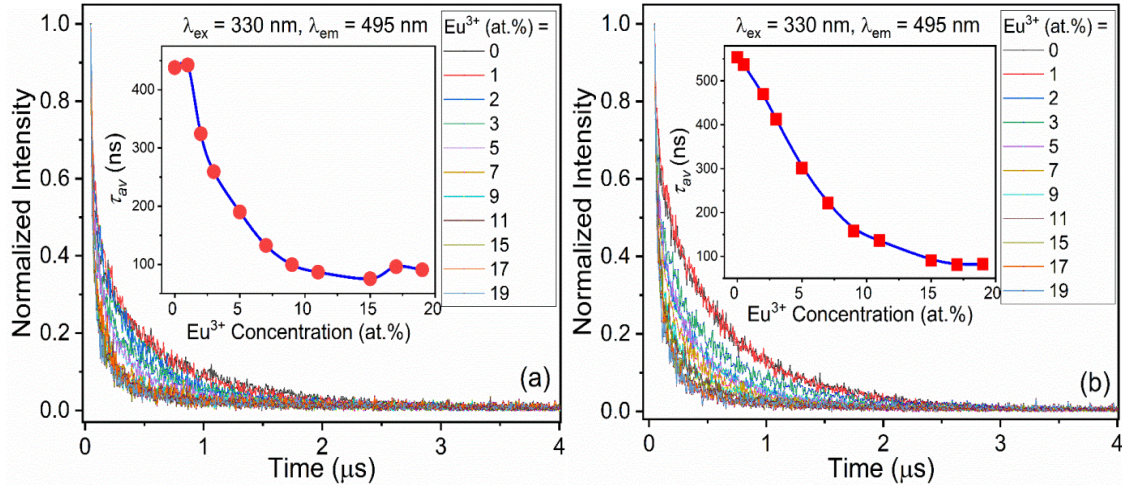


Fig. 4.18. PL Decay lifetime curves of Bi^{3+} ($\lambda_{\text{em}} = 495 \text{ nm}$ and $\lambda_{\text{ex}} = 330 \text{ nm}$) of (a) 500 and (b) 900 °C annealed $\text{Y}_2\text{O}_3:\text{Eu}^{3+}$ ($x \text{ at.}\%$)/ Bi^{3+} (1 at.%) samples. Inset shows the PL decay time, τ_{av} (ns) against the Eu^{3+} concentration.

states of Eu^{3+} . This also can be understood from the Eqn. (4.5), where the probability of energy transfer through dipole-dipole interactions is inversely proportional to the lifetime of sensitizer. This clearly corroborates with the results obtained in the steady state luminescence studies (discussed in the previous section). The calculated fit parameters and decay lifetimes are presented in Table 4.2.

Table 4.2. Decay lifetime (τ_{av}) values of Bi^{3+} in $\text{Y}_2\text{O}_3:\text{Eu}^{3+}$ ($x \text{ at.}\%$)/ Bi^{3+} (1 at.%) samples annealed at 500 °C and 900 °C. Excitation wavelength, $\lambda_{\text{ex}} = 330 \text{ nm}$ and emission wavelength, $\lambda_{\text{em}} = 495 \text{ nm}$.

Eu^{3+} (at.%)	500 °C		900 °C	
	τ_{av} (ns)	R^2	τ_{av} (ns)	R^2
0	438	0.99	554	0.99
1	443	0.99	537	0.99
2	325	0.99	470	0.99
3	260	0.98	413	0.99
5	190	0.98	302	0.99
7	133	0.97	222	0.99
9	99	0.97	158	0.99
11	87	0.98	136	0.98
15	75	0.98	91	0.98
17	96	0.98	81	0.99
19	91	0.98	82	0.98

The luminescence decay curves of $^5\text{D}_0$ level of Eu^{3+} in $\text{Y}_2\text{O}_3:\text{Eu}^{3+}$ (x at.%) / Bi^{3+} (1 at.%) of the 500 and 900 °C annealed samples are displayed in Fig. 4.19. The emission decay from $^5\text{D}_0$ level was monitored at 611 nm, and excitation wavelengths were 330 and 371 nm. All the decay curves follow the exponential decay equation (Eqn. 4.7). The average decay lifetime calculated using the Eqn. (4.8) are presented in Tables 4.3 and 4.4. The decay lifetime of Eu^{3+} increases up to 1.49 and 1.9 ms, respectively, for the 500 and 900 °C annealed samples with 9 at.% Eu^{3+} under the 330 nm excitation and, thereafter, it decreases with further increase in concentration. While, under the 371 nm excitation, the decay lifetime of Eu^{3+} increases up to 1.38 and 2 ms respectively for the 500 and 900 °C annealed with 9 at.% Eu^{3+} and then decreases as the concentration is beyond 9 at.%.

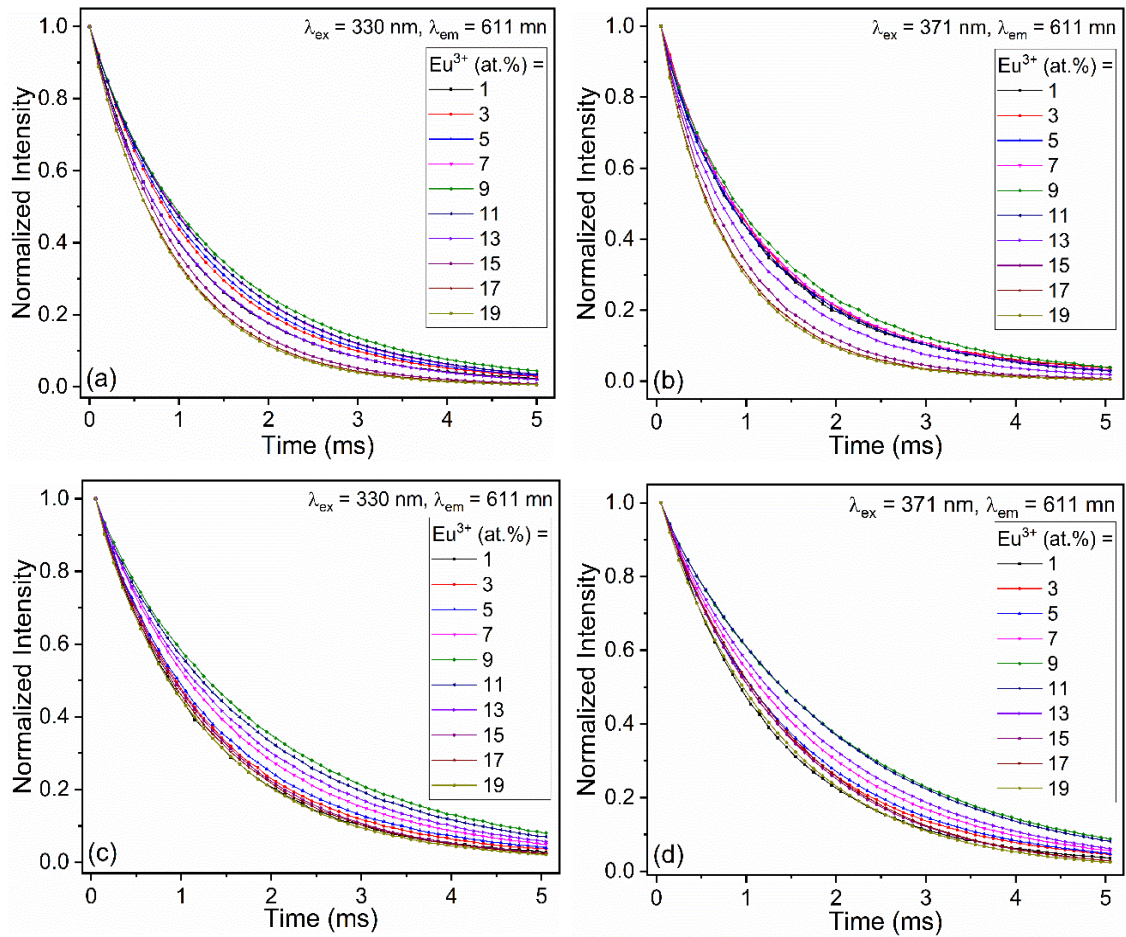


Fig. 4.19. PL Decay lifetime curves of $^5\text{D}_0$ level of Eu^{3+} of (a & b) 500 and (c & d) 900 °C annealed $\text{Y}_2\text{O}_3:\text{Eu}^{3+}$ (x at.%) / Bi^{3+} (1 at.%) samples. Excitation wavelengths: (a & c) 330 and (b & d) 371 nm.

Such behaviour in the decrease in decay lifetime with increasing concentration after certain amount is common among the lanthanides due to cross relaxation quenching effect. The quantum yield measurements were performed using the integrating sphere

Table 4.3. Decay lifetime (τ_{av}) values of $^5\text{D}_0$ level of Eu^{3+} in $\text{Y}_2\text{O}_3:\text{Eu}^{3+}$ (x at.%) / Bi^{3+} (1 at.%) samples annealed at 500 °C and 900 °C. Excitation wavelength, $\lambda_{ex} = 330$ nm and emission wavelength, $\lambda_{em} = 611$ nm.

Eu^{3+} (at.%)	500 °C		900 °C	
	τ_{av} (ms)	R^2	τ_{av} (ms)	R^2
1	1.16	0.99	1.31	0.99
3	1.27	0.99	1.48	0.99
5	1.24	0.99	1.62	0.99
7	1.30	0.99	1.84	0.99
9	1.38	0.99	2.00	0.99
11	1.27	0.99	1.99	0.99
13	1.12	0.99	1.76	0.99
15	0.92	0.99	1.42	0.99
17	0.86	0.99	1.46	0.99
19	0.84	0.99	1.35	0.99

Table 4.4. Decay lifetime (τ_{av}) values of $^5\text{D}_0$ level of Eu^{3+} in $\text{Y}_2\text{O}_3:\text{Eu}^{3+}$ (x at.%) / Bi^{3+} (1 at.%) samples annealed at 500 °C and 900 °C. Excitation wavelength, $\lambda_{ex} = 371$ nm and emission wavelength, $\lambda_{em} = 611$ nm.

x (at.%)	500 °C		900 °C	
	τ_{av} (ms)	R^2	τ_{av} (ms)	R^2
1	1.18	0.99	1.25	0.99
3	1.31	0.99	1.33	0.99
5	1.32	0.99	1.41	0.99
7	1.36	0.99	1.53	0.99
9	1.49	0.99	1.90	0.99
11	1.39	0.99	1.79	0.99
13	1.18	0.99	1.66	0.99
15	1.01	0.99	1.32	0.99
17	0.94	0.99	1.30	0.99
19	0.92	0.99	1.25	0.99

(details of the measurement can be found elsewhere [30]) and details are given in Table 4.5. The highest quantum yield is found to be 24% in the 900 °C annealed $\text{Y}_2\text{O}_3:\text{Eu}^{3+}$ (2 at.%) / Bi^{3+} (1 at.%). Again, when we carefully observe the decay lifetime and quantum yield of each sample under different heating conditions, clear increase in these values is observed. This may be understood due to the reduction in quenching centres as well as

improved crystallization with increase annealing temperature thereby decreasing the non-radiative transition probabilities [50,52,53].

Table 4.5. Quantum yields of $\text{Y}_2\text{O}_3:\text{Eu}^{3+}$ (x at.%) / Bi^{3+} (1 at.%) samples annealed at 500 °C and 900 °C. Excitation wavelength, $\lambda_{\text{ex}} = 330$ nm.

Eu^{3+} (at.%)	ϕ (%)	
	500 °C	900 °C
1	4	17
2	3	24
3	5	17
5	3	19
7	6	18
9	4	16
11	3	14
13	3	16
15	4	19
17	3	18
19	4	13

4.3.4.5. CIE chromaticity studies

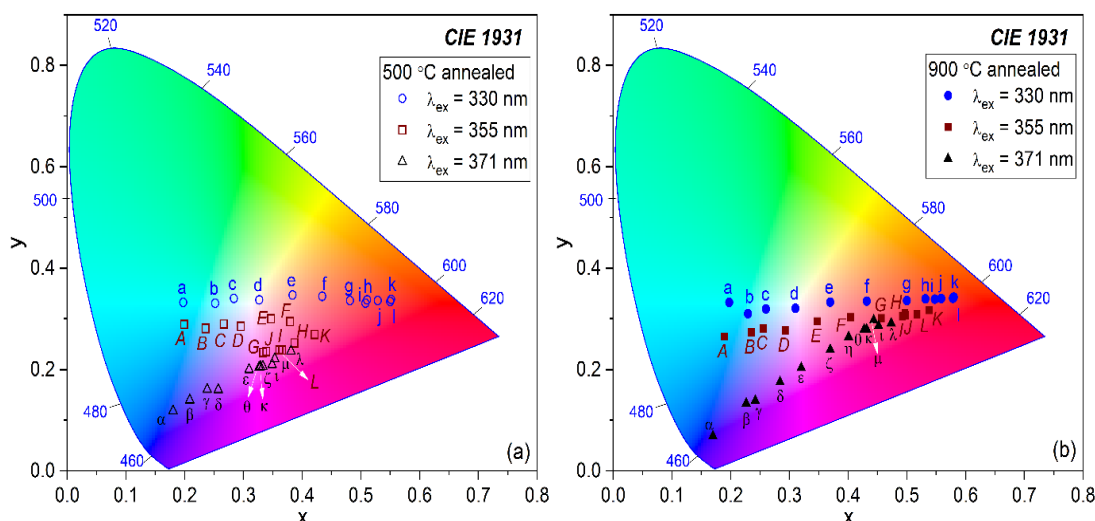


Fig.4.20. CIE chromaticity coordinate positions of $\text{Y}_2\text{O}_3:\text{Eu}^{3+}$ (x at.%) / Bi^{3+} (1 at.%) for (a) 500 and (b) 900 °C annealed samples excited at 330, 355 and 371 nm respectively (CIE Coordinates, See Table 4.6).

For better prediction of the trueness in the colour of the light output by the samples, the Commission International de l'Eclairage (CIE) chromaticity diagram was employed. The CIE coordinates and positions in the CIE diagram of the 500 and 900 °C annealed

$\text{Y}_2\text{O}_3:\text{Eu}^{3+}$ (x at.%) / Bi^{3+} (1 at.%) samples under the 330, 355 and 371 nm excitation are presented in Fig. 4.20 and Table 4.6.

Table 4.6. CIE coordinates of 500 °C and 900 °C annealed $\text{Y}_2\text{O}_3:\text{Eu}^{3+}$ (x at.%) / Bi^{3+} (1 at.%) under the different excitation wavelengths (λ_{ex}) i.e. 330 nm (C_2), 355 nm and 371 nm (S_6) respectively. Positions in the CIE diagram under 330, 355 and 371 (See Fig. 4.20).

x at. %	500 °C			900 °C		
	330	355	371	330	355	371
0	a (0.20,0.33)	A (0.20,0.29)	α (0.18,0.12)	a (0.20,0.33)	A (0.19,0.26)	α (0.17,0.07)
1	b (0.25,0.33)	B (0.24,0.28)	β (0.21,0.14)	b (0.23,0.31)	B (0.24,0.27)	β (0.23,0.13)
2	c (0.28,0.34)	C (0.27,0.29)	γ (0.24,0.16)	c (0.26,0.32)	C (0.26,0.28)	γ (0.24,0.14)
3	d (0.33,0.34)	D (0.30,0.29)	δ (0.26,0.16)	d (0.31,0.32)	D (0.29,0.28)	δ (0.28,0.18)
5	e (0.38,0.35)	E (0.35,0.30)	ϵ (0.31,0.20)	e (0.37,0.33)	E (0.35,0.29)	ϵ (0.32,0.20)
7	f (0.43,0.34)	F (0.38,0.29)	ζ (0.33,0.21)	f (0.43,0.34)	F (0.40,0.30)	ζ (0.37,0.24)
9	g (0.48,0.34)	G (0.33,0.23)	-	g (0.50,0.34)	G (0.46,0.30)	η (0.40,0.26)
11	h (0.51,0.34)	H (0.39,0.25)	ι (0.35,0.21)	h (0.53,0.34)	H (0.50,0.31)	ι (0.45,0.29)
13	i (0.51,0.33)	I (0.36,0.24)	θ (0.33,0.20)	i (0.55,0.34)	I (0.49,0.31)	θ (0.43,0.28)
15	J (0.53,0.34)	J (0.34,0.24)	κ (0.33,0.21)	j (0.56,0.34)	J (0.50,0.31)	κ (0.43,0.28)
17	K (0.55,0.34)	K (0.42,0.27)	λ (0.38,0.24)	k (0.58,0.34)	K (0.54,0.32)	λ (0.47,0.29)
19	L (0.55,0.33)	L (0.37,0.24)	μ (0.35,0.22)	l (0.58,0.34)	L (0.52,0.31)	μ (0.44,0.30)

Under the 330 nm excitation, the colour of the emission light output varies from bluish green to red which passes through white region with the increase of Eu^{3+} concentration. At a particular composition, i.e. $\text{Y}_2\text{O}_3:\text{Eu}^{3+}$ (3 at.%) / Bi^{3+} (1 at.%), the CIE coordinates fall in the white area (See Fig. 4.20). While, the emission colour varies from bluish to red when excited at 355 nm. On the other hand, the colour variation is from blue to red under the 371 nm excitation. In order to verify the various colour of emission, the photographs of the light emission from the samples under the direct exposure of light are illustrated in Fig. 4.21. Under different excitation wavelengths, we also have observed the different colour emission. For this, we have taken a particular concentration sample i.e. $\text{Y}_2\text{O}_3:\text{Eu}^{3+}$ (3 at.%) / Bi^{3+} (1 at.%). The related coordinates and

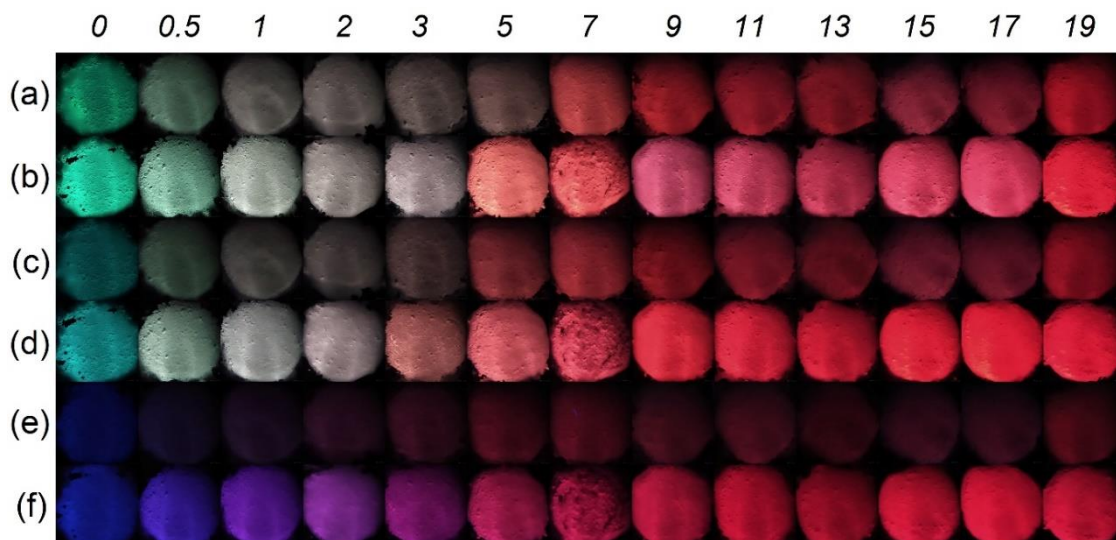


Fig. 4.21. Physical photographs of $\text{Y}_2\text{O}_3:\text{Eu}^{3+}$ (x at.%) / Bi^{3+} (1 at.%) (Eu^{3+} concentration in at.% is indicated on the top row) 500 °C annealed samples excited at (a) 330 nm, (c) 355 nm and (e) 371 nm, along with 900 °C annealed samples excited at (b) 330 nm, (d) 355 nm and (f) 371 nm, respectively.

positions in CIE diagram are given in Fig. 4.22 and Table 4.7. In Figure 4.23, the photographs are shown for the 500 and 900 °C annealed samples under the exposure of different excitation wavelengths from UV to blue. It can be suggested that the emission colour from the investigated samples can tuned by changing the excitation wavelengths as well.

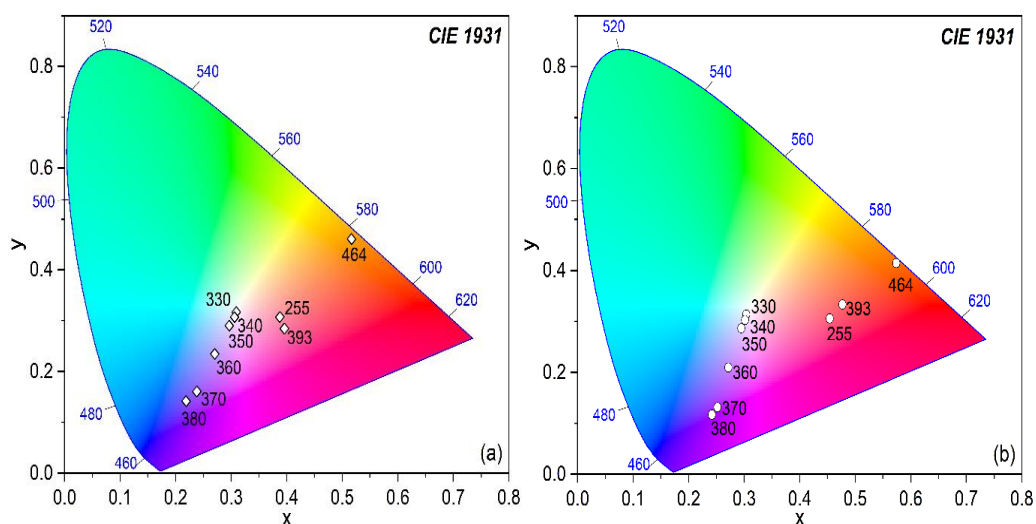


Fig. 4.22. CIE chromaticity coordinate positions of $\text{Y}_2\text{O}_3:\text{Eu}^{3+}$ (3 at.%) / Bi^{3+} (1 at.%) for (a) 500 and (b) 900 °C annealed samples under different wavelengths (positioned in the colour space). (Also see Table 4.7).

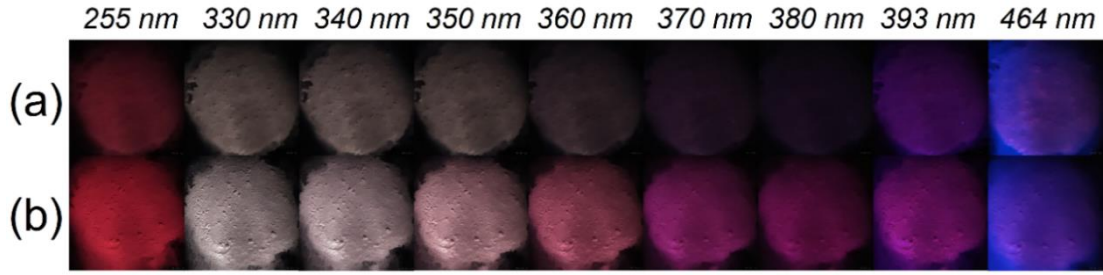


Fig. 4.23. Physical photographs of $\text{Y}_2\text{O}_3:\text{Eu}^{3+}$ (3 at.%) / Bi^{3+} (1 at.%) for (a) 500 °C and (b) 900 °C annealed samples excited at different wavelength (Top row indicates the excitation wavelengths).

Table 4.7. CIE coordinates for $\text{Y}_2\text{O}_3:\text{Eu}^{3+}$ (3 at.%) / Bi^{3+} (1 at.%) sample heated at 500 and 900 °C under different excitation wavelengths. CIE Positions (See Fig. 4.22).

λ_{ex} (nm)	500 °C	900 °C
255	(0.40,0.28)	(0.45,0.31)
330	(0.31,0.32)	(0.30,0.31)
340	(0.31,0.31)	(0.30,0.30)
350	(0.30,0.29)	(0.29,0.29)
360	(0.27,0.23)	(0.27,0.21)
370	(0.24,0.16)	(0.25,0.13)
380	(0.22,0.14)	(0.24,0.12)
393	(0.39,0.31)	(0.48,0.33)
464	(0.52,0.46)	(0.57,0.41)

4.3.5. Photoluminescence studies of Bi^{3+} sensitized $\text{Y}_2\text{O}_3:\text{Sm}^{3+}$

4.3.5.1. Steady state PL study

Fig. 4.24 shows the excitation spectra of 900 °C annealed Bi^{3+} (1 at.%) sensitized $\text{Y}_2\text{O}_3:\text{Sm}^{3+}$ (1, 2, 4, 6, 8, 10, and 12 at.%) samples monitored at 606 nm. Similar to the excitation spectra of $\text{Y}_2\text{O}_3:\text{Bi}^{3+}/\text{Eu}^{3+}$ discussed in Sec. 4.3.4.2, the spectra consist of (i) excitation peaks related to the $\text{Y}_2\text{O}_3:\text{Sm}^{3+}$ and (ii) excitation peaks originated from the Bi^{3+} . The small broad peak observed at 255 nm could be due to the charge transfer band of O^{2-} to Sm^{3+} [66]. And, other sharp peak in the longer wavelength region at 406, 422, 467 and 492 nm is due to the $^7\text{H}_{5/2} \rightarrow ^6\text{P}_{3/2}$, $^7\text{H}_{5/2} \rightarrow ^6\text{D}_{5/2}$, $^7\text{I}_{11/2} \rightarrow ^6\text{P}_{3/2}$, and $^7\text{H}_{5/2} \rightarrow ^6\text{G}_{7/2}$ transitions respectively within the $f-f$ shell of Sm^{3+} [6,67-70]. The excitation peaks at 330, 347 and 370 nm are originated from the Bi^{3+} absorption. These peaks are due to

the presence of two types of lattice sites namely, C_2 and S_6 having octahedral coordination in cubic Y_2O_3 (as discussed in 4.3.4.1 and 4.3.4.2).

Fig. 4.25 illustrates the emission spectra of $\text{Y}_2\text{O}_3:\text{Bi}^{3+}$ (1 at.%)/ Sm^{3+} (1 at.%) samples. The excitation wavelengths are 330 nm (Bi^{3+} , related to C_2 site), 370 nm (Bi^{3+} , related to S_6 site) and direct excitations at 406 nm. Comparing the emission peak at 606 nm, it can be observed that the emission intensity is highest when excited at 330 nm than other remaining excitations. This suggests that the Bi^{3+} sensitization in $\text{Y}_2\text{O}_3:\text{Sm}^{3+}$ can render the energy transfer from the Bi^{3+} absorption to the excited states of Sm^{3+} resulting improved emission intensity (discussed later). The remaining part of the study will be concentrated with the excitations related to the Bi^{3+} absorption only.

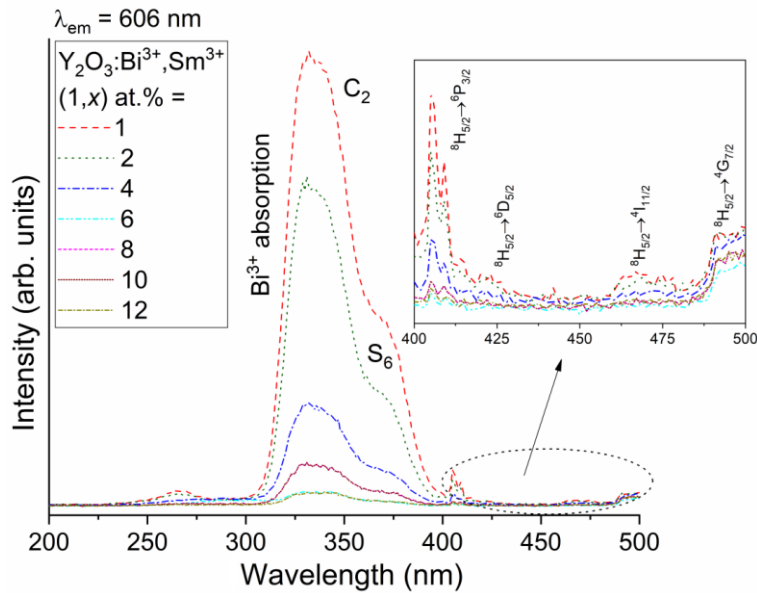


Fig. 4.24. PL excitation spectra of 900 °C annealed Bi^{3+} (1 at.%) sensitized $\text{Y}_2\text{O}_3:\text{Sm}^{3+}$ (1, 2, 4, 6, 8, 10 and 12 at.%) samples monitored at $\lambda_{\text{em}} = 606$ nm

The emission spectra consist of two types: (i) the broad emission peak with two humps at ~ 417 and 504 nm in the region of ~ 380 to 575 nm and (ii) sharp emission peaks in the region of ~ 550 to 700 nm. The broad band emission is related to the Bi^{3+} originated from $^3\text{P}_1 \rightarrow ^1\text{S}_0$. The presence of these two distinct humps in the emission band is due to the Bi^{3+} occupying at 2 (two) different symmetry sites (discussed in Sec. 6.3.4.1). The sharp emission peaks mentioned in (ii) are related to the transitions within the $f-f$ electronic energy levels of Sm^{3+} . These emission peaks are related to the transitions originated from the $^4\text{G}_{5/2} \rightarrow ^6\text{H}_{5/2}$ (at 564, 568 and 574 nm) and $^4\text{G}_{5/2} \rightarrow ^6\text{H}_{5/2}$ (at 606, 615 and 621 nm) are related to magnetic dipole transitions. While, the transition at $^4\text{G}_{5/2}$

$\rightarrow^6\text{H}_{9/2}$ (at 654 and 665 nm) is due to pure electric dipole transition [4,67-70]. In all the cases, the transition at $^4\text{G}_{5/2} \rightarrow ^6\text{H}_{5/2}$ (at 606, 615 and 621 nm) is dominant even though it due to magnetic dipole transition, $\Delta J = \pm 1$, it is also dominated with electric dipole transition [71,72].

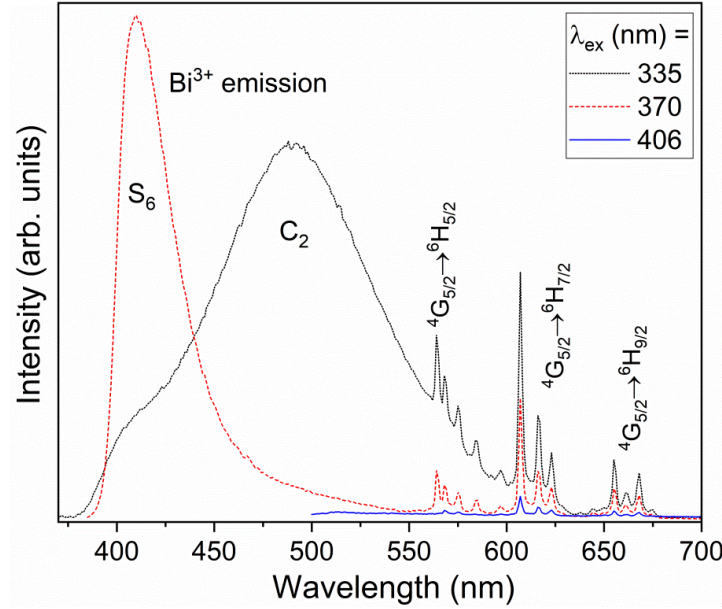


Fig. 4.25. PL emission spectra of 900 °C annealed $\text{Y}_2\text{O}_3:\text{Bi}^{3+}(1 \text{ at.})/\text{Sm}^{3+} (1 \text{ at.})$ samples under different excitations at 335 nm (Bi^{3+} , related to C_2 site) and 375 nm (Bi^{3+} , related to S_6 site) and 406 nm ($f-f$ absorption).

4.3.5.2. Mechanism of energy transfer: Bi^{3+} to Sm^{3+}

Fig. 4.26 shows the emission spectra of $\text{Y}_2\text{O}_3:\text{Bi}^{3+} (1 \text{ at.})/\text{Sm}^{3+} (0, 1, 2, 4, 6, 8, 10 \text{ and } 12 \text{ at.})$ samples under the excitation of 330 nm. Similar PL emission spectra under the 370 nm excitation are given at Fig 4.27. From both the figures, it is observed that the intensity of emission band related to the Bi^{3+} is decreased with the increase in Sm^{3+} concentration.

This is due to the increase in the non-radiative energy transfer to the excited states of randomly distributed Sm^{3+} ions at the expense of radiative transition within Bi^{3+} . This suggests the occurrence of energy transfer in both the cases. The efficiency of the energy transfer is calculated using Eqn. 4.2. Fig. 4.28 shows the energy transfer efficiencies of 500 and 900 °C annealed samples under the excitation of 330 nm. In both cases the energy transfer efficiency reaches $\sim 90\%$.

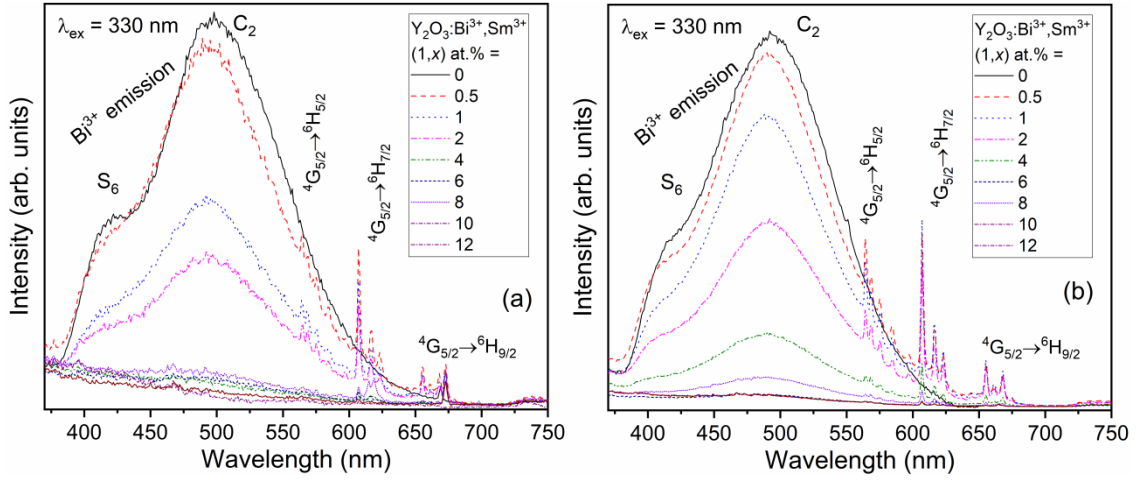


Fig. 4.26. Normalized PL emission of (a) 500 and (b) 900 °C annealed $\text{Y}_2\text{O}_3:\text{Bi}^{3+}$ (1 at. %)/ Sm^{3+} (0, 0.5, 1, 2, 4, 6, 8, 10 and 12 at. %) samples under the excitation at 330 nm.

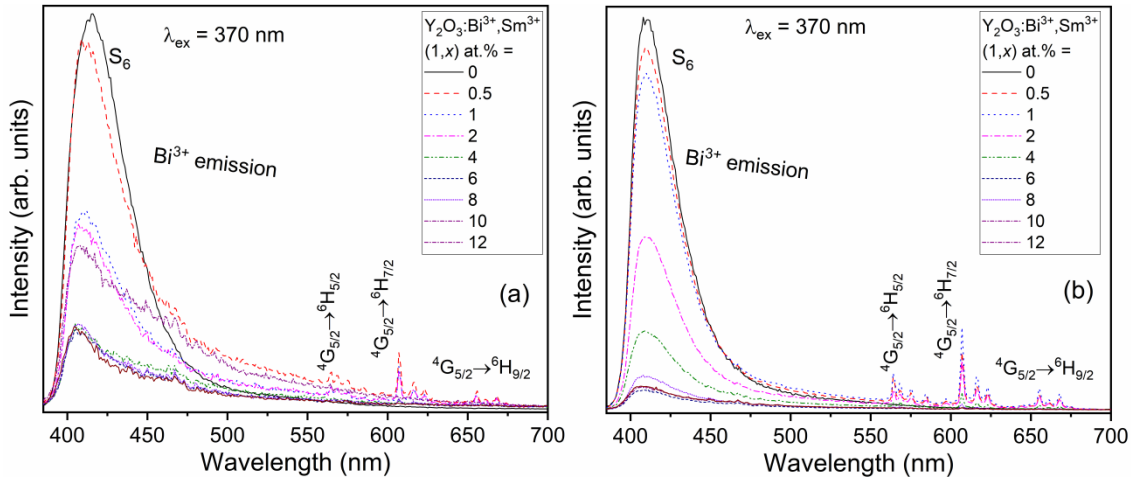


Fig. 4.27. Normalized PL emission of (a) 500 and (b) 900 °C annealed $\text{Y}_2\text{O}_3:\text{Bi}^{3+}$ (1 at. %)/ Sm^{3+} (0, 0.5, 1, 2, 4, 6, 8, 10 and 12 at. %) samples under the excitation at 370 nm.

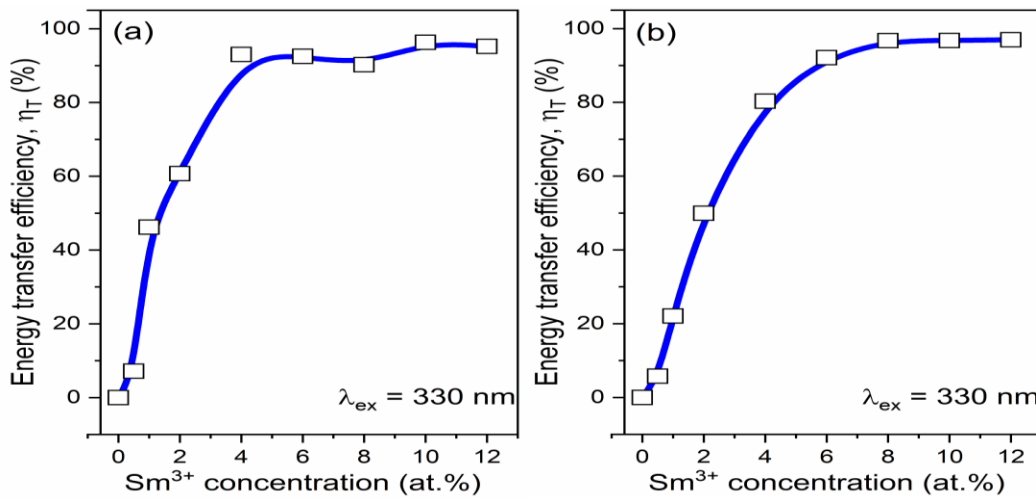


Fig. 4.28. Energy transfer efficiency (η_T) of different concentration of Sm^{3+} (0, 0.5, 1, 2, 4, 6, 8, 10 and 12 at. %) in Bi^{3+} (1 at. %) sensitized Y_2O_3 samples annealed at (a) 500 and (b) 900 °C.

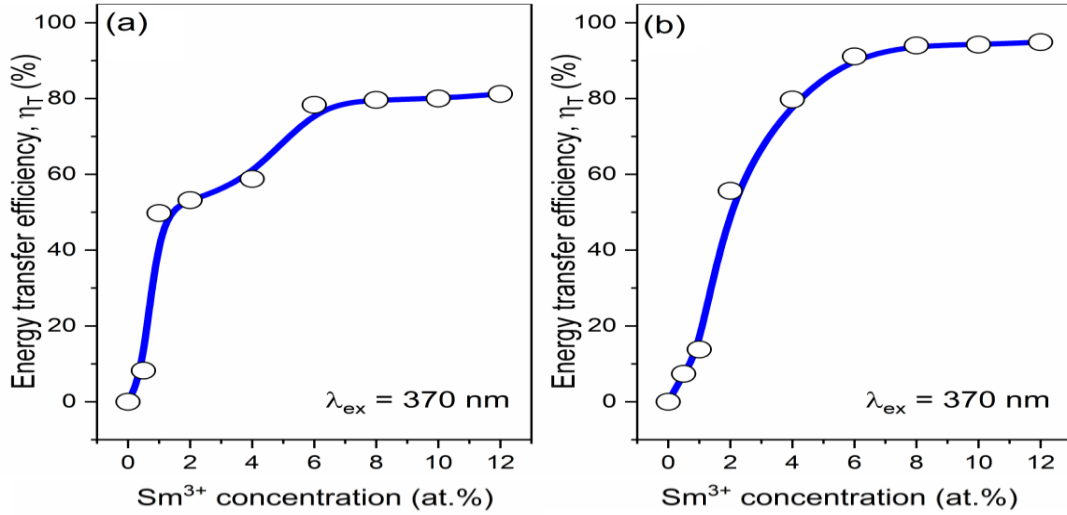


Fig. 4.29. Energy transfer efficiency (η_T) of different concentration of Sm^{3+} (0, 0.5, 1, 2, 4, 6, 8, 10 and 12 at.%) in Bi^{3+} (1 at.%) sensitized Y_2O_3 samples annealed at (a) 500 and (b) 900 °C.

Fig. 4.29 shows the energy transfer efficiencies of 500 and 900 °C annealed samples under the excitation of 370 nm. The energy transfer efficiency reaches in the case of 500 °C annealed reaches ~ 80%. While, the efficiency reaches nearly ~90% for 900 °C annealed samples.

As discussed in Sec. 4.3.4.3, the energy transfer occurs through either/both (i) exchange interactions and (ii) multipolar interactions. These interactions depend on the distance between the acceptor and donor. The critical distance between them is calculated using Eqn. 4.3, The critical concentration (x_c) value is 2 at.%. The critical distance (R_c) is found to be ~15 and 17 Å respectively for 900 and 500 °C annealed samples. Both the value is greater than the restricted distance (~ 5 Å) of exchange interaction. This establishes the presence of multipolar type of energy transfer. On the basis of Reisfeld's approximation equation (Eqn. 4.6), the best fit is observed with the values of $n = 6$ and 8. On the basis of these fitting parameters, it may be understood that the energy transfer from the Bi^{3+} to the excited states of Sm^{3+} occurs mainly through both *dipole – dipole* for the 500 °C annealed samples (See Fig. 4.30). On the other hand, the multipolar interaction is contributed by both *dipole – dipole* and *dipole – quadrupole* for 900 °C annealed samples (See Fig. 4.31). Fig. 4.30 and 4.31 shows the typical fitting using Eqn. 4.6 for 500 and 900 °C annealed samples. The respective excitation wavelengths are given in the figure caption.

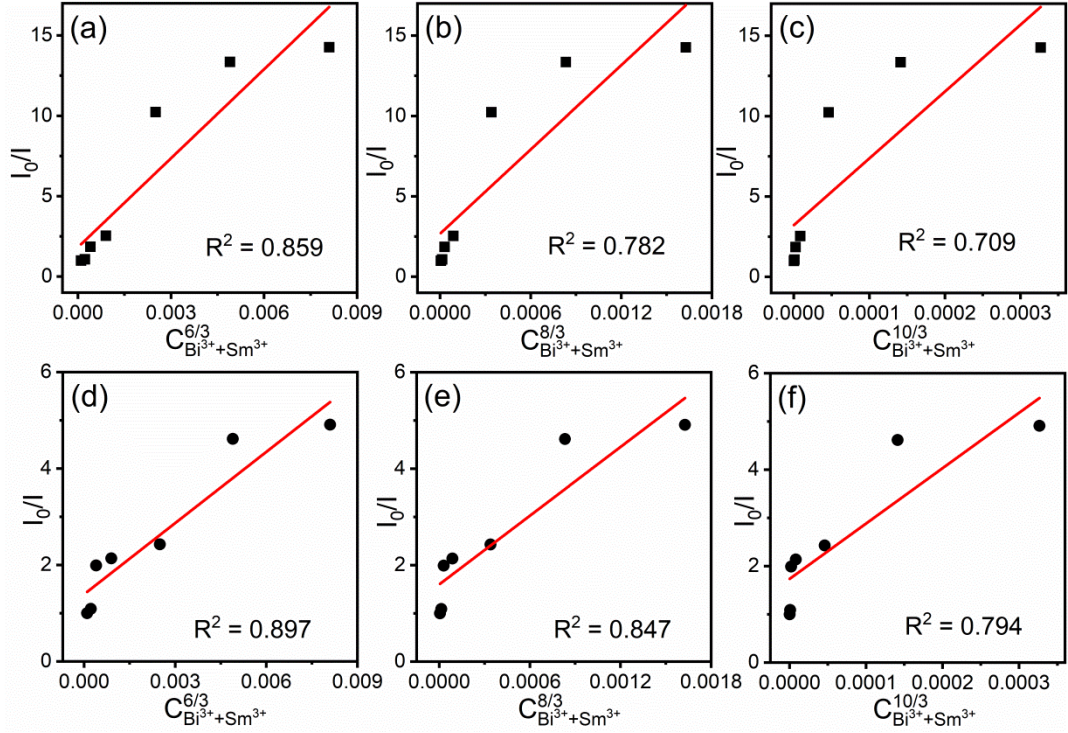


Fig. 4.30. Dependence of I_{S_0}/I_S of Bi^{3+} on (a) $C_{\text{Bi}^{3+}+\text{Sm}^{3+}}^{6/3}$, (b) $C_{\text{Bi}^{3+}+\text{Sm}^{3+}}^{8/3}$, (c) $C_{\text{Bi}^{3+}+\text{Sm}^{3+}}^{10/3}$ ($\lambda_{\text{ex}} = 330 \text{ nm}$) and (d) $C_{\text{Bi}^{3+}+\text{Sm}^{3+}}^{6/3}$, (e) $C_{\text{Bi}^{3+}+\text{Sm}^{3+}}^{8/3}$, (f) $C_{\text{Bi}^{3+}+\text{Sm}^{3+}}^{10/3}$ ($\lambda_{\text{ex}} = 370 \text{ nm}$) for samples annealed at 500°C .

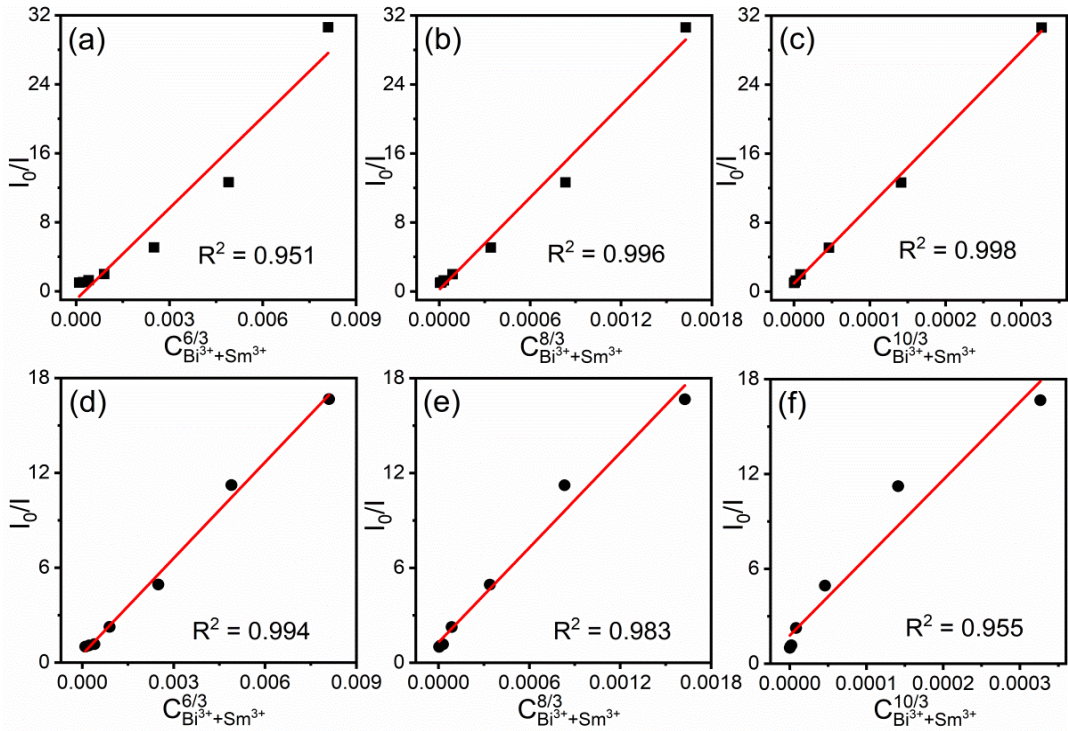


Fig. 4.31. Dependence of I_{S_0}/I_S of Bi^{3+} on (a) $C_{\text{Bi}^{3+}+\text{Sm}^{3+}}^{6/3}$, (b) $C_{\text{Bi}^{3+}+\text{Sm}^{3+}}^{8/3}$, (c) $C_{\text{Bi}^{3+}+\text{Sm}^{3+}}^{10/3}$ ($\lambda_{\text{ex}} = 330 \text{ nm}$) and (d) $C_{\text{Bi}^{3+}+\text{Sm}^{3+}}^{6/3}$, (e) $C_{\text{Bi}^{3+}+\text{Sm}^{3+}}^{8/3}$, (f) $C_{\text{Bi}^{3+}+\text{Sm}^{3+}}^{10/3}$ ($\lambda_{\text{ex}} = 370 \text{ nm}$) for samples annealed at 000°C .

4.3.5.3. PL decay lifetime and quantum yield study

Fig. 4.32 shows the decay profiles of Bi³⁺ (1 at.%) in Y₂O₃:Sm³⁺ (0, 1, 2, 4, 6, 8 and 10 at.%) samples annealed at (a) 500 and (b) 900 °C. Excitation and emission wavelengths of Bi³⁺ were monitored at 330 and 504 nm respectively. The decay profiles are better fitted with the second order exponential decay equation (Eqn. 4.7). Similar behaviour is also observed in Bi³⁺ sensitized Y₂O₃Eu³⁺ (Sec. 4.3.4.4). The average decay lifetime can be calculated using Eqn. 4.8. The calculated decay lifetime of Bi³⁺ against the Sm³⁺ concentrations are given in Table 4.8. In both cases, the decay lifetime is found to decrease when the concentration of Sm³⁺ is increase from 0 to 12 at.% (See inset Fig. 4.32). The decay lifetime trend clearly ascertains the increase in the non-radiative transfer of energy to the excited states of Sm³⁺ at the expense of radiative transition in Bi³⁺. This result supports the energy transfer discussed from the steady state luminescence studies.

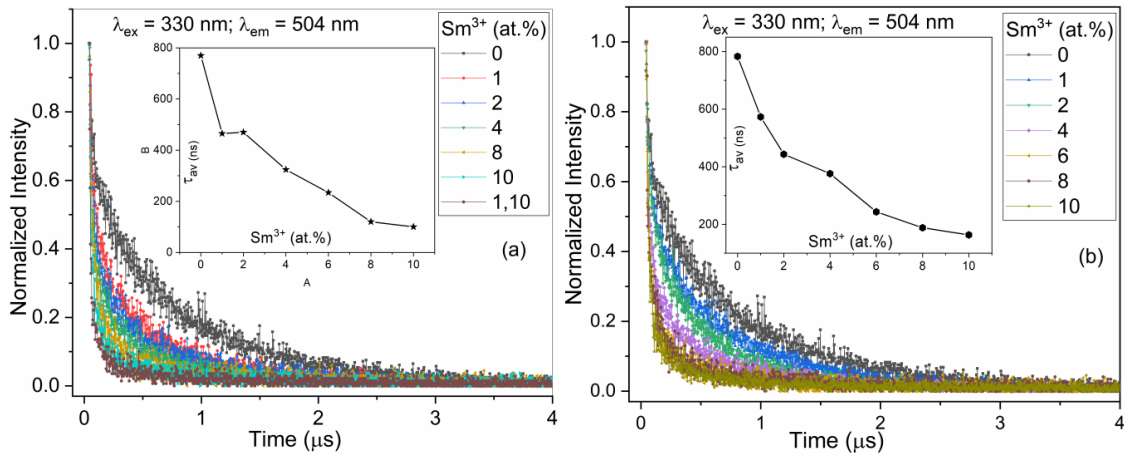


Fig. 4.32. TCSPC decay profiles of Bi³⁺ (1 at.%) in Y₂O₃:Sm³⁺ (0, 1, 2, 4, 6, 8, and 10 at.%) samples annealed at (a) 500 and (b) 900 °C. Excitation and emission wavelengths were monitored at 330 and 504 nm respectively. Inset shows the calculated average lifetime values at different concentration of Sm³⁺.

Table 4.8: Decay lifetime (τ_{av}) values of Bi³⁺ in Y₂O₃:Sm³⁺ (x at.%) / Bi³⁺ (1 at.%) samples annealed at 500 °C and 900 °C. Excitation wavelength, λ_{ex} = 330 nm and emission wavelength, λ_{em} = 504 nm.

Sm ³⁺ (at.%)	500 °C		900 °C	
	τ_{av} (ns)	R^2	τ_{av} (ns)	R^2
0	770	0.99	783	0.99
1	465	0.99	573	0.99
2	470	0.99	443	0.99
4	324	0.98	376	0.99
6	234	0.98	243	0.99
8	190	0.97	188	0.99
10	100	0.97	164	0.99

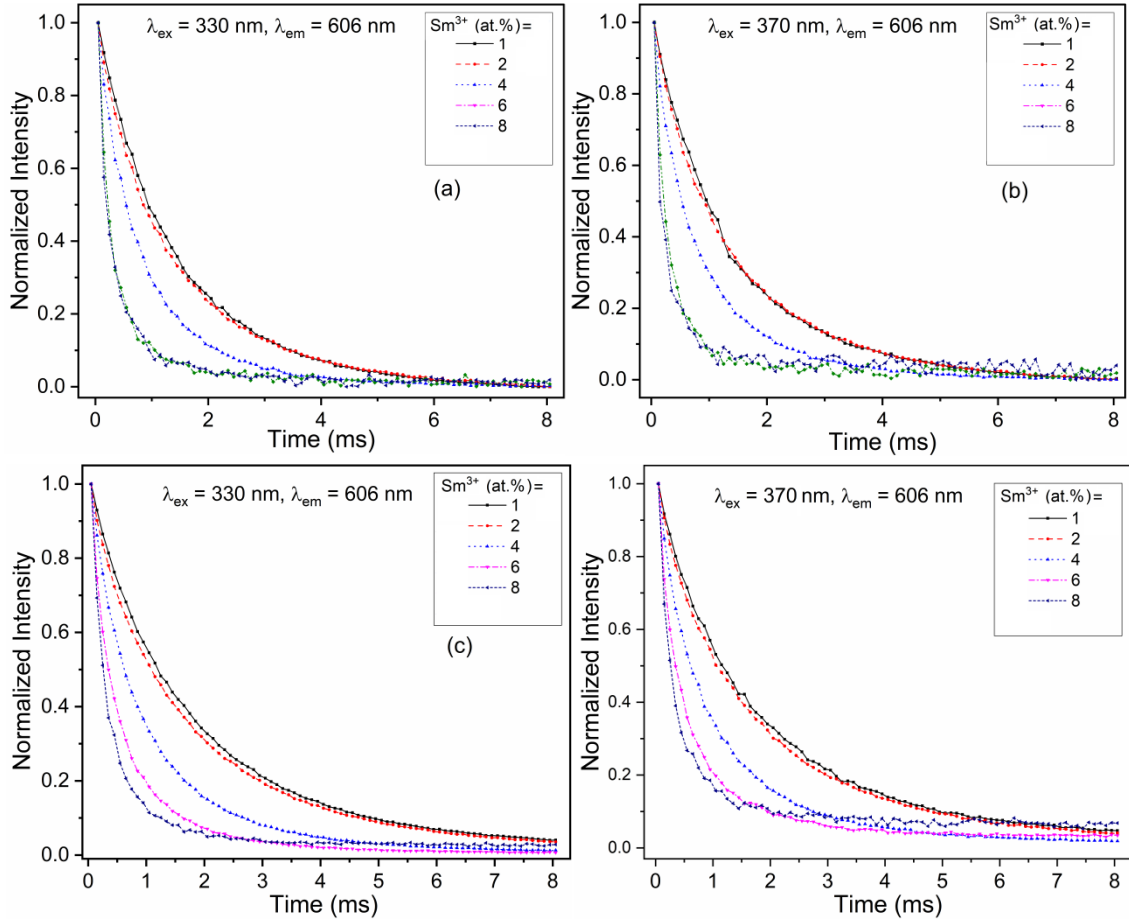


Fig. 4.33. PL Decay lifetime curves of $^5\text{G}_{5/2}$ level of Sm^{3+} of (a & b) 500 and (c & d) 900 °C annealed $\text{Y}_2\text{O}_3:\text{Sm}^{3+}$ (x at.%) / Bi^{3+} (1 at.%) samples. Excitation wavelengths: (a & c) 330 and (b & d) 370 nm.

Table 4.9. Decay lifetime (τ_{av}) values of $^5\text{G}_{5/2}$ level of Sm^{3+} in $\text{Y}_2\text{O}_3:\text{Sm}^{3+}$ (x at.%) / Bi^{3+} (1 at.%) samples annealed at 500 °C and 900 °C. Excitation wavelength, $\lambda_{ex} = 330$ and 370 nm and emission wavelength, $\lambda_{em} = 606$ nm.

Sm^{3+} (at.%)	500 °C				900 °C			
	$\lambda_{exc} = 330$		$\lambda_{exc} = 370$		$\lambda_{exc} = 330$		$\lambda_{exc} = 370$	
	τ_{av} (ms)	R^2	τ_{av} (ms)	R^2	τ_{av} (ms)	R^2	τ_{av} (ms)	R^2
1	1.40	0.99	1.37	0.99	1.98	0.99	1.98	0.99
2	1.34	0.99	1.35	0.99	1.92	0.99	1.94	0.99
4	0.82	0.99	0.84	0.99	1.38	0.99	1.34	0.99
6	0.35	0.99	0.40	0.99	0.97	0.99	1.00	0.99
8	0.31	0.99	0.28	0.99	0.62	0.99	0.88	0.99

Fig. 4.33 shows the decay curves of $^5\text{G}_{5/2}$ level of Sm^{3+} emission in $\text{Y}_2\text{O}_3:\text{Bi}^{3+}$ (1 at.%) / Sm^{3+} (1, 2, 4, 6, and 8 at.%) samples by monitoring at 606 nm emission.

Excitation wavelengths are 330 (a and c) and 370 nm (b and d). All the decay profiles follow the second order exponential decay (Eqn. 4.7). The average decay lifetime was calculated using Eqn. 4.8 and given in Table 4.9. The decay lifetime varies from 0.31 to 1.98 ms when the excitation was used at 330 nm. On the other hand, under direct excitation at 464 nm, the lifetime value increases from 0.28 to 1.98 ms. From the Table 4.8, it can be observed that the decay lifetime value in both the cases decreases with the increase of Sm^{3+} concentration beyond 1 at.%. Such decrease in the decay lifetime of lanthanide ions emission can be attributed to the increase in the non-radiative transitions due to the cross relaxation among lanthanide ions. Such behaviour has been reported earlier [66,72]. On the other hand, the decay lifetime is improved in both the excitations when the samples are annealed at 900 °C. This might due to the improved luminescence after annealing.

4.3.5.4. CIE chromaticity studies

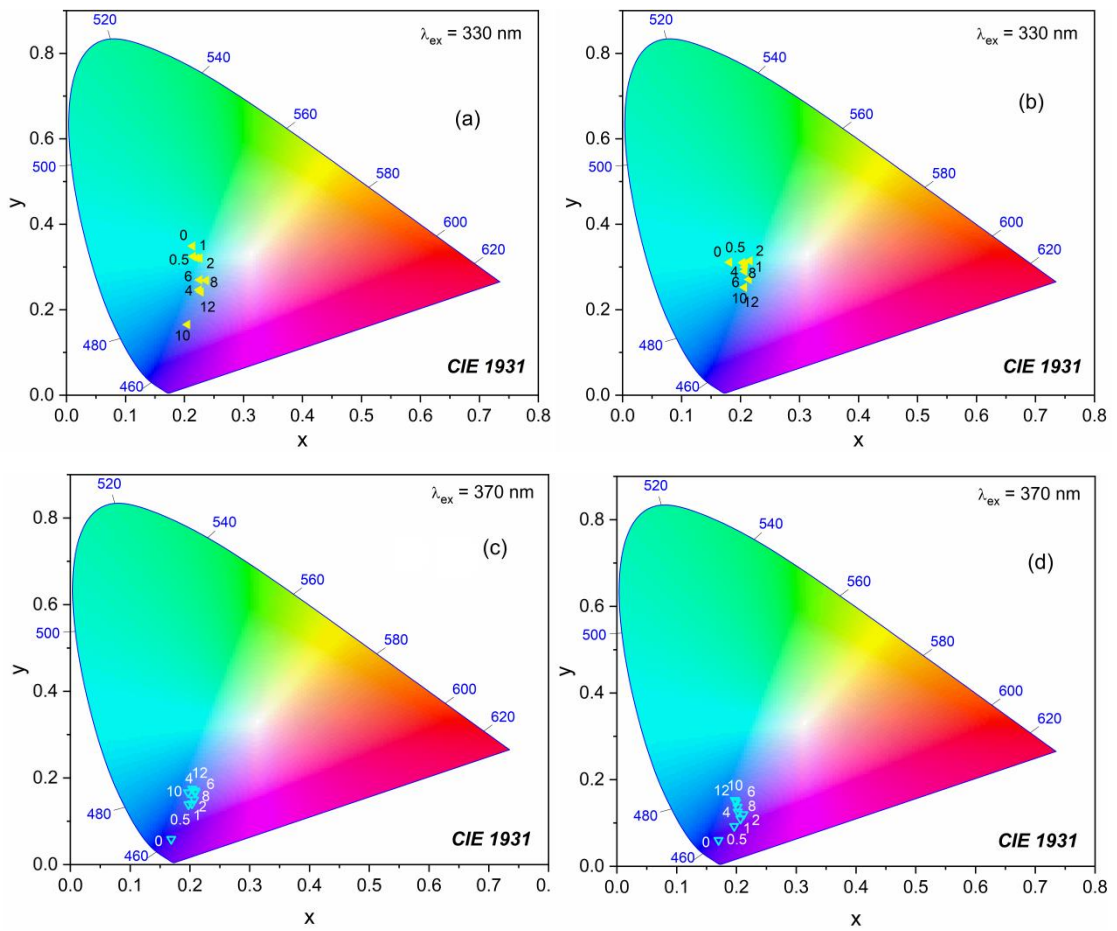


Fig. 4.34. CIE chromaticity coordinate positions of $\text{Y}_2\text{O}_3:\text{Bi}^{3+}$ (1 at.)/ Sm^{3+} (0.5, 1, 2, 4, 6, 8, 10 and 12 at.%) samples excited at (a and b) 330 nm, (c and d) 370 nm.

Fig. 4.34 illustrates the CIE chromaticity of the Sm^{3+} emission in $\text{Y}_2\text{O}_3:\text{Bi}^{3+}$ (1 at.%) / Sm^{3+} (0, 0.5, 1, 2, 4, 6, 8, 10 and 12 at.%) samples under (a) 330 and (b) 370 nm. From the figure, it can be observed that the emission is concentrated in the blue region when the excitation is 370 nm. This might be due to dominance of Bi^{3+} emission at ~403 nm. While, under 330 nm excitation the emission is spread in the bluish green region. Even though there is enough energy transfer occur in the higher concentration region i.e. ≥ 4 at.%, the intensity of the orange-red emission of the Sm^{3+} has already started to quench after 2 at.% due to concentration quenching. Therefore, the emission region from all the samples investigated falls in the blue-green part of the CIE space. Thus, we may understand that the Bi^{3+} sensitized $\text{Y}_2\text{O}_3:\text{Sm}^{3+}$ phosphors may not be suitable as red emitting phosphor.

4.4. Conclusions

Bi^{3+} sensitized Eu^{3+} and Sm^{3+} doped Y_2O_3 were successfully synthesized by hydrothermal method with post annealing at 500 and 900 °C. The optimal concentration for sensitizer (Bi^{3+}) is found to be 1 at.%, while for activator, it is found to be 7 and 17 at.% for Eu^{3+} and 1 – 2 at.% for Sm^{3+} respectively, for the 500 and 900 °C annealed samples. The efficiency of the energy transfer from the sensitizer to activator ions increases with the increase of activator concentration. The dipole-dipole and dipole-quadrupole interaction are mainly responsible for the occurrence of resonance type of energy transfer. The energy transfer observed from the steady state luminescence is well corroborated by the decay lifetime studies of Bi^{3+} . Tuning of colour as well as white emission can be achieved by careful and appropriate selection of excitation wavelength and activator (Eu^{3+}) concentration. This is substantiated from the CIE studies and photographs taken under the direct exposure of UV to blue light sources. The quantum yield reaches up to 24% for Bi^{3+} (1 at.%) sensitized $\text{Y}_2\text{O}_3:\text{Eu}^{3+}$ (2 at.%). However, in the case of $\text{Y}_2\text{O}_3:\text{Bi}^{3+}/\text{Sm}^{3+}$, mostly the emission color is observed to be found in the blue-greenish region in the CIE space. The $\text{Y}_2\text{O}_3:\text{Bi}^{3+}/\text{Sm}^{3+}$ is not a promising as red phosphor.

References

1. M. Shang, C. Li, J. Lin, Chem. Soc. Rev. 43 (2014) 1372–1386.
2. L. Chen, K.J. Chen, C.C. Lin, C.I. Chu, S.F. Hu, M.H. Lee, R.S. Liu, J. Comb. Chem. 12 (2010) 587–594.
3. N.S. Singh, N.K. Sahu, D. Bahadur, J. Mater. Chem. C. 2 (2014) 548–555.
4. S.D. Meetei, E.C. Devi, S.D. Singh, Results Phys. 13 (2019) 101975.
5. S. Sarkar, M. Chatti, V.N.K.B. Adusumalli, V. Mahalingam, ACS Appl. Mater. Interfaces. 7 (2015) 25702–25708.
6. R. Wangkhem, N.S. Singh, N.P. Singh, S.D. Singh, L.R. Singh, J. Lumin. 203 (2018) 341–348.
7. K. Li, R.V. Deun, J. Alloys Compd. 787 (2019) 86–95.
8. M. Guo, K. Yi, S. Shao, Y. Zhang, G. Hu, J. Zhao, H. He, J. Shao, Opt. Mater. 109 (2020) 110304.
9. H. Dong, S.R. Du, X.Y. Zheng, G.M. Lyu, L.D. Sun, L.D. Li, P.Z. Zhang, C. Zhang, C.H. Yan, 115 (2015) 10725–10815.
10. N.S. Singh, H. Kulkarni, L. Pradhan, D. Bahadur, Nanotechnology. 24 (2013) 065101.
11. X. Wang, J. Shi, P. Li, S. Zheng, X. Sun, H. Zhang, J. of Lumin. 209 (2019) 420–426.
12. S. Cheng, L. Liu, Q. Yang, Y. Li, S. Zeng, J. Rare Earths 37 (2019) 931–936.
13. K. Bando, K. Sakano, Y. Noguchi, Y. Shimizu, J. Light Vis. Environ. 22 (1998) 2–5.
14. X. Huang, Nat. Photonics. 8 (2014) 748–749.
15. G. Li, Y. Tian, Y. Zhao, J. Lin, Chem. Soc. Rev. 44 (2015) 8688–8713.
16. L.S. Chi, R.S. Liu, B.J. Lee, J. Electrochem. Soc. 152 (2005) J93–J98.
17. P. Schlotter, R. Schmidt, J. Schneider, Appl. Phys. A Mater. Sci. Process. 64 (1997) 417–418.
18. X. Li, J.D. Budai, F. Liu, J.Y. Howe, J. Zhang, X.J. Wang, Z. Gu, C. Sun, R.S. Meltzer, Z. Pan, Light Sci. Appl. 2 (2013) e50.
19. D. Zhang, G. Li, Z. Leng, L. Li, J. Alloys Compd. 815 (2020) 152645.
20. Y. Hua, J.S. Yu, Ceram. Int. 46 (2020) 26646–26659.
21. D.R. Taikar, J. Alloys Compd. 828 (2020) 154405.
22. L. Zhang, P. Li, A. Zhao, X. Li, J. Tang, F. Zhang, G. Jia, C. Zhang, J. Alloys Compd. 816 (2020) 152546.
23. W. Zhao, S. Qi, J. Liu, B. Fan, J. Alloy Compd. 787 (2019) 469–475.
24. Y. Shimizu, K. Sakano, Y. Noguchi, T. Moriguchi, US Pat. 1999, 5998925A.
25. P. Du, J.S. Yu, Sci. Rep. 7 (2017) 316–325.
26. V. Bachmann, C. Ronda, O. Oeckler, W. Schnick, A. Meijerink, Chem. Mater. 21 (2009) 316–325.
27. K. Uheda, N. Hirosaki, Y. Yamamoto, A. Naito, T. Nakajima, H. Yamamoto, Electrochem. Solid-State Lett. 9 (2006) H22.
28. S. Li, Q. Zhu, L. Wang, D. Tang, Y. Cho, X. Liu, N. Hirosaki, T. Nishimura, T. Sekiguchi, Z. Huang, R.J. Xie, J. Mater. Chem. C. 4 (2016) 8197–8205.
29. D. Wilhelm, D. Baumann, M. Seibald, K. Wurst, G. Heymann, H. Huppertz, Chem. Mater. 29 (2017) 1204–1209.
30. R. Wangkhem, T. Yaba, N. Shanta Singh, R.S. Ningthoujam, J. Appl. Phys. 123 (2018) 124303.
31. Y. Zhang, J. Xu, Q. Cui, B. Yang, Sci. Rep. 7 (2017) 42464.
32. M. Janulevicius, P. Marmokas, M. Misevicius, J. Grigorjevaite, L. Mikoliunaite, S. Sakirzanovas, A. Katelnikovas, Sci. Rep. 6 (2016) 26098.

33. H. Wang, M. Yu, C. Lin, X. Liu, J. Lin, J. Phys. Chem. C. 111 (2007) 11223–11230.
34. W. Wang, P. Zhu, Opt. Express. 26 (2018) 34820-34829.
35. M. Yang, Y. Sui, S. Wang, X. Wang, Y. Wang, S. Lü, T. Lü, W. Liu, J. Alloys Compd. 509 (2011) 266-270.
36. T.W. Chou, S. Mylswamy, R.S. Liu, S.Z. Chuang, Solid State Commun. 136 (2005) 205–209.
37. C.A. Kodaira, R. Stefani, A.S. Maria, M.C.F.C. Felinto, H.F. Brito, J. Lumin. 127 (2007) 616-622
38. I. Khan, G. Rooh, I. Ullah, N. Srisittipokakun, S. Kothan, A. Alhuthali, M. Shoiab, A. Hussain, J. Kaewkhao, J. Non- Cryst. Solids 578 (2022) 121283.
39. M.K. Jung, W.J. Park, D.H. Yoon, Sens. Actuators B Chem. 126 (2007) 328-331
40. G. Ju, Y. Hu, L. Chen, X. Wang, Z. Mu, H. Wu, F. Kang, J. Lumin. 132 (2012) 1853-1859
41. R.S. Yadav, S.B. Rai, Opt. Laser Technol. 111 (2019) 169.
42. L.G. Jacobsohn, M.W. Blair, S.C. Tornga, L.O. Brown, B.L. Bennett, R.E. Muenchausen, J. Appl. Phys. 104 (2008) 124303.
43. A. Scarangella, F. Fabbri, R. Reitano, F. Rossi, F. Priolo, M. Miritello, Sci. Rep. 7 (2017) 17325.
44. A.M. van de Craats, G. Blasse, Chem. Phys. Lett. 243 (1995) 559–563.
45. R.S. Yadav, S.B. Rai, J. Alloys Compd. 700 (2017) 228-237.
46. G. Ju, Y. Hu, L. Chen, X. Wang, Z. Mu, H. Wu, F. Kang, J. Electrochem. Soc. 158 (2011) J294-J299.
47. L.R. Singh, R.S. Ningthoujam, V. Sudarsan, I. Srivastava, S.D. Singh, G.K. Dey, S.K. Kulshreshtha, Nanotechnology. 19 (2008) 055201.
48. H.J. Devi, W.R. Singh, R.S. Loitongbam, J. Fluoresc. 26 (2016) 875–889.
49. P.A. Tanner, L. Fu, Chem. Phys. Lett. 470 (2009) 75–79.
50. Y. Zhang, J. Guo, T. White, T.T.Y. Tan, R. Xu, J. Phys. Chem. C 111 (2007) 7893-7897
51. M.K. Devaraju, S. Yin, T. Sato, Eur. J. Inorg. Chem. 2009 (2009) 4441-4445.
52. H. Choi, S.H. Cho, S. Khan, K.R. Lee, S. Kim, J. Mater. Chem. C. 2 (2014) 6017–6024.
53. S. Ray, P. Pramanik, A. Singha, A. Roy, J. Appl. Phys. 97 (2005) 094312.
54. A.K. Parchur, R.S. Ningthoujam, RSC Adv. 2 (2012) 10859–10868.
55. X.Y. Chen, W. Zhao, R.E. Cook, G.K. Liu, Phys. Rev. B - Condens. Matter Mater. Phys. 70 (2004) 205122.
56. G. Nishimura, M. Tanaka, A. Kurita, T. Kushida, J. Lumin. 48–49 (1991) 473–476.
57. G. Nishimura, T. Kushida, Phys. Rev. B. 37 (1988) 9075–9078.
58. R. Reisfeld, L. Boehm, J. Solid State Chem. 4 (1972) 417 – 424.
59. G. Blasse, Phys. Lett. A. 28 (1968) 444–445.
60. D.L. Dexter, J. Chem. Phys. 21 (1953) 836–850.
61. W.M. Yen, S. Shionoya, H. Yamamoto (Eds.), Phosphor Handbook, second ed., CRC Press, Taylor & Francis Group, Florida, 2007.
62. C.H. Huang, T.W. Kuo, T.M. Chen, ACS Appl. Mater. Interfaces. 2 (2010) 1395–1399.
63. T. Yaba, R. Wangkhem, N. Shanta Singh, J. Alloys Compd. 843 (2020) 156022 – 156031.
64. D. Huang, P. Dang, H. Lian, Q. Zeng, J. Lin, Inorg. Chem. 58 (2019) 15507–15519.

65. Z. Xia, S. Miao, M. Chen, M.S. Molokeev, Q. Liu, *Structure, Inorg. Chem.* 54 (2015) 7684–7691.
66. Y. Hua, J.-U. Kim, J.S. Yu, *J. Am. Ceram. Soc.* 104 (2021) 4065.
67. N.S. Singh, R.S. Ningthoujam, G. Phaomei, S.D. Singh, A. Vinu, R.K. Vatsa, *Dalton Trans.* 41 (2012) 4404-4412.
68. E. Cavalli, A. Belletti, R. Mahiou, P. Boutinaud, *J. Lumin.* 130 (2010) 733.
69. E. Cavalli, *J. Lumin.* 183 (2017) 172-177.
70. O. Tegus, B. Amurinsana, S. Zhiqiang, *J. Lumin.* 215 (2019) 116624.
71. G. Lakshminarayana, J. Qiu, *J. Lumin.* 476 (2009) 470 – 476.
72. P.S. May, D.H. Metcalf, F.S. Richardson, R.C. Carter, C.E. Miller, R.A. Palmer, *J. Lumin.* 51 (1991) 249.

Chapter 5

Photoluminescence properties of $\text{Gd}_2\text{O}_3:\text{Ln}^{3+}$ ($\text{Ln}^{3+} = \text{Eu}^{3+} \text{ \& } \text{Sm}^{3+}$)

5.1. Introduction

Rare earth oxides such as Y_2O_3 , La_2O_3 , Lu_2O_3 , Gd_2O_3 , etc. activated with various lanthanides are considered as excellent phosphor materials. They are advantages over the sulfide-based phosphors for their stability chemically and optically [1,2]. These oxides preferred over many other host materials due to low phonon energy. They possess various applications such as cathode ray tubes [3,4] display [4-6], lamps [5,6], biological applications [7-10] as well as solid state lighting (SSL) [11-13]. Among them, application towards the SSL has become prominent lately. This is because of the fact that the conversion of phosphors is generally adopted for generation of white light. In this aspect, various red emitting phosphors are reported. Among them, $\text{Na}_2\text{Y}_2\text{B}_2\text{O}_7:\text{Eu}^{3+}$ [14], $\text{BaZrGe}_3\text{O}_9:\text{Eu}^{3+}$ [15], Eu^{3+} activated La_2MoO_6 - La_2WO_6 composite [16], $\text{La}_2\text{Ce}_2\text{O}_7:\text{Eu}^{3+}$ [17], $\text{CaMoO}_4:\text{Eu}^{3+}$ [18-20], $\text{CaWO}_4:\text{Eu}^{3+}$ [21-23], and $\text{YVO}_4:\text{Eu}^{3+}$ [24,25], $\text{Y}_2\text{O}_3:\text{Eu}^{3+}$ [26-29], $\text{Y}_2\text{O}_2\text{S}:\text{Eu}^{3+}$ [30] etc. may be mentioned.

The Gd_2O_3 having low phonon energy ($\sim 600 \text{ cm}^{-1}$) is a good host material for various lanthanides such as Dy^{3+} , Tb^{3+} , Eu^{3+} , Sm^{3+} so on. Generally, it exists in sesquioxides exhibiting hexagonal, monoclinic, and cubic structures [31-34]. When Gd_2O_3 exists in cubic, cation site offers two non-equivalent sites viz., C_2 (non-centrosymmetric) and S_6 (centrosymmetric) [33,34]. One advantage Gd_2O_3 compared to other rare earth oxides hosts is the presence of charge transfer band (CTB) arising due to the S-I absorption within Gd^{3+} in the UV region [35-40]. This can render energy transfer to the activators. There are various reports on the luminescence properties Gd_2O_3 doped these lanthanides i.e., $\text{Gd}_2\text{O}_3:\text{Tb}^{3+}$ [41-43], $\text{Gd}_2\text{O}_3:\text{Dy}^{3+}$ [44-46]. $\text{Gd}_2\text{O}_3:\text{Eu}^{3+}$ phosphor has been widely reported as potential red phosphor. Lately, these phosphors are reported as potential for solid state lighting applications [38,46]. While, various applications such as dual imaging of optical and magnetic resonance imaging, sensing etc. are also reported [7-10]. Similarly, photoluminescence properties of $\text{Gd}_2\text{O}_3:\text{Sm}^{3+}$ are also reported [47-49].

In this chapter, simple hydrothermal technique with subsequent post annealing for was adopted for preparing cubic $Gd_2O_3:Eu^{3+}$ and $Gd_2O_3:Sm^{3+}$. The photoluminescence properties of steady state and decay dynamics of are investigated. We have also studied the possibility of tuning emission with the variation of Eu^{3+} concentration using Commission International de l'Eclairage (CIE) chromaticity diagram.

5.2. Experimental methods

5.2.1. Materials

Gadolinium (III) nitrate hexahydrate ($Gd(NO_3)_3 \cdot 6H_2O$, 99.9%, Alfa Aesar), europium (III) nitrate hexahydrate ($Eu(NO_3)_3 \cdot 6H_2O$, 99.9%, Alfa Aesar), and samarium (III) nitrate hexahydrate ($Sm(NO_3)_3 \cdot 6H_2O$, 99.9%, Alfa Aesar) were used as received for the sources of Gd^{3+} , Eu^{3+} , and Sm^{3+} respectively. Polyvinyl pyrrolidone (PVP, $M_w \sim 40000$, Sigma Aldrich) was used as capping agent.

5.2.2. Synthesis of Eu^{3+} doped Gd_2O_3 phosphors

Hydrothermal technique was adopted to synthesize Eu^{3+} doped Gd_2O_3 phosphors (denoted as $Gd_2O_3:Eu^{3+}$). For the synthesis of $Gd_2O_3:Eu^{3+}$ (1 at.%) sample, 2.2 mg of $Eu(NO_3)_3 \cdot 6H_2O$ and 449 mg of $Gd(NO_3)_3 \cdot 6H_2O$ were taken. To this, 150 mg of polyvinyl pyrrolidone (PVP) was also added. The final volume was made 30 mL with the addition of DIW. The pH of the solution was fixed at 10 using ammonium hydroxide solution (NH_4OH , ~25% NH_3 , Sigma Aldrich). Finally, the solution was transferred to a Teflon lined stainless steel autoclave and heated at 180 °C for 18 h in an oven. The precipitate was centrifuged and washed several times with DIW and acetone. All the remaining samples were synthesized following the same procedure. The as-prepared samples were annealed 900 °C for 4 h in the air.

5.2.3. Synthesis of Sm^{3+} doped Gd_2O_3 phosphors

Following the similar procedure mentioned in the Sec 5.2.2, $Gd_2O_3:Sm^{3+}$ phosphors were also synthesized adopting hydrothermal method. In a typical synthesis of 1 at.% Sm^{3+} doped Gd_2O_3 sample, 2.2 mg of $Sm(NO_3)_3 \cdot 6H_2O$ and 449 mg of $Gd(NO_3)_3 \cdot 6H_2O$ were dissolved together. To this, 150 mg of polyvinyl pyrrolidone (PVP) was also added. The whole solution was kept under hydrothermal condition for 18 h at 180 °C.

The remaining samples were also prepared with similar process. The as-prepared samples were annealed 900 °C for 4 h in the air.

5.2.4. Characterization

X-ray diffractometer (Bruker D8 advance) with Cu $K\alpha$ radiation was used for crystalline phase identification. Fourier transform infrared (FT-IR) spectrometer (Shimadzu make IR-Affinity-1S) was used to record the FT-IR spectra of the prepared samples. Morphology of the particles was studied using the transmission electron microscopy (TEM) images recorded with JEOL 2000FX. The steady state and dynamics of photoluminescence (PL) as well as quantum yield (QY) were measured using Fluoromax-4CP spectrofluorometer (HORIBA make) equipped 150 W Xenon lamp and 25 W μ s Xenon flash lamp. All the PL measurements were carried out on the glass slides at room temperature with a resolution ± 1 nm. K-sphere ‘petite’ integrating sphere from Photon Technology International (PTI) was used for QY measurements. For calculation of absolute QY, $\phi(\%) = \frac{I_{emission}}{I_{quartz} - I_{sample}}$ was used. $I_{emission}$ = luminescence emission intensity of the sample, I_{quartz} = the intensity of light used to excite only the quartz slide and I_{sample} = the intensity of the light used for exciting the sample on the quartz slide. The photon absorbed by the sample is given by the difference between the last two. All the measurements were taken in the emission mode. The QY measurements were carried out on the quartz slides at room temperature.

5.3. Results and discussion

5.3.1. X-ray diffraction study

X-ray diffraction (XRD) patterns of the as prepared samples are illustrated in Fig. 5.1. The diffraction peaks is well indexed to the hexagonal $Gd(OH)_3$ (ICDD# 01-083-2037) [50]. The diffraction peaks are sharp indicating the formation of well crystalline $Gd(OH)_3:Eu^{3+}$ and $Gd(OH)_3:Sm^{3+}$ when prepared at 180 °C hydrothermally. Upon annealing at 900 °C for 4 h, these as prepared samples are transformed from hexagonal phase to the cubic phase of Gd_2O_3 (ICDD# 00-012-0797) [51]. Fig. 5.2 shows the XRD patterns of 900 °C annealed samples of $Gd_2O_3:Eu^{3+}$ and $Gd_2O_3:Sm^{3+}$. All the patterns show the cubic phase Gd_2O_3 (ICDD# 00-012-0797) [51]. No possible impurity phases such as Eu_2O_3 , Sm_2O_3 , etc. are observed. The crystallite size was calculated using

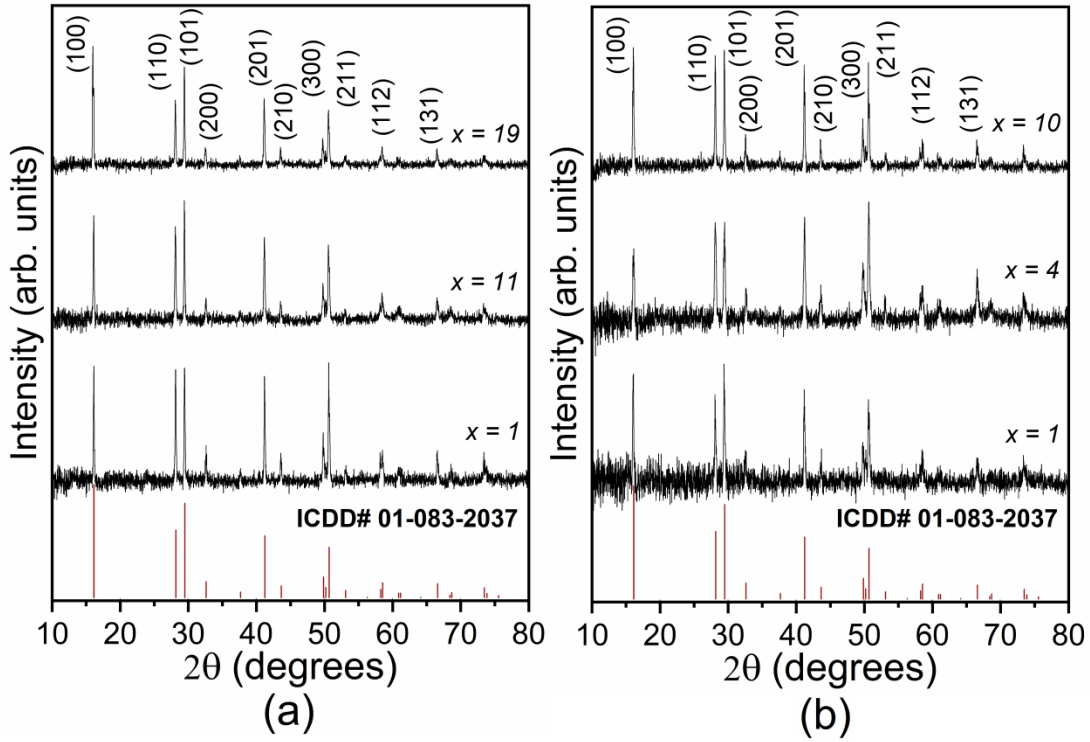


Fig. 5.1. XRD patterns of as-prepared (a) $\text{Gd}(\text{OH})_3:\text{Eu}^{3+}$ ($\text{Eu}^{3+} = 1, 11$ and 19 at.%) and (b) $\text{Gd}(\text{OH})_3:\text{Sm}^{3+}$ ($\text{Sm}^{3+} = 1, 4$ and 10 at.%).

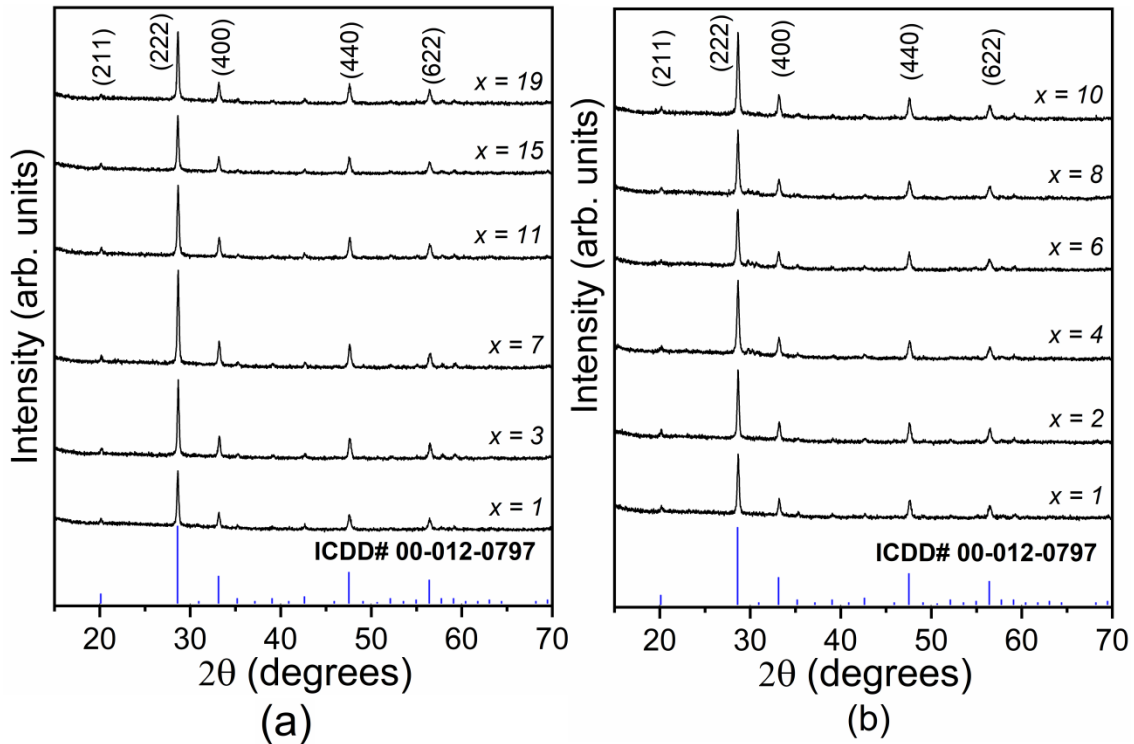


Fig. 5.2 XRD patterns of 900 °C annealed samples of (a) $\text{Gd}_2\text{O}_3:\text{Eu}^{3+}$ ($\text{Eu}^{3+} = 1, 3, 7, 11, 15$ and 19 at.%) and (b) $\text{Gd}_2\text{O}_3:\text{Sm}^{3+}$ ($\text{Sm}^{3+} = 1, 2, 4, 6, 8$ and 10 at.%).

Scherrer relation, $D = \frac{\kappa\lambda}{\beta \cos\theta}$. The crystallite size calculated for the as prepared hexagonal phase varies from $\sim 37 - 60$ nm. While, the variation in the crystallite size for the Gd_2O_3 samples becomes less. The crystallite size varies from $\sim 27 - 34$ nm (Table 5.1).

Table 5.1. Calculated crystallite size for Eu^{3+} or Sm^{3+} doped $Gd(OH)_3$ and $900^\circ C$ annealed Gd_2O_3 samples, using Scherrer relation.

Eu^{3+} (%)	Crystallite size (nm)		Sm^{3+} (%)	Crystallite size (nm)	
	ASP	$900^\circ C$		ASP	$900^\circ C$
1	37	31	1	47	31
5	-	32	2	-	29
9	60	31	4	40	27
11	-	29	6	-	28
17	50	32	8	-	27
21	-	34	10	42	30

5.3.2. Fourier transform infrared spectroscopy study

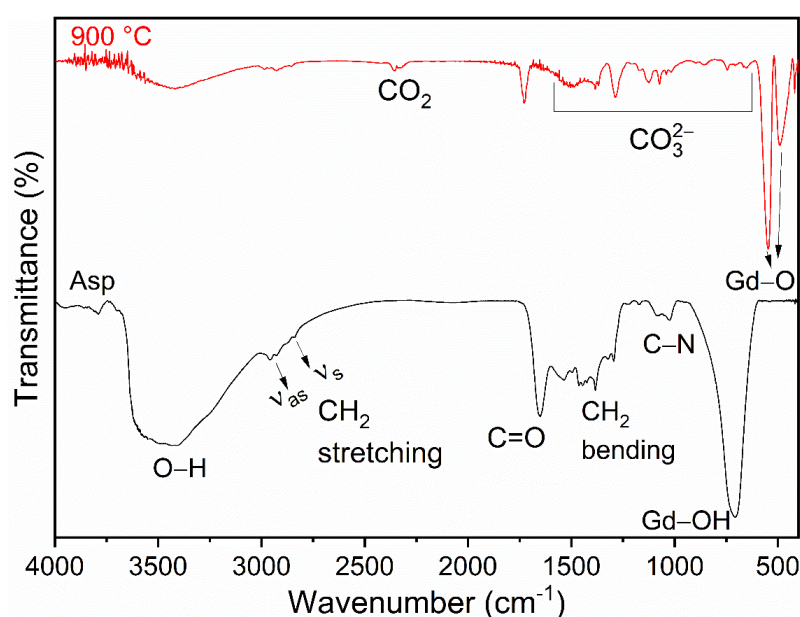


Fig. 5.3. FT-IR spectra of as-prepared $Gd(OH)_3:Eu^{3+}$ (5 at.%) (bottom) and (b) $900^\circ C$ annealed $Gd_2O_3:Eu^{3+}$ (5 at.%) samples (top).

FT-IR spectra of as-prepared $Gd(OH)_3:Eu^{3+}$ (5 at.%) and $900^\circ C$ annealed $Gd_2O_3:Eu^{3+}$ (5 at.%) samples are shown in Fig. 5.3. The absorption band at 3420 cm^{-1} corresponds to the $-OH$ stretching vibrations [13,21]. The bands at 2958 and 2856 cm^{-1} are due to the asymmetric and symmetric stretching vibrations of CH_2 , while the

bending vibration is observed at $1382, 1456\text{ cm}^{-1}$ [52-54]. The split vibrational peaks at 1023 and 1085 cm^{-1} correspond to the C–N vibrations of PVP [55]. The absorption peak at 1651 cm^{-1} is due to the asymmetric stretching of C=O bond [54,55]. The C=O vibration of pure PVP is normally observed at $\sim 1661\text{ cm}^{-1}$ [55]. However, this peak is red shifted at 1651 cm^{-1} . Such red shifting at $\sim 1647\text{ cm}^{-1}$ when PVP is used as capping agent in AgSe was reported due to band weakening after partial donation of oxygen to Ag [55]. Therefore, the –OH bending vibration which is usually observed at $\sim 1651\text{ cm}^{-1}$ [53] could not be observed. This might be due to the merger with the C=O vibrational peak. The presence of red shifted C=O bond and splitting of C–N vibrational bands of PVP implicates the surface functionalization in the as-prepared sample. The Gd–OH vibration band is observed at 707 cm^{-1} and suggests the formation of $Gd(OH)_3$ [50,51]. When the as prepared samples are heated at $900\text{ }^\circ\text{C}$, Gd–O vibration bands at 546 and 490 cm^{-1} are appeared instead of Gd–OH suggesting the formation of Gd_2O_3 . Carbonate absorption are observed at $1495, 1385, 1087$, and 1022 cm^{-1} [56-59].

5.3.3 Transmission electron microscopy study

TEM images of as-prepared and $900\text{ }^\circ\text{C}$ annealed samples are shown in Fig. 5.4 and 5.5 respectively. Particles are in rod shape with an average diameter of $180 - 400\text{ nm}$ and $800 - 1046\text{ nm}$ in length (Fig. 5.4(a)).

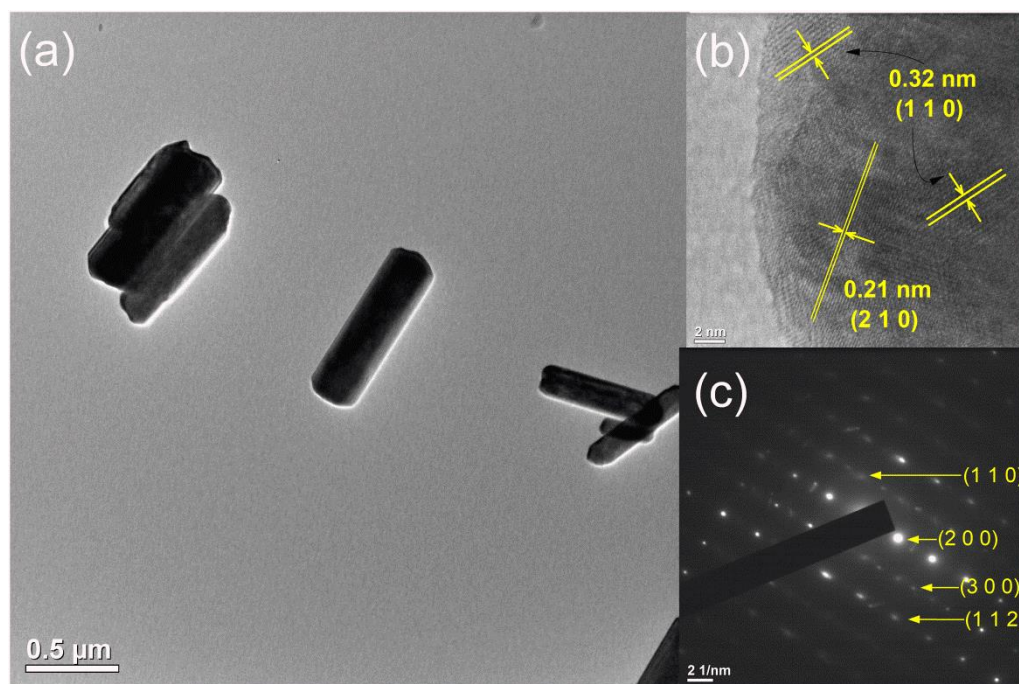


Fig. 5.4. TEM images (a) along with HR-TEM (b) and SAED images (c) of a selected region of as-prepared $Gd(OH)_3:Eu^{3+}$ (9 at.%).

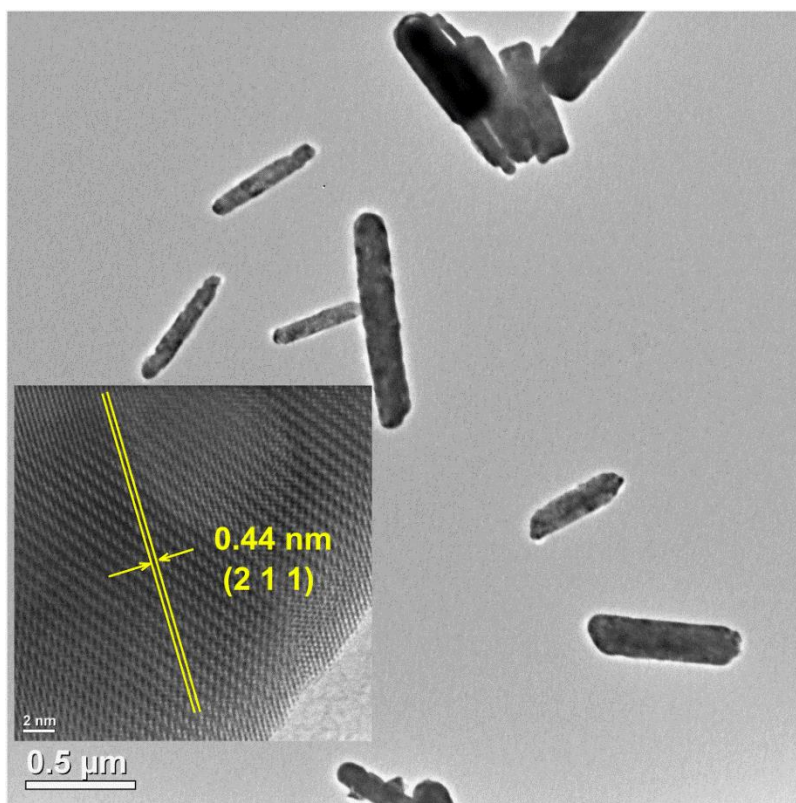


Fig. 5.5. TEM image along with HR-TEM image of 900 °C annealed $Gd_2O_3:Eu^{3+}$ (39 at.%).

Whereas, the particles with $\sim 100 - 300$ nm in diameter and $\sim 500 - 1000$ nm in length are observed in annealed samples (Fig. 5.5(a)). The measured interplanar spacing of 0.21 and 0.32 nm of as-prepared sample corresponds to (210) and (110) planes of hexagonal $Gd(OH)_3$ (Fig. 5.4(b)). The diffraction planes from the SAED images (Fig. 5.4(c)) are also matched with that of $Gd(OH)_3$ thus confirms the formation of crystalline $Gd(OH)_3$. On the other hand, interplanar spacing of 0.44 nm corresponds to (211) plane of cubic Gd_2O_3 (Fig. 5.5inset).

5.3.4. Photoluminescence studies of $Gd_2O_3:Eu^{3+}$

5.3.4.1. Steady state PL study

Excitation spectra of $Gd_2O_3:Eu^{3+}$ ($Eu^{3+} = 1, 3, 7, 11, 15, 19, 21$ and 25 at.%) samples are illustrated in Fig. 5.6. All the excitation spectra consists a broad peak in the 230 to 290 nm peaking at 265 nm and 274 nm.

The former peak related to the charge transfer band (CTB) band as a result of electron transfer from the $2p$ orbitals of oxygen to the empty $4f$ orbitals of the Eu^{3+} (denoted as Eu-O CTB) [8,27,38,46,60]. On the other hand, the sharp peak observed at 274 nm is due to the $^8S_{7/2} \rightarrow ^6I_{7/2-17/2}$ transition within the Gd^{3+} [35-40]. And, other sharp

peak in the longer wavelength region at 363 (${}^7F_0 \rightarrow {}^5D_4$), 381 (${}^7F_0 \rightarrow {}^5G_2$) 393 (${}^7F_0 \rightarrow {}^5L_6$) and 464 (${}^7F_0 \rightarrow {}^5D_2$) nm are due to transitions within $f-f$ shell of Eu^{3+} (indicated inside the parenthesis) [8,18,21,38,61]. The excitation intensity increases with the increase of Eu^{3+} concentration upto 19 at.% and thereafter the intensity is decreased. The careful observation in the Eu-O CTB, the peak is red shifted from ~ 256 to 266 nm.

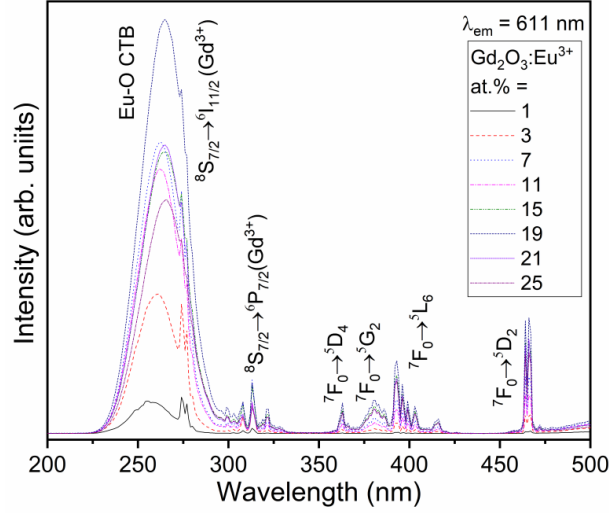


Fig. 5.6. PL excitation spectra of $Gd_2O_3:Eu^{3+}$ ($Eu^{3+} = 1, 3, 7, 11, 15, 19, 21$ and 25 at.%) samples monitored at $\lambda_{em} = 611$ nm

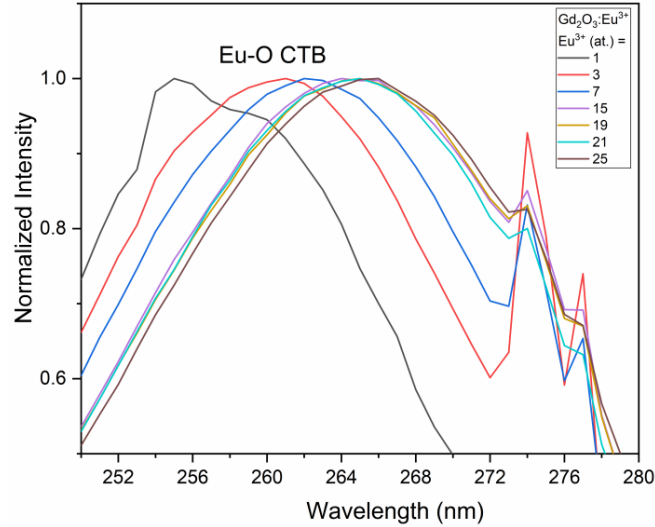


Fig. 5.7. Expanded region ($\sim 250 - 280$ nm) region of PL excitation spectra of $Gd_2O_3:Eu^{3+}$ ($Eu^{3+} = 1, 3, 7, 11, 15, 19, 21$ and 25 at.%) samples monitored at $\lambda_{em} = 611$ nm

The shift is obvious when the concentration of Eu^{3+} is increased from 1 to 7 at.%. Thereafter, the shift in the Eu-O CTB is almost constant from 11 to 25 at.% (See Fig. 5.7). Fig. 5.8 shows the emission spectra of $Gd_2O_3:Eu^{3+}$ (7 at.%) samples under different excitations at 255 nm (Eu-O CT), 274 nm (Gd^{3+} , S-I), and direct excitations at 393 (Eu^{3+} , ${}^7F_0 \rightarrow {}^5L_6$) and 464 (Eu^{3+} , ${}^7F_0 \rightarrow {}^5D_2$) nm.

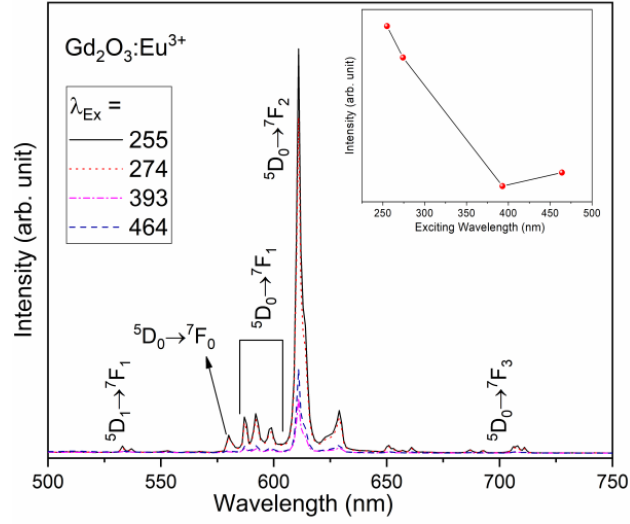


Fig. 5.8. PL emission spectra of $\text{Gd}_2\text{O}_3:\text{Eu}^{3+}$ (7 at.%) samples under different excitations at 257 nm (Eu–O CT), 274 nm (Gd^{3+} , S–I), 335 nm, 393 (Eu^{3+} , ${}^7\text{F}_0 \rightarrow {}^5\text{L}_6$) and 464 (Eu^{3+} , ${}^7\text{F}_0 \rightarrow {}^5\text{D}_2$) nm. Inset shows the comparison of emission intensities at these excitation wavelengths.

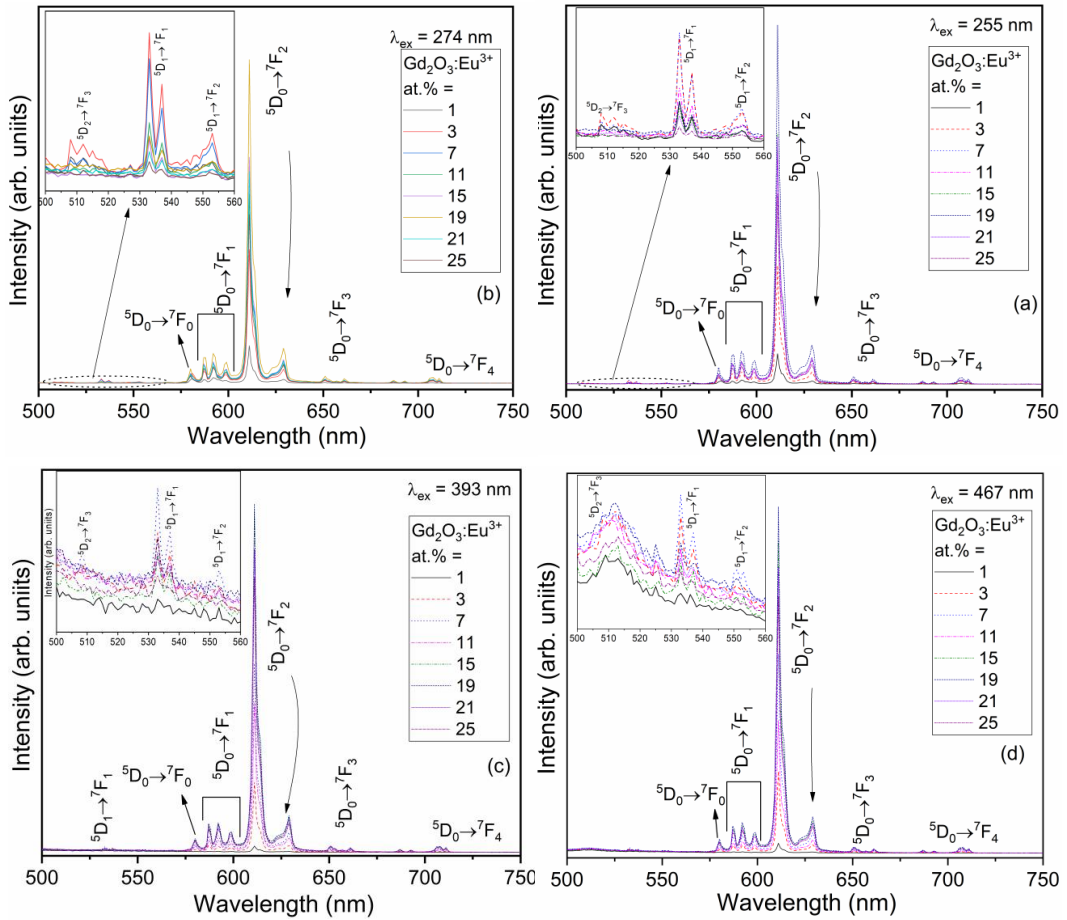


Fig. 5.9. PL emission spectra of $\text{Gd}_2\text{O}_3:\text{Eu}^{3+}$ ($\text{Eu}^{3+} = 1, 3, 7, 11, 15, 19, 21$ and 25 at.%) samples. $\lambda_{\text{ex}} =$ (a) 255, (b) 274 (c) 393 and (d) 464 nm.

Considering the 611 nm emission which is highest among other peaks, it is clearly seen that the emission intensity is highest when excited at 255 nm compared to the remaining excitations. This clearly suggests the efficient transfer of excited photons from the Eu-O CTB to the excited states of Eu^{3+} . Similarly, migration of energy to the Eu^{3+} is also observed from S-I absorption of the Gd^{3+} .

Fig. 5.9 illustrates the emission spectra of $Gd_2O_3:Eu^{3+}$ (1, 3, 7, 11, 15, 19, 21 and 25 at.%) samples under the (a) 255, (b) 274, (c) 393 and (d) 464 nm excitation. All the emission spectra consist of sharp emission peaks in the region of ~ 500 to 750 nm. These are related to the transitions within the $f-f$ electronic energy levels of Eu^{3+} . These transitions are categorized as (i) magnetic dipole transitions: $^5D_2 \rightarrow ^7F_3$ at 512 nm, $^5D_1 \rightarrow ^7F_1$ at 533 and 537 nm, $^5D_1 \rightarrow ^7F_2$ at 553, $^5D_0 \rightarrow ^7F_1$ at 587, 592 and 599 nm, $^5D_0 \rightarrow ^7F_3$ at 651 nm. (ii) Electric dipole transitions: $^5D_0 \rightarrow ^7F_2$ at 611 and 629 nm and (iii) electric quadrupole: $^5D_0 \rightarrow ^7F_4$ at 708 and 711 nm, respectively [8,18,21,38,61]. Apart from these emission peaks, a peak at 581 nm is also observed. This is due to the strictly forbidden $^5D_0 \rightarrow ^7F_0$ transition (discussed later). Among all these Eu^{3+} transitions, emission at 611 nm is strongest.

The emission peak due to the electric dipole transitions ($^5D_0 \rightarrow ^7F_2$) is stronger than the magnetic dipole transitions ($^5D_0 \rightarrow ^7F_1$). According to Judd-Ofelt theory, the electric dipole transitions is dependent on the environment of around the Eu^{3+} while the magnetic dipole transitions is independent [50,51,57]. This can be understood by considering the crystal structure of Gd_2O_3 . In cubic Gd_2O_3 , non-centrosymmetric, C_2 symmetry sites contributes $\sim 75\%$ while the centrosymmetric, S_6 symmetry has $\sim 25\%$ contribution [51,62]. When the Eu^{3+} occupies the non-centrosymmetric sites, the electric dipole transition becomes forced electric dipole and dominant among other transitions. The occupation of Eu^{3+} in C_2 site is further corroborated by the presence of 3 (three) Stark components in $^5D_0 \rightarrow ^7F_1$ transition in all the spectra. This is against the allowed 2 (two) components whenever Eu^{3+} occupies centrosymmetric site [63]. The asymmetric environment around the Eu^{3+} can be further understood from the asymmetric ratio (A). The asymmetric ratio (A) is defined by the ratio of integrated emission intensity of $^5D_0 \rightarrow ^7F_2$ to $^5D_0 \rightarrow ^7F_1$ is considered. The asymmetric ratio (A) is given by

$$A = \frac{\int_{603}^{633} I_{ed} d\lambda}{\int_{585}^{602} I_{md} d\lambda} \quad (5.1)$$

where, I_{ed} refers to $^5D_0 \rightarrow ^7F_2$ and I_{md} is $^5D_0 \rightarrow ^7F_1$. The integration limits are wavelengths (nm). Fig. 5.10 shows the asymmetric ratio of the $Gd_2O_3:Eu^{3+}$ (1, 3, 7, 11, 15, 19, 21 and 25 at.%) samples under the excitation wavelengths of 255, 374, 393 and 464 nm (calculated from the original data of the Fig. 5.9). In all the cases, the 'A' value increases with the increase of Eu^{3+} concentration and becomes roughly constant after 7 at.%. This suggests the increase occupancy of the C_2 sites by the Eu^{3+} . Thus, the emission is predominantly from the Eu^{3+} located in the C_2 sites [35].

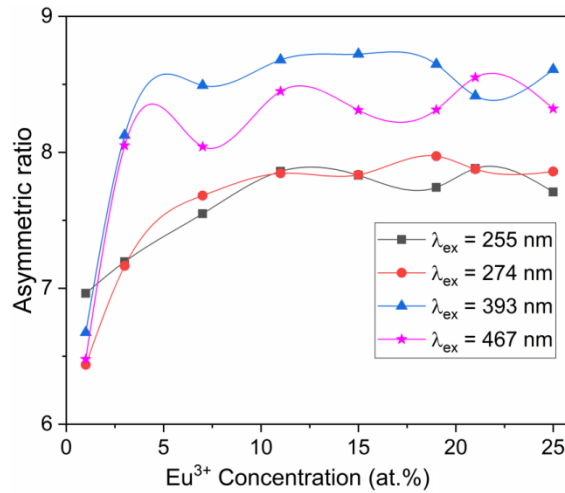


Fig. 5.10. Asymmetric ratio at different concentration of Eu^{3+} in $Gd_2O_3:Eu^{3+}$ ($Eu^{3+} = 1, 3, 7, 11, 15, 19, 21$ and 25 at.%) samples. $\lambda_{ex} = 255, 274, 393$ and 464 nm.

This increase in the asymmetric ratio indicates the increase in lattice substitution of Eu^{3+} in the C_2 sites of Gd^{3+} in $Gd_2O_3:Eu^{3+}$ [62,63]. The asymmetric ratios in all the cases are within ~6-9. This suggests that the Eu^{3+} is located in the asymmetric environment irrespective of variation of Eu^{3+} concentrations. Also, the nature of the environment around the Eu^{3+} is independent of excitation wavelengths.

Again, the observation of strictly forbidden $^5D_0 \rightarrow ^7F_0$ transition at 581 nm may be looked as a perturbation in the surrounding of the Eu^{3+} which may be due to the asymmetric nature at C_2 sites. As explained thoroughly in Chapter 3 and 4, such observation cannot be explained by Judd and Ofelt theory which is based on the closure approximation of mixing higher lying odd parity states with $4f$ states. The most probable mechanism is due to J -mixing with the dominant contribution from mixing of 7F_0 and 7F_2 in comparison with other higher lying f -manifolds in the ground state as proposed by G. Nishimura and T. Kushida [64]. This idea is further extended by other authors

with the consideration second order crystal field parameter [65,66]. The second order crystal field parameter is calculated using [65]

$$\frac{I_{0 \rightarrow 0}}{I_{0 \rightarrow 2}} = \frac{4B_{20}^2}{75\Delta_{20}^2} \quad (5.2)$$

where, B_{20} is the second order crystal field parameter, and Δ_{20} is the energy separation between 7F_0 and 7F_2 which value was taken as 900 cm^{-1} . Fig. 5.11 shows the variation B_{20} versus the concentration under excitation of 255 and 274 nm. The B_{20} values vary from 728 to 1258 cm^{-1} and 728 to 1387 cm^{-1} under the respective excitations of 255 and 274 nm. Similar trend was also in the case of Y_2O_3 (See Sec. 4.3.4.2, Chapter 4). These high values indicate the perturbation around the Eu^{3+} environment.

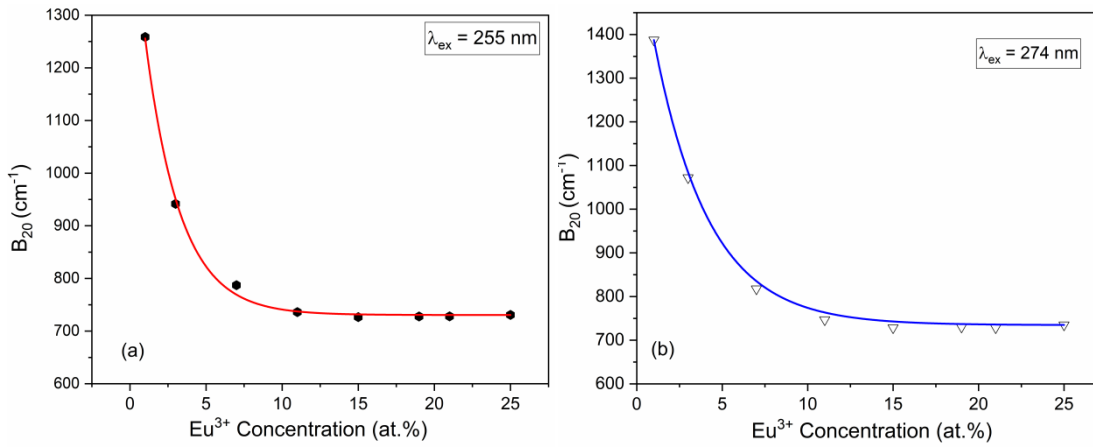


Fig. 5.11. Variation of B_{20} versus Eu^{3+} concentration of $Gd_2O_3:Eu^{3+}$ ($Eu^{3+} = 1, 3, 7, 11, 17, 21$ and 25 at.%) samples. Excitation wavelengths (λ_{ex}) are indicated in the graph. Dash (red) line is guide to the eye.

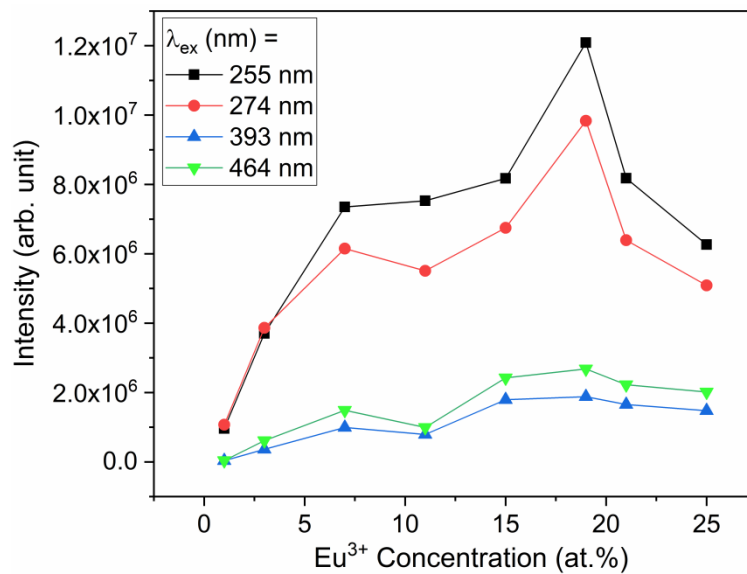


Fig. 5.12. Integrated emission intensities of $Gd_2O_3:Eu^{3+}$ ($Eu^{3+} = 1, 3, 7, 11, 15, 19, 21$ and 25 at.%) samples. $\lambda_{ex} = 255, 274, 393$ and 464 nm.

Fig. 5.12 shows the integrated emission intensities of dominant $^5D_0 \rightarrow ^7F_2$ (611 nm) of $Gd_2O_3:Eu^{3+}$ (1, 3, 7, 11, 15, 19, 21 and 25 at.%) samples. The excitation wavelengths are 255, 374, 393 and 464 nm. In all the cases, the luminescence intensity increases with the increase of Eu^{3+} concentration. The maximum intensity of the luminescence is observed at 19 at.% of Eu^{3+} . Thereafter, the intensity decreases with the increase of concentration. Such phenomenon of the decreasing luminescence intensity after certain concentration of is quite common in lanthanide activated phosphors. When the concentration becomes high, the distance between the Eu^{3+} becomes shorter and leads to cross-relaxation among them which is non-radiative. This increases the probability of non-radiative transitions.

5.3.4.2. PL decay lifetime and quantum yield study

Fig. 5.13 shows the decay curves of 5D_0 level of Eu^{3+} emission in $Gd_2O_3:Eu^{3+}$ (1, 3, 7, 11, 15, 19, 21 and 25 at.%) samples excited at 255 and 464 nm by monitoring 611 nm emission. All the decay profiles follow the second order exponential decay,

$$I(t) = I_1 e^{-\frac{t}{\tau_1}} + I_2 e^{-\frac{t}{\tau_2}} \quad (5.3)$$

where I_1 and I_2 stand for intensities at two different times. The τ_1 and τ_2 represent the corresponding lifetimes.

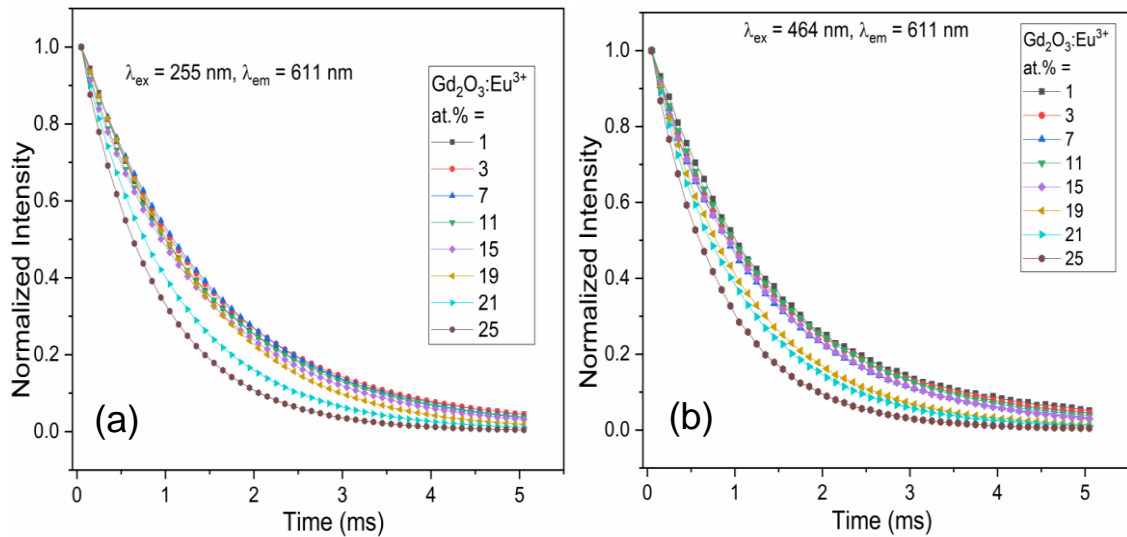


Fig. 5.13. PL decay curves of 5D_0 level of Eu^{3+} emission in $Gd_2O_3:Eu^{3+}$ (1, 3, 7, 11, 15, 17, 21 and 25 at.%) samples under (a) 255 and (b) 464 excitation and the emission is monitored at 611 nm.

Typical fitting is given in Fig. 5.14. The average decay lifetime can be calculated using,

$$\tau_{av} = \frac{I_1\tau_1^2 + I_2\tau_2^2}{I_1\tau_1 + I_2\tau_2} \quad (5.4)$$

The average decay lifetime calculated using Eqn. 5.4 is given in Table 5.2. The average decay lifetime under the excitation of 255 nm varies from 0.88 to 1.77 ms.

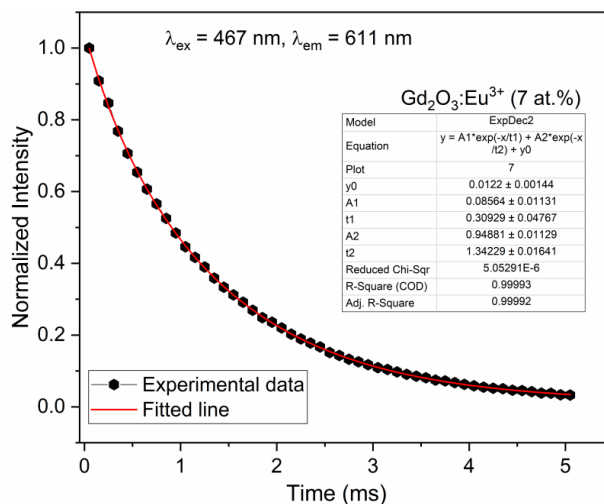


Fig. 5.14. Typical fitting of decay curve for Eu^{3+} emission ($\lambda_{ex} = 464$ nm and $\lambda_{em} = 611$ nm) in $Gd_2O_3:Eu^{3+}$ (7 at.%) sample.

Table 5.2. The average lifetime calculated for the decay curves of 5D_0 level of Eu^{3+} and Quantum yield in $Gd_2O_3:Eu^{3+}$ (1, 3, 7, 11, 15, 19, 21 and 25 at.%) samples.

Eu^{3+} (%)	Decay lifetime, τ_{av} (ms)				Quantum Yield (%)
	$\lambda_{exc} = 255$ nm		$\lambda_{exc} = 464$ nm		$\lambda_{exc} = 255$ nm
	τ_{av}	R^2	τ_{av}	R^2	
1	1.67(1)	0.99	1.41(1)	0.99	5
3	1.77(2)	0.99	1.39(1)	0.99	5
7	1.50(1)	0.99	1.32(1)	0.99	-
11	1.44(1)	0.99	1.42(1)	0.99	6
15	1.38(2)	0.99	1.34(2)	0.99	-
19	1.33(1)	0.99	1.10(1)	0.99	7
21	1.06(1)	0.99	1.01(1)	0.99	5
25	0.88(2)	0.99	0.82(2)	0.99	

While, under direct excitation at 464 nm, the lifetime value changes from 0.82 to 1.42 ms. From the Table 5.2, it is observed that the decay lifetime value in both the cases are more in the Eu^{3+} range of 1 to 11 at.%. Thereafter, the lifetime steadily decreases with the further increase of Eu^{3+} concentration. Such decrease in the decay

lifetime of lanthanide ions emission beyond certain concentration is attributed to the increase in the non-radiative transitions due to the cross relaxation among lanthanide ions. Such behaviour has been reported earlier [13,18]. The absolute quantum yield measurements were performed following the report [18,21]. The quantum yields for $Gd_2O_3:Eu^{3+}$ (19 at.%) under 255 nm excitation are found to be 7%. The quantum yields of some the $Gd_2O_3:Eu^{3+}$ (x at.%) samples under 255 nm excitation are given in Table 5.2.

5.3.4.3. CIE chromaticity studies

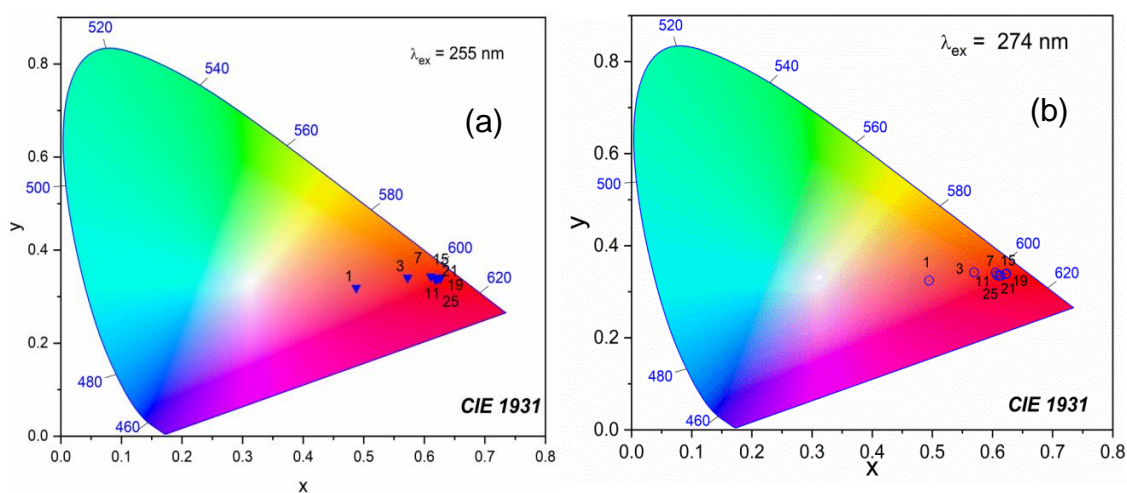


Fig. 5.15. CIE chromaticity coordinate positions of $Gd_2O_3:Eu^{3+}$ (0, 1, 3, 5, 7, 9, 11, 13, 15, 17, 19, 21 and 23 at.%) samples excited at (a) 255 and (b) 274 nm.

The Commission International de l'Eclairage (CIE) chromaticity was analysed to understand the colour of the emission from different samples with the variation of Eu^{3+} concentration as well as excitation wavelength. The CIE positions of the $Gd_2O_3:Eu^{3+}$ (1, 3, 7, 11, 15, 19, 21 and 25 at.%) samples under the excitations of 255 and 274 nm are indicated in the diagram (Fig. 5.15). Under both the excitation wavelengths, it is clearly observed that the colour of the emission is mostly concentrated in the red region.

5.3.5. Photoluminescence studies of $Gd_2O_3:Sm^{3+}$

5.3.5.1. Steady state PL study

Fig. 5.16 shows the excitation spectra of $Gd_2O_3:Sm^{3+}$ (0.5, 1, 2, 4, 6, 8, 10, and 12 at.%) samples monitored at 606 nm. All the excitation spectra consist of sharp peaks from (i) related to the S-I absorption of Gd^{3+} and (ii) excitation peaks originated from

the f - f transitions of Sm^{3+} . Absorption peaks due to Gd^{3+} are observed at 242, 254 and 274 nm. These are arisen due to the transition from ground state $^8\text{S}_{7/2}$ to the different excited states of $^6\text{D}_{5/2}$, $^6\text{D}_{9/2}$ and $^6\text{I}_{7/2-17/2}$ transitions within the Gd^{3+} [35,36]. And, other sharp peaks in the longer wavelength region are observed at 313 ($^7\text{H}_{5/2} \rightarrow ^4\text{G}_{9/2}$), 346 ($^7\text{H}_{5/2} \rightarrow ^4\text{K}_{17/2}$), 362 ($^7\text{H}_{5/2} \rightarrow ^4\text{D}_{3/2}$), 378 ($^7\text{H}_{5/2} \rightarrow ^6\text{P}_{7/2}$), 406 ($^7\text{H}_{5/2} \rightarrow ^6\text{P}_{3/2}$), 422 ($^7\text{H}_{5/2} \rightarrow ^6\text{D}_{5/2}$), 467 ($^7\text{I}_{11/2} \rightarrow ^6\text{P}_{3/2}$), and 492 nm ($^7\text{H}_{5/2} \rightarrow ^6\text{G}_{7/2}$) [67-70]. These are originated from the f - f shell of Sm^{3+} .

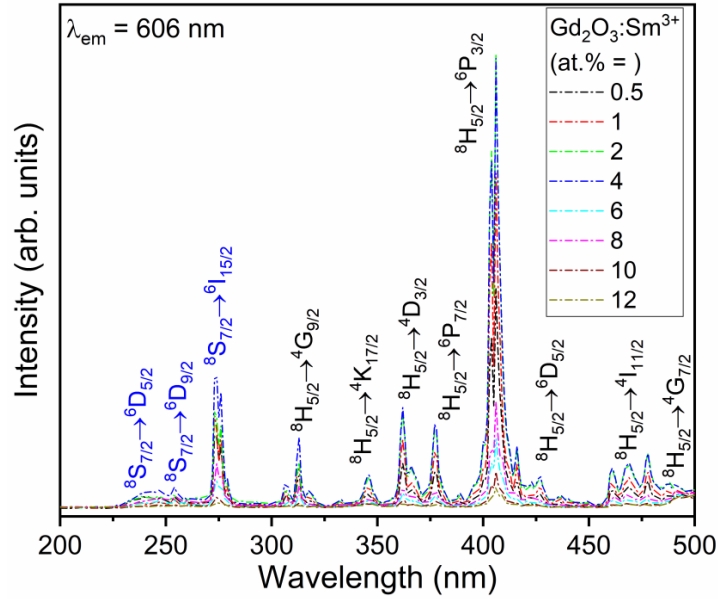


Fig. 5.16. PL excitation spectra of $\text{Gd}_2\text{O}_3:\text{Sm}^{3+}$ (0.5, 1, 2, 4, 6, 8, 10 and 12 at.%) samples monitored at $\lambda_{\text{em}} = 606$ nm.

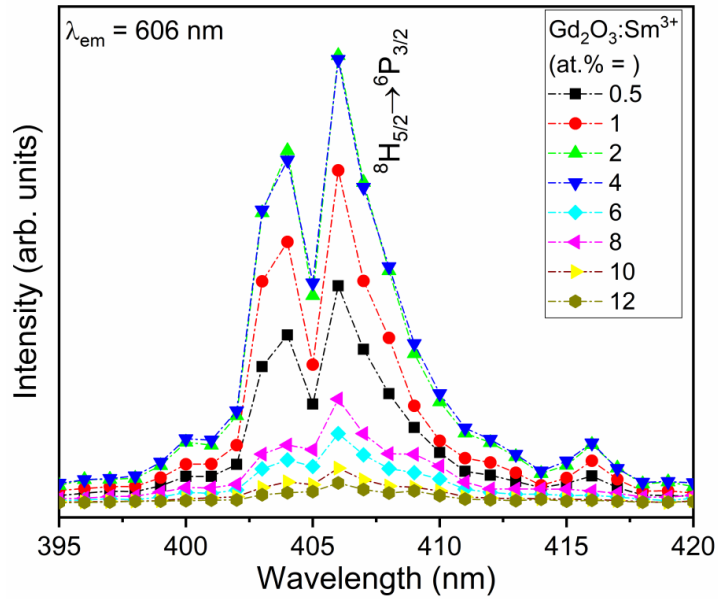


Fig. 5.17. PL excitation spectra of $\text{Gd}_2\text{O}_3:\text{Sm}^{3+}$ (0.5, 1, 2, 4, 6, 8, 10 and 12 at.%) samples in the region of 395 – 420 nm.

Fig. 5.17 shows the expanded portion the excitation spectra indicating the highest peak at 406 nm. From the figure, it is clearly observed that the intensity of the peak increases with the increase of concentration upto 2 – 4 at.% of Sm^{3+} . Thereafter, the intensity decreases with the increase of Sm^{3+} concentration.

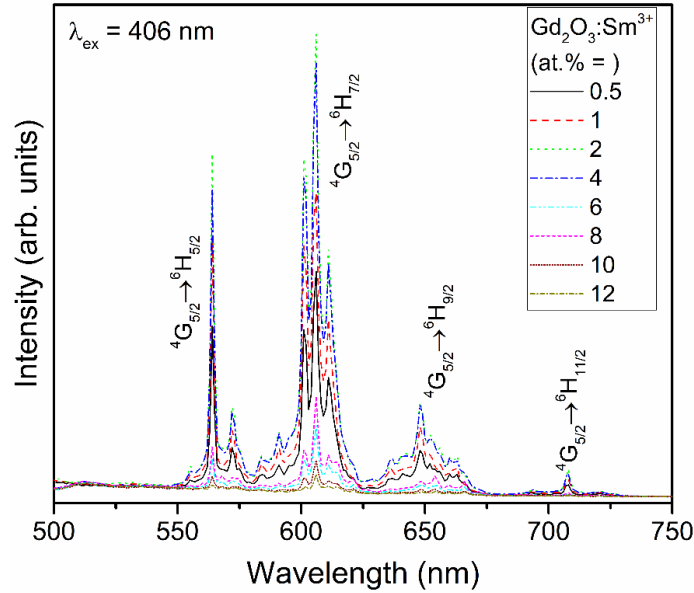


Fig. 5.18. PL emission spectra of $Gd_2O_3:Sm^{3+}$ (0.5, 1, 2, 4, 6, 8, 10 and 12 at.%) samples monitored at $\lambda_{ex} = 406$ nm.

Fig. 5.18 illustrates the emission spectra of $Gd_2O_3:Sm^{3+}$ (0.5, 1, 2, 4, 6, 8, 10, and 12 at.%) samples under the direct excitations at 406 nm. The sharp emission peaks in the region of ~ 500 to 750 nm are observed. These sharp emission peaks are related to the transitions within the $f-f$ electronic energy levels of Sm^{3+} . These emission peaks are related to the transitions originated from the $^4G_{5/2} \rightarrow ^6H_{5/2}$ (at 564 and 572 nm) and $^4G_{5/2} \rightarrow ^6H_{7/2}$ (at 602, 606 and 611 nm) are related to magnetic dipole transitions. While, the transition at $^4G_{5/2} \rightarrow ^6H_{9/2}$ (at 654 and 665 nm) is due to pure electric dipole transition [67-72]. In all the cases, the transition at $^4G_{5/2} \rightarrow ^6H_{5/2}$ (at 602, 606 and 611 nm) is dominant. Since the $\Delta J = \pm 1$, it should be magnetic dipole transition by quantum mechanical selection rule. However, this transition is considered to be dominated by electric dipole transition [71,72].

Considering the highest emission peak at 606 nm, we can observed the emission intensity is gradually increases with the increase of Sm^{3+} concentration and found to saturate at 2 – 4 at.% of Sm^{3+} . On further increase of the doping concentration, it is clearly seen that the intensity of the emission is decreased. This is obvious phenomenon in the emission by lanthanide doping. Such decrease in the emission against the higher

concentration of the doping is known as concentration quenching. This quenching occurs when the distance between the doping lanthanide ions is less than certain critical distance, cross relaxation among them dominates. The dominance of cross relaxation induces the increase non-radiative transitions. Fig. 5.19 shows the expanded portion the emission spectra indicating the highest peak at 606 nm.

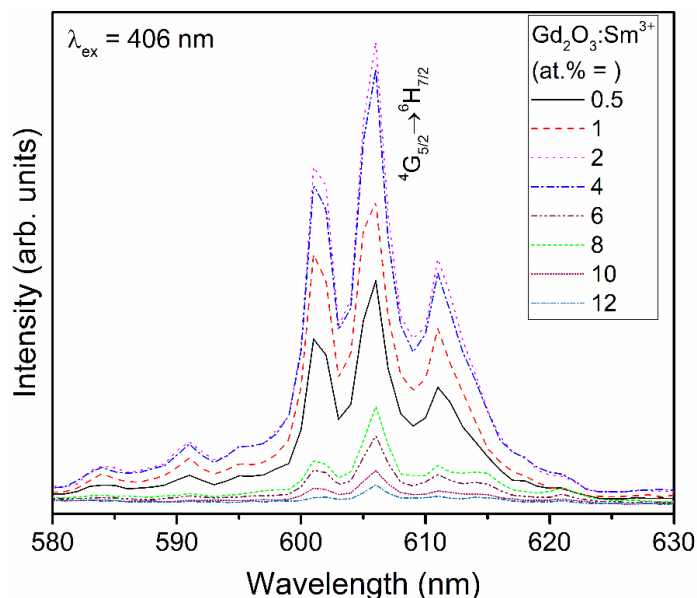


Fig. 5.19. PL emission spectra of $Gd_2O_3:Sm^{3+}$ (0.5, 1, 2, 4, 6, 8, 10 and 12 at.%) samples in the region of 580 – 630 nm.

5.3.5.2. PL decay lifetime and quantum yield study

Fig. 5.20 shows the decay profiles of $^5G_{5/2}$ level of Sm^{3+} emission in $Gd_2O_3:Sm^{3+}$ (0.5, 1, 2, 4, 6, 8, 10 and 12 at.%) samples by monitoring at 606 nm emission. Excitation wavelength is 406 nm. All the decay profiles follow the second order exponential decay (Eqn. 5.3). The average decay lifetime was calculated using Eqn. 5.4 and given in Table 5.3.

The decay lifetime varies from 0.22 to 1.71 ms. From the Table 5.3, it can be observed that the decay lifetime value in both the cases decreases with the increase of Sm^{3+} concentration. Such decrease in the decay lifetime of emission by lanthanide ions can be ascribed to the increase in the non-radiative transitions. Non-radiative transitions are due to the cross relaxation among lanthanide ions. The quantum yields for $Gd_2O_3:Sm^{3+}$ (2 and 4 at.%) under 406 nm excitation are found to be 5 and 6% respectively (Table 5.3).

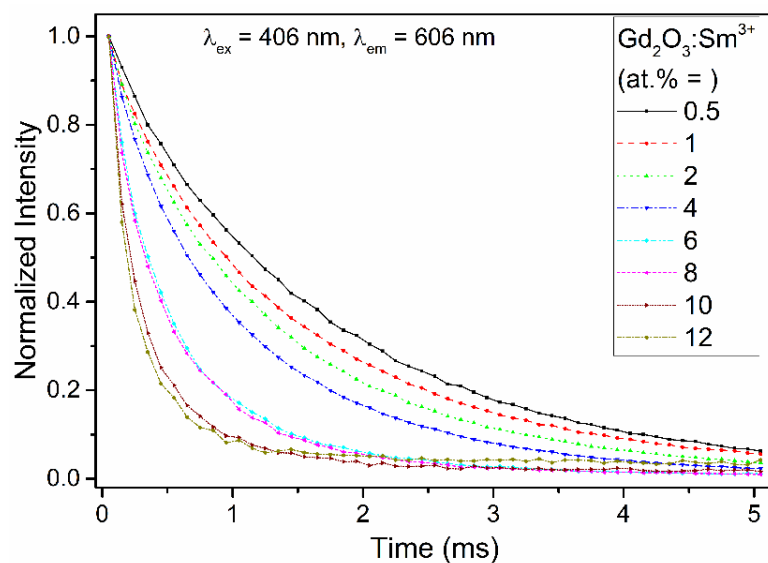


Fig. 5.20. PL decay curves of $^5\text{G}_{5/2}$ level of Sm^{3+} emission in $\text{Gd}_2\text{O}_3:\text{Sm}^{3+}$ (1, 2, 4, 6, 8, 10 and 12 at.%). $\lambda_{\text{em}} = 606$ nm and $\lambda_{\text{ex}} = 406$ nm.

Table 5.3: The average lifetime calculated for the decay curves of $^5\text{G}_{5/2}$ level of Sm^{3+} by monitoring at 606 nm emission and Quantum yield in $\text{Gd}_2\text{O}_3:\text{Sm}^{3+}$ (0.5 1, 2, 4, 6, 8, 10 and 12 at.%) samples.

Sm^{3+} (%)	Decay lifetime, τ_{av} (ms)						Quantum Yield (%)
	A_1	t_1	A_2	t_2	τ_{av}	R^2	Φ
0.5	0.086	0.225	0.947	1.732	1.71(1)	0.99	-
1	0.149	0.271	0.873	1.543	1.35(2)	0.99	-
2	0.154	0.224	0.889	1.341	1.17(2)	0.99	5
4	0.265	0.284	0.793	1.219	0.98(1)	0.99	6
6	0.556	0.217	0.575	0.793	0.52(1)	0.99	-
8	0.489	0.154	0.676	0.696	0.46(1)	0.99	-
10	0.797	0.128	0.477	0.543	0.29(1)	0.99	-
12	0.893	0.109	0.438	0.449	0.22(1)	0.99	-

5.3.5.3. CIE chromaticity studies

Fig. 5.21 illustrates the CIE chromaticity of the Sm^{3+} emission in $\text{Gd}_2\text{O}_3:\text{Sm}^{3+}$ (0.5 1, 2, 4, 6, 8, 10 and 12 at.%) samples when excited at 406 nm. From the figure, it can be observed that the emission is spread over the region of yellow and orange- red region. Samples with the Sm^{3+} concentration 2 and 4 at.% gives the emission in the orange-red region dominated with red colour. These samples under the excitation at 406 nm can promising for red component phosphor for near-UV LED excited phosphor converted white emitting LEDs.

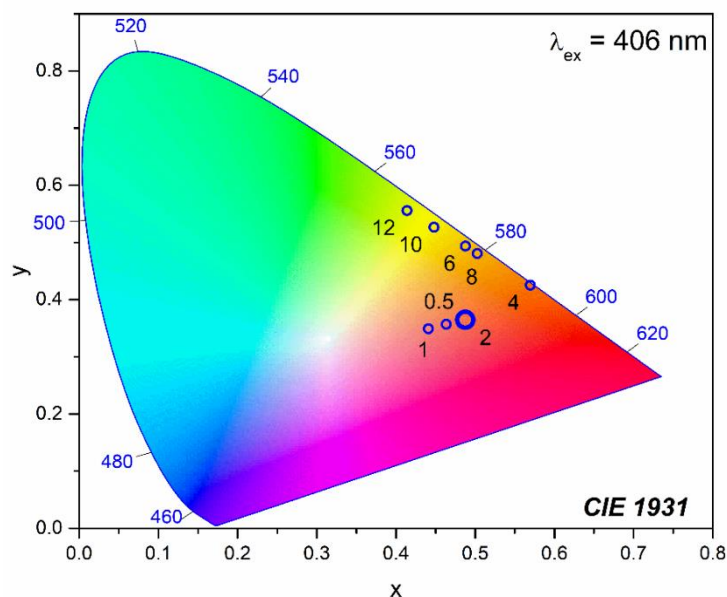


Fig. 5.21. CIE chromaticity coordinate positions of $Gd_2O_3:Sm^{3+}$ (0.5, 1, 2, 4, 6, 8, 10 and 12 at.%) samples excited at 406 nm.

5.4. Conclusions

Eu^{3+} and Sm^{3+} doped Gd_2O_3 were successfully synthesized by hydrothermal method with post annealing at 900 °C. The as prepared samples have shown to crystallize in than hexagonal phase. Subsequent heating at 900 °C changes to crystalline cubic phase. In $Gd_2O_3:Eu^{3+}$, the maximum emission of Eu^{3+} is observed at 19 at.% concentration. High asymmetric value of the emission in the entire concentration of Eu^{3+} studied indicates the fair asymmetric environment of Eu^{3+} in Gd_2O_3 . While, the high value of second order crystal field parameter also suggests the high perturbation due to the asymmetric nature in the surroundings of Eu^{3+} . Both the steady state and decay dynamics of the PL corroborates the occurrence quenching due to the increase in non-radiative transitions. CIE coordinates suggest red emission by all the samples. In $Gd_2O_3:Sm^{3+}$, all the emission are observed in the orange-red region. The highest emission intensity is observed at 2 – 4 at.% of Sm^{3+} . Quenching of emission after 2 – 4 at.% of Sm^{3+} is observed. This is due to the increase in non-radiative transition because of cross-relaxation. This has been corroborated from the decay lifetime of studies of $^5G_{5/2}$ emission of Sm^{3+} . Under the 406 nm excitation, 2 and 4 at.% of Sm^{3+} doped Gd_2O_3 samples show the orange-red emission in the CIE study. These samples could be a potential red emitting phosphor component for near UV LED converted white LEDs.

References

1. M. Flynn, A.H. Kitai, J. Electrochem. Soc. 148 (2001) H149
2. M. Yu, J. Lin, Y.H. Zhou, S.B. Wang, Mater. Lett. 56 (2002) 1007
3. T. Hirai, T. Hirano, I. Komasaawa, J. Colloid Interface Sci. 253 (2002) 62.
4. K.-M. Lin, Y.-Y Li, Nanotechnology, 17 (2006) 4048 – 4052.
5. C.H. Kim, E.II Kwon, C.H. Cicillini, J. Alloys Compd, 311 (2000) 33.
6. B. Mercier, C. Dujardin, G. Ledoux, C. Louis, O. Tillement, J. Appl. Phys. 96 (2004) 650.
7. J.Y. Choe *et al.*, Appl. Phys. Lett. 78 (2001) 3800.
8. D. Ghosh, M. N. Luwang, J. Lumin. 171 (2016) 1-8.
9. Z. Liu, X. Liu, Q. Yuan, K. Dong, L. Jiang, Z. Li, J. Ren, X. Qu, J. Mater. Chem. 22 (2012) 14982.
10. T. Paik, T.R. Gordon, A.M. Prantner, H. Yun, C.B. Murray, ACS Nano, 7 (2013) 2850.
11. X. Huang, Nat. Photonics 8 (2014) 748-749.
12. M. Shang, C. Li, J. Lin, Chem. Soc. Rev. 43 (2014) 1372-1386.
13. N. S. Singh, N. K. Sahu, D. Bahadur, J. Mater. Chem. C 2 (2014) 548.
14. T. Sakthivel, G. Annadurai, R. Vijayakumar, X. Huang, J. Lumin. 205 (2019) 129-135.
15. Q. Zhang, X. Wang, X. Ding, and Y. Wang, Inorg. Chem. 56 (2017) 6990–6998.
16. P. Du, J. S. Yu, Sci. Rep. 7 (2017) 11953.
17. S. Shi, L. Wang, M. Fang, L. Fu, L. D. Carlos, R. A. S. Ferreira, J. Wang, S. Wang, J. Alloys Compd. 814 (2020) 15226-15232.
18. R. Wangkhem, T. Yaba, N. S. Singh, R. S. Ningthoujam, J. Appl. Phys. 123 (2018) 124303.
19. S. Yan, J. Zhang, X. Zhang, S. Lu, X. Ren, Z. Nie, X. Wang, J. Phys. Chem. C, 111 (2007) 13256-13260.
20. A. Xie, X. Yuan, S. Hai, J. Wang, F. Wang and L. Li, J. Phys. D: App. Phys. 42 (2009) 1-7.
21. T. Yaba, R. Wangkhem, N. S. Singh, J. Alloys Compd., 843 (2020) 156022-156031.
22. P. Du, L.K. Bharat, J.S. Yu, J. Alloys Compd. 633 (2015) 37–41.
23. R.B. Pode, S.J. Dhoble, Phys. Stat. Sol. (b) 203 (1997) 571-577.
24. L. Chen, K.J. Chen, C.C. Lin, C.I. Chu, S.F. Hu, M.H. Lee, R.S. Liu, J. Comb. Chem. 12 (2010) 587–594.
25. S. Takeshita, T. Isobe, S. Niikura, J. Lumin. 128 (2008) 1515 – 1522.
26. L. S. Chi, R. S. Liu, B. J. Lee, J. Electrochem. Soc. 152(8) (2005) J93-J98.
27. W. Wang, P. Zhu, Opt. Express 26 (2018) 34820-34829.
28. P. Zhu, W. Wang, H. Zhu, P. Vargas, A. Bont, IEEE Photonics J. 10 (2018) 1-10.
29. G. Ju, Y. Hu, L. Chen, X. Wang, Z. Mu, H. Wu, F. Kang, J. Electrochem. Soc. 158 (2011) J294-J299.
30. T. W. Chou, S. Mylswamy, R. S. Liu, S. Z. Chuang, Solid State Commun. 136 (2005) 205-209.
31. B. Liu, J. Li, G. Duan, Q. Li, Z. Liu, J. Lumin. 206 (2019) 348-358.
32. X. T. Wei, Y. H. Chen, X. R. Cheng, M. Yin, W. Xu, Appl. Phys. B 99 (2010) 763-768.
33. L. Xu, Y. Li, Q. Pan, D. Wang, S. Li, G. Wang, Y. Chen, P. Zhu, W. Qin, ACS Appl. Mater. Interfaces 12 (2020) 18934-18943.
34. B. Bihari, H. Eilers, B. M. Tissue, J. Lumin. 75 (1997) 1-10.
35. X. Wu, S. Hu, C. Tan, Y. Liu, Opt. Commun. 328 (2014) 23.

36. Q. Li, J. Lin, J. Wu, Z. Lan, Y. Wang, F. Peng, M. Huang, J. Lumin. 134 (2013) 59.
37. J.F. Martel, S. Jandl, B. Viana, D. Vivien, J. Solid State Chem. 61 (2000) 1455.
38. R. S. Ningthoujam, R. Shukla, R. K. Vatsa, V. Duppel, L. Kienle, A. K. Tyagi, J. Appl. Phys. 105 (2008) 084304.
39. G. Blasse, B.C. Grabmeier, *Luminescent Materials*, Springer-Verlag, (1994) New York.
40. W.M. Yen, S. Shionoya, H. Yamamoto, *Phosphor Handbook*, CRC Press, Taylor & Francis, (2007) New York
41. G. Blasse, G.J. Dirksen, A. Meyerink, D.R. Terrell, L. Neyens, Mater. Chem. Phys. 19 (1988) 547.
42. Z. Xu, J. Yang, Z. Hou, C. Li, C. Zhang, S. Huang, J. Lin, Mater. Res. Bull. 44 (2009) 1850.
43. R. Fu, M. Ou, C. Yang, Y. Hu, H. Yin, J. Lumin. 222 (2020) 117154.
44. S. Nambram, S.D. Singh, Mater. Today Proc.
 <https://doi.org/10.1016/j.matpr.2022.04.508>
45. L. Peng, T. Han, H. Chen, T. Zhang, J. Rare Earths 31 (2013) 235.
46. V. Bedekar, D.P. Dutta, M. Mohapatra, S.V. Godbole, R. Ghildiyal, A.K. Tyagi, Nanotechnology 20 (2009) 125707.
47. G. Boopathi, S.G. Raj, G.R. Kumar, R. Mohan, Mater. Today Proc. 2 (2015) 3684.
48. Q. Li, J. Lin, J. Wu, Z. Lan, Y. Wang, F. Peng, M. Huang, J. Limun. 134 (2013) 59.
49. J.F. Martel, S. Jandl, B. Viana, D. Vivien, J. Solid State Chem. 61 (2000) 1455.
50. M. Buijs, A. Mayerink, and G. Blasse, J. Lumin. 37 (1987) 9-20.
51. M. L. Debasu, D. Ananias, A. G. Macedo, J. Rocha, L. D. Carlos, J. Phys. Chem. C 115 (2011) 15297–15303.
52. G. Liu, Y. Zhang, J. Yin, and W. F. Zhang, J. Lumin. 128 (2008) 2008-2012.
53. B. Qian, H. Zou, D. Meng, X. Zhou, Y. Song, K. Zheng, C. Miao and Y. Sheng, CrystEngCom. 20(45) (2018) 7322-73288.
54. R.G.A. Kumar, S. Hata, K.G. Gopchandran, J. Ceram. Int. 39(8) (2013) 9125-9136.
55. K. M. Koczur, S. Mourdikoudis, L. Polavarapu, S.E. Skrabalak, Dalton Trans. 44 (2015) 17883-17905.
56. N.K. Sahu, N. Shanta Singh, R.S. Ningthoujam, D. Bahadur, ACS Photonics 1 (2014) 337-246.
57. R. Joshi, B.P. Singh, C.L. Prajapat, Y. Kashyap, C. Nayak, D. Bhattacharyya, R.S. Ningthoujam, J. Phys. Chem. C 125 (2021) 17971-17982.
58. H. Liu, B. Zhang, H. Shi, Y. Tang, K. Jiao, X. Fu, J. Mater. Chem. 18 (2008) 2573-2580.
59. G. Liu, G. Hong, J. Wang, X. Dong, J. Alloys Compd. 4332 (2007) 200-204.
60. H. Deng, F. Chen, C. Yang, M. Chen, L. Li, D. Chen, Nanotechnology 29(41) (2018) 415601.
61. X. Liu, C. Lin, J. Lin, Appl. Phys. Lett. 90 (2007) 081904
62. G. Pappalardo, R. B. Hunt, Jr., J. Electrochem. Soc. 132 (1985) 721-730
63. E. Zych, J. Phys.: Condens. Matter 14 (2002) 5637–5650.
64. G. Nishimura, T. Kushida, Phys. Rev. B. 37 (1988) 9075–9078.
65. S. Ray, P. Pramanik, A. Singha, A. Roy J. Appl. Phys. 97 (2005) 094312.
66. A.K. Parchur, R.S. Ningthoujam, RSC Adv. 2 (2012) 10859–10868.
67. R. Wangkhem, N. S. Singh, N. P. Singh, S. D. Singh, L. R. Singh, J. Lumin. 203 (2018) 341-348.

68. N.S. Singh, R.S. Ningthoujam, G. Phaomei, S.D. Singh, A. Vinu, R.K. Vatsa, Dalton Trans. 41 (2012) 4404-4412.
69. O. Tegus, B. Amurinsana, S. Zhiqiang, J. Lumin. 215 (2019) 116624.
70. E. Cavalli, A. Belletti, R. Mahiou, P. Boutinaud, J. Lumin. 130 (2010) 733.
71. G. Lakshminarayana, J. Qiu, J. Lumin. 476 (2009) 470 – 476.
72. P.S. May, D.H. Metcalf, F.S. Richardson, R.C. Carter, C.E. Miller, R.A. Palmer, J. Lumin. 51 (1991) 249.

Chapter 6

Photoluminescence properties and energy transfer in Bi^{3+} sensitized $\text{Gd}_2\text{O}_3:\text{Ln}^{3+}$ ($\text{Ln}^{3+} = \text{Eu}^{3+}$ & Sm^{3+})

6.1. Introduction

Lanthanide activated inorganic phosphors have recently found themselves in various applications such as biological imaging [1,2], sensing [3,4] as well as solid state lighting (SSL) [5-7]. Among them, application towards the SSL has become prominent lately. This is because of the fact that the conversion of phosphors is generally adopted for generation of white light. One such commercial white emission device is the conversion of yellow phosphor (e.g., yttrium aluminate garnet, $\text{Y}_3\text{Al}_5\text{O}_{12}:\text{Ce}^{3+}$) with blue light emitting diode (LED). However, the output of the light is cool white light with Correlated Colour Temperature (CCT) value ≥ 4000 K due to the lack of proper red component. In order to develop the warm white light LED packaging with CCT value ~ 2700 K, highly efficient blue LED (e.g. GaN or InGaN) chips are used as a source to convert the green and red phosphors. Another approach which recently gained attention is the use of individual red, green and blue emitting phosphors with near UV/UV LED chips. In both the approaches, efficient red phosphor is required for producing warm white light.

Acknowledging the necessity of the development of efficient red phosphors, many researchers have recently focused in multiple directions with various types of phosphors. Among them, Eu^{2+} activated phosphors such as nitridolithoaluminate $\text{Sr}_4[\text{LiAl}_{11}\text{N}_{14}]:\text{Eu}^{2+}$ [8], $\text{SrLiAl}_3\text{N}_4:\text{Eu}^{2+}$ [9], $\text{Sr}[\text{Li}_2\text{Al}_2\text{O}_2\text{N}_2]:\text{Eu}^{2+}$ [10], $\text{Ca}[\text{LiAl}_3\text{N}_4]:\text{Eu}^{2+}$ [11] etc. have shown as promising red emitting component for SSL applications. However, the emission band of such phosphors extends beyond 700 nm and is considered waste thereby reducing their efficiency. Alternative to these, reports on Eu^{3+} activated red emitting phosphors synthesized using simple chemical method are available. For instance, $\text{Na}_2\text{Y}_2\text{B}_2\text{O}_7:\text{Eu}^{3+}$ [12], $\text{BaZrGe}_3\text{O}_9:\text{Eu}^{3+}$ [13], Eu^{3+} activated La_2MoO_6 - La_2WO_6 composite [14], $\text{La}_2\text{Ce}_2\text{O}_7:\text{Eu}^{3+}$ [15] etc. may be mentioned. Also, Bi^{3+} sensitized $\text{CaMoO}_4:\text{Eu}^{3+}$ [16-18,], $\text{CaWO}_4:\text{Eu}^{3+}$ [19-21], and $\text{YVO}_4:\text{Eu}^{3+}$ [22,23], as potential red components excitable by near UV/blue LED for SSL applications.

Lanthanide activated rare-earth oxides such as Bi^{3+} sensitized and unsensitized $\text{Y}_2\text{O}_3:\text{Eu}^{3+}$ [24-27], $\text{Y}_2\text{O}_2\text{S}:\text{Eu}^{3+}$ [28], etc. are also reported to be potential red component for near UV/UV LED converted white light emission. Like Y_2O_3 , thermally, chemically and physically stable Gd_2O_3 having low phonon energy ($\sim 600 \text{ cm}^{-1}$) is also an efficient red phosphor when activated with Eu^{3+} . $\text{Gd}_2\text{O}_3:\text{Eu}^{3+}$ phosphor has been widely reported on various applications such as dual imaging of optical and magnetic resonance imaging [29,30], sensing etc. [31,32]. Similarly, photoluminescence properties of $\text{Gd}_2\text{O}_3:\text{Sm}^{3+}$ are also reported [33-35]. However, the reports on the applications of display, lighting etc. are scarce [36-39]. It is well documented that the Eu^{3+} activated Gd_2O_3 phosphors possess europium-oxygen ($\text{Eu}/\text{Sm}-\text{O}$) charge transfer band (CTB) in the UV region nm and Gadolinium (Gd) absorption at $\sim 278 \text{ nm}$ [29-39]. This absorption band renders efficient energy transfer to the $\text{Eu}^{3+}/\text{Sm}^{3+}$ for enhanced emission. However, the commercially available UV LEDs are in the range of $360 - 400 \pm 15 \text{ nm}$ [22]. Therefore, extending the excitation wavelength at least beyond 350 nm becomes important for using $\text{Gd}_2\text{O}_3:\text{Eu}^{3+}$ or/and $\text{Gd}_2\text{O}_3:\text{Sm}^{3+}$ as potential red phosphor in SSL applications. In this connection, Xu *et al.*, have reported the red emitting Eu-MOFs (metal organic frameworks) as suitable red emitter for excitable with UV LEDs [30]. Also, sensitization with Bi^{3+} which has strong broad band absorption in the range of $340 - 350 \text{ nm}$ can be useful. Generally, rare earth oxides exist in sesquioxides exhibiting hexagonal, monoclinic, and cubic structures [41-44]. When Gd_2O_3 exists in cubic, cation site offers two non-equivalent sites viz., C_2 (non-centrosymmetric) and S_6 (centrosymmetric) [42,43]. It is reported that, when Bi^{3+} sensitizes the $\text{Gd}_2\text{O}_3:\text{Eu}^{3+}$ and $\text{Gd}_2\text{O}_3:\text{Sm}^{3+}$, the emission of Eu^{3+} and Sm^{3+} can be greatly enhanced through energy transfer from Bi^{3+} absorption $\sim 320 - 380 \text{ nm}$ related to $6s^2 \rightarrow 6s6p$ [22,39,44]. Therefore, Bi^{3+} sensitization may be an alternative to bring the excitation wavelength of the $\text{Gd}_2\text{O}_3:\text{Eu}^{3+}$ and $\text{Gd}_2\text{O}_3:\text{Sm}^{3+}$ in the desired wavelength region of the UV LEDs.

In this chapter, we have adopted the simple hydrothermal technique with subsequent post annealing for preparing cubic $\text{Gd}_2\text{O}_3:\text{Eu}^{3+}$ and $\text{Gd}_2\text{O}_3:\text{Sm}^{3+}$ sensitized with Bi^{3+} . We have thoroughly investigated the luminescence properties and energy transfer mechanisms from the sensitiser (donor) to the activator ions with steady state and decay dynamics of luminescence. We have also studied the possibility of tuning

emission with the variation of Eu^{3+} concentration using Commission International de l'Eclairage (CIE) chromaticity diagram.

6.2. Experimental methods

6.2.1. Materials

Gadolinium (III) nitrate hexahydrate ($\text{Gd}(\text{NO}_3)_3 \cdot 6\text{H}_2\text{O}$, 99.9%, Alfa Aesar), europium (III) nitrate hexahydrate ($\text{Eu}(\text{NO}_3)_3 \cdot 6\text{H}_2\text{O}$, 99.9%, Alfa Aesar), samarium (III) nitrate hexahydrate ($\text{Sm}(\text{NO}_3)_3 \cdot 6\text{H}_2\text{O}$, 99.9%, Alfa Aesar), bismuth (III) nitrate pentahydrate ($\text{Bi}(\text{NO}_3)_3 \cdot 5\text{H}_2\text{O}$, 99.99%, Alfa Aesar), were used as received for the sources of Gd^{3+} , Eu^{3+} , Sm^{3+} and Bi^{3+} respectively. Polyvinyl pyrrolidone (PVP, $M_w \sim 40000$, Sigma Aldrich) was used as capping agent.

6.2.2. Synthesis of Bi^{3+} sensitized Gd_2O_3 doped with Eu^{3+} phosphors

Hydrothermal technique was adopted to synthesize Bi^{3+} sensitized $\text{Gd}_2\text{O}_3:\text{Eu}^{3+}$ phosphors (denoted as $\text{Gd}_2\text{O}_3:\text{Bi}^{3+}/\text{Eu}^{3+}$). For the synthesis of 1 at.% Bi^{3+} sensitized $\text{Gd}_2\text{O}_3:\text{Eu}^{3+}$ (1 at.%) sample, 2.5 mg of $\text{Bi}(\text{NO}_3)_3 \cdot 5\text{H}_2\text{O}$ was dissolved in 2 mL of deionized water (DIW) under continuous stirring. To the above, 2.2 mg of $\text{Eu}(\text{NO}_3)_3 \cdot 6\text{H}_2\text{O}$ and 379 mg of $\text{Gd}(\text{NO}_3)_3 \cdot 6\text{H}_2\text{O}$ were added. 150 mg of polyvinyl pyrrolidone (PVP) was also added to the above solution. The final volume was made 30 mL with the addition of DIW. The pH of the solution was fixed at 10 using ammonium hydroxide solution (NH_4OH , ~25% NH_3 , Sigma Aldrich). Finally, the solution was transferred to a Teflon lined stainless steel autoclave and heated at 180 °C for 18 h in an oven. The precipitate was centrifuged and washed several times with DIW and acetone. All the remaining samples were synthesized following the same procedure. The as-prepared samples were annealed 900 °C for 4 h in the air.

6.2.3. Synthesis of Bi^{3+} sensitized Gd_2O_3 doped with Sm^{3+} phosphors

Following the similar procedure mentioned in the above section, Bi^{3+} sensitized $\text{Gd}_2\text{O}_3:\text{Sm}^{3+}$ phosphors (denoted as $\text{Gd}_2\text{O}_3:\text{Bi}^{3+}/\text{Sm}^{3+}$) were also synthesized adopting hydrothermal method. In a typical synthesis of 1 at.% Bi^{3+} sensitized $\text{Gd}_2\text{O}_3:\text{Sm}^{3+}$ (1 at.%) sample, 2.4 mg of $\text{Bi}(\text{NO}_3)_3 \cdot 5\text{H}_2\text{O}$ was dissolved in 2 mL of deionized water (DIW) under continuous stirring. To the above, 2.2 mg of $\text{Sm}(\text{NO}_3)_3 \cdot 6\text{H}_2\text{O}$ and 447 mg of $\text{Gd}(\text{NO}_3)_3 \cdot 6\text{H}_2\text{O}$ were added. 150 mg of polyvinyl pyrrolidone (PVP) was also added to the above solution. The whole solution is kept under hydrothermal condition for 18 h at

180 °C. The remaining samples were also prepared with similar process. The as-prepared samples were annealed 900 °C for 4 h in the air.

6.2.4. Characterization

X-ray diffractometer (Bruker D8 advance) with Cu $K\alpha$ radiation was used for crystalline phase identification. Fourier transform infrared (FT-IR) spectrometer (Shimadzu make IR-Affinity-1S) was used to record the FT-IR spectra of the prepared samples. Morphology of the particles was studied using the transmission electron microscopy (TEM) images recorded with JEOL 2000FX. The steady state and dynamics of photoluminescence (PL) as well as quantum yield (QY) were measured using Fluoromax-4CP spectrofluorometer (HORIBA make) equipped 150 W Xenon lamp and 25 W μs Xenon flash lamp. The fluorescence decay lifetime of Bi^{3+} was recorded by Time correlated single photon counting (TCSPC) technique (HORIBA make DeltaFlex) with pulse LED (340 ± 10 nm) source (pulse width < 1.2 ns). All the PL measurements were carried out on the glass slides at room temperature. K-sphere ‘petite’ integrating sphere from Photon Technology International (PTI) was used for QY measurements. For calculation of absolute QY, $\phi(\%) = \frac{I_{\text{emission}}}{I_{\text{quartz}} - I_{\text{sample}}}$ was used.

I_{emission} = luminescence emission intensity of the sample, I_{quartz} = the intensity of light used to excite only the quartz slide and I_{sample} = the intensity of the light used for exciting the sample on the quartz slide. The photons absorbed by the sample is given by the difference between the last two. All the measurements were taken in the emission mode. The QY measurements were carried out on the quartz slides at room temperature.

6.3. Results and discussion

6.3.1. X-ray diffraction study

X-ray diffraction (XRD) patterns of the as prepared samples are illustrated in Fig. 6.1. From the figure, it is clearly observed that the diffraction peaks can be well indexed to the hexagonal $\text{Gd}(\text{OH})_3$ (ICDD# 01-083-2037) [45]. No additional peaks are observed as well as the peaks are sharp indicating the formation of well crystalline $\text{Gd}(\text{OH})_3:\text{Eu}^{3+}$ and $\text{Gd}(\text{OH})_3:\text{Sm}^{3+}$ sensitized with Bi^{3+} (1 at.%) when prepared at 180 °C hydrothermally. Upon annealing at 900 °C for 4 h, these as prepared samples have converted to the cubic phase of Gd_2O_3 (ICDD# 00-012-0797) [43]. Fig. 6.2 shows the

XRD patterns of 900 °C annealed samples of Bi^{3+} (1 at.%) sensitized $\text{Gd}_2\text{O}_3:\text{Eu}^{3+}$ and $\text{Gd}_2\text{O}_3:\text{Sm}^{3+}$. All the patterns show the cubic phase Gd_2O_3 (ICDD# 00-012-0797) [46].

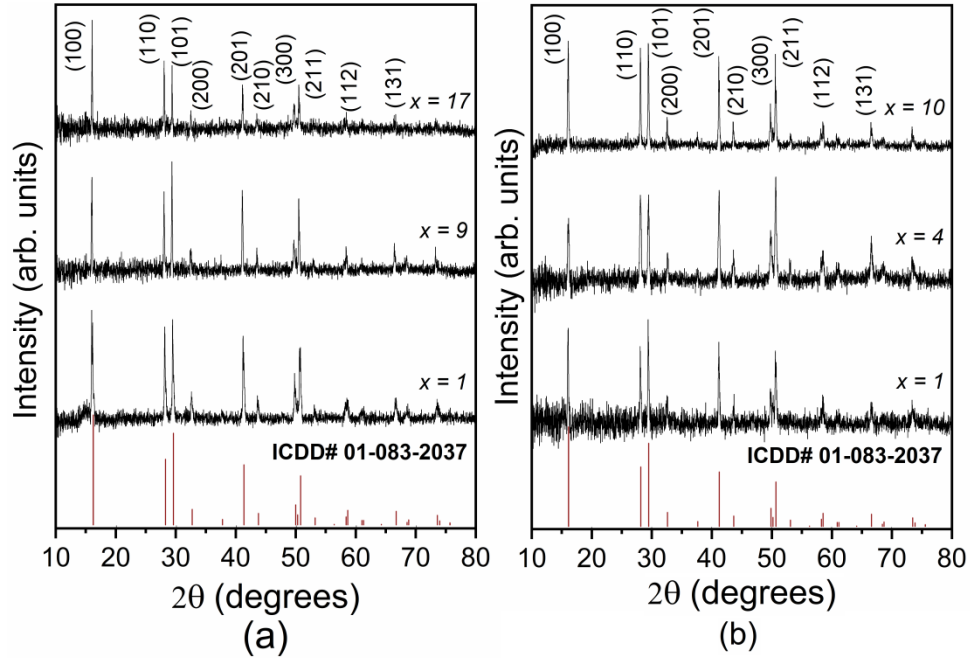


Fig. 6.1 XRD patterns of as-prepared 1 at.% Bi^{3+} sensitized (a) $\text{Gd}(\text{OH})_3:\text{Eu}^{3+}$ ($\text{Eu}^{3+} = 1, 9$ and 17 at.%) and (b) $\text{Gd}(\text{OH})_3:\text{Sm}^{3+}$ ($\text{Sm}^{3+} = 1, 4$ and 10 at.%).

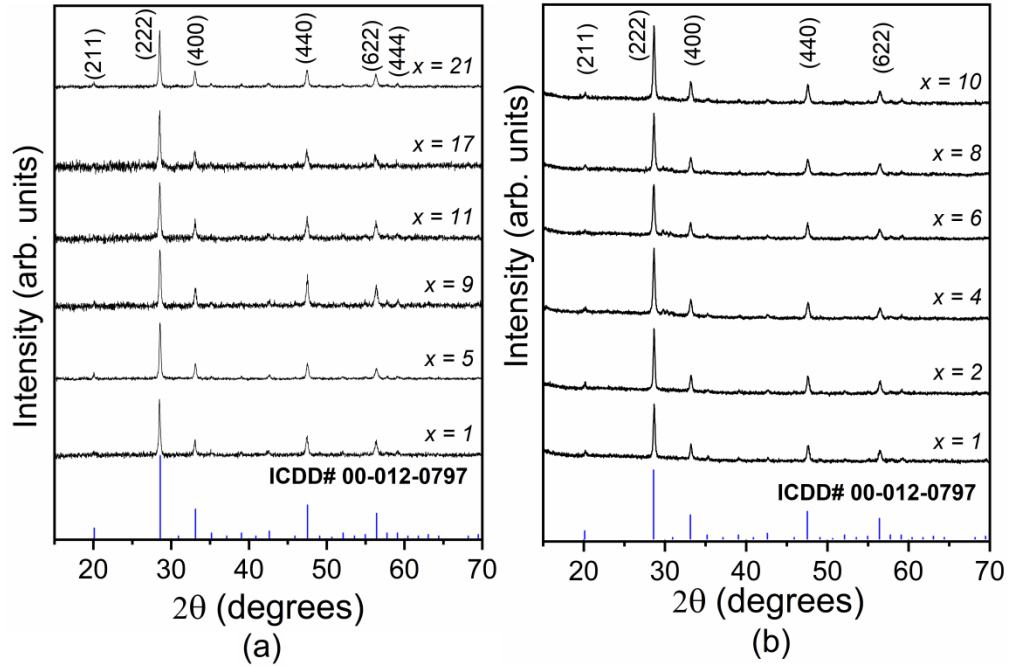


Fig. 6.2 XRD patterns of 900 °C annealed samples of 1 at.% Bi^{3+} sensitized (a) $\text{Gd}_2\text{O}_3:\text{Eu}^{3+}$ ($\text{Eu}^{3+} = 1, 5, 9, 11, 17$ and 21 at.%) and (b) $\text{Gd}_2\text{O}_3:\text{Sm}^{3+}$ ($\text{Sm}^{3+} = 1, 2, 4, 6, 8$ and 10 at.%).

The possible impurity phases such as Eu_2O_3 , Sm_2O_3 , Bi_2O_3 etc. are not observed. This suggests the lattice substitution of Gd^{3+} sites by the Eu^{3+} and/or Sm^{3+} and/or Bi^{3+} ions in the host matrix. The crystallite size was calculated using Scherrer relation, $D = \frac{\kappa\lambda}{\beta \cos\theta}$. The crystallite size calculated for the as prepared hexagonal phase varies from ~34 – 54 nm. While, the variation in the crystallite size for the Gd_2O_3 samples becomes less. The crystallite size varies from ~28 – 33 nm (Table 6.1).

Table 6.1: Calculated crystallite size for 1 at.% Bi^{3+} sensitized and Eu^{3+} or Sm^{3+} doped $\text{Gd}(\text{OH})_3$ and 900 °C annealed Gd_2O_3 samples, using Scherrer relation.

Eu^{3+} (%)	Crystallite size (nm)		Sm^{3+} (%)	Crystallite size (nm)	
	ASP	900 °C		ASP	900 °C
1	34	33	1	44	30
5	-	32	2	-	28
9	54	30	4	37	28
11	-	28	6	-	29
17	47	31	8	-	28
21	-	32	10	39	29

6.3.2. Fourier transform infrared spectroscopy study

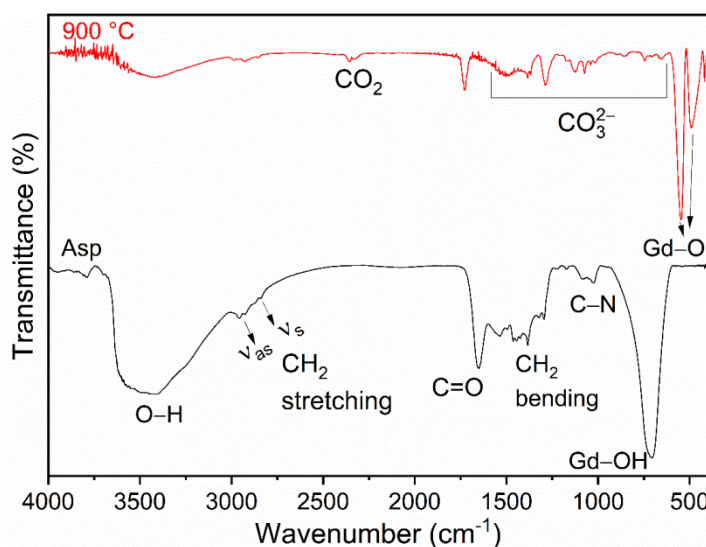


Fig. 6.3. FT-IR spectra of as-prepared $\text{Gd}(\text{OH})_3:\text{Bi}^{3+}$ (1 at.)/ Eu^{3+} (3 at.%) (below) and (b) 900 °C annealed $\text{Gd}_2\text{O}_3:\text{Bi}^{3+}$ (1 at.)/ Eu^{3+} (3 at.%) (above) samples.

FT-IR spectra of as-prepared Bi^{3+} (1 at.%) sensitized $\text{Gd}(\text{OH})_3:\text{Eu}^{3+}$ (3 at.%) and $\text{Gd}_2\text{O}_3:\text{Eu}^{3+}$ (3 at.%) samples are shown in Fig. 6.3. The absorption band at 3420 cm^{-1} corresponds to the $-\text{OH}$ stretching vibrations. The bands at 2958 and 2856 cm^{-1} correspond to the asymmetric and symmetric stretching vibrations of CH_2 , while the absorption due to the bending vibration is observed at $1382, 1456\text{ cm}^{-1}$ [47-9]. The split

vibrational peaks at 1023 and 1085 cm^{-1} correspond to the C–N vibrations of PVP [50]. The absorption peak at 1651 cm^{-1} is due to the asymmetric stretching of C=O bond [49,50]. The C=O vibration of pure PVP is normally observed at ~ 1661 cm^{-1} [50]. However, this peak is red shifted at 1651 cm^{-1} . Such red shifting at ~ 1647 cm^{-1} when PVP is used as capping agent in AgSe was reported due to band weakening after partial donation of oxygen to Ag [50]. Therefore, the –OH bending vibration which is usually observed at ~ 1651 cm^{-1} [48] could not be observed. This might be due to the merger with the C=O vibrational peak. The presence of red shifted C=O bond and splitting of C–N vibrational bands of PVP might be the implication of surface functionalization in the as-prepared sample. The Gd–OH vibration band is observed at 707 cm^{-1} and suggests the formation of $\text{Gd}(\text{OH})_3$ [45,46]. When the as prepared samples are heated at 900 °C, Gd–O vibration bands at 546 and 490 cm^{-1} are appeared instead of Gd–OH suggesting the formation of Gd_2O_3 . Bands at observed at 1495, 1385, 1087, and 1022 cm^{-1} are due to carbonate anions [52–54]. Apart from these, some of the peaks related to capping agent i.e., CH_2 stretching, C=O vibration etc. are also seen but the intensity is reduced compared to as prepared samples. This might be due to strong attachment to the surface of Gd_2O_3 even after annealing at 900 °C.

6.3.3 Transmission electron microscopy study

TEM images of as-prepared and 900 °C annealed samples are shown in Fig. 6.4 and 6.5 respectively. Particles are in rod shape with an average diameter of 118 – 244 nm and 606 – 1046 nm in length (Fig. 6.4(a)).

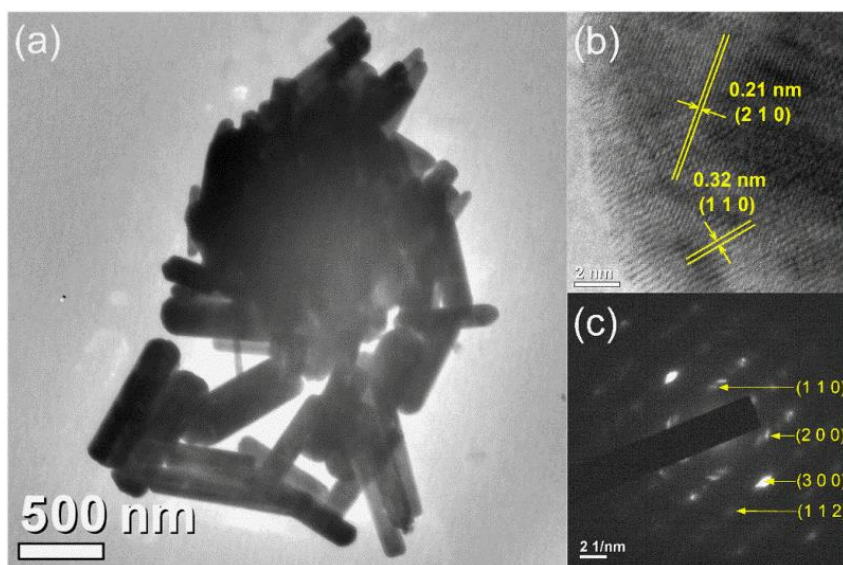


Fig. 6.4. TEM images (a) along with HR-TEM (b) and SAED images (c) of a selected region of as-prepared $\text{Gd}(\text{OH})_3:\text{Bi}^{3+}$ (1 at.)/ Eu^{3+} (9 at.).

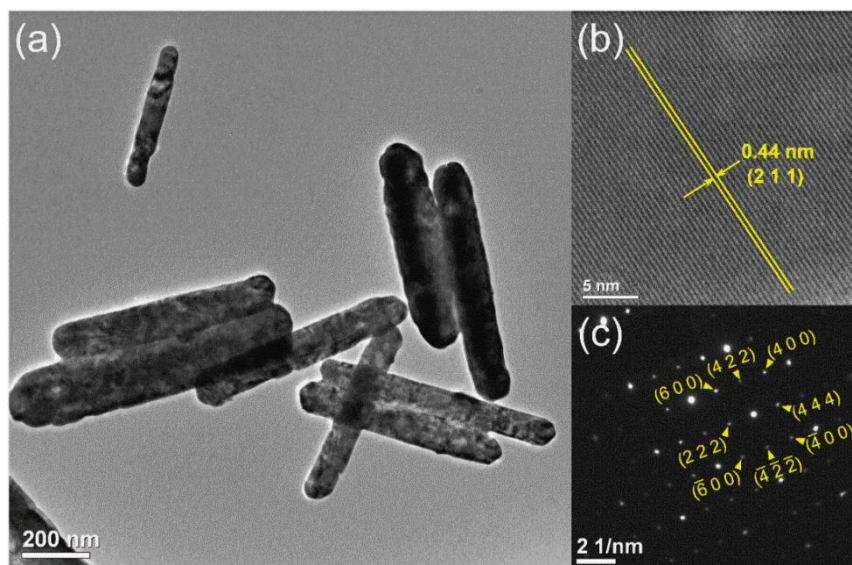


Fig. 6.5. TEM images (a) along with HR-TEM (b) and SAED images (c) of a selected region of 900 °C annealed $\text{Gd}_2\text{O}_3:\text{Bi}^{3+}$ (1 at. %)/ Eu^{3+} (9 at. %).

Whereas, the particles with 70 – 169 nm in diameter and 429 – 875 nm in length are observed in annealed samples (Fig. 6.5(a)). The measured interplanar spacing of 0.21 and 0.32 nm of as-prepared sample corresponds to (210) and (110) planes of hexagonal $\text{Gd}(\text{OH})_3$ (Fig. 6.4(b)). The diffraction planes from the SAED images (Fig. 6.4(c)) are also matched with that of $\text{Gd}(\text{OH})_3$ thus confirms the formation of crystalline $\text{Gd}(\text{OH})_3$. On the other hand, interplanar spacing of 0.44 nm corresponds to (211) plane of cubic Gd_2O_3 (Fig. 6.5(b)). Also, the diffraction planes from the SAED image (Fig. 6.5(c)) are well matched with that of Gd_2O_3 . This confirms the formation of crystalline Gd_2O_3 .

6.3.4. Photoluminescence (PL) studies of Bi^{3+} sensitized $\text{Gd}_2\text{O}_3:\text{Eu}^{3+}$

6.3.4.1. Steady state PL study

Excitation spectra of Bi^{3+} (0.25, 0.5, 1, 2, 4, 6 and 8 at. %) sensitized $\text{Gd}_2\text{O}_3:\text{Eu}^{3+}$ samples are illustrated in Fig. 6.6. All the excitation spectra can be broadly divided into 2 components viz., (i) excitation peaks related to the $\text{Gd}_2\text{O}_3:\text{Eu}^{3+}$ and (ii) excitation peaks originated from the sensitizer (Bi^{3+} in the present case). The excitation peaks related to $\text{Gd}_2\text{O}_3:\text{Eu}^{3+}$ are observed at 257 nm. This is related to the charge transfer (CT) band as a result of electron transfer from the 2p orbitals of oxygen to the empty 4f orbitals of the Eu^{3+} [2,4,7,16,19,26-32]. On the other hand, the sharp peak observed at 274 nm is due to the $^8\text{S}_{7/2} \rightarrow ^6\text{I}_{7/2-17/2}$ transition within the Gd^{3+} [43,44]. And, other sharp peak in the longer wavelength region at 464 nm is due to the $^7\text{F}_0 \rightarrow ^5\text{D}_2$ transition within f-f shell of Eu^{3+} .

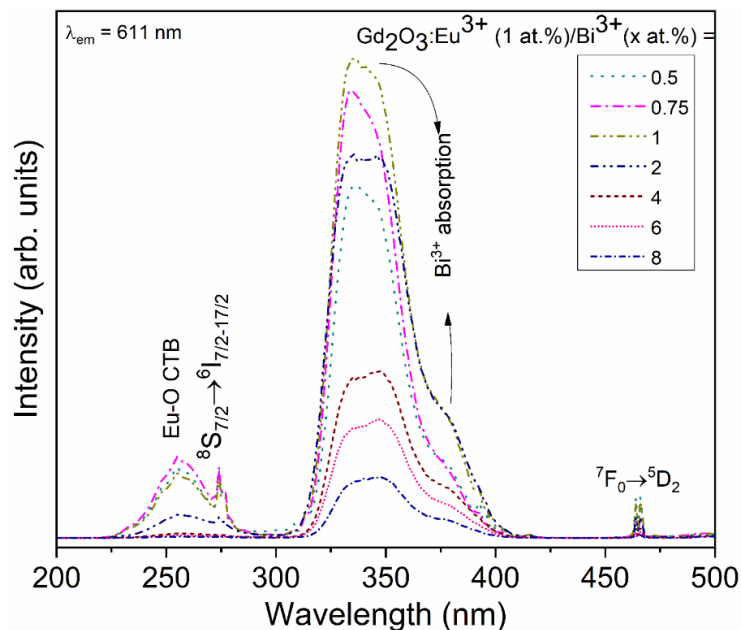


Fig. 6.6. PL excitation spectra of Bi^{3+} (0.25, 0.5, 1, 2, 4, 6 and 8 at.%) sensitized $\text{Gd}_2\text{O}_3:\text{Eu}^{3+}$ (1 at.%) samples monitored at $\lambda_{\text{em}} = 611$ nm

The excitation peaks at 335, 347 and 380 nm are related to the Bi^{3+} absorption. These peaks can be understood from the symmetry points of the cubic Gd_2O_3 . In the cubic Gd_2O_3 , there are 2 (two) types of lattice sites namely, C_2 and S_6 having octahedral coordination. C_2 has 4 (four) equatorial Gd–O bond and 2 (two) apical Gd–O with two different bond distances leading to the non-centrosymmetric. While, S_6 has equal bond distances of Gd–O with inversion symmetry [52,55]. Thus, 2 (two) different lattice sites are available for the doping ions to occupy in the host Gd_2O_3 . During the doping process, when Bi^{3+} ions occupy the C_2 symmetry sites, two excitation peaks at 335 and 347 nm are observed. This is due to the spin orbit interaction leading to the splitting of excited state 3P_1 into two transitions at 335 nm ($^1A \rightarrow ^3A$) and 347 nm ($^1A \rightarrow ^3B$). While, the peak at 380 nm is originated due to the occupation of S_6 sites by the Bi^{3+} . Earlier, similar results in $\text{Y}_2\text{O}_3:\text{Bi}^{3+}$ with more details have been reported [55].

Fig. 6.7 shows the emission spectra of $\text{Gd}_2\text{O}_3:\text{Bi}^{3+}$ (1 at.%) / Eu^{3+} (7 at.%) samples under different excitations at 257 nm (Eu–O CT), 274 nm (Gd^{3+} , S–I), 335 nm (Bi^{3+} , related to C_2 site), 380 nm (Bi^{3+} , related to S_6 site) and direct excitations at 393 and 464 nm. Considering the highest emission peak at 611 nm (discussed later), it is clearly seen that the emission intensity is highest when excited at 335 nm compared to the remaining excitations. This clearly suggests that the sensitization of $\text{Gd}_2\text{O}_3:\text{Eu}^{3+}$ with

Bi^{3+} enhances the energy transfer to the Eu^{3+} resulting improved emission intensity (discussed later).

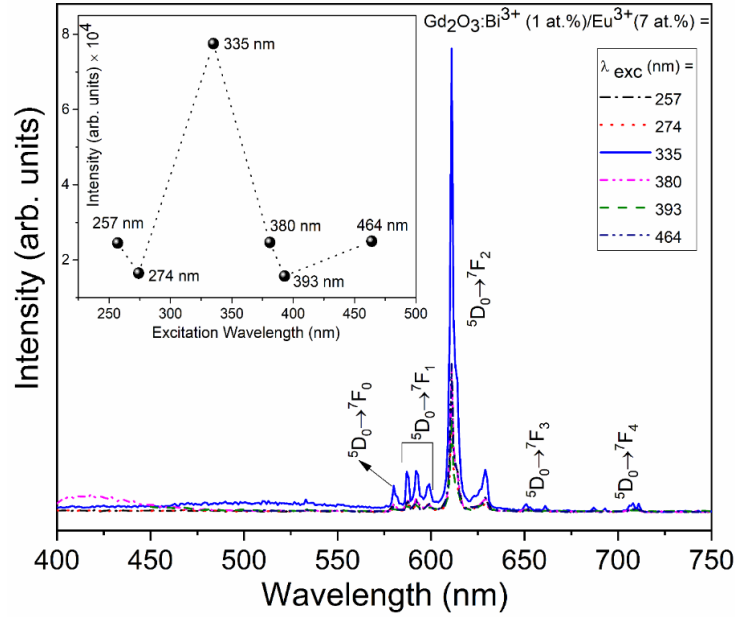


Fig. 6.7. PL emission spectra of $\text{Gd}_2\text{O}_3:\text{Bi}^{3+}(1 \text{ at.})/\text{Eu}^{3+}(7 \text{ at.})$ samples under different excitations at 257 nm (Eu–O CT), 274 nm (Gd^{3+} , S–I), 335 nm (Bi^{3+} , related to C_2 site) and 380 nm (Bi^{3+} , related to S_6 site). Inset shows the comparison of emission intensities at these excitation wavelengths.

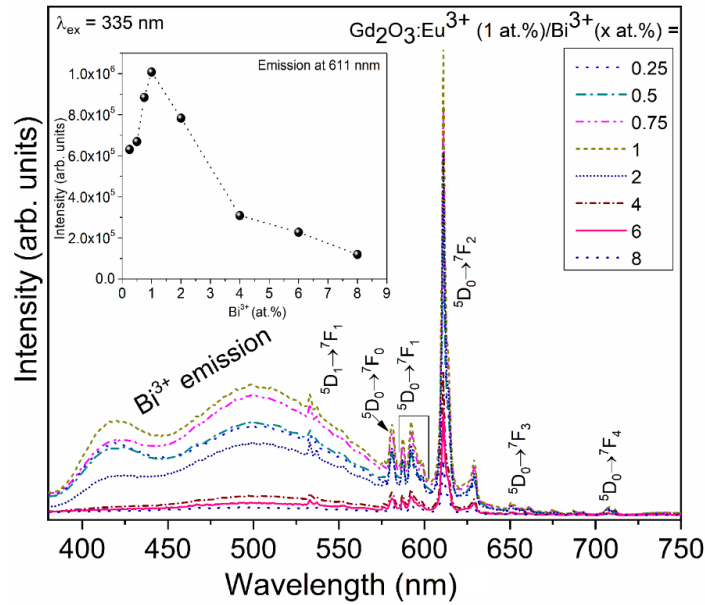


Fig. 6.8. PL emission spectra of Bi^{3+} (0.25, 0.5, 1, 2, 4, 6 and 8 at.%) sensitized $\text{Gd}_2\text{O}_3:\text{Eu}^{3+}(1 \text{ at.})$ samples under the 335 nm excitation. Inset shows the comparison of emission intensities at different concentration of Bi^{3+} .

Fig. 6.8 illustrates the emission spectra of Bi^{3+} (0.25, 0.5, 1, 2, 4, 6 and 8 at.%) sensitized $\text{Gd}_2\text{O}_3:\text{Eu}^{3+}(1 \text{ at.})$ samples under the 335 nm excitation. All the emission spectra consist of two types: (i) the broad emission peak with two humps at ~417 and 504 nm in the region of ~380 to 575 nm and (ii) sharp emission peaks in the region of ~

575 to 750 nm as well as at 533 and 537 nm. The broad band emission is related to the Bi^{3+} originated from $^3\text{P}_1 \rightarrow ^1\text{S}_0$. The presence of these two distinct humps in the emission band is due to the Bi^{3+} occupying at 2 (two) different symmetry sites. The emission at 417 nm is due to the Bi^{3+} occupying at S_6 site. While, the emission observed at 504 nm is originated when the Bi^{3+} occupies at C_2 site [39,44,55]. The sharp emission peaks mentioned in (ii) are related to the transitions within the $f-f$ electronic energy levels of Eu^{3+} . These transitions are due to the magnetic dipole transitions: $^5\text{D}_1 \rightarrow ^7\text{F}_1$ at 533 and 537 nm, $^5\text{D}_0 \rightarrow ^7\text{F}_1$ at 587, 592 and 599 nm (discussed later), $^5\text{D}_0 \rightarrow ^7\text{F}_3$ at 651 nm; electric dipole transitions: $^5\text{D}_0 \rightarrow ^7\text{F}_2$ at 611 and 629 nm; and electric quadrupole: $^5\text{D}_0 \rightarrow ^7\text{F}_4$ at 708 and 711 nm, respectively [42,43,55-57]. Apart from these emission peaks, a peak at 581 nm is also observed. This is due to the strictly forbidden $^5\text{D}_0 \rightarrow ^7\text{F}_0$ transition. Similar observation was earlier reported by us in Bi^{3+} sensitized $\text{Y}_2\text{O}_3:\text{Eu}^{3+}$ [55]. Among all these Eu^{3+} transitions, emission at 611 nm is strongest. Considering this peak, emission intensity of Eu^{3+} is plotted against the various concentrations of Bi^{3+} (inset of Fig. 6.8). It is clearly observed that the emission intensity of Eu^{3+} increases with the increase of Bi^{3+} concentration and found to be maximum at 1 at.%. The emission intensity decreases with the further increase of Bi^{3+} beyond 1 at.%. This might be due to the clustering of more Bi^{3+} ions with the increase concentration which eventually leads to the increase in the non-radiative transitions within Bi^{3+} . Similar trends were also observed in our earlier reports in $\text{CaMoO}_4:\text{Bi}^{3+}/\text{Eu}^{3+}$ and $\text{Y}_2\text{O}_3:\text{Bi}^{3+}/\text{Eu}^{3+}$ [16,55].

The emission peak due to the electric dipole transitions ($^5\text{D}_0 \rightarrow ^7\text{F}_2$) is much stronger than the magnetic dipole transitions ($^5\text{D}_0 \rightarrow ^7\text{F}_1$). According to Judd-Ofelt theory, the electric dipole transitions depend strongly on the environment of Eu^{3+} while the magnetic dipole transitions is independent of surroundings [45,43,52]. To understand the observed results, crystal structure of Gd_2O_3 must be taken into account. In cubic Gd_2O_3 , contribution of the non-centrosymmetric, C_2 symmetry sites is ~75% while the centrosymmetric, S_6 symmetry contributes only ~25% [46,60]. When the Eu^{3+} occupies the non-centrosymmetric sites, the electric dipole transition becomes dominant. The occupation of Eu^{3+} in C_2 site can be ascertained from the observance of 3 (three) Stark components in $^5\text{D}_0 \rightarrow ^7\text{F}_1$ transition against the allowed 2 (two) components whenever Eu^{3+} occupies centrosymmetric site [58,59]. To understand the asymmetric environment around the Eu^{3+} , asymmetric ratio (A) defined by the ratio of

integrated emission intensity of $^5\text{D}_0 \rightarrow ^7\text{F}_2$ to that of magnetic dipole transition, $^5\text{D}_0 \rightarrow ^7\text{F}_1$ is considered. The asymmetric ratio (A) is given by

$$A = \frac{\int_{603}^{633} I_{ed} d\lambda}{\int_{585}^{602} I_{md} d\lambda} \quad (6.1)$$

where, I_{ed} refers to $^5\text{D}_0 \rightarrow ^7\text{F}_2$ and I_{md} is $^5\text{D}_0 \rightarrow ^7\text{F}_1$. The integration limits are wavelengths (nm). Fig. 6.9 shows the asymmetric ratio of the $\text{Gd}_2\text{O}_3:\text{Bi}^{3+}$ (1 at.%) / Eu^{3+} (1, 3, 5, 7, 9, 11, 13, 15, 17, 19, 21 and 23 at.%) samples under the excitation wavelengths of 335 and 380 nm (calculated from the original data of the Fig. 6.10). In the case of 335 nm excitation, the ‘ A ’ value increases with the increase of Eu^{3+} concentration and becomes roughly constant after 10 at.%. This suggests the increase occupancy of the C_2 sites by the Eu^{3+} . Thus, the emission is predominantly from the Eu^{3+} located in the C_2 sites [36].

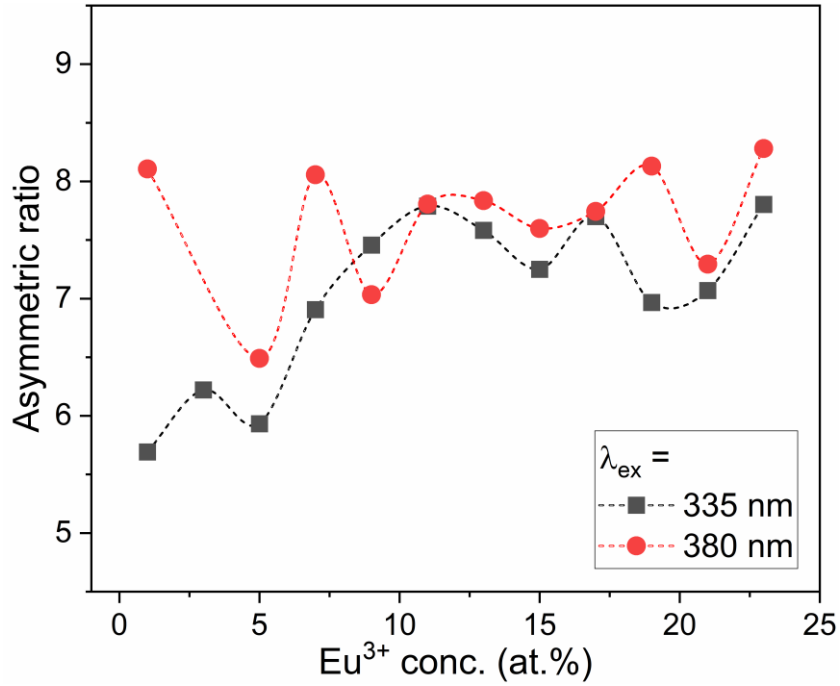


Fig. 6.9. Asymmetric ratio at different concentration of Eu^{3+} in $\text{Gd}_2\text{O}_3:\text{Bi}^{3+}$ (1 at.%) / Eu^{3+} (1, 3, 5, 7, 9, 11, 13, 15, 17, 19, 21 and 23 at.%) samples at 335 and 380 nm excitation.

This increase in the asymmetric ratio is attributed to the increase in lattice substitution of Eu^{3+} in the C_2 sites of Gd^{3+} in $\text{Gd}_2\text{O}_3:\text{Bi}^{3+}/\text{Eu}^{3+}$ [59,60]. However, under the 380 nm excitation, the asymmetric ratio is not much affected by the variation of Eu^{3+} concentration. Overall, the asymmetric ratios in both the cases are found in the range of 6-8. This suggests that the environment around the Eu^{3+} is asymmetric irrespective of variation of Eu^{3+} concentrations. This also ascertains that the asymmetric nature of Eu^{3+} surrounding is independent of excitation wavelengths. It is also corroborated by the

dominant electric dipole transitions in the steady state emission studies under different excitation wavelengths (Fig. 6.7).

6.3.4.2. Mechanism of energy transfer: Bi^{3+} to Eu^{3+}

Fig. 6.10 shows the normalized emission (normalized at 611 nm) spectra of $\text{Gd}_2\text{O}_3:\text{Bi}^{3+}$ (1 at.%) / Eu^{3+} (0, 1, 3, 5, 7, 9, 11, 13, 15, 17, 19, 21 and 23 at.%) samples under the excitation of (a) 335 and (b) 380 nm. In both the figures, it is clearly observed that the emission intensity of broad band related to the Bi^{3+} gradually decreases with the increase in Eu^{3+} concentration. This is due to the increase in the non-radiative energy transfer to the excited states of randomly distributed Eu^{3+} ions over the radiative transition within Bi^{3+} . The extent of decrease in the Bi^{3+} emission is almost similar under both the excitations. This suggests that the energy transfer in both the cases is efficient.

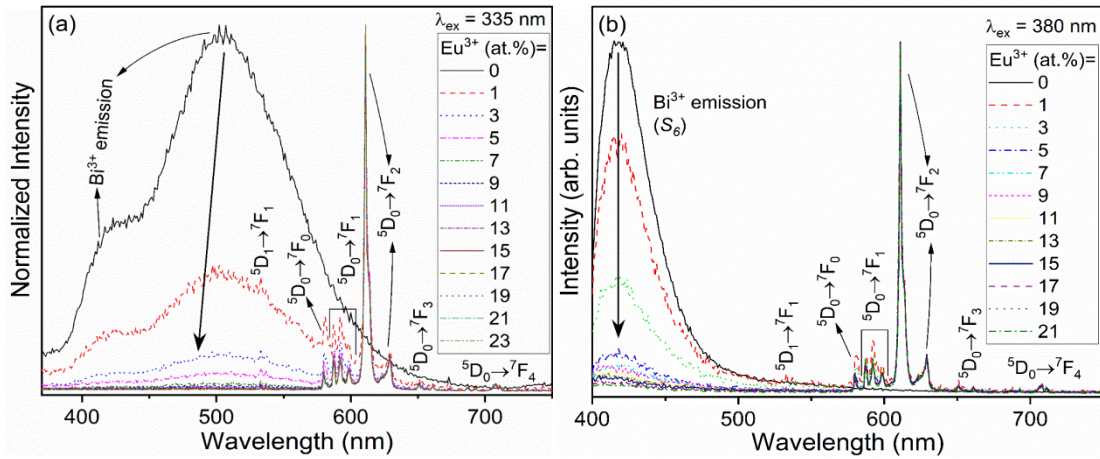


Fig. 6.10. Normalized PL emission (normalized at 611 nm) $\text{Gd}_2\text{O}_3:\text{Bi}^{3+}$ (1 at.%) / Eu^{3+} (0, 1, 3, 5, 7, 9, 11, 13, 15, 17, 19, 21 and 23 at.%) samples under the excitation of (a) 335 and (b) 380 nm.

To quantify the energy transfer efficiency (η) from the sensitizer (Bi^{3+}) to the excited states of activator (Eu^{3+}), the following equation was used,

$$\eta = 1 - \frac{I_s}{I_{s_0}} \quad (6.2)$$

where I_s and I_{s_0} are the emission intensities of the Bi^{3+} in the presence and absence of Eu^{3+} respectively. The energy transfer efficiency in both the cases reaches upto nearly 97% suggesting efficient transfer of energy from donor to the activator (See Fig. 6.11). Generally, the energy transfer occurs through 2 (two) mechanisms viz., (i) exchange

interactions and (ii) multipolar interactions. Both the interactions depend on the distance between the acceptor and donor.

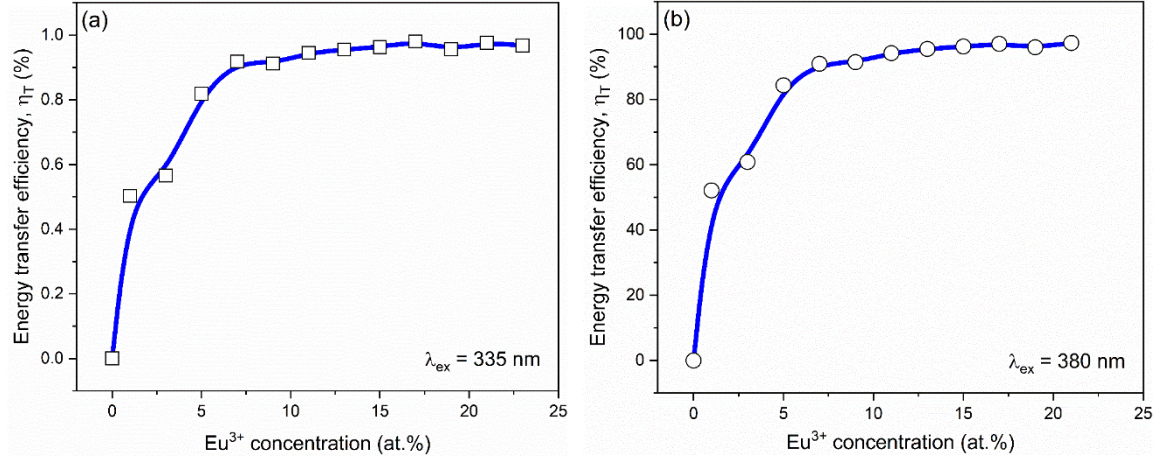


Fig. 6.11. Energy transfer efficiency (η) from the sensitizer (Bi^{3+}) to the excited states of activator (Eu^{3+}) in $\text{Gd}_2\text{O}_3:\text{Bi}^{3+}$ (1 at.%) / Eu^{3+} (0, 1, 3, 5, 7, 9, 11, 13, 15, 17, 19, 21 and 23 at.%) samples under the excitation of (a) 335 and (b) 380 nm.

The critical distance between them can be calculated using [16,55,61],

$$R_c = 2 \left[\frac{3V}{4\pi x_c N} \right]^{1/3} \quad (6.3)$$

where, R_c is critical distance, V represents the volume of the unit cell, x_c is the critical concentration and N denotes the number of cation sites in the unit cell of the host (both S_6 and C_2 sites). In the present case of Gd_2O_3 , the value of $N = 32$. In the present study of Gd_2O_3 , the unit cell volume is 1195 \AA^3 . The critical concentration (x_c) value is 18 at.%. The critical distance (R_c) calculated using Eqn. (6.3) is found to be 7 \AA . This value exceeds the restricted distance of exchange interaction i.e., $\sim 5 \text{ \AA}$. This indicates that the multipolar interactions are dominant during the energy transfer from Bi^{3+} to the excited states of Eu^{3+} ions in Gd_2O_3 . According to Dexter, such multipolar interactions between the donors and the activators during resonance energy transfer are of 3 (three) kinds: (i) dipole-dipole, (ii) dipole-quadrupole or (iii) quadrupole-quadrupole interactions. These kinds of interactions can be understood with the Reisfeld's approximation [43,61-63],

$$\frac{I_{s0}}{I_s} \propto C_{\text{Bi}^{3+}+\text{Eu}^{3+}}^{n/3} \quad (6.4)$$

where, C is the total concentration of the donors (Bi^{3+}) and the activators (Eu^{3+}) present in the sample. Based on the values of ' n ', the corresponding interactions are dipole-dipole ($n = 6$), dipole-quadrupole ($n = 8$) or quadrupole-quadrupole ($n = 10$) types. From the linear fit using Eqn. (6.4) with different values of n ($= 6, 8, 10$) shown in Fig. 6.12, the best fit is obtained when $n = 6$. This shows that the majority of the multipolar interactions occur through dipole-dipole interactions in both the cases.

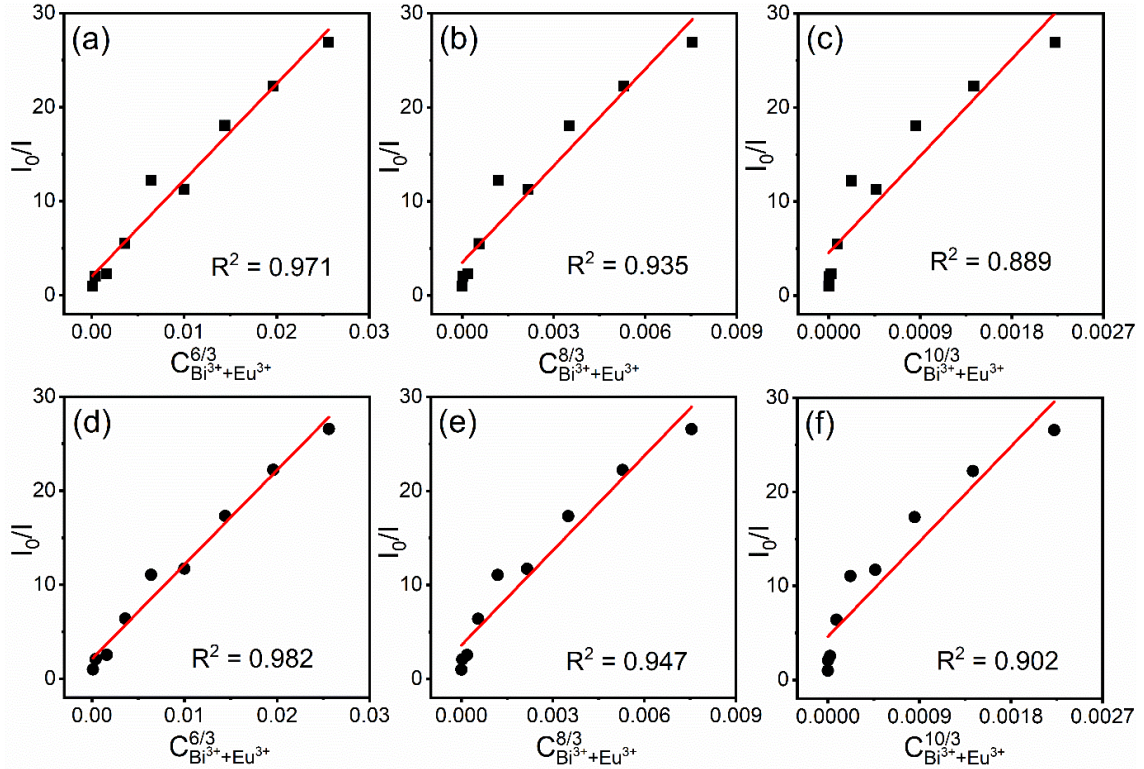


Fig. 6.12. Dependence of I_{S0}/I_S of Bi^{3+} on $C_{\text{Bi}^{3+}+\text{Eu}^{3+}}^{n/3}$ where $n = 6$ (dipole-dipole), $n = 8$ (dipole-quadrupole) and $n = 10$ (quadrupole-quadrupole) interactions respectively, at 335 nm excitation, C_2 symmetry site (a-c) and at 380 nm excitation, S_6 symmetry site (d-f) in $\text{Gd}_2\text{O}_3:\text{Bi}^{3+}$ (1 at.%) / Eu^{3+} (0, 1, 3, 5, 7, 9, 11, 13, 15, 17, 19, 21 and 23 at.%) samples.

6.3.4.3. PL decay lifetime and quantum yield study

To understand better on the occurrence of energy transfer, investigating luminescence decay dynamics of sensitizer is important. Therefore, the decay dynamics of Bi^{3+} luminescence related to the C_2 site in $\text{Gd}_2\text{O}_3:\text{Bi}^{3+}/\text{Eu}^{3+}$ were measured. However, the decay dynamics of Bi^{3+} related to S_6 site were not measured due to the unavailability of the exciting source with us.

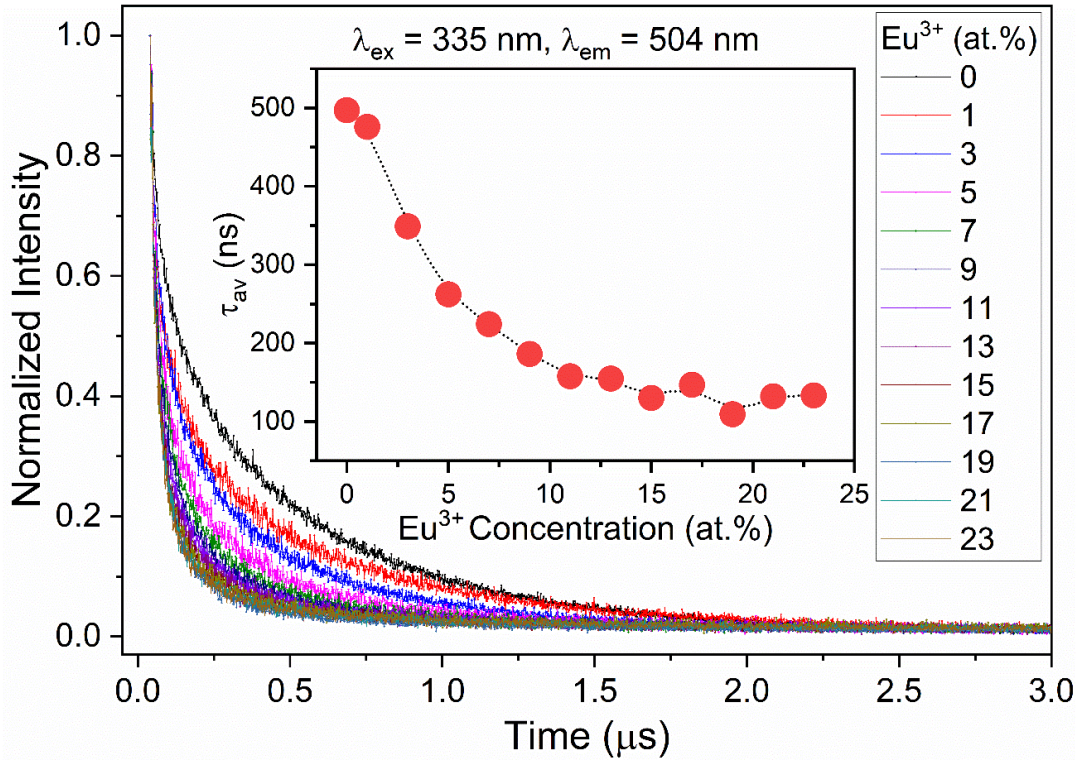


Fig. 6.13. TCSPC decay profiles of Bi^{3+} (1 at.%) in $\text{Gd}_2\text{O}_3:\text{Eu}^{3+}$ (0, 1, 3, 5, 7, 9, 11, 13, 15, 17, 19, 21 and 23 at.%). Excitation and emission wavelengths were monitored at 335 and 504 nm respectively. Inset shows the calculated average lifetime values at different concentration of Eu^{3+} .

Fig. 6.13 shows the decay profiles of Bi^{3+} (1 at.%) in $\text{Gd}_2\text{O}_3:\text{Eu}^{3+}$ (0, 1, 3, 5, 7, 9, 11, 13, 15, 17, 19, 21 and 23 at.%). Excitation and emission wavelengths were monitored at 335 and 500 nm respectively. The decay profiles are better fitted with the second order exponential decay equation,

$$I(t) = I_1 e^{-\frac{t}{\tau_1}} + I_2 e^{-\frac{t}{\tau_2}} \quad (6.5)$$

where I_1 and I_2 stand for intensities at two different times. The τ_1 and τ_2 represent the corresponding lifetimes. Similar behaviour of the luminescence decay by the Bi^{3+} and Ce^{3+} were also earlier reported when use as sensitizer [64,65]. Such behaviour in Bi^{3+} sensitized $\text{Y}_2\text{O}_3:\text{Eu}^{3+}$ was also recently reported by us [55]. Typical fitting is given in Fig. 6.14. The average decay lifetime can be calculated using,

$$\tau_{av} = \frac{I_1 \tau_1^2 + I_2 \tau_2^2}{I_1 \tau_1 + I_2 \tau_2} \quad (6.6)$$

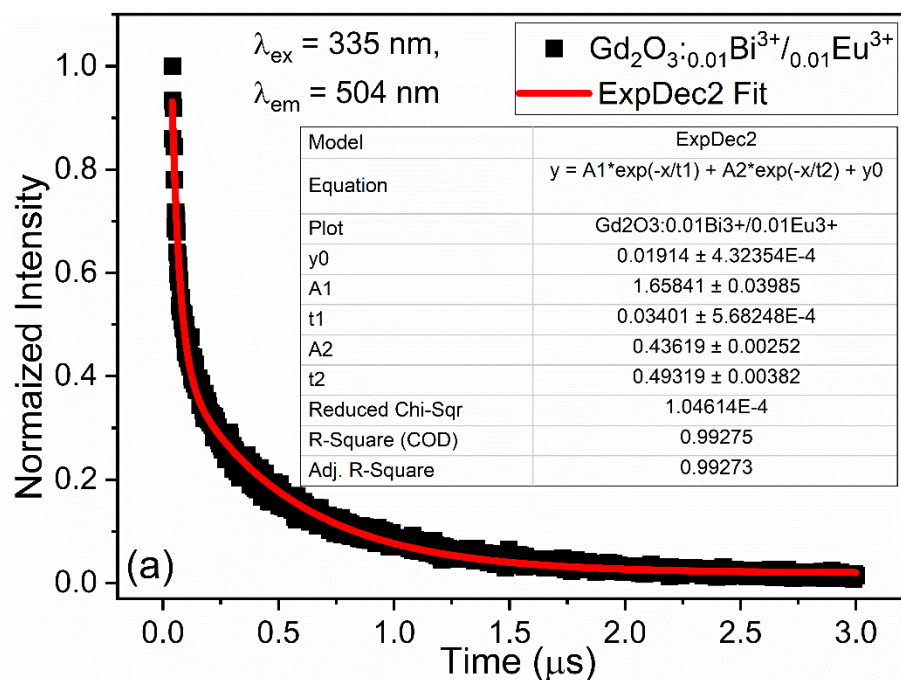


Fig. 6.14. Typical fitting of decay curve for Bi^{3+} emission ($\lambda_{\text{ex}} = 335 \text{ nm}$ and $\lambda_{\text{em}} = 504 \text{ nm}$) in 900°C annealed $\text{Gd}_2\text{O}_3:\text{Bi}^{3+}$ (1 at.%) / Eu^{3+} (1 at.%) sample.

From the calculated values of Bi^{3+} decay lifetime, it is clearly observed that the decay lifetime is found to decrease from 497 ns to 109 ns with the increase of Eu^{3+} (activator) concentration. The details of decay lifetime and fitting parameters are given in Table 6.2. The decay lifetime trend clearly ascertains the increase in the non-radiative transfer of energy to the ^5D excited states of Eu^{3+} at the expense of radiative transition in Bi^{3+} . This result supports the energy transfer discussed from the steady state luminescence studies.

Fig. 6.15 shows the decay curves of $^5\text{D}_0$ level of Eu^{3+} emission in $\text{Gd}_2\text{O}_3:\text{Bi}^{3+}$ (1 at.%) / Eu^{3+} (1, 3, 5, 7, 9, 11, 13, 15, and 17 at.%) samples by monitoring at 611 nm emission. Excitation wavelength is 335 nm. The decay profiles $^5\text{D}_0$ level under the direct excitation at 464 nm is shown in Fig. 6.16. All the decay profiles follow the second order exponential decay (Eqn. 6.5). Typical fitting is shown in Fig. 6.17. The average decay lifetime was calculated using Eqn. 6.6. The decay lifetime varies from 0.81 to 1.45 ms when the excitation was used at 335 nm.

Table 6.2: Calculated fitting parameters of decay lifetime of Bi^{3+} emission in $\text{Gd}_2\text{O}_3:\text{Bi}^{3+}$ (1 at.%) / Eu^{3+} (0, 1, 3, 5, 7, 9, 11, 13, 15, 17, 19, 21 and 23 at.%) samples at 335 nm excitation and emission monitored at 504 nm.

Eu^{3+} (at.%)	A_1	τ_1	A_2	τ_2	τ_{av} (ns)	R^2
0	0.925	0.049	0.542	0.564	497	1.00
1	1.360	0.042	0.404	0.581	476	0.99
3	1.460	0.041	0.409	0.449	349	0.99
5	2.016	0.034	0.343	0.382	262	0.99
7	1.999	0.035	0.296	0.352	224	0.99
9	2.468	0.031	0.278	0.320	186	0.99
11	3.111	0.027	0.267	0.297	158	0.99
13	3.038	0.028	0.233	0.305	155	0.99
15	3.267	0.027	0.228	0.274	130	0.99
17	3.158	0.028	0.199	0.314	147	0.98
19	3.331	0.027	0.216	0.248	109	0.99
21	3.260	0.028	0.187	0.300	132	0.98
23	3.678	0.026	0.174	0.319	133	0.98

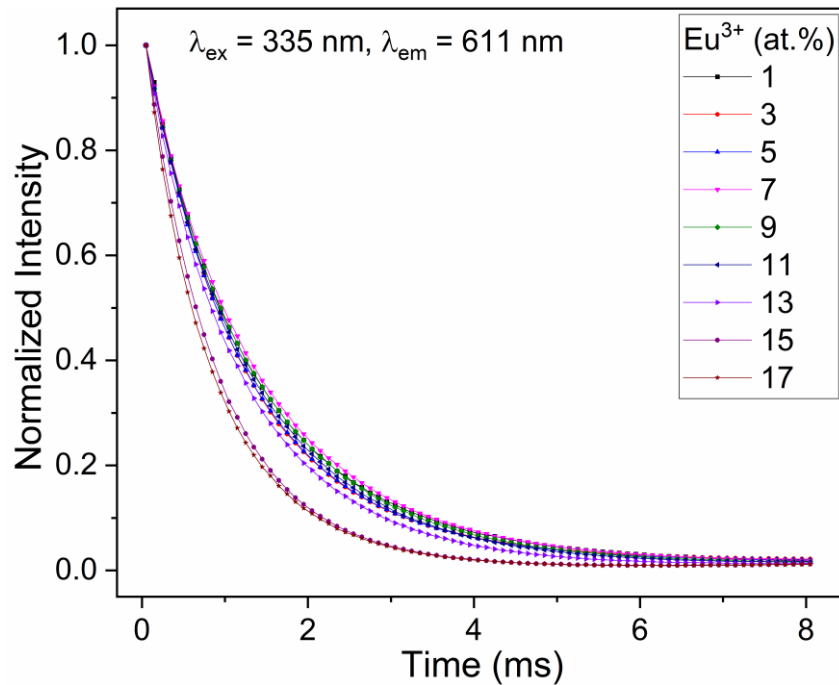


Fig. 6.15. PL decay curves of $^5\text{D}_0$ level of Eu^{3+} emission in $\text{Gd}_2\text{O}_3:\text{Bi}^{3+}$ (1 at.%) / Eu^{3+} (1, 3, 5, 7, 9, 11, 13, 15, and 17 at.%) samples under 335 nm excitation and the emission is monitored at 611 nm.

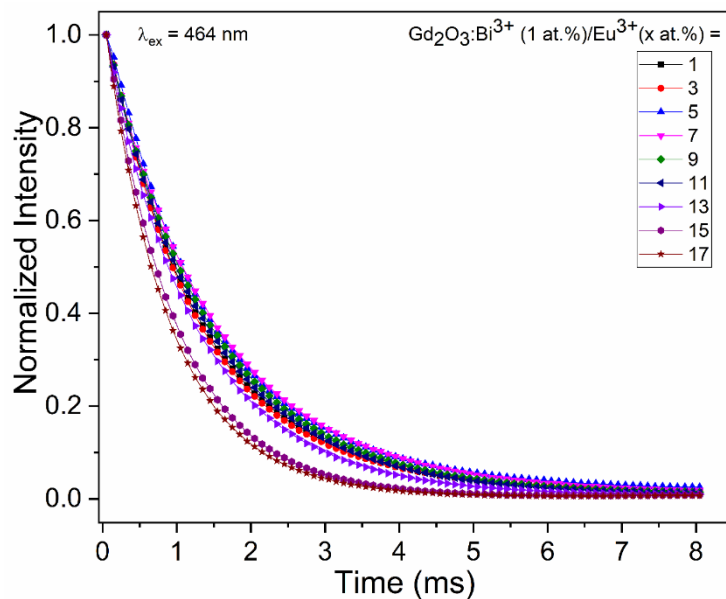


Fig. 6.16. PL decay curves of $^5\text{D}_0$ level of Eu^{3+} emission in $\text{Gd}_2\text{O}_3:\text{Bi}^{3+}$ (1 at.)/ Eu^{3+} (1, 3, 5, 7, 9, 11, 13, 15, and 17 at.%) samples under 464 nm excitation and the emission is monitored at 611 nm.

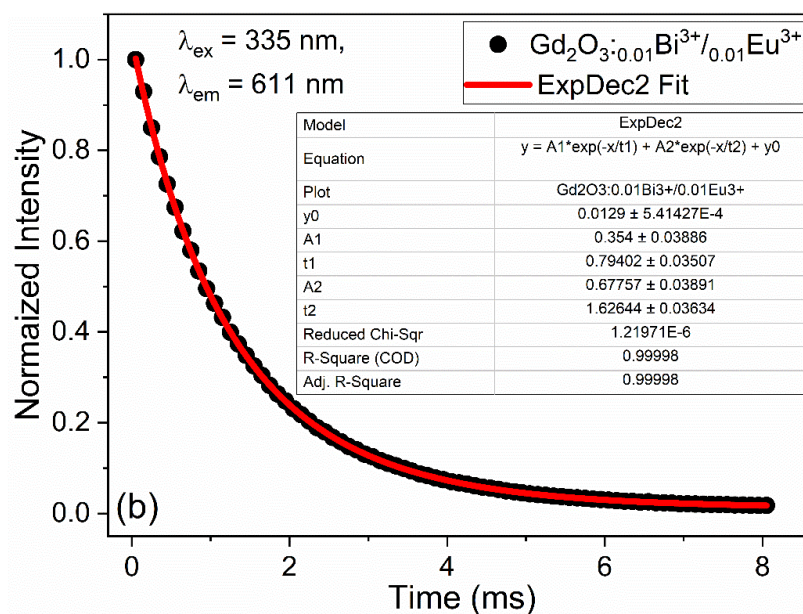


Fig. 6.17. Typical fitting of decay curve for Eu^{3+} emission ($\lambda_{\text{ex}} = 335$ nm and $\lambda_{\text{em}} = 611$ nm) in 900 °C annealed $\text{Gd}_2\text{O}_3:\text{Bi}^{3+}$ (1 at.)/ Eu^{3+} (1 at.%) sample.

Table 6.3: The average lifetime calculated for the decay curves of $^5\text{D}_0$ level of Eu^{3+} by monitoring at 611 nm emission and Quantum yield in $\text{Gd}_2\text{O}_3:\text{Bi}^{3+}$ (1 at.%) / Eu^{3+} (1, 3, 5, 7, 9, 11, 13, 15, and 17 at.%) samples.

Eu^{3+} (%)	Decay lifetime, τ_{av} (ms)				Quantum Yield (%)
	$\lambda_{\text{exc}} = 335 \text{ nm}$		$\lambda_{\text{exc}} = 464 \text{ nm}$		$\lambda_{\text{exc}} = 335 \text{ nm}$
	τ_{av}	R^2	τ_{av}	R^2	
1	1.29	0.99	1.38	0.99	7
3	1.31	0.99	1.38	0.99	8
5	1.43	0.99	1.54	0.99	-
7	1.45	0.99	1.56	0.99	8
9	1.37	0.99	1.47	0.99	-
11	1.33	0.99	1.42	0.99	7
13	1.20	0.99	1.25	0.99	-
15	0.89	0.99	0.96	0.99	9
17	0.81	0.99	0.90	0.99	10

On the other hand, under direct excitation at 464 nm, the lifetime value increases from 0.9 to 1.56 ms. The average lifetime calculated are given in Table 6.3. From the table, it can be observed that the decay lifetime value in both the cases increases with the increase of Eu^{3+} concentration upto 7 at.%. Thereafter, the lifetime steadily decreases with the further increase of Eu^{3+} concentration. Such decrease in the decay lifetime of lanthanide ions emission beyond certain concentration is attributed to the increase in the non-radiative transitions due to the cross relaxation among lanthanide ions. Such behaviour has been reported earlier [4,16,19]. The quantum yield measurements were performed following the report [16]. The quantum yields for $\text{Gd}_2\text{O}_3:\text{Eu}^{3+}$ (1 at.%) and $\text{Gd}_2\text{O}_3:\text{Eu}^{3+}$ (1 at.%) / Bi^{3+} (1 at.%) under 464 nm excitation are found to be 10 and 12% respectively. The quantum yields of some the $\text{Gd}_2\text{O}_3:\text{Eu}^{3+}$ (x at.%) / Bi^{3+} (1 at.%) samples under 335 nm excitation are given in Table 6.3.

6.3.4.4. CIE chromaticity studies

The Commission International de l'Eclairage (CIE) chromaticity was analysed to understand the colour of the emission from different samples with the variation of Eu^{3+} concentration as well as excitation wavelength. The CIE positions of the $\text{Gd}_2\text{O}_3:\text{Bi}^{3+}$ (1

at.%) / Eu^{3+} (0, 1, 3, 5, 7, 9, 11, 13, 15, 17, 19, 21 and 23 at.%) samples under the excitations of 335 and 380 nm are indicated in the diagram (Fig. 6.18). When the excitation wavelength was 335 nm (Fig. 6.18(a)), it is clearly observed that the colour of the emission is nicely tuned from bluish green region to red. On the other hand, the colour of the emission is varied from blue to red colour under the excitation of 380 nm (Fig. 6.18(b)). These results clearly suggest the possibility of tuning the emission colour by

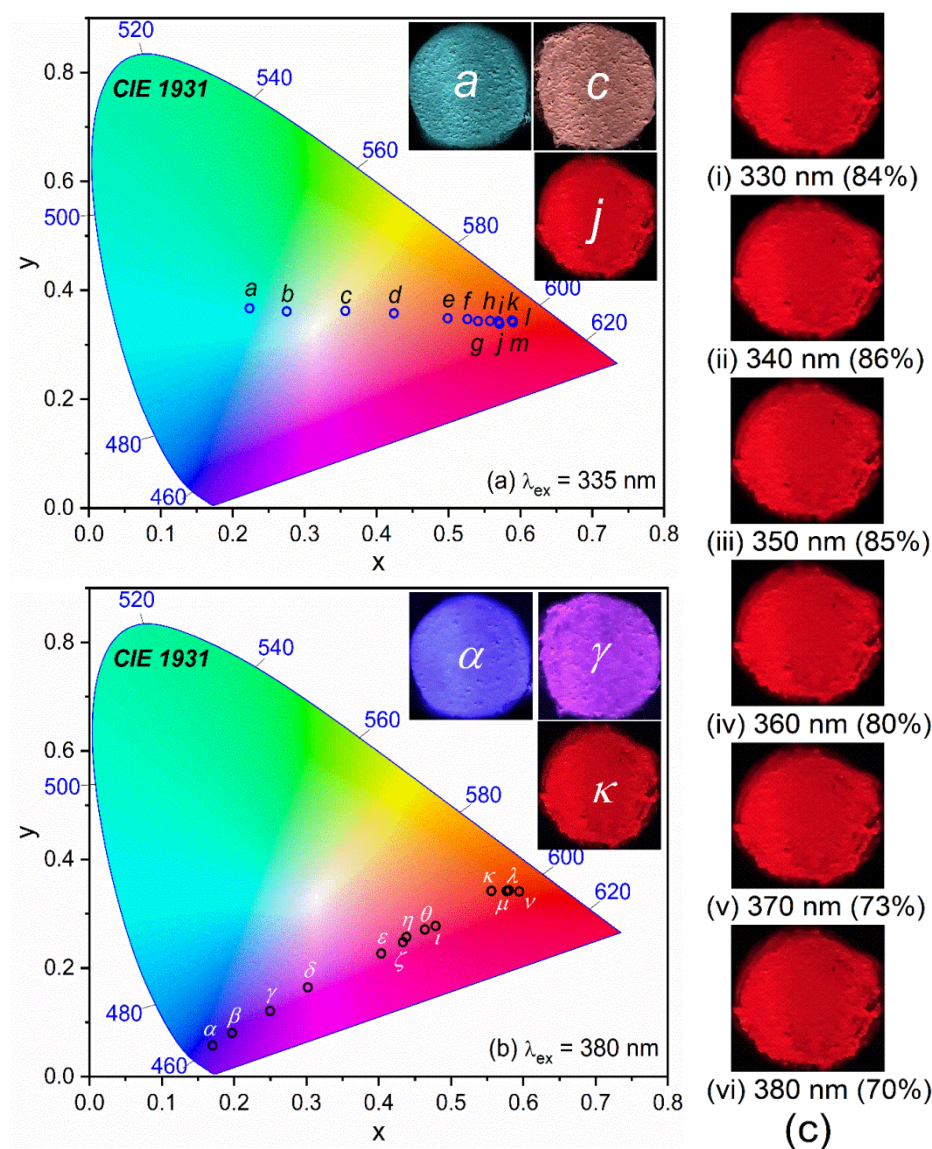


Fig. 6.18. CIE chromaticity coordinate positions of $\text{Gd}_2\text{O}_3:\text{Bi}^{3+}$ (1 at.%) / Eu^{3+} (0, 1, 3, 5, 7, 9, 11, 13, 15, 17, 19, 21 and 23 at.%) samples excited at (a) 335 nm, (b) 380 nm (Details of CIE coordinate and position on the colour space are tabulated in Table 6.4) and (c) physical photograph of $\text{Gd}_2\text{O}_3:\text{Bi}^{3+}$ (1 at.%) / Eu^{3+} (17 at.%) excited at different wavelengths where the colour saturation is mentioned inside the parenthesis.

Table 6.4: CIE chromaticity coordinates and position in the color space (Fig. 6.18) of $\text{Gd}_2\text{O}_3:\text{Bi}^{3+}$ (1 at.%) / Eu^{3+} at 335 nm and 380 nm excitation.

Eu^{3+} (at.%)	$\lambda_{\text{ex}} = 335 \text{ nm}$		$\lambda_{\text{ex}} = 380 \text{ nm}$	
	Position	CIE Coordinate	Position	CIE Coordinate
0	a	(0.22, 0.37)	α	(0.17, 0.06)
1	b	(0.28, 0.36)	β	(0.20, 0.08)
3	c	(0.36, 0.36)	γ	(0.30, 0.16)
5	d	(0.42, 0.36)	δ	(0.40, 0.23)
7	e	(0.50, 0.35)	ϵ	(0.43, 0.25)
9	f	(0.53, 0.35)	ζ	(0.44, 0.26)
11	g	(0.54, 0.34)	η	(0.46, 0.27)
13	h	(0.56, 0.34)	θ	(0.48, 0.28)
15	i	(0.57, 0.34)	ι	(0.49, 0.29)
17	j	(0.59, 0.36)	κ	(0.56, 0.34)
19	k	(0.60, 0.36)	λ	(0.58, 0.34)
21	l	(0.60, 0.35)	μ	(0.58, 0.34)
23	m	(0.61, 0.35)	ν	(0.59, 0.34)

varying the concentration of Eu^{3+} in Gd_2O_3 when sensitized with Bi^{3+} . The positions of CIE coordinates are given in Table 6.4. Insets of the Fig. 6.18(a) & (b) show the photographic evidence of the colour tunability for some samples under the direct exposure of UV light. The vertically stacked photographs (Fig. 6.18(c)) are the images under the exposure of UV light with various wavelengths in the region of 330 – 380 nm for $\text{Gd}_2\text{O}_3:\text{Bi}^{3+}$ (1 at.%) / Eu^{3+} (17 at.%). The purity of the colour by the emitter can be understood by calculating the colour saturation value. Colour saturation (also known as chroma or tone) refers to the amount of mixing of white light with the hue or the pure colour (in this case *Red*). Higher the value signifies purer in the light emission, while lesser represents pale in the colour. The colour saturation values are also given (Fig. 6.18(c)). The CIE colour coordinates and a typical calculation of colour saturation are shown in Fig. 6.19. This shows that the Bi^{3+} sensitized $\text{Gd}_2\text{O}_3:\text{Eu}^{3+}$ can be potential candidate as red emitting phosphor for UV LED converted white LEDs for solid state lighting applications.

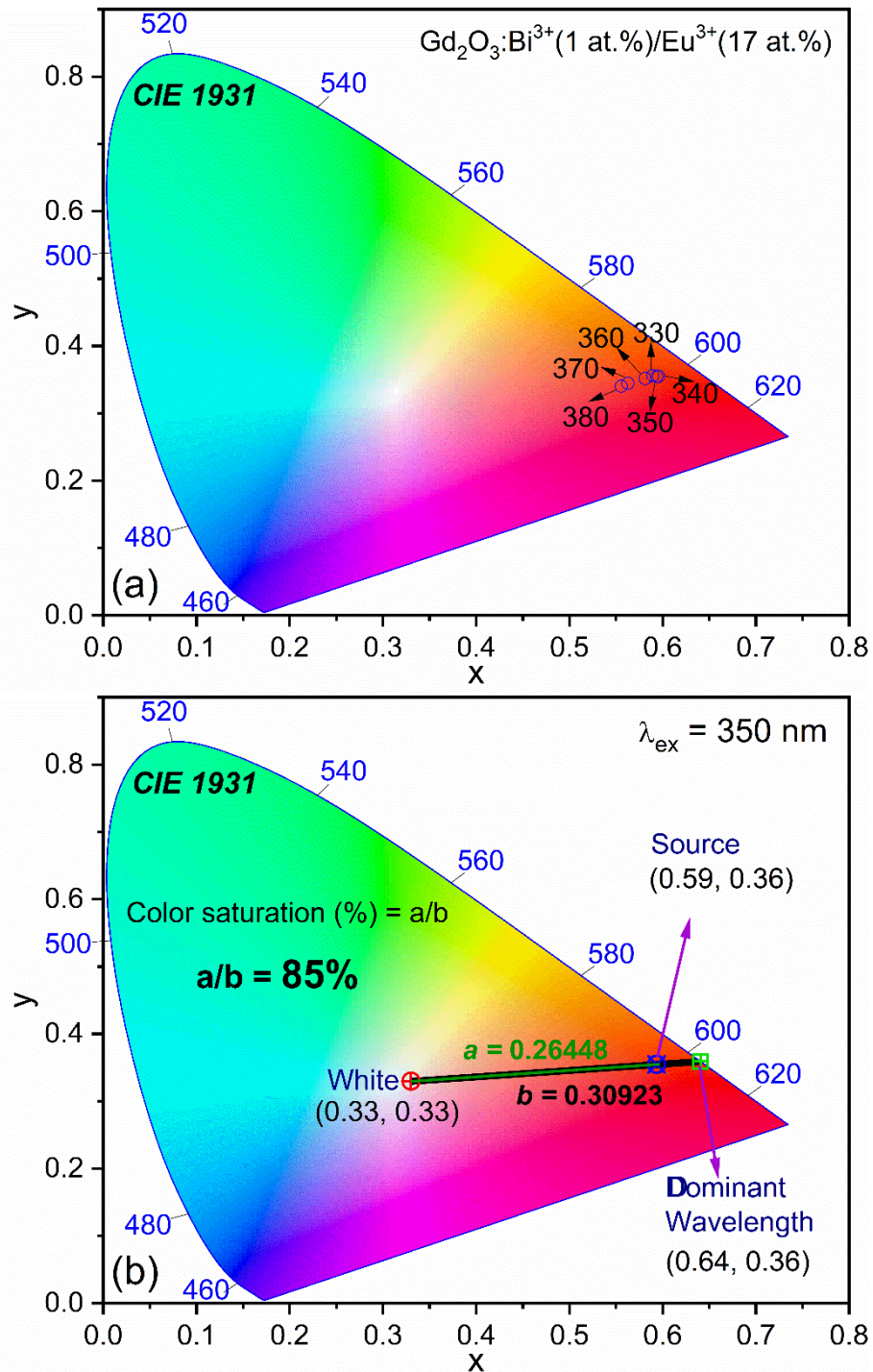


Fig. 6.19. (a) CIE color coordinates of $\text{Gd}_2\text{O}_3:\text{Bi}^{3+}$ (1 at.%) / Eu^{3+} (17 at.%) at different excitation wavelength ($\lambda_{\text{ex}} = 330, 340, 350, 360, 370$, and 380 nm) and (b) Color saturation calculated from CIE chromaticity coordinates for Bi^{3+} (1 at.%) sensitized $\text{Gd}_2\text{O}_3:\text{Eu}^{3+}$ (17 at.%) sample at 350 nm excitation. **a** = distance between source coordinate and equal energy locus (1/3, 1/3: white); **b** = distance between equal energy locus (1/3, 1/3: white) and dominant wavelength.

6.3.5. Photoluminescence studies of Bi^{3+} sensitized $\text{Gd}_2\text{O}_3:\text{Sm}^{3+}$

6.3.5.1. Steady state PL study

Fig. 6.20 shows the excitation spectra of Bi^{3+} (1 at.%) sensitized $\text{Gd}_2\text{O}_3:\text{Sm}^{3+}$ (1, 2, 4, 6, 8, 10, and 12 at.%) samples monitored at 606 nm. Similar to the excitation spectra of $\text{Gd}_2\text{O}_3:\text{Bi}^{3+}/\text{Eu}^{3+}$ discussed in Sec. 6.3.4.1, the spectra consist of (i) excitation peaks related to the $\text{Gd}_2\text{O}_3:\text{Sm}^{3+}$ and (ii) excitation peaks originated from the Bi^{3+} . The sharp peak observed at 274 nm is due to the $^8\text{S}_{7/2} \rightarrow ^6\text{I}_{15/2}$ transition within the Gd^{3+} [36,37]. And, other sharp peak in the longer wavelength region at 406, 422, 467 and 492 nm is due to the $^7\text{H}_{5/2} \rightarrow ^6\text{P}_{3/2}$, $^7\text{H}_{5/2} \rightarrow ^6\text{D}_{5/2}$, $^7\text{I}_{11/2} \rightarrow ^6\text{P}_{3/2}$, and $^7\text{H}_{5/2} \rightarrow ^6\text{G}_{7/2}$ transitions respectively within the $f-f$ shell of Sm^{3+} [4,66-69]. The excitation peaks at 335, 347 and 380 nm are originated from the Bi^{3+} absorption. These peaks are due to the presence of two types of lattice sites namely, C_2 and S_6 having octahedral coordination in cubic Gd_2O_3 (as discussed in 6.3.4.1).

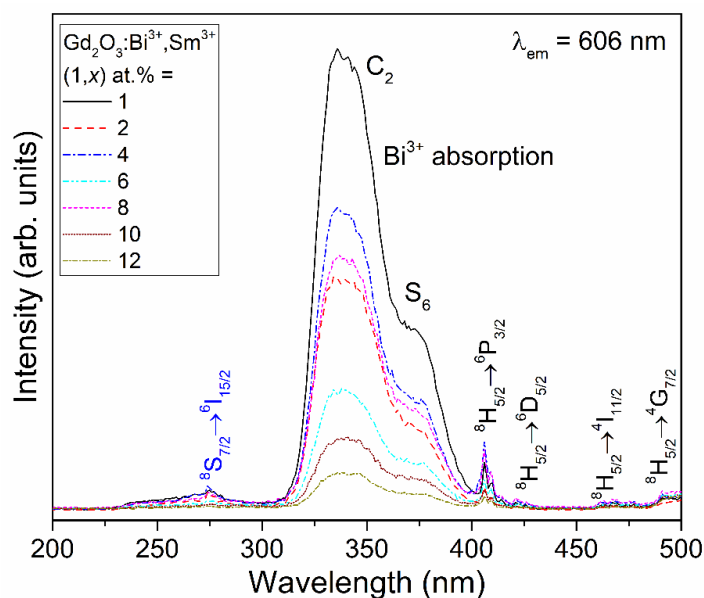


Fig. 6.20. PL excitation spectra of Bi^{3+} (1 at.%) sensitized $\text{Gd}_2\text{O}_3:\text{Sm}^{3+}$ (1, 2, 4, 6, 8, 10 and 12 at.%) samples monitored at $\lambda_{\text{em}} = 606$ nm

Fig. 6.21 illustrates the emission spectra of $\text{Gd}_2\text{O}_3:\text{Bi}^{3+}$ (1 at.%)/ Sm^{3+} (2 at.%) samples under different excitations at 274 nm (Gd^{3+} , S-I), 335 nm (Bi^{3+} , related to C_2 site), 375 nm (Bi^{3+} , related to S_6 site) and direct excitations at 406 nm. Comparing the emission peak at 606 nm, it can be observed that the emission intensity is highest when excited at 335 nm than other remaining excitations. This suggests that the sensitization of $\text{Gd}_2\text{O}_3:\text{Sm}^{3+}$ with Bi^{3+} can render the energy transfer to the Sm^{3+} resulting improved

emission intensity (discussed later). The remaining part of the study will be concentrated with the excitations related to Bi^{3+} absorption only.

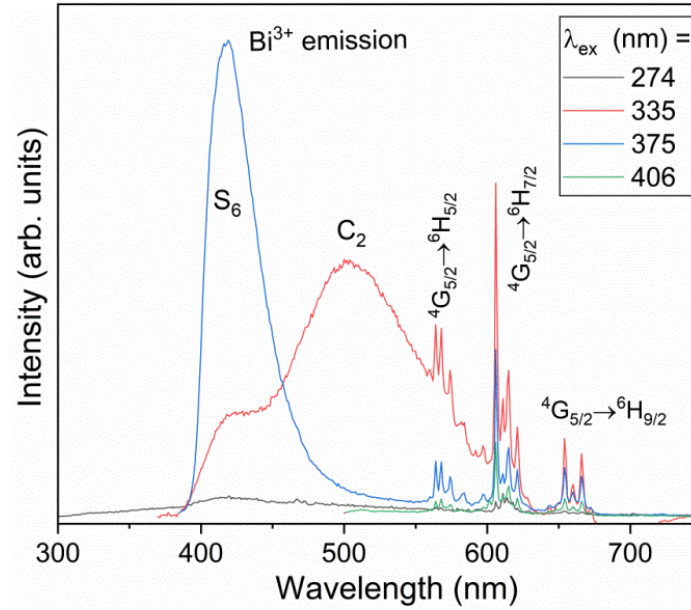


Fig. 6.21. PL emission spectra of $\text{Gd}_2\text{O}_3:\text{Bi}^{3+}$ (1 at.)/ Sm^{3+} (2 at.%) samples under different excitations at 274 nm (Gd^{3+} , S-I), 335 nm (Bi^{3+} , related to C_2 site) and 375 nm (Bi^{3+} , related to S_6 site) and 406 nm ($f-f$ absorption).

The emission spectra consist of two types: (i) the broad emission peak with two humps at ~ 417 and 504 nm in the region of ~ 380 to 575 nm and (ii) sharp emission peaks in the region of ~ 550 to 700 nm. The broad band emission is related to the Bi^{3+} originated from $^3\text{P}_1 \rightarrow ^1\text{S}_0$. The presence of these two distinct humps in the emission band is due to the Bi^{3+} occupying at 2 (two) different symmetry sites (discussed in Sec. 6.3.4.1). The sharp emission peaks mentioned in (ii) are related to the transitions within the $f-f$ electronic energy levels of Sm^{3+} . These emission peaks are related to the transitions originated from the $^4\text{G}_{5/2} \rightarrow ^6\text{H}_{5/2}$ (at 564, 568 and 574 nm) and $^4\text{G}_{5/2} \rightarrow ^6\text{H}_{5/2}$ (at 606, 615 and 621 nm) are related to magnetic dipole transitions. While, the transition at $^4\text{G}_{5/2} \rightarrow ^6\text{H}_{9/2}$ (at 654 and 665 nm) is due to pure electric dipole transition [4,66-70]. In all the cases, the transition at $^4\text{G}_{5/2} \rightarrow ^6\text{H}_{5/2}$ (at 606, 615 and 621 nm) is dominant even though it due to magnetic dipole transition, $\Delta J = \pm 1$, it is also dominated with electric dipole transition [70,71].

6.3.5.2. Mechanism of energy transfer: Bi^{3+} to Sm^{3+}

Fig. 6.22 shows the emission spectra of $\text{Gd}_2\text{O}_3:\text{Bi}^{3+}$ (1 at.)/ Sm^{3+} (0, 1, 2, 4, 6, 8, 10 and 12 at.%) samples under the excitation of (a) 335 and (b) 375 nm. From both the

figures, the gradual decrease in the intensity of emission band related to the Bi^{3+} is observed with the increase in Sm^{3+} concentration.

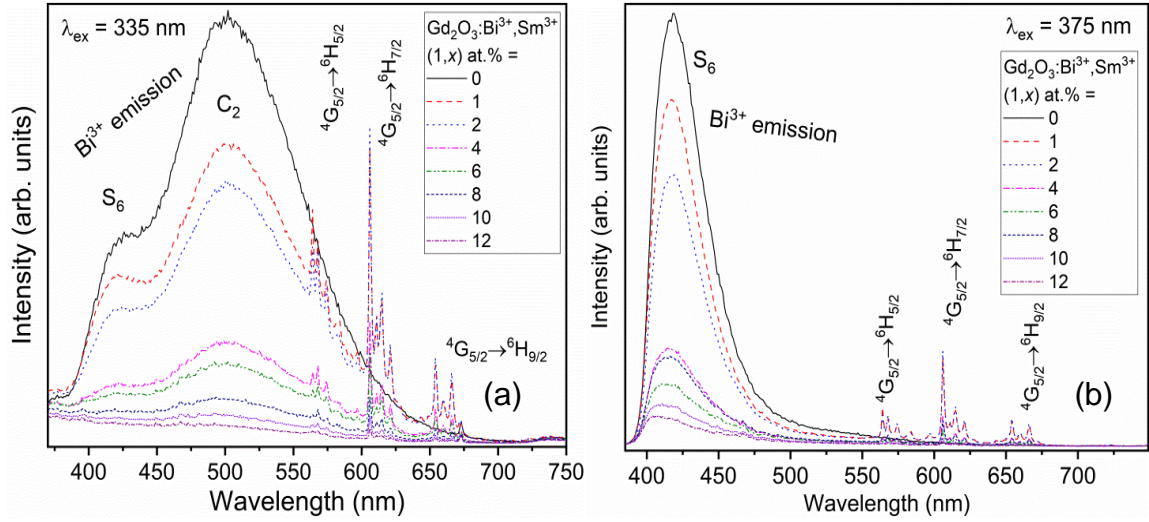


Fig. 6.22. Normalized PL emission $\text{Gd}_2\text{O}_3:\text{Bi}^{3+}$ (1 at.%)/ Sm^{3+} (0, 1, 2, 4, 6, 8, 10 and 12 at.%) samples under the excitation of (a) 335 and (b) 375 nm.

This is due to the increase in the non-radiative energy transfer to the excited states of randomly distributed Sm^{3+} ions over the radiative transition within Bi^{3+} . This suggests the occurrence of energy transfer in both the cases. The efficiency of the energy transfer is calculated using Eq. 6.2. Fig. 6.23 shows the energy transfer efficiency under the excitation of 335 and 375 nm. The energy transfer efficiency reaches $\sim 90\%$ in both the cases.

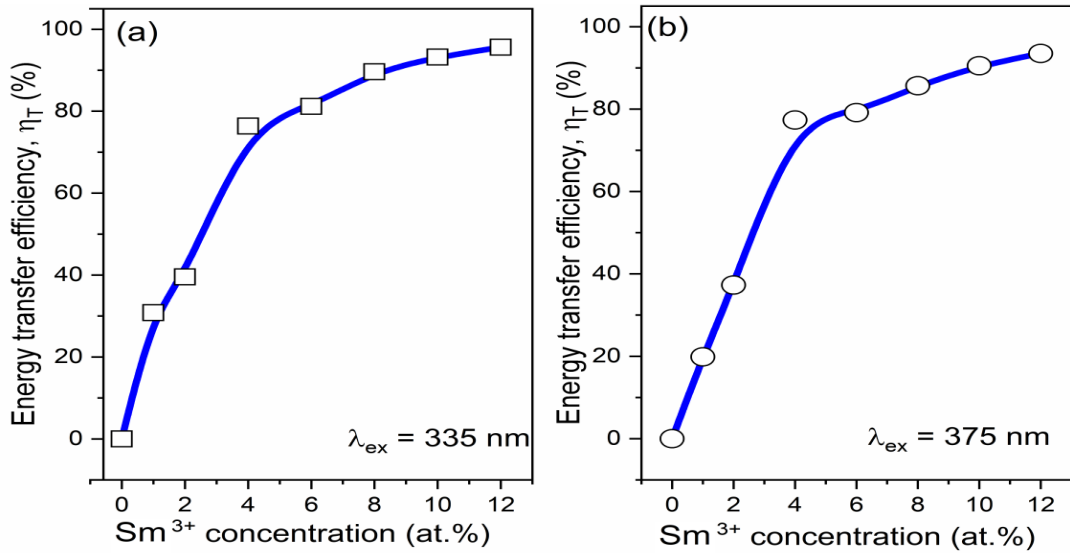


Fig. 6.23. Energy transfer efficiency (η) from the sensitizer (Bi^{3+}) to the excited states of activator (Sm^{3+}) in $\text{Gd}_2\text{O}_3:\text{Bi}^{3+}$ (1 at.%)/ Sm^{3+} (0, 1, 2, 4, 6, 8, 10 and 12 at.%) samples under the excitation of (a) 335 and (b) 375 nm.

As discussed in Sec. 6.3.4.2, the energy transfer occurs through (i) exchange interactions and (ii) multipolar interactions. These interactions depend on the distance between the acceptor and donor. The critical distance between them is calculated using Eq. 6.3, The critical concentration (x_c) value is 3 at.%. The critical distance (R_c) calculated using Eqn. (4) is found to be $\sim 13 \text{ \AA}$. This value is greater than the restricted distance ($\sim 5 \text{ \AA}$) of exchange interaction. This establishes the presence of multipolar type of energy transfer. On the basis of Reisfeld's approximation equation (Eq. 6.4), the best fit is observed with the values of $n = 6$ and 8. On the basis of these fitting parameters, it may be understood that the energy transfer from the Bi^{3+} to the excited states of Sm^{3+} occurs mainly through both *dipole – dipole* and *dipole-quadrupole*. Fig. 6.24 shows the typical fitting using Eq. 6.4.

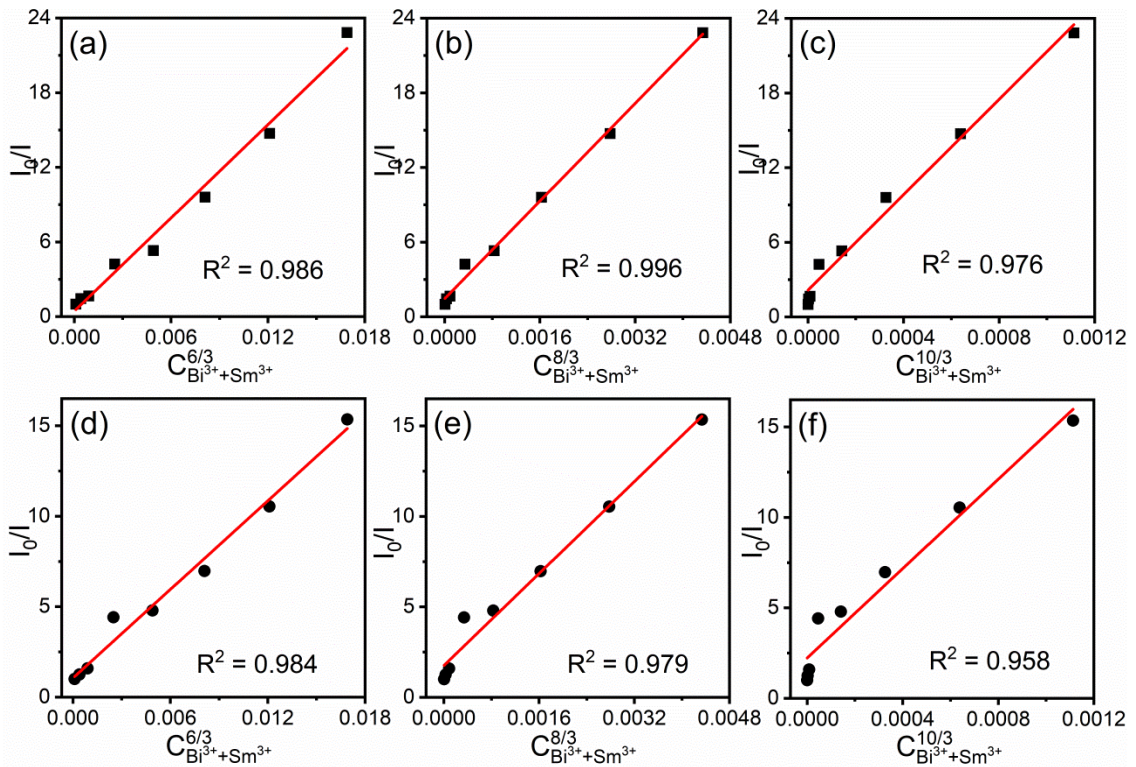


Fig. 6.24. Dependence of I_{S0}/I_S of Bi^{3+} on $C_{\text{Bi}^{3+}}/C_{\text{Bi}^{3+}+\text{Sm}^{3+}}^{n/3}$ where $n = 6$ (dipole-dipole), $n = 8$ (dipole-quadrupole) and $n = 10$ (quadrupole-quadrupole) interactions respectively, at 335 nm excitation, C_2 symmetry site (a-c) and at 375 nm excitation, S_6 symmetry site (d-f) in $\text{Gd}_2\text{O}_3:\text{Bi}^{3+}$ (1 at.%) / Sm^{3+} (0, 1, 2, 4, 6, 8, 10, and 12 at.%) samples.

6.3.5.3. PL decay lifetime and quantum yield study

Fig. 6.25 shows the decay profiles of Bi^{3+} (1 at.%) in $\text{Gd}_2\text{O}_3:\text{Sm}^{3+}$ (0, 1, 2, 4, 6, 8, 10 and 12 at.%). Excitation and emission wavelengths were monitored at 335 and 500 nm respectively. The decay profiles are better fitted with the second order exponential

decay equation (Eq. 6.5). Similar behaviour is also observed in Bi^{3+} sensitized Gd_2O_3 (Sec. 6.3.4.3). The average decay lifetime can be calculated using Eq. 6.6 and calculated values are given in Table 6.5. The decay lifetime is found to decrease from 531 to 107 ns when the concentration of Sm^{3+} is increase from 0 to 12 at.%. The decay lifetime trend clearly ascertains the increase in the non-radiative transfer of energy to the excited states of Sm^{3+} at the expense of radiative transition in Bi^{3+} . This result supports the energy transfer discussed from the steady state luminescence studies.

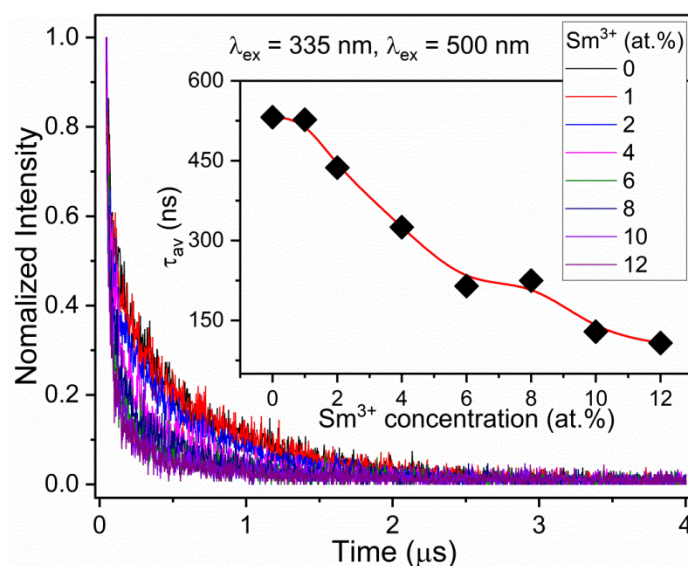


Fig. 6.25. TCSPC decay profiles of Bi^{3+} (1 at.%) in $\text{Gd}_2\text{O}_3:\text{Sm}^{3+}$ (0, 1, 2, 4, 6, 8, 10 and 12 at.%). Excitation and emission wavelengths were monitored at 335 and 500 nm respectively. Inset shows the calculated average lifetime values at different concentration of Sm^{3+} .

Table 6.5: Calculated fitting parameters of decay lifetime of Bi^{3+} emission in $\text{Gd}_2\text{O}_3:\text{Bi}^{3+}$ (1 at.%)/ Sm^{3+} (0, 1, 2, 4, 6, 8, 10 and 12 at.%). Excitation at 335 nm and emission monitored at 500 nm.

Sm^{3+} (at.%)	A_1	τ_1	A_2	τ_2	τ_{av} (ns)	R^2
0	1.18	0.049	0.46	0.629	531	0.99
1	1.45	0.039	0.45	0.625	527	0.98
2	1.93	0.035	0.40	0.558	437	0.97
4	1.97	0.039	0.30	0.478	325	0.97
6	2.77	0.032	0.20	0.408	214	0.96
8	3.21	0.027	0.29	0.381	225	0.95
10	5.15	0.023	0.20	0.320	128	0.95
12	5.36	0.021	0.21	0.274	107	0.95

Fig. 6.26 shows the decay curves of $^5\text{G}_{5/2}$ level of Sm^{3+} emission in $\text{Gd}_2\text{O}_3:\text{Bi}^{3+}$ (1 at.%)/ Sm^{3+} (1, 2, 4, 6, 8, 10 and 12 at.%) samples by monitoring at 606 nm emission. Excitation wavelength is 335 nm (left) and the direct excitation at 464 nm (right). All the decay profiles follow the second order exponential decay (Eqn. 6.5). The average decay lifetime was calculated using Eqn. 6.6 and given in Table 6.6.

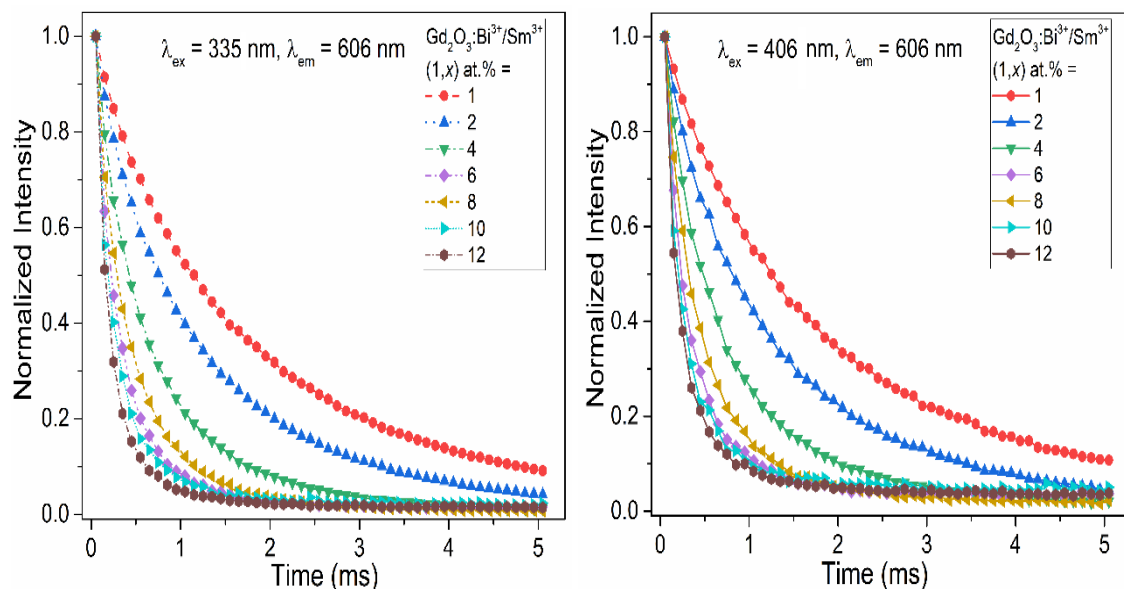


Fig. 6.26. PL decay curves of $^5\text{G}_{5/2}$ level of Sm^{3+} emission in $\text{Gd}_2\text{O}_3:\text{Bi}^{3+}$ (1 at.%)/ Sm^{3+} (1, 2, 4, 6, 8, 10 and 12 at.%) monitored at 606 nm. Excitation wavelengths (a) 335 nm (left) and 406 nm (right)

Table 6.6: The average lifetime calculated for the decay curves of $^5\text{G}_{5/2}$ level of Sm^{3+} by monitoring at 606 nm emission and Quantum yield in $\text{Gd}_2\text{O}_3:\text{Bi}^{3+}$ (1 at.%)/ Sm^{3+} (1, 2, 4, 6, 8, 10 and 12 at.%) samples.

Sm ³⁺ (%)	Decay lifetime, τ_{av} (ms)				Quantum Yield
					(%)
	$\lambda_{\text{exc}} = 335 \text{ nm}$		$\lambda_{\text{exc}} = 464 \text{ nm}$		$\lambda_{\text{exc}} = 335 \text{ nm}$
	τ_{av}	R^2	τ_{av}	R^2	
1	1.77	0.99	1.86	0.99	5
2	1.30	0.99	1.36	0.99	7
4	0.79	0.99	0.88	0.99	-
6	0.38	0.99	0.42	0.99	-
8	0.52	0.99	0.57	0.99	-
10	0.32	0.99	0.35	0.99	-
12	0.29	0.99	0.34	0.99	-

The decay lifetime varies from 0.29 to 1.77 ms when the excitation was used at 335 nm. On the other hand, under direct excitation at 464 nm, the lifetime value increases from 0.34 to 1.86 ms. From the Table 6.6, it can be observed that the decay lifetime value in both the cases decreases with the increase of Sm^{3+} concentration beyond 1 at.%. Such decrease in the decay lifetime of lanthanide ions emission can be attributed to the increase in the non-radiative transitions due to the cross relaxation among lanthanide ions. Such behaviour has been reported earlier [66,72]. The quantum yields for $\text{Gd}_2\text{O}_3:\text{Bi}^{3+}$ (1 at.%) / Sm^{3+} (1 and 2 at.%) under 335 nm excitation are found to be 5 and 7% respectively (Table 6.6).

6.3.5.4. CIE chromaticity studies

Fig. 6.27 illustrates the CIE chromaticity of the Sm^{3+} emission in $\text{Gd}_2\text{O}_3:\text{Bi}^{3+}$ (1 at.%) / Sm^{3+} (1, 2, 4, 6, 8, 10 and 12 at.%) samples under (a) 335 and (b) 375 nm.

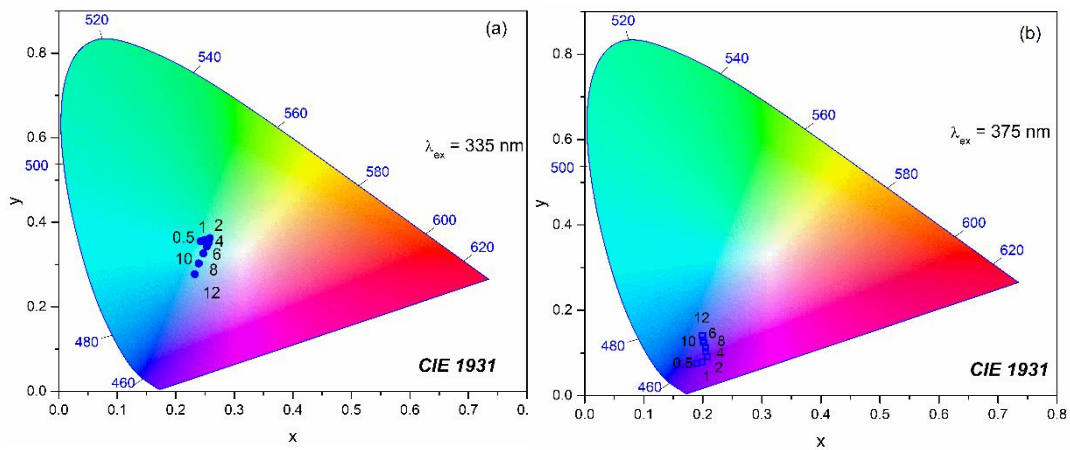


Fig. 6.27. CIE chromaticity coordinate positions of $\text{Gd}_2\text{O}_3:\text{Bi}^{3+}$ (1 at.%) / Sm^{3+} (0.5, 1, 2, 4, 6, 8, 10 and 12 at.%) samples excited at (a) 335 nm, (b) 375 nm.

From the figure, it can be observed that the emission is concentrated in the blue and green region for all the samples. This might be due to dominance of Bi^{3+} emission over the orange-red emission from the Sm^{3+} . Even though there is enough energy transfer occur in the higher concentration region i.e. ≥ 4 at.%, the intensity of the orange-red emission of the Sm^{3+} has already started to quench after 2 at.% due to concentration quenching. Therefore, the emission region from all the samples investigated falls in the blue-green part of the CIE space. Thus, we may understand that the Bi^{3+} sensitized $\text{Gd}_2\text{O}_3:\text{Sm}^{3+}$ phosphors may not be suitable as red emitting phosphor.

6.4. Conclusions

Bi^{3+} sensitized Eu^{3+} and Sm^{3+} doped Gd_2O_3 were successfully synthesized by hydrothermal method with post annealing at 900 °C. The as prepared samples are crystallized in hexagonal phase and subsequently changes to crystalline cubic phase post annealing. The occupancy of sensitizer in two different symmetry sites enables to excite $\text{Gd}_2\text{O}_3:\text{Eu}^{3+}$ and $\text{Gd}_2\text{O}_3:\text{Sm}^{3+}$ at different wavelengths. Efficient energy transfer upto 97% from Bi^{3+} to the excited states of Eu^{3+} is observed. While, the energy transfer efficiency in the case Sm^{3+} is reached ~90%. The energy transfer is resonant type and occurs mainly through dipole-dipole interaction in $\text{Gd}_2\text{O}_3:\text{Bi}^{3+}/\text{Eu}^{3+}$. Whereas, the energy transfer is contributed by both dipole-dipole and dipole-quadrupole interactions $\text{Gd}_2\text{O}_3:\text{Bi}^{3+}/\text{Sm}^{3+}$. Both the steady state and decay dynamics of the PL corroborates the occurrence of energy transfer in both the cases. The emission colour can be tuned from blue/bluish green to red with the variation of activator concentration and the excitation wavelength in $\text{Gd}_2\text{O}_3:\text{Bi}^{3+}/\text{Eu}^{3+}$. Under the excitation in the wavelength range ~330 – 380 nm, colour saturation of the red emission is observed to be high. This could be a potential red emitting phosphor component for UV LED converted white LEDs. However, in the case of $\text{Gd}_2\text{O}_3:\text{Bi}^{3+}/\text{Sm}^{3+}$, mostly the emission color is observed to be found in the blue-greenish region in the CIE space. The $\text{Gd}_2\text{O}_3:\text{Bi}^{3+}/\text{Sm}^{3+}$ may not be a promising red phosphor.

References

1. H. Dong, S.-R. Du, X.-Y. Zheng, G.-M. Lyu, L.-D. Sun, L.-D. Li, P.-Z. Zhang, C. Zhang, C.-H. Yan, *Chem. Rev.* 115(19) (2015) 10725-10815.
2. H. Deng, F. Chen, C. Yang, M. Chen, L. Li, D. Chen, *Nanotechnology* 29(41) (2018) 415601.
3. H. Kim, H. Jeong, S.-H. Byeon, *ACS Appl. Mater. Interfaces* 8(24) (2016) 15497-15505.
4. R. Wangkhem, N. S. Singh, N. P. Singh, S. D. Singh, L. R. Singh, *J. Lumin.* 203 (2018) 341-348.
5. X. Huang, *Nat. Photonics* 8 (2014) 748-749.
6. M. Shang, C. Li, J. Lin, *Chem. Soc. Rev.* 43 (2014) 1372-1386.
7. N. S. Singh, N. K. Sahu, D. Bahadur, *J. Mater. Chem. C* 2 (2014) 548.
8. D. Wilhelm, D. Baumann, M. Seibald, K. Wurst, G. Heymann, H. Huppertz, *Chem. Mater.* 29 (2017) 1204-1209.
9. D. P. Cui, Q. C. Xiang, Z. Song, Z. G. Xia, Q. L. Liu, *J. Mater. Chem. C* 4 (2016) 7332-7338.
10. G. J. Hoerder, M. Seibald, D. Baumann, T. Schröder, S. Peschke, P. C. Schmid, T. Tyborski, P. Pust, I. Stoll, M. Bergler, C. Patzig, S. Reißaus, M. Krause, L. Berthold, T. Höche, D. Johrendt, H. Huppertz, *Nat. Commun.* 10 (2019) 1824.
11. P. Pust, A. S. Wochnik, E. Baumann, P. J. Schmidt, D. Wiechert, C. Scheu, W. Schnick, *Chem. Mater.* 26 (2014) 3544-3549.
12. T. Sakthivel, G. Annadurai, R. Vijayakumar, X. Huang, *J. Lumin.* 205 (2019) 129-135.
13. Q. Zhang, X. Wang, X. Ding, and Y. Wang, *Inorg. Chem.* 56 (2017) 6990-6998.
14. P. Du, J. S. Yu, *Sci. Rep.* 7 (2017) 11953.
15. S. Shi, L. Wang, M. Fang, L. Fu, L. D. Carlos, R. A. S. Ferreira, J. Wang, S. Wang, *J. Alloys Compd.* 814 (2020) 15226-15232.
16. R. Wangkhem, T. Yaba, N. S. Singh, R. S. Ningthoujam, *J. Appl. Phys.* 123 (2018) 124303.
17. S. Yan, J. Zhang, X. Zhang, S. Lu, X. Ren, Z. Nie, X. Wang, *J. Phys. Chem. C*, 111 (2007) 13256-13260.
18. A. Xie, X. Yuan, S. Hai, J. Wang, F. Wang and L. Li, *J. Phys. D: App. Phys.* 42 (2009) 1-7.
19. T. Yaba, R. Wangkhem, N. S. Singh, *J. Alloys Compd.*, 843 (2020) 156022-156031.
20. P. Du, L.K. Bharat, J.S. Yu, *J. Alloys Compd.* 633 (2015) 37-41.
21. R.B. Pode, S.J. Dhoble, *Phys. Stat. Sol. (b)* 203 (1997) 571-577.
22. L. Chen, K.J. Chen, C.C. Lin, C.I. Chu, S.F. Hu, M.H. Lee, R.S. Liu, *J. Comb. Chem.* 12 (2010) 587-594.
23. S. Takeshita, T. Isobe, S. Niikura, *J. Lumin.* 128 (2008) 1515 - 1522.
24. L. S. Chi, R. S. Liu, B. J. Lee, *J. Electrochem. Soc.* 152(8) (2005) J93-J98.
25. W. Wang, P. Zhu, *Opt. Express* 26 (2018) 34820-34829.
26. P. Zhu, W. Wang, H. Zhu, P. Vargas, A. Bont, *IEEE Photonics J.* 10 (2018) 1-10.
27. G. Ju, Y. Hu, L. Chen, X. Wang, Z. Mu, H. Wu, F. Kang, *J. Electrochem. Soc.* 158 (2011) J294-J299.

28. T. W. Chou, S. Mylswamy, R. S. Liu, S. Z. Chuang, *Solid State Commun.* 136 (2005) 205-209.
29. H. Deng, F. Chen, C. Yang, M. Chen, L. Li, D. Chen, *Nanotechnology* 29(41) (2018) 415601.
30. J. Liu, X. Tian, N. Luo, C. Yang, J. Xiao, Y. Shao, X. Chen, G. Yang, D. Chen, L. Li, *Langmuir* 30(43) (2014) 13005–13013.
31. D. Ghosh, M. N. Luwang, *J. Lumin.* 171 (2016) 1-8.
32. N. Vashistha, A. Chandra, M. Singh, *New J. Chem.* 44 (2020) 14211-14227.
33. X. Wu, S. Hu, C. Tan, Y. Liu, *Opt. Commun.* 328 (2014) 23.
34. Q. Li, J. Lin, J. Wu, Z. Lan, Y. Wang, F. Peng, M. Huang, *J. Limun.* 134 (2013) 59.
35. J.F. Martel, S. Jandl, B. Viana, D. Vivien, *J. Solid State Chem.* 61 (2000) 1455.
36. R. S. Ningthoujam, R. Shukla, R. K. Vatsa, V. Duppel, L. Kienle, A. K. Tyagi, *J. Appl. Phys.* 105 (2008) 084304.
37. G. Kaur, S. K. Singh, S. B. Rai, *J. Appl. Phys.* 107 (2010) 073514.
38. B. Liu, J. Li, G. Duan, Q. Li, Z. Liu, *J. Lumin.* 206 (2019) 348-358.
39. X. T. Wei, Y. H. Chen, X. R. Cheng, M. Yin, W. Xu, *Appl. Phys. B* 99 (2010) 763-768.
40. L. Xu, Y. Li, Q. Pan, D. Wang, S. Li, G. Wang, Y. Chen, P. Zhu, W. Qin, *ACS Appl. Mater. Interfaces* 12 (2020) 18934-18943.
41. B. Bihari, H. Eilers, B. M. Tissue, *J. Lumin.* 75 (1997) 1-10.
42. M. Buijs, A. Mayerink, and G. Blasse, *J. Lumin.* 37 (1987) 9-20.
43. M. L. Debasu, D. Ananias, A. G. Macedo, J. Rocha, L. D. Carlos, *J. Phys. Chem. C* 115 (2011) 15297–15303.
44. G. Liu, Y. Zhang, J. Yin, and W. F. Zhang, *J. Lumin.* 128 (2008) 2008-2012.
45. B. Qian, H. Zou, D. Meng, X. Zhou, Y. Song, K. Zheng, C. Miao and Y. Sheng, *CrystEngCom.* 20(45) (2018) 7322-73288.
46. R.G.A. Kumar, S. Hata, K.G. Gopchandran, *J. Ceram. Int.* 39(8) (2013) 9125-9136.
47. K. M. Koczur, S. Mourdikoudis, L. Polavarapu, S.E. Skrabalak, *Dalton Trans.* 44 (2015) 17883-17905.
48. N.K. Sahu, N. Shanta Singh, R.S. Ningthoujam, D. Bahadur, *ACS Photonics* 1 (2014) 337-246.
49. R. Joshi, B.P. Singh, C.L. Prajapat, Y. Kashyap, C. Nayak, D. Bhattacharyya, R.S. Ningthoujam, *J. Phys. Chem. C* 125 (2021) 17971-17982.
50. H. Liu, B. Zhang, H. Shi, Y. Tang, K. Jiao, X. Fu, *J. Mater. Chem.* 18 (2008) 2573-2580.
51. G. Liu, G. Hong, J. Wang, X. Dong, *J. Alloys Compd.* 4332 (2007) 200-204.
52. N. Dhananjaya, H. Nagabhushana, S.C. Sharma, B. Rudraswamy, C. Shivakumar, B.M. Nagabhushana, *J. Alloys Compd.* 587 (2014) 755-762.
53. A. Jain, G.A. Hirata, *Ceram. Int.* 42(5) (2016) 6428–6435.
54. S. Gai, P. Yang, D. Wang, C. Li, N. Niu, F. Hea, X. Li, *CrystEngCom.* 13(17) (2011) 5480-5487.
55. O. S. Singh, R. Wangkhem, N. S. Singh, *J. Alloys Compd.* 875 (2021) 160059.
56. E. Zych, *J. Phys.: Condens. Matter* 14 (2002) 5637–5650.
57. G. Pappalardo, R. B. Hunt, Jr., *J. Electrochem. Soc.* 132 (1985) 721-730

58. O. Meza, E. G. Villabona-Leal, L. A. Diaz-Torres, H. Desirena, J. L. Rodríguez-López, Elías Pérez, *J. Phys. Chem. A* 118 (2014) 1390–1396.
59. N. Shanta Singh, R. S. Ningthoujam, L. Romila Devi, N. Yaiphaba, V. Sudarsan, S. Dorendrajit Singh, R. K. Vatsa, R. Tewari, *J. Appl. Phys.* 104 (2010) 104307.
60. N. Yaiphaba, R. S. Ningthoujam, N. Shanta Singh, R. K. Vatsa, N. Rajmuhon Singh, Sangita Dhara, N. L. Misra, R. Tewari, *J. Appl. Phys.* 107 (2010) 034301.
61. R. Reisfeld, L. Boehm, *J. Solid State Chem.* 4 (1972) 417–424.
62. G. Blasse, *Phys. Lett. A* 28 (1968) 444–445.
63. D.L. Dexter, *J. Chem. Phys.* 21 (1953) 836–850.
64. D. Huang, P. Dang, H. Lian, Q. Zeng, J. Lin, *Inorg. Chem.* 58 (2019) 15507–15519.
65. Z. Xia, S. Miao, M. Chen, M.S. Molokeev, Q. Liu, *Inorg. Chem.* 54 (2015) 7684–7691.
66. N.S. Singh, R.S. Ningthoujam, G. Phaomei, S.D. Singh, A. Vinu, R.K. Vatsa, *Dalton Trans.* 41 (2012) 4404–4412.
67. E. Cavalli, A. Belletti, R. Mahiou, P. Boutinaud, *J. Lumin.* 130 (2010) 733.
68. E. Cavalli, *J. Lumin.* 183 (2017) 172–177.
69. O. Tegus, B. Amurinsana, S. Zhiqiang, *J. Lumin.* 215 (2019) 116624.
70. G. Lakshminarayana, J. Qiu, *J. Lumin.* 476 (2009) 470 – 476.
71. P.S. May, D.H. Metcalf, F.S. Richardson, R.C. Carter, C.E. Miller, R.A. Palmer, *J. Lumin.* 51 (1991) 249.
72. N.S. Singh, R. Wangkhem, T. Yaba, S. Devi, M.N. Luwang, N. Yaiphaba, H.S. Devi, T.D. Singh, *J. Alloys Compd.* 726 (2017) 1161 – 1167.



नागालैण्ड विश्वविद्यालय

NAGALAND UNIVERSITY

(संसद द्वारा पारित अधिनियम 1989, क्रमांक 35 के अंतर्गत स्थापित केंद्रीय विश्वविद्यालय)
(A Central University established by an Act of Parliament No.35 of 1989)

मुख्यालय : लुमामी, जिला : जुन्हेबोटो (नागालैण्ड), पिनकोड - 798627

Hqrs: Lumami, Dist. Zunheboto (Nagaland), Pin Code - 798627

वेबसाइट / Website : www.nagalanduniversity.ac.in

Ph.D. Thesis Certificate on Plagiarism Check

Name of Research Scholar	OINAM SHANTAJIT SINGH
Ph.D. Registration Number	854/2020
Title of Ph.D. thesis	Study on Photoluminescence Properties of unsensitized and Bi ³⁺ sensitized M ₂ O ₃ :Ln ³⁺ (M = Gd, Y & Ln ³⁺ = Eu ³⁺ , Sm ³⁺) Phosphors
Name & Institutional Address of the Supervisor	Dr. Naorem Shanta Sigh, Department of Physics, Nagaland University
Name of the Department and School	Department of Physics, School of Science
Date of submission	29-5-2022
Date of plagiarism check	29-5-2022
Percentage of similarity detected by the URKUND software	3 %

I hereby declare/ certify that the Ph.D. Thesis/ M. Phil. Dissertation submitted by me is complete in all respect, as per the guidelines of Nagaland University (NU) for this purpose. I also certify that the Thesis/ Dissertation (soft copy) has been checked for plagiarism using URKUND similarity check software. It is also certified that the contents of the electronic version of the thesis/dissertation are the same as the final hardcopy of the thesis /dissertation. Copy of the Report generated by the URKUND software is also enclosed.

Date:

Place:

(OINAM SHANTAJIT SINGH)

Name & Signature of the Scholar

(Dr. NAOREM SHANTA SINGH)












Name & Signature of the Supervisor

With seal

Document Information

Analyzed document	Study on Photoluminescence Properties of unsensitized and Bi ³⁺ sensitized M ₂ O ₃ -Ln ₃ (M = Gd, Y & Ln ₃ = Eu ³⁺ , Sm ³⁺) Phosphors.docx (D138343062)
Submitted	2022-05-29T12:41:00.0000000
Submitted by	Naorem Shanta Singh
Submitter email	ssnaorem@nagalanduniversity.ac.in
Similarity	3%
Analysis address	ssnaorem.naga@analysis.arkund.com

Sources included in the report

SA	Yatish Thesis.pdf.pdf Document Yatish Thesis.pdf.pdf (D115930611)		2
SA	Anns George-Synthesis Structural and Luminescence Characterization of Eu³⁺ Dy³⁺ Doped Calcium Antimonate Phosphors.pdf Document Anns George-Synthesis Structural and Luminescence Characterization of Eu ³⁺ Dy ³⁺ Doped Calcium Antimonate Phosphors.pdf (D137597897)		2
W	URL: https://kundoc.com/download/a-reddish-orange-emitting-samarium-doped-na3yvo42-nanocrystals-for-single-phased_5e3eeff2097c470d228b4627.html Fetched: 2022-01-02T10:16:45.1470000		6
SA	L.LAKSHMI DEVI_Physics.pdf Document L.LAKSHMI DEVI_Physics.pdf (D105637775)		4
SA	Krishnapriya T-Structural and luminescent characteristics of Eu³⁺ Dy³⁺ doped CaZn₂ (PO₄)₂ and Na₆CaP₂O₉ phosphors for optoelectronic applications.pdf Document Krishnapriya T-Structural and luminescent characteristics of Eu ³⁺ Dy ³⁺ doped CaZn ₂ (PO ₄) ₂ and Na ₆ CaP ₂ O ₉ phosphors for optoelectronic applications.pdf (D137601718)		2
SA	Phd Thesis Sajesh Draft2.docx Document Phd Thesis Sajesh Draft2.docx (D130631628)		1
SA	thesis S P HARGUNANI PHYSICS SCIENCE & TECHNOLOGY (1).docx Document thesis S P HARGUNANI PHYSICS SCIENCE & TECHNOLOGY (1).docx (D111248353)		1
SA	Sajesh PhD thesis draft.docx Document Sajesh PhD thesis draft.docx (D130047240)		4
W	URL: https://www.semanticscholar.org/paper/Excitation-and-activator-concentration-induced-and-Singh-Wangkhem/e1a4b0cab6fd241d5b9860bb780eed9a6fc49fa3 Fetched: 2022-05-29T12:41:23.1000000		1
SA	Kukku Paper.pdf Document Kukku Paper.pdf (D41579933)		2
SA	sreeja - thesis.pdf Document sreeja - thesis.pdf (D53786596)		2

List of Publications

1. **O. Shantajit Singh**, Ranjoy Wangkhem, N. Yaiphaba, Th. David Singh, N. Shanta Singh, " Bi^{3+} sensitized $\text{Gd}_2\text{O}_3:\text{Eu}^{3+}$: A potential red phosphor for UV LED pumped white light emission" Journal of Alloys and Compounds 902 (2022) 163831 [[10.1016/j.jallcom.2022.163831](https://doi.org/10.1016/j.jallcom.2022.163831)]
2. **O. Shantajit Singh**, Ranjoy Wangkhem, N. Shanta Singh, "Excitation and activator concentration induced color tuning and white light generation from Bi^{3+} sensitized $\text{Y}_2\text{O}_3:\text{Eu}^{3+}$: Energy transfer studies", Journal of Alloys and Compounds 875 (2021) 160059. [[10.1016/j.jallcom.2021.160059](https://doi.org/10.1016/j.jallcom.2021.160059)]

Paper presented in Conference/Seminar(s)

1. O. Shantajit Singh *et al.*, *Bi³⁺ sensitized Gd₂O₃:Eu³⁺ as a potential red phosphor*, National Seminar on Emerging Research in Chemical Sciences (ERCS-2022), April 11 & 12, 2022, Department of Chemistry, D. M. College of Science, Imphal Manipur.
2. O. Shantajit Singh *et al.*, *Photoluminescence studies of Bi³⁺ sensitized Y₂O₃ nanoparticles: energy transfer study and colour tunability for pcLEDs*, International Conference on Chemical and Biological Sciences in Drug Discovery (IC-CBSDD-2019), March 8-10, 2019, P. G. Department of Chemistry, Berhampur University, Bhanja Bihar, Odisha-760007, India,
3. O. Shantajit Singh *et al.*, *Synthesis and Photoluminescence Studies of Bi³⁺ Sensitized Y₂O₃:Eu³⁺ Nanoparticles as a Red Emission Source for pcLEDs*, National Seminar Cum Workshop in Nanoscience (NSWN-2018), Hands on Training on Sophisticated instrument, May 29-31, 2018, Department of Nanotechnology, NEHU, India.
4. O. Shantajit Singh *et al.*, *Color Tuning and Energy Transfer Studies of Bi³⁺ sensitized Y₂O₃:Eu³⁺ nanoparticles for pcLEDs*, 5th International Conference on Advanced Nanomaterials and Nanotechnology (ICANN-2017), December 18-21, 2017, Centre for Nanotechnology, IIT Guwahati, India.